Measuring the Drell-Yan Cross Section at High Mass in the Dimuon Channel

Robert Scot Hickling
Queen Mary University London

Submitted to QMUL in fulfilment
of the requirements for the award of the
degree of **Doctor of Philosophy**

January 23, 2015

Declaration

I, Robert Hickling, confirm that the research included within this thesis is my own work or that where it has been carried out in collaboration with, or supported by others, that this is duly acknowledged below and my contribution indicated. Previously published material is also acknowledged below.

I attest that I have exercised reasonable care to ensure that the work is original, and does not to the best of my knowledge break any UK law, infringe any third party's copyright or other Intellectual Property Right, or contain any confidential material.

I accept that the College has the right to use plagiarism detection software to check the electronic version of the thesis.

I confirm that this thesis has not been previously submitted for the award of a degree by this or any other university.

Signature:

Date: January 23, 2015

Abstract

A measurement of the Drell-Yan fiducial cross section in the dimuon channel is presented differentially in terms of dimuon invariant mass, double differentially in terms of dimuon invariant mass and rapidity and double differentially in terms of dimuon invariant mass and muon separation $\Delta\eta_{\mu\mu}$. The cross sections are measured using 20.3 fb^{-1} of ATLAS data taken during 2012 at a centre of mass energy of $\sqrt{s} = 8$ TeV.

Dedicated studies determining muon performance corrections for monte carlo isolation and trigger efficiencies and techniques for estimating backgrounds using data driven methods are described in detail. The fiducial cross sections agree within 10% of theoretical predictions in the regions where the statistical uncertainties are subdominant. Excluding the systematic uncertainty associated with the detector luminosity, a systematic uncertainty of below 2.5% is observed for the $m_{\mu\mu} < 300$ GeV region for both the single and double differential cross section measurements. Theoretical predictions to NNLO in QCD including NLO higher order electroweak effects and a photon induced process component are found to underestimate the measurement by 3%. For the $m_{\mu\mu} < 300$ GeV region the uncertainty of the measurement is smaller or of the same order as the theoretical predictions, which indicates that the results will provide useful information into the constraining and tuning of future physics models.

Acknowledgements

I would like to thank everyone who has helped me throughout my Phd. I would especially like to thank my Phd supervisor Eram Rizvi for his guidance in what is a very interesting area of research. He was always patient and understanding when problems in the analysis arose. John Morris provided useful guidance for the L1 Calorimeter study as well as helping with various computer based problems. The friends I made while on attachment at CERN aided my analysis through numerous discussions over many a beer in the local bars of Geneva. I would also like to thank my family for their continuing support.

Contents

Chapter 1.

Introduction

The LHC is the highest energy particle accelerator currently in operation. With a centre of mass energy of 8 TeV it has access to a kinematic phase space never previously studied by experiment. With a successful two years of running through 2011 and 2012 the data obtained gives the scientific community opportunity to test the standard model more rigorously and precisely than ever before. Using data collected by the ATLAS detector in 2012 a precise study of the Drell-Yan process in the high mass region is made in this thesis. As the high mass region has been inaccessible by previous experiments, this study will provide new insights into the structure of the proton and dynamics of particle interactions.

Chapter two contains a review of the standard model of particle physics as well as any theoretical framework required for understanding the function and importance of the Drell-Yan process. Special attention has been paid to the description of the structure of the proton using parton distribution functions and their potential to be studied using Drell-Yan experimental data.

Chapter three gives a review of the sub detector systems contained within the ATLAS experiment. A detailed description of the muon detector systems is given along with a explanation of the reconstruction of muon objects using the ATLAS software.

Chapter four describes a study carried out on the level-one calorimeter trigger system aimed at improving the increasing rates of the E_T^{miss} and forward jet triggers. A reduction of up to a factor of 10 was achieved by increasing background noise cuts implemented in the forward calorimeter systems.

Chapter five contains information on the data and MC samples that are used. The data was collected throughout 2012 at a centre of mass energy of 8 TeV. The MC samples

used are listed in tables along with the correction factors applied to the MC at the truth level.

Chapter six describes the selections applied to the data and the studies determining the muon performance scale factors. Dedicated tag and probe studies have be done to calculate scale factors to correct the MC to data for the isolation and trigger efficiencies.

Chapter seven explains the methods used to determine the expected backgrounds within the analysis phase space. Special attention is taken to describing the data driven mulit-jet background estimation as this cannot be reliably predicted by MC. The remaining backgrounds are predicted by MC and discussed in this chapter.

Chapter eight shows control plots of the data compared to the estimated signal and backgrounds in relevant kinematic variables.

Chapter nine describes how the raw data is unfolded to give cross section results. The determination of the systematic and statistical uncertainties on the cross section are discussed along with the final results for the Drell-Yan cross sections. A comparison is made between the results obtained in this dimuon channel analysis and theoretically calculated predictions

A summary of all of the results is given in the chapter ten conclusions.

The ATLAS collaboration contains over 3000 members and as such all analyses are produced as part of a team effort. Within this analysis additional outside information has been provided for the muon reconstruction, momentum scale and resolution scale factors, the cross section theoretical predictions and the dielectron cross section results. In addition the configuration of the FCal noise cut schemes discussed in the detector study in chapter four have been determined by another analysis. The remaining studies described within this thesis have been carried out by the author. All plots have been produced by the author unless a reference is given.

Chapter 2.

Theory

2.1. The Standard Model

The Standard Model of particle physics is a theory that describes fundamental particles and their interactions as a combination of three quantum field theories (QFT) describing the electromagnetic, weak and strong interactions. Restricting the theory to remain symmetric under certain gauge transformations allows lagrangians describing the dynamics of the system to be constructed. The application of Noethers theorem then predicts these symmetries to manifest themselves as laws of conservation in nature. These laws of conservation have been observed in such properties as charge, energy and angular momentum.

The symmetry of the Standard Model can by split into the non-Abelian gauge theories $SU(2)\times U(1)$ that describe the electromagnetic and weak interactions and the abelian $SU(3)$ group that describes the strong interaction. The electromagnetic interaction describes the dynamics of electric and magnetic fields, the weak interaction relates to the radioactive decay of atomic nuclei and the strong interaction describes the quark-gluon interactions. A combination of these three forces results in the the $SU(3) \times SU(2) \times U(1)$ Standard Model, which accurately describes the three strongest of the four fundamental interactions. The fourth unaccounted for interaction, gravity is not included in the standard model as attempts to describe it in the quantum field theory mathematical framework have been unsuccessful. Despite the accuracy of the predictions of the standard model, this fact indicates that the model is incomplete and an active area of theoretical research exists to remedy this problem.

There are two types of particles in the standard model, the half integer spin fermions, which make up the matter in the universe and the integer spin gauge bosons, which mediate interactions between them.

The fermion particles in the standard model consist of two groups, the leptons and the quarks. The leptons are split into three generations of charged particles with associated neutrinos. At particle accelerators such as the LHC the leptons are created in abundance and are easy to reconstruct accurately. This means they can be used as handles on the underlying physical processes that produce them. For the analysis presented here the muon is used as a primary decay signature. The associated neutrinos have no charge and are known to oscillate between flavour eigenstates. This property implies that the neutrinos have mass which originally was contradictory to the Standard Model but has since been incorporated using neutrino mixing theory. Currently experiments have been unable to reach the accuracy needed to measure the neutrino mass, but upper limits can be determined. A summary of the fermions is given in table 2.1.

Particle	Symbol	Spin ($\hbar$)	EM Charge (e)	Mass (MeV)
Electron	e	1/2	-1	0.51
Electron Neutrino	ν_e	1/2	0	< 0.002
Muon	μ	1/2	-1	105.66
Muon Neutrino	ν_μ	1/2	0	< 0.19
Tau	τ	1/2	-1	1776.82
Tau Neutrino	ν_τ	1/2	0	< 18.2

Table 2.1.: A summary of the fermion properties. The particles are divided into the first, second and third generations. EM charge is described in terms of electron charge [1].

The quarks can be arranged into three generations and have non integer charges of $+2/3$ or $-1/3$. Additionally the quarks have a colour charge relating to one of fundamental interactions, the strong interaction. The colour charges of a particle system must always equal zero and so all quarks exist in a bound colourless state. Particles made up of quarks are called Hadrons. The properties of the quarks are summarised in table 2.2.

The fields of the fundamental interactions of the standard model are mediated by the exchange of a gauge boson. The photon mediates the electromagnetic force, the gluon

Particle	Symbol	Spin ($\hbar$)	EM Charge (e)	Mass (GeV)
Up	u	1/2	+2/3	0.002
Down	d	1/2	-1/3	0.005
Strange	s	1/2	+2/3	0.095
Charm	c	1/2	-1/3	1.275
Bottom	b	1/2	+2/3	4.18
Top	t	1/2	-1/3	173.21

Table 2.2.: A summary of the quark properties. The particles are divided into the first, second and third generations. EM charge is described in terms of electron charge [1].

mediates the strong force and the $W^{\pm}$ and Z bosons mediate the charge current and neutral current parts of the weak force respectively [1]. The properties of the bosons are listed in table 2.3. While the photon and the gluon particles are massless, the W and Z bosons have a relatively large mass. This creates a problem with the symmetry of the standard model that is explained with introduction of the Higgs mechanism.

Particle	Symbol	Spin ($\hbar$)	EM Charge (e)	Mass (GeV)
Photon	γ	1	0	0
Z	Z	1	0	91.1876
$W^{\pm}$	$W^{\pm}$	1	± 1	80.385
Gluon	g	1	0	0
Higgs	H	0	0	125.7

Table 2.3.: A summary of the fermion properties. EM charge is described in terms of electron charge [1].

[1]The charged current weak interaction can exchange a negative or positive charge via either the W^+ or W^-

2.2. Quantum Electrodynamics

The Standard Model can be described by a Lagrangian equation that details the dynamics of the system. Different terms of the Lagrangian explain the workings of the different fundamental interactions. The theory that describes the electromagnetic interaction is called Quantum Electrodynamics (QED). The term of the Standard Model Lagrangian that describes QED can be built from a Lagrangian describing a fermion field ψ, written as follows:

$$\mathcal{L} = i\bar{\psi}\gamma^{\mu}\delta_{\mu}\psi - m\psi\bar{\psi} \tag{2.1}$$

where γ^{μ} are the dirac matrices and m is the mass of the gauge boson.

Symmetries observed in nature such as charge conservation can be explained as a system that remains invariant under a local gauge transformation. A local gauge transformation is a phase transformation of the form $\psi(x) \rightarrow \psi(x)e^{i\alpha(x)}$, where $\alpha(x)$ is a real number with a space-time dependance. Applying such a transformation to equation 2.1 shows that the Lagrangian is not invariant in its current form. To impose invariance on the system δ_{μ} must be replaced with the covariant derivative D_{μ} thats satisfies the condition $D_{\mu}\psi(x) \rightarrow D_{\mu}\psi(x)e^{i\alpha(x)}$. To construct this covariant derivative a vector field A_{μ}, called the gauge field must be introduced to cancel unwanted terms. This is done using the form:

$$D_{\mu} = \delta_{\mu} - ieA_{\mu} \tag{2.2}$$

where A_{μ} transforms as:

$$A_{\mu} \rightarrow A_{\mu} + \frac{1}{e}\delta_{\mu}\alpha \tag{2.3}$$

where e is the electron charge.

To complete the Lagrangian for QED a kinetic energy term is introduced that also remains invariant under local gauge transformations. This requirements means that the term can only include the gauge invariant electromagnetic field tensor $F_{\mu\nu}$, which is described as follows:

$$F_{\mu\nu} = \delta_{\mu}A_{\mu} - \delta_{\nu}A_{\mu} \tag{2.4}$$

The full Lagrangian for QED can then be written as follows:

$$\mathcal{L}_{QED} = \bar{\psi}(i\gamma^{\mu}D_{\mu}\psi - m)\psi - \frac{1}{4}F_{\mu\nu}F^{\mu\nu} \tag{2.5}$$

The application of a local gauge transformation now leaves the QED Lagrangian invariant under the condition that the term involving the gauge boson mass m is zero. This forces the condition that the gauge boson for the electromagnetic interaction must be massless. The electromagnetic interaction is mediated by the massless photon so this condition fulfilled. However a problem arises when attempts are made to incorporate the weak interaction into the description.

The combination of QED with the weak interaction is called electroweak theory. When a similar local gauge transformation is applied to electroweak interactions the non zero mass of the W and Z bosons leaves the Lagrangian no longer invariant. The masses of these particles can be added into the standard model description by spontaneous symmetry breaking. To restore local gauge invariance an additional scalar field is added to the Lagrangian in the form of the Higgs field. The Higgs field potential is as follows:

$$V(\phi) = \frac{1}{2}\mu^2\phi^2 + \frac{1}{4}\lambda\phi^4 \tag{2.6}$$

For situations where $\mu^2 > 0$ the potential describes a scalar field with mass μ with a vacuum expectation value of $\phi = 0$. However for situations where $\mu^2 > 0$, the potential has a minima of $\phi^2 = -\mu^2/\lambda$ leading to a non zero vacuum expectation value. The vacuum state is now no longer gauge invariant under local gauge transformations leaving gauge boson mass terms, which give the mass of the W and Z bosons. Also as a result of the non zero vacuum expectation value, a gauge boson coupled to mass is predicted called the Higgs boson. The generating of these masses by this mechanism is called spontaneous symmetry breaking.

The Higgs mechanism was predicted in 1964 and ever since experiments have been search for the predicted Higgs boson to confirm the theory [2] [3]. After 40 years of searching for the Higgs boson the ATLAS and CMS detectors at the LHC discovered a new particle at $m_H = 125.7$ GeV, which shared properties of the predicted Higgs boson [4] [5].

2.3. Renormalisation and Running Coupling

The strength of the electromagnetic interaction is described by the fine structure constant:

$$\alpha = \frac{e}{4\pi} \tag{2.7}$$

where e signifies the charge. Experimental observations show that the strength of the electromagnetic interaction has an energy scale dependance. At low energies and large distance the interaction decreases in strength. This is known as the 'running' of the coupling. The effect is caused by fermion anti-fermion pairs spontaneously being created by the photon propagator. These additional loop processes are a polarisation in the vacuum between the particles, which acts as a screen of charge. As the distance between the two particles is reduced the polarised medium between the two also decreases, increasing the interaction strength. This effect leads to a coupling constant that is proportional to the momentum transfer Q, between the interacting particles. To include all the additional loop processes that occur in the interaction, perturbation theory is required. The coupling constant is built from the leading order interaction with the higher order loop processes added as part of a geometric series. However due to the infinite number of possible higher order corrections an arbitrary limit has to be introduced to stop the series diverging to infinity. This process is called renormalisation and allows us to describe the coupling constant with the following equation:

$$\alpha(Q^2) = \frac{\alpha(\mu_R^2)}{1 - \frac{\alpha(\mu_R^2)}{3\pi}\log(\frac{Q^2}{{\mu_R}^2})} \tag{2.8}$$

where μ_R is the renormalisation momentum and is usually chosen to be on scale of the measured physics. The logarithmic dependance of Q means that the higher the order of corrections, the lower the contribution to the interaction. This quality of QED means that renormalisation can provide a very accurate theoretical description of the electromagnetic interaction.

2.4. Quantum Chromodynamics

The theory that describes the strong interaction in the standard model is called quantum chromodynamics (QCD). The strong interaction describes the interactions between quarks

and gluons and is coupled to the colour charge. There are 6 types of colour charge that both the quarks and gluons can have, red, green, blue, anti red, anti green and anti blue $(r, g, b, \bar{r}, \bar{g}, \bar{b})$. The QCD Lagrangian is given by:

$$\mathcal{L}_{QCD} = -\frac{1}{4}F^a_{\alpha\beta}F^{\alpha\beta}_a + \sum_{f=1}^{n_f}\bar{q}_f(i\gamma^\mu D_\mu - m_f)q_f \tag{2.9}$$

where the term $F^a_{\alpha\beta}$ is the field strength tensor given by:

$$F^a_{\alpha\beta} = [\delta_\alpha A^a_\beta - \delta_\beta A^a_\alpha - g_s f^{abc} A^b_\alpha A^c_\beta] \tag{2.10}$$

For these equation q_f and $\bar{q}_f$ represent the quarks and antiquark fields respectively, m_f denotes the quark masses, D_μ is the covariant derivative and the sum runs over f, the different quark flavours. For the field strength tensor the indices a, b and c run over the eight colour combinations of the gluon field and g_s is related to the strong coupling constant by the relation $\alpha_s = g_s^2/4\pi$. The third term in equation 2.10 leads to triplet and quartic gluon self interactions. The fact that gluons can self interact leads to an interesting property of the strong interaction called asymptotic freedom. As in QED, particle anti-particle pairs can be spontaneously produced and annihilated by the propagating boson. However unlike QED the gluon can produce additional gluons via triplet and quartic self interactions. These additional gluon pairs have an opposite effect to the charge screening seen in QED and increase the strength of the interaction with respect to decreasing Q. This property of QCD is called asymptotic freedom and at high Q allows perturbative calculations of cross sections to be made using deep inelastic scattering (DIS) experiments discussed in section 2.6. This inability to escape the strong interaction results in quarks clustering together in colourless states. This effect called colour confinement, explains why no individual quarks have ever been experimentally observed. If the distance between two quarks is large enough, the colour field between them has enough energy to produce quark anti-quark pairs. These quark anti-quark pairs will again form more quarks in a process that continues until the quarks hadronise into colourless hadrons. At proton-proton colliders this results in jets of multiple hadrons being produced as the collision energy is enough to separate partons.

As seen in QED the addition of higher order loop process changes the strength of the strong interaction. A similar prescription to the QED case is applied, however with the addition of the gluon self coupling terms the $\log(Q^2/\mu_R^2)$ term in the strong running

coupling changes sign. The strong coupling constant is given as

$$\alpha_s(Q^2) = \frac{\alpha_s(\mu_R^2)}{1 + \frac{\alpha_s(\mu_R^2)}{12\pi}(33 - 2n_f)\log(\frac{Q^2}{\mu_R 2})} \tag{2.11}$$

where n_f is the number of flavours of the quarks. It can be noted from this equation that the effects of QED would be duplicated in QCD if there were 17 flavours of quarks as this would change the sign of the log term in the denominator. For low Q^2 the strength of the coupling becomes large and the perturbation theory breaks down. Equation 2.11 can be rewritten as:

$$\alpha(Q^2) = \frac{12\pi}{(33 - 2n_f)\log(\frac{Q^2}{\Lambda^2})} \tag{2.12}$$

where Λ^2 gives a energy limit on perturbation theory in QCD. For energies $Q^2 > \Lambda^2$ we can use perturbation theory to describe the strong interaction but for $Q^2 < \Lambda^2$ a non perturbative approach has to be used.

2.5. Parton Distribution Functions

Due to colour confinement quarks always exist in bound colourless states. One such state, the proton is made of three valence quarks (two up quarks and one down quark), which give it its +1 charge and internal quantum numbers. However this is not the complete description of the proton as the colour field produced by the quarks and gluons within the hadron can spontaneously produce virtual quark anti-quark pairs. These virtual quark anti-quark pairs, called sea quarks constantly fluctuate in and out of existence producing a complicated internal structure of the proton. Due to the low energies of the quarks within the proton, perturbative physics cannot be applied without experimental observation providing insight into the structure. Parton distribution functions (PDF) are probability densities of the quarks and gluons existing within the proton based on momentum transfer Q and longitudinal momentum fraction x (also known as Bjorken x). At the LHC protons are collided, meaning PDFs play a crucial role in all physics calculations.

Calculating the cross section of a proton proton interaction can be difficult due to the complicated internal structure of the proton. Factorisation theorem simplifies the problem by splitting the calculation into a calculation of the underlying quark quark interaction

and the experimentally determined PDFs. The total cross section for a proton proton interaction σ_{AB} can be given as:

$$\sigma_{AB} = \int dx_a \, dx_b \, f_{a/A}(x_a) \, f_{b/B}(x_b) \, \sigma_{ab\to X} \tag{2.13}$$

where A and B are the interacting protons, a and b are the interacting quarks, X is the interaction products, and $f_{a/A}(x_a)$ and $f_{b/B}(x_b)$ are the parton PDFs. However this system fails to explain processes that include the emission of real and virtual gluons. Gluons emitted collinear with the quark and anti-quarks particles lead to large logarithms contributions in the perturbative expansion that cause a divergence in the calculation. To remove these divergences the PDFs are redefined to an appropriate scale called the factorisation scale μ_F, which separates the short and long distance physics. Typically this scale is taken to be equal to the momentum transfer Q^2 of the hard scattering process.[2] The introduction of a factorisation scale results in scale dependant PDFs. This scale dependance is required to vanish when all orders of the perturbative expansion are calculated. This requirement results in a set of evolution equations that can be derived relating PDFs at different scales [6]. These evolution equations (DGLAP equations) for the quarks q_i and gluon g follow:

$$\frac{\delta q_i(x,\mu^2)}{\delta \log \mu^2} = \frac{\alpha_s}{2\pi} \int_x^1 \frac{dz}{z} \left[P_{q_i q_j}(z,\alpha_s) q_j(\frac{x}{z},\mu^2) + P_{q_i g}(z,\alpha_s) g(\frac{x}{z},\mu^2) \right] \tag{2.14}$$

$$\frac{\delta g(x,\mu^2)}{\delta \log \mu^2} = \frac{\alpha_s}{2\pi} \int_x^1 \frac{dz}{z} \left[P_{g q_i}(z,\alpha_s) q_j(\frac{x}{z},\mu^2) + P_{gg}(z,\alpha_s) g(\frac{x}{z},\mu^2) \right] \tag{2.15}$$

where the P_{ab} terms are splitting functions that give the probability of parton a producing parton b with a momentum fraction z. The splitting functions are perturbative expansions in orders of $(\alpha_s \log \mu_F^2)^n$ and have been calculated to next-to leading (NLO) order and next -to-next to leading order (NNLO). The Q^2 dependance in the PDFs comes purely from the DGLAP equations, which can be used to recalculate the PDFs at different energy scales. The PDF dependance on the momentum fraction z in determined experimentally.

[2]This follows the renormalisation scale μ_R also typically taken to be Q^2. Commonly $\mu_F = \mu_R = Q^2$

2.6. Current PDF Precision

A combination of deep inelastic scattering (DIS) and proton proton collider experiments are used to constrain PDFs. Deep inelastic scattering experiments scatter probe leptons off hadrons and use the kinematic information of the scattered lepton to infer properties of the proton PDFs. The hadron within this process is either part of a stationary target as with fixed target experiments or collided with the lepton as with electron proton collider experiments. The fixed target experiments can provide constrains to the PDFs at low Q^2 and high x but fail to probe higher Q^2 and low x due to the small centre of mass energy ($\sqrt{s}$) of the collision. Electron proton colliders such as the HERA experiment have a much larger $\sqrt{s}$ and as such have access to a larger kinematic range. Proton proton colliders can again provide an even larger Q^2 range due to the larger size of the colliding particles and hence the $\sqrt{s}$.

There are a number of different groups that combine these experimental results into the PDFs. Each group has slightly different ways of producing the central value of the PDFs as well as the associated uncertainties. As more experimental data is taken the differences in approach should yield smaller differences and values should converge. Figure 2.1 shows the ratio of a selection of PDFs across a varying $\sqrt{\hat{s}}$ (Q). The coloured area shows the uncertainties of the PDFs and this is observed to be 2% at its lowest and rising to above 10% at low and high Q. The analysis described in this thesis covers a region up to $Q = 1.5$ TeV where the uncertainty can reach 5%.

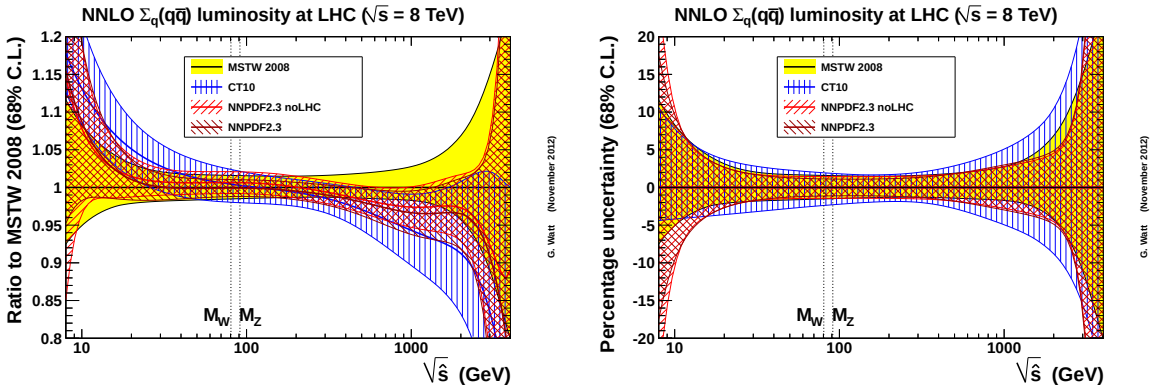

Figure 2.1.: Ratio of quark anti-quark luminosities for MSTW [7] to either CT10 [8] or NNPDF [9] (left). Uncertainty on the PDF in percentage (right) [10].

2.7. The Drell-Yan Process

Th Drell-Yan process was proposed in 1970 to explain the appearance of lepton decay products in hadron-hadron collisions [11]. A quark and anti-quark from the colliding hadrons annihilate producing a virtual photon or Z boson that decays into a lepton anti-lepton pair. The relative clean signature of the lepton decay products mean this process can be measured to a good degree of accuracy. Measurements on the cross section in terms of the Z/γ^* mass and rapidity can provide constraints on PDF models and is explained in the following section. The Drell-Yan process in the dimuon channel is the physics process studied in this thesis. The Feynman diagram for the process is shown in figure 2.2.

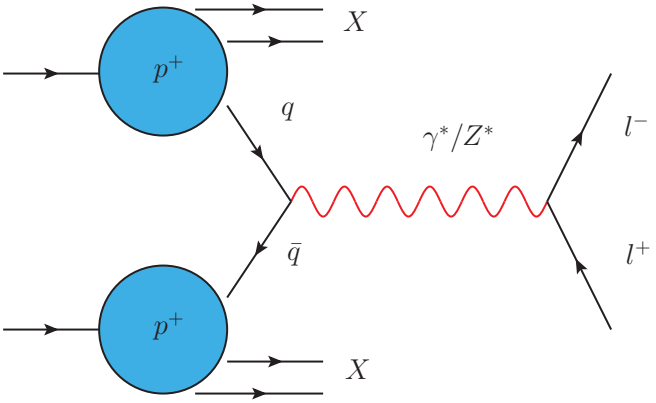

Figure 2.2.: Feynman diagram of the Drell-Yan process.

2.7.1. Drell-Yan Cross Section

Using the factorisation theorem the leading order Drell-Yan cross section can be derived. The cross section for the sub process $q\bar{q} \to \gamma^* \to l^+l^-$ can be taken directly from QED as follows:

$$\hat{\sigma}(q\bar{q} \to \gamma^* \to l^+l^-) = \frac{4\pi\alpha^2}{3\hat{s}} \frac{1}{N} Q_q^2 \tag{2.16}$$

where $\hat{s} = Q^2 = M^2$ the invariant mass of the dilepton decay products, Q_q is the quark electric charge and $1/N = 1/3$ reflects the fact that quark and anti-quarks can only annihilate with like colour charges to leave a colour singlet state.

Due to the varying momentum fractions of the incoming quark and anti-quark there is a spectrum of invariant masses. This makes it more appropriate to describe the cross section in terms of differential mass.

$$\frac{d\hat{\sigma}}{dM^2} = \frac{\hat{\sigma_0}}{N} Q_q^2 \delta(\hat{s} - M^2),\ \hat{\sigma_0} = \frac{4\pi\alpha^2}{3M^2} \tag{2.17}$$

where $\delta(\hat{s} - M^2)$ is a delta function forcing $\hat{s} = M^2$. The momentum of the incoming partons in the centre-of-mass frame of the hadrons are given by:

$$p_1^\mu = \frac{\sqrt{s}}{2}(x_1, 0, 0, x_1),\ p_2^\mu = \frac{\sqrt{s}}{2}(x_2, 0, 0, x_2) \tag{2.18}$$

where $\hat{s} = x_1 x_2 s$. Combining equation 2.17 with equation 2.13 gives the differential hadronic cross section.

$$\frac{d\sigma}{dM^2} = \frac{\hat{\sigma_0}}{N} \int_0^1 dx_1 dx_2 \delta(x_1 x_2 s - M^2) \left[\sum_k Q_k^2 (q_k(x_1, M^2)\bar{q}_k(x_2, M^2) + [1 \leftrightarrow 2] \right] \tag{2.19}$$

The rapidity of the dilepton system relative to the beam axis (relative to the z component of the momentum p_Z) can be derived from equation 2.18 as follows:

$$y = \frac{1}{2} \log \frac{E + p_z}{E - p_z} = \frac{1}{2} \log \frac{x_1}{x_2} \tag{2.20}$$

where E is the energy of the incoming parton. The parton momentum fractions can then be given by:

$$x_1 = \frac{M}{\sqrt{s}} e^y,\ x_2 = \frac{M}{\sqrt{s}} e^{-y} \tag{2.21}$$

By inserting x_1 and x_2 into equation 2.19 the double differential cross section in terms of mass and rapidity can be given as follows:

$$\frac{d\sigma}{dM^2 dy} = \frac{\hat{\sigma_0}}{Ns} \left[\sum_k Q_k^2 (q_k(x_1, M^2)\bar{q}_k(x_2, M^2) + [1 \leftrightarrow 2] \right] \tag{2.22}$$

It follows that cross section measurements made in terms of di-lepton mass and rapidity can provide direct constraints on the quark PDFs within the colliding hadrons. Figure

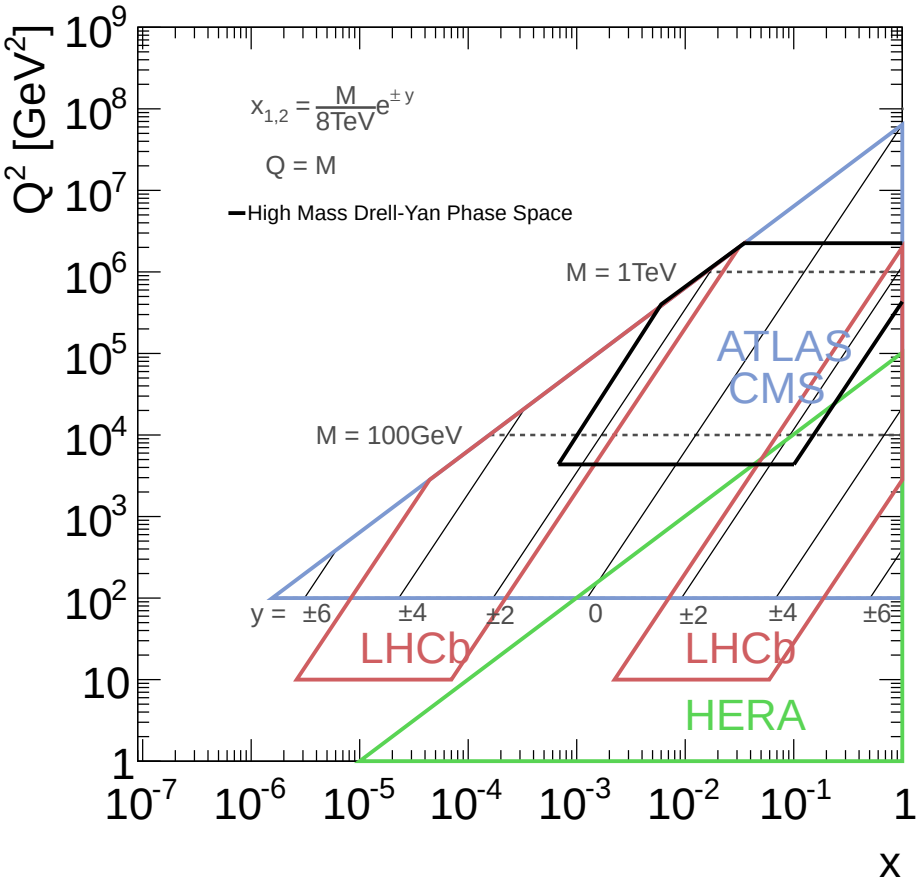

Figure 2.3.: x, Q^2 phase space that is obtainable by the LHC and HERA experiments. The relationship between the detector variables y and M and the PDF variables x and Q^2 is also shown

2.3 shows the x, Q^2 phase space that the LHC (hadron-hadron collsion) and HERA (deep inelastic scattering) experiments can probe.

The differential equations 2.19 and 2.22 give the total hadronic cross section for energies in which the process $q\bar{q} \to \gamma^* \to l^+l^-$ is the only contribution. At energies close to the Z boson mass the process $q\bar{q} \to Z \to l^+l^-$ will be more energetically favourable. The cross section for the combined Z and γ^* mediated subprocess is as follows:

$$\sigma(q\bar{q} \to Z/\gamma^* \to l^+l^-) = \frac{4\pi\alpha^2}{3\hat{s}} \frac{1}{N} \left[Q_q^2 - 2Q_q V_l V_q \chi_1(\hat{s}) + (A_l^2 + V_l^2)(A_q^2 + V_q^2)\chi_2(\hat{s})\right] \tag{2.23}$$

where the first term is taken directly from the QED sub process cross section and the second term accounts for the neutral charge weak contribution. $V_{l/q}$ and $A_{l/q}$ represent the vector and axial couplings respectively and the variables $\chi_1(\hat{s})$ and $\chi_2(\hat{s})$ are defined as follows:

$$\chi_1(\hat{s}) = \kappa \frac{\hat{s}(\hat{s} - M_Z^2)}{(\hat{s} - M_Z^2)^2 + \Gamma_Z^2 M_Z^2} \tag{2.24}$$

$$\chi_2(\hat{s}) = \kappa^2 \frac{\hat{s}^2}{(\hat{s} - M_Z^2)^2 + \Gamma_Z^2 M_Z^2} \tag{2.25}$$

$$\kappa = \frac{\sqrt{2} G_F M_Z^2}{4\pi\alpha} \tag{2.26}$$

where G_F is the Fermi constant, M_Z is the mass of the Z boson and Γ_Z is the Z decay width. When the centre-of-mass energy $\sqrt{\hat{s}} \ll M_Z$ the χ variables become small and equation 2.23 returns the value obtained from the purely QED subprocess. Conversely when $\hat{s} = M_Z^2$, equation 2.23 is dominated by the χ_2 term. The decay width of the Z boson is small in relation to its mass and can be neglected. Applying this narrow width approximation and using equations 2.13 and 2.23 a Z boson production cross section can be described as follows:

$$\sigma(q\bar{q} \to Z) = \frac{\pi}{3} \sqrt{2} G_F M_Z^2 (V_q^2 + A_q^2) \delta(\hat{s} - M_Z^2) \tag{2.27}$$

The total cross sections are then calculated by multiplying this cross section by the final state branching ratios.

2.7.2. The Analysis Measurement

The main aim of the analysis described is to produce information for constraining PDFs as well as providing insights on QCD dynamics. As described in the previous section both single and double differential cross section measurements in terms of mass and rapidity can help constrain PDFs. In a previous ATLAS analysis based on 2011 data, a single differential cross section in terms of mass was made but due to the limited statistics useful double differential measurements could not be achieved [12]. Using the increased statistics

provided by the 2012 running of the ATLAS detector, double differential measurements have been made and are described in this thesis. A double differential measurement in terms of dimuon mass and muon separation $|\Delta\eta_{\mu\mu}|$ is also made to gain access to the photon PDFs [13]. The three cross section measurements that are made as part of this analysis are listed as followed.

- Single differential fiducial cross section measurement in terms of dimuon mass ($\frac{d\sigma}{dm_{\mu\mu}}$).
- Double differential fiducial cross section measurement in terms of dimuon mass and rapidity ($\frac{d^2\sigma}{dm_{\mu\mu}dy_{\mu\mu}}$).
- Double differential fiducial cross section measurement in terms of dimuon mass and muon separation $|\Delta\eta_{\mu\mu}|$ ($\frac{d^2\sigma}{dm_{\mu\mu}d|\Delta\eta_{\mu\mu}|}$).

Chapter 3.

The Large Hadron Collider and the ATLAS Experiment

The Large Hadron Collider (LHC) [14] is a hadron collider located at the CERN laboratory in Geneva. Designed to reach centre-of-mass energies of 14 TeV it is the highest energy particle accelerator ever built. The LHC was designed to produce proton-proton as well as heavy ion collisions with the former being the subject of this thesis. Located at four points on the 27 km underground ring are the LHC main experiments. The Compact Muon Solenoid (CMS) [15] and ATLAS [16] experiments are multipurpose detectors able to recognise a range of decay signatures. The LHCb experiment [17] is a forward detector designed to probe b and c hadron physics and the ALICE detector [18] was built to measure heavy ion collisions. This chapter gives an overview of the LHC accelerator in proton-proton collision mode before concentrating on the details of the ATLAS experiment.

3.1. The Large Hadron Collider

To LHC delivers beams of protons that are collided within each of the four main detectors. To increase the energy of these proton beams a series of legacy particle accelerators at CERN are used. Firstly protons are stripped from hydrogen atoms and accelerated to 50 MeV using a linear accelerator (Linac II). These protons are then fed into the Proton Synchrotron Booster (PSB) which accelerates them to an energy of 1.4 TeV. The protons are then squeezed into densely packed bunches by the Proton Synchrotron (PS) to allow more protons into the next stage of acceleration. The Super Proton Synchrotron (SPS)

then accelerates the protons up to an energy of 450 GeV. Finally proton beams are sent in opposite directions around the LHC ring where they can be accelerated up to the design colliding energy.

A fault in the LHC magnet system in 2008 caused a delay to the start of the LHC program. Due to this fault in the magnet system it was decided that the LHC would run at half its design energy in 2011. At the end of 2011 an excess of events were found in a Higgs boson search channel so the decision was made to increase the centre-of-mass energy to 8 TeV for 2012. The full design energy is hoped to be reached after a technical shutdown that finishes in 2015.

The physics processes of interest at the LHC are often very rare meaning a large number of collisions need be produced. The rate that a process occurs is given by the cross section σ. The rate of production of a particular process can then be given by the following equation:

$$\frac{dn}{dt} = \sigma\mathcal{L} \tag{3.1}$$

where $\mathcal{L}$ is the instantaneous luminosity of the collider. At particle accelerators this value needs to be as large as possible to keep rates high in the face of potentially small cross sections. The instantaneous luminosity is given by:

$$\mathcal{L} = f n_b \frac{n_p^2}{A} \tag{3.2}$$

where f is the rotation frequency of the beams, n_b is the number of particle bunches per beam, A is the transverse colliding area of the beam and n_p is the number of protons in the beam. Maximising the luminosity of the collider can be achieved either by having a large number of protons in a beam per colliding area or having a large number of bunches spaced closely together. However increasing these variables leads to a high number of proton-proton scatters per beam collision. These additional interactions, called pile-up events, can originate either from the same or previous bunches and they affect the way the detector responds to the measured signal events. Pile-up originating from the same bunch is called in-time pileup and is generally quantified by recording the number of primary interaction vertices reconstructed in each event. Pileup originating from different bunches is called out of time pile-up and can be gauged by the average number of interactions per bunch crossing, $\langle\mu\rangle$. Out of time pileup is in particular a problem for the calorimetry

system as some of the drift times within these detectors are larger than the bunch spacing. The calorimetry of the ATLAS detector is explained in further detail in section 3.5.

The LHC design instantaneous luminosity at 14 TeV is $10^{34}\,\mathrm{cm}^{-2}\mathrm{s}^{-1}$. Running at 7 TeV in 2011 the detector reached an peak luminosity of $3.65 \times 10^{33}\,\mathrm{cm}^{-2}\mathrm{s}^{-1}$. Running at 8 TeV in 2012 the peak luminosity was increased to $7.73 \times 10^{33}\,\mathrm{cm}^{-2}\mathrm{s}^{-1}$. Integrating the instantaneous luminosity over the runs quantifies the amount of data that has been collected. The recorded integrated luminosity is $5.6\,\mathrm{fb}^{-1}$ for 2011 and $22.8\,\mathrm{fb}^{-1}$ for 2012.[1]

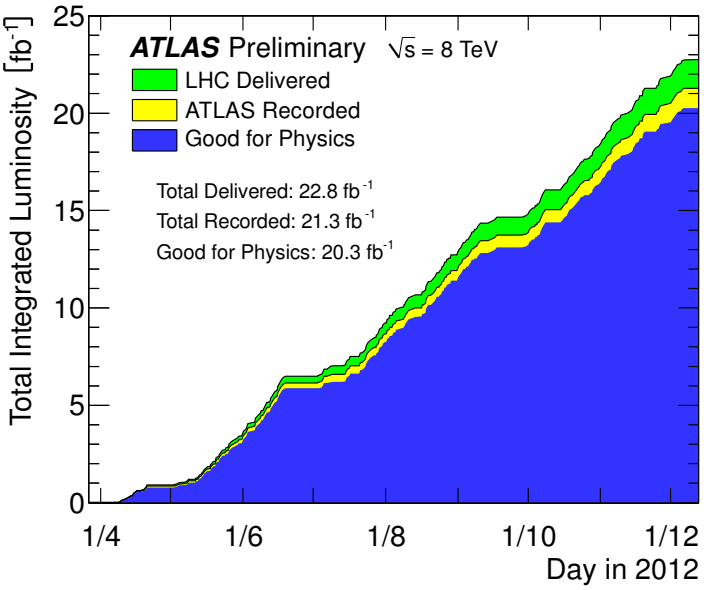

Figure 3.1.: Plot showing integrated luminosity delivered, recorded and then good for physics analysis by the ATLAS detector as a function of time for 2012 [19].

3.2. The ATLAS Detector

The ATLAS detector is a multiple purpose detector designed to reconstruct an array of different physics signatures. The structure consists of a series of sub-detectors housed both in a barrel shape around the beam pipe and in two end caps at either end of the barrel. The three main sub detectors are the inner detector (ID), which is used to measure charged particle trajectories, the electromagnetic and hadronic calorimeters, which measure particle energy deposits and the muon spectrometer, specifically designed to measure muon

[1]The units fb are femto-barns, where the barn is a common particle physics unit, $1\mathrm{b} = 10^{-28}\,\mathrm{m}^2$

signatures. In addition to the these sub detectors there is a solenoid magnetic located outside the inner detector and a toroidal magnet external to the calorimeters.

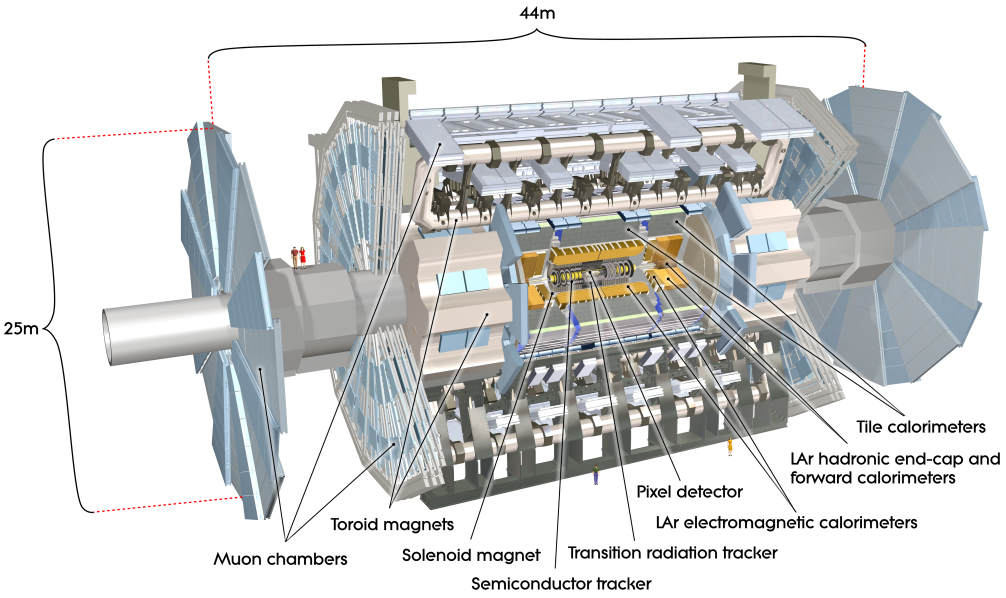

Figure 3.2.: ATLAS Detector cut away [16].

3.3. Detector Kinematic Variables

The coordinate system within the ATLAS detector defines the z axis as along the beam pipe, the y axis as pointing upwards and the x axis as pointing towards the centre of the LHC ring. The coordinate $(0, 0, 0)$ in this system is known as the interaction point (IP). The angles ϕ and θ are the azimuthal angle around the beam pipe (x-y plane) and the angle from the beam axis (z axis) respectively. More commonly the polar angle is described in terms of pseudorapidity, given by

$$\eta = -\ln\left[\tan\frac{\theta}{2}\right] \tag{3.3}$$

where pseudorapidity is derived in the high energy limit from equation 2.20. Pseudorapidity is preferred because particle production is generally constant as a function of rapidity and differences in rapidity are Lorentz invariant.

Protons colliding in the ATLAS detector travel along the beam pipe and as such have no transverse momentum. This property can be used when studying the decay products of the collision, as the conservation of momentum will require their momenta to balance. For this reason the transverse component of a variable such as the energy E_T and momentum p_T are used. Additionally another useful variable is the missing transverse energy of an event E_T^{miss}. The E_T^{miss} of an event is the energy that is predicted by the conservation of energy of the detected particles but not accounted for in the deposits made in the detector. Most commonly this missing energy is due to the detector being unable to detect neutrinos but could also arise from exotic particles in extensions to the standard model.

3.4. Tracking Overview

The inner detector (ID) covers the $|\eta| < 2.5$ region and is designed to track charged particle trajectories and locate interaction vertices. The momentum of the charged particles can also be measured with the application of a magnetic field applied by a 2T solenoid magnetic located externally to the ID. The curvature of the particles' trajectory due to Lorentz force is proportional to the momentum of the particle. This relation allows the inner detector to reconstruct the particle momentum to a p_T resolution of 0.05%.

The inner detector consists of three components, the silicon pixel detector, the semi conductor tracker (SCT) and the transition radiation tracker (TRT). The pixel detector is primarily used for determining primary and secondary vertices, the SCT is used for measuring particle momenta and the TRT is used to enhance the tracking capability of the inner detector as well as aiding electron identification. A diagram of the inner detector is shown in figure 3.3 [16].

The silicon pixel detector is located around the vertex region and has the highest granularity of the inner detector sub systems. In the barrel region it consists of three cylindrical silicon pixel layers at 50.5 mm, 88.5 mm and 122.5 mm from the beam axis. For the endcap region the pixel detectors are located on disks 495 mm, 580 mm and 650 mm from the interaction point. Each of these layers is made of individual sensor elements partitioned in $R - \phi$ and z, with a mimimum size of $50{\times}400$ μm^2. The accuracy in the barrel is 10 μm (R-ϕ) and 115 μm(z) and in the disks is 10 μm (R-ϕ) and 115 μm(R).

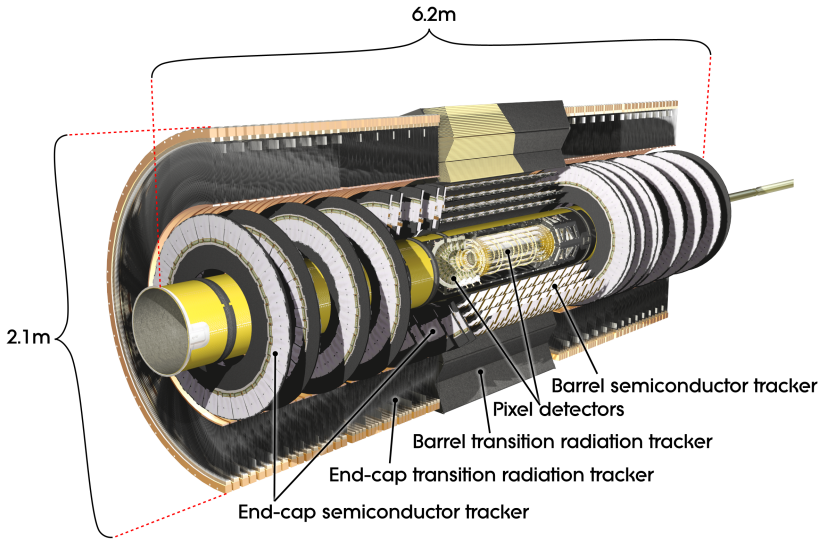

Figure 3.3.: ATLAS inner detector cut away [16].

The SCT comprises of four double layers of silicon microstrip sensors that give eight precise measurements per track. In the barrel region the double layers have one strip that is aligned axially and one strip that is aligned with a 40 mrad stereo angle. The second strip's angular offset allows for a measurement to be made in the z direction by comparing the overlapping active areas. In the endcap regions the microstrips run radially, again with an offset strip at a 40 mrad angle. The accuracy of the detector in the barrel is 17 μm (R-ϕ) and 580 μm(z) and in the end caps are 17 μm (R-ϕ) and 580 μm(R).

The TRT provides (R-ϕ) tracking information up to $|\eta| < 2.0$ using 4 mm diameter straw drift tubes arranged axially. The straw tubes are filled with a mixture of 70% Xe, 20% CO_2 and 10% CF_4, which provide absorption from the transition radiation, stability while under high voltage and an increased electron drift time respectively. These straws are then sandwiched between layers of radiator material, which is used to induce transition radiation from the traversing charged particles. In the barrel the 144 cm length straw tubes are arranged into 36 layers located at radii of 55-108 mm. The tubes in the end caps are 37 cm and are located at a radii of 62-112 mm. The TRT has a low spatial resolution of 130 μm but due to the large fiducial volume, an incident particle will produce a lot of hits, increasing the trajectory information [16].

3.5. Calorimetry Overview

The ATLAS calorimeters are housed outside the inner detector and cover a region of $|\eta| < 4.9$. The calorimetry system is split into three main sub systems, the electromagnetic and hadronic calorimeters that cover the $|\eta| < 3.2$ region and the forward calorimeter that covers the forward $3.1 < |\eta| < 4.9$ region. By definition the forward calorimeter is in the endcap region only, while the electromagnetic and hadronic calorimeters have both barrel and endcap components.

All of the calorimeters used in the ATLAS detector are sampling calorimeters. Sampling calorimeters have alternating layers of absorbing material, which causes the particles to shower, and detecting material, which measures the energy deposition of the shower.

In design, consideration of calorimeter depth has to be taken into account. The electromagnetic and hadronic showers must be contained within the calorimetry to limit any punch-through into the muon system. The electromagnetic showers have a narrow transverse profile and are described using radiation length[2] X_0. Hadronic showers have a larger transverse area and are parameterised by the interaction length[3] λ.

The electromagnetic calorimeter is a sampling lead-LAr calorimeter with accordion shaped electrodes and lead absorber plates that provide full ϕ symmetry. The thickness of the lead in the absorber plates varies as a function of η to optimize the energy resolution in the calorimeter. The electromagnetic calorimeter is divided into the barrel calorimeter ($|\eta| < 1.475$) with a design thickness of $> 22X_0$ and the end caps ($1.375 < |\eta| < 3.2$) with a design thickness of $> 24X_0$. The $|\eta| < 2.5$ region in the barrel the electromagnetic calorimeter has been sub divided into three sampling layers with a presampler in front of the first of these layers. The presampler is placed in a region $|\eta| < 1.8$ and is used to correct for energy loss of incident electrons and photons in the inner detector. The first sampling layer is finely segmented in η allowing for electron pion separation and precision position measurements to be made. The second layer is used along with the first layer to determine the η direction of the photon cluster. The third layer is built with much coarser granularity than the previous layers as the photon clusters are much broader by this point.

[2]Radiation length X_0 describes the mean distance an electron travels before its energy is reduced to $1/e$ via bremsstrahlung radiation

[3]Interaction length λ describes the average distance a hadron travels through a medium before undergoing an interaction

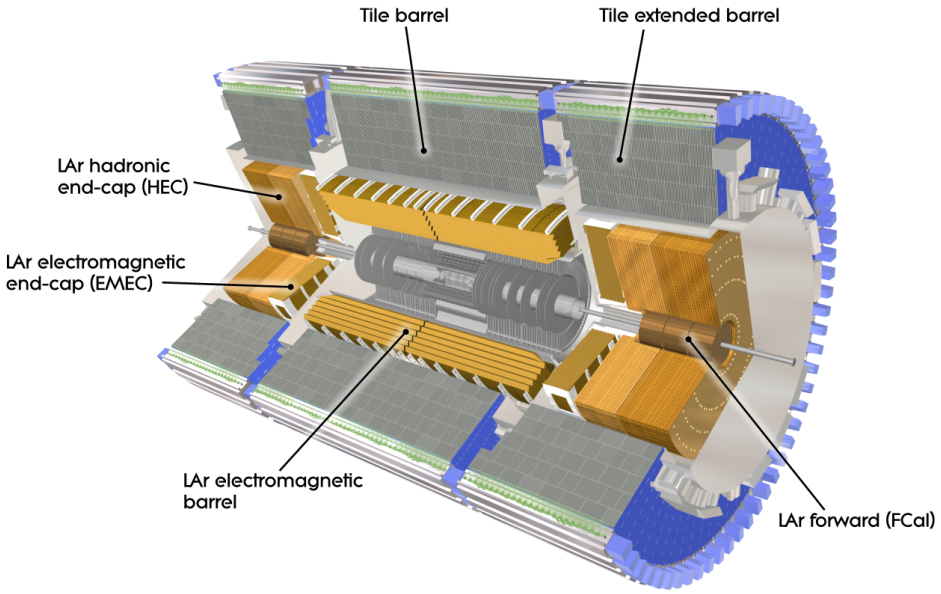

Figure 3.4.: ATLAS calorimetry systems cut away [16].

The hadronic calorimeter is made up of two components, the tile calorimeter and the hadronic endcap. The tile calorimeter is external to the electromagnetic barrel calorimeter and covers the region $|\eta| < 1.0$ with a central barrel detector and the region $0.8 < |\eta| < 1.7$ with two extended barrel detectors. It is a sampling detector that uses steel as the absorption material and scintillating tiles as the active medium. It sits between 2.28 and 4.25 m from the beam axis and is divided into three layers of 1.5, 4.1 and 1.8 interaction lengths for the barrel and 1.5, 2.6 and 3.3 interaction lengths for the extended barrel.

The hadronic endcap (HEC) is split into two wheels at both ends of the detector covering the range $1.5 < \eta < 3.2$. This gives it an overlap region with both the extended tile calorimeter and the forward calorimeter. Each of the wheels is built from copper and divided into two layers of 32 modules. The active material of the calorimeter is LAr, as with the electromagnetic calorimeter, and is sandwiched between the copper plates in 8.5 mm gaps.

The forward calorimeter (FCAL) is located at $3.1 < |\eta| < 4.7$ and is used for detecting electromagnetic and hadronic activity. To avoid neutron backscattering the forward calorimeter sits 1.2m back from the outside face of the electromagnetic calorimeter endcaps. This means that the FCAL has to be a high density in order to fit it in the 10 interaction lengths required in its design. Each endcap has three modules, the first (FCal1) is made

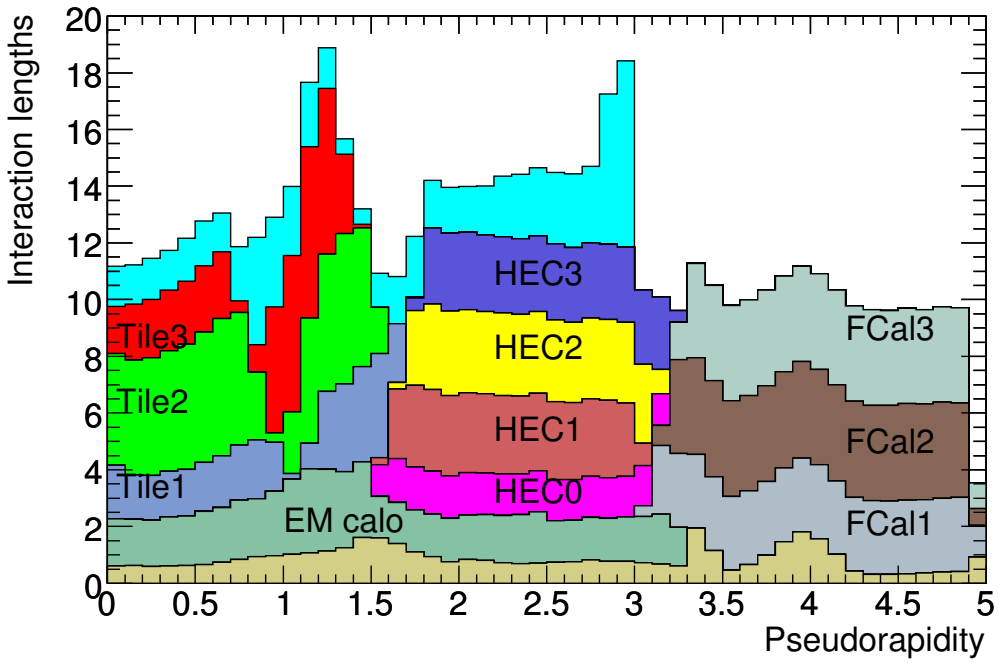

Figure 3.5.: ATLAS calorimeter detector depth in interaction lengths (λ) [16].

of copper built primarily for detecting electromagnetic interactions and the second two (FCal2 and FCal3) are made of tungsten used for hadronic detection. The active material sandwiched between the absorbers is again LAr. The FCAL location close to the beam pipe means that it has a high particle flux but also has an important role in the calculation of missing energy within the detector. Figure 3.5 shows the depths of each of the sub detectors in terms of X_0 [16].

3.6. Muon Spectrometer

The outermost detector is the muon spectrometer (MS), positioned as such due to the high penetrating nature of the muon particle. As most other particles decay before they reach the MS, the detector can identify muons with a high level of accuracy. The MS determines the momentum of the incident muons by measuring how their trajectory changes in an applied magnetic field. The magnetic field is provided by a large barrel toroid for the $|\eta| < 1.4$ region and by two endcap toroids for the $1.6 < |\eta| < 2.7$ region. The gap between these two η regions is called the transition region and relies on both the barrel

and endcap toroids. The strong magnetic field coupled with the large size of the MS allows the momentum of highly energetic muons to be measured. This is important as often the relatively small magnetic field strength in the ID system does not allow for this kind of measurement. The MS alone can measure muon momenta ranging from 3 GeV up to 3 TeV and provides muon transverse momentum resolution of 10% at 1 TeV [16].

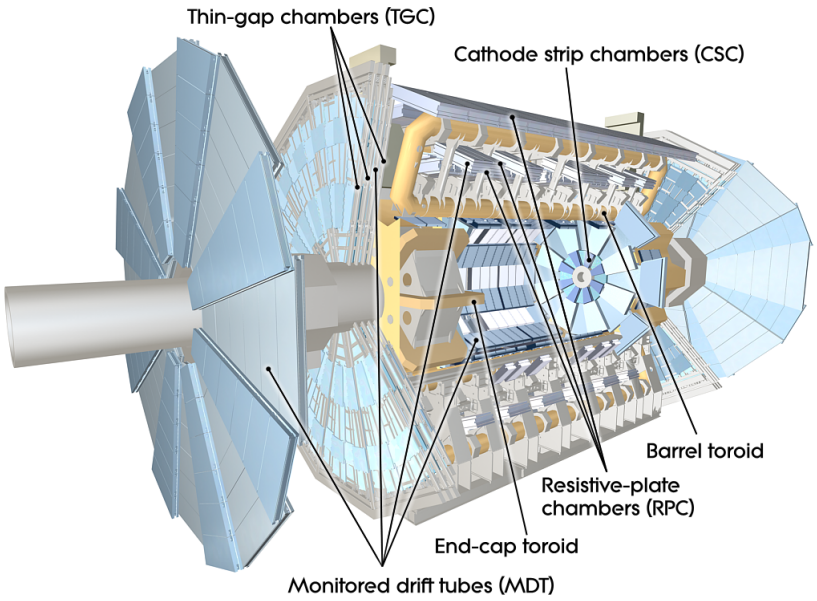

Figure 3.6.: ATLAS muon Spectrometer cut away [16].

The muons are measured in the MS by both the trigger chambers, consisting of the Resistive Plate Chambers (RPC) and the Thin Gap Chambers (TGC) and the high precision tracking chambers, which consists of the Monitored Drift Tubes (MDT) and the Cathode Strip Chambers (CSC).

The MDTs provide the precision tracking measurement for the majority of the MS volume and consist of three to eight layers of aluminium tubes filled with a gas mixture at absolute pressure of 3 bar. As muons traverse the tubes they ionise the gas, freeing electrons and allowing them to drift at a constant velocity in an applied electric field. The time taken for the electrons to drift towards the wire producing the electric field gives a muon position resolution of 80 μm. The MDTs are placed in chambers that consist of layers of tubes separated by a small gap. The positional resolution of one of these chambers is 35 μm.

In the forward region the flux of particles is much greater and as such the MDTs cannot provide a measurement due to the long drift time of the electrons in the ionised

gas. Therefore for the $2 < |\eta| < 2.7$ region, CSCs are used to perform the precision measurement. The CSCs work in a similar way to the MDTs with two layers of strips separated by a gas mixture that is ionised by incident muons. However with the CSCs the freed electrons drift to wires between the strips inducing a charge in the wire that spreads to surrounding wires, allowing a position measurement to be made. Aligning the two layers of strips orthogonally allows a 3D measurement to be made that achieves a resolution of 40 μm in the bending plane and 5 mm in the transverse plane.

The drift time of the electrons in the ionised gas again causes a problem when looking at the muon trigger system. Information required by the level one trigger system needs to be provided quicker than the 700 ns drift time of the electrons in the MDT. Trigger chambers that provide a quicker but more approximate measurement of the muon momentum and position are employed. Resistive Plate Chambers (RPCs) are used in the barrel $0 < |\eta| < 1.05$ region and Thin Gap Chambers (TGCs) are used in the forward endcap $1.05 < |\eta| < 2.4$ region.

The RPCs contain two high voltage plates separated by 2 mm in an ionisable gas mixture. Electrons produced when incident muons ionise the gas, drift towards the plates within the short time of 5 ns. An electrical charge is induced in metallic strips located on the outside of the two plates allowing an electronic readout to be made. The metallic strips located on the two plates are arranged orthogonally to allow an η-ϕ measurement to be made with a position resolution of 10 mm.

Due to the higher average momentum and particle flux in the forward region $1.05 < |\eta| < 2.4$, higher granularity detectors are needed to maintain the p_T resolution seen in the barrel. The TGCs employed in this region are multi-wire proportional chambers that provide not only information for the level-one trigger system but also give an additional handle on the azimuthal co-ordinate of the muon track. Two cathodes are placed 2.8 mm apart in a gas mixture with multiple anode wires in-between. The small gaps between the wires mean a good time resolution and high rate capability can be achieved. The spatial resolution of the TGCs is 2-6 mm in R and 3-7 mm in ϕ. As the muon trigger system only covers a region of $|\eta| < 2.4$ (full ϕ coverage is provided), online trigger measurements are only made on muons within this phase space.

In the barrel region close to $\eta = 0$ a drop in acceptance is observed due to a gap between the two halves of the MS. This gap is needed to allow cables to run into the trigger and data acquisition (TDAQ) systems. As a result of this gap in the MS only the

inner detector subsystems can reconstruct muons in this region leading to a lower efficiency. Other regions that suffer from a drop in efficiency are $\phi \sim 1.2$ where the ATLAS detector feet are located and the $\eta = 1.2$ region between the barrel and endcap detector systems. Also in some ϕ regions in this transition region a lower efficiency is observed due to some of the layers of chambers not being installed for RUN 1 [16].

To measure the muon position and momentum to the high level of precision required, the alignment of all of the individual muon chambers needs to be determined. This is done using an optical alignment system that measures changes and distortions to a light shone on a target containing image sensors. Using this system allows for the chamber to chamber position to be known along with any possible distortions of the MDTs due to gravity. The alignment of the barrel to the endcap detector is done using a track based alignment procedure. This method can also help add information to the muon chamber alignment.

3.7. Triggers

During the running of the LHC the rate of collisions can reach 1 GHz. Due to the limitations on the computing only a fraction of those events can be recorded. A trigger system has to be employed that reduces the rate by only selecting 'interesting' events. The ATLAS detector trigger system is split into a Level-1 trigger (L1) and a High-Level Trigger (HLT), which itself is split into the Level-2 trigger (L2) and the event filter (EF).

The L1 trigger uses a limited amount of the total detector information to search for signatures of interest such as high p_T particles, jets, E_T^{miss} etc. This detector information is produced by either the reduced granularity parts of the calorimeter or the muon spectrometer trigger chambers. The L1 trigger decision is made by the central trigger processor that has a 'menu' of predetermined triggers with varying kinematic requirements. Some of these triggers still produce a high rate and as such have to be pre-scaled. Pre-scaling randomly selects a predefined fraction of events that pass the trigger and discards them to reduce the rate. Once the L1 trigger has identified a physics signature that passes one of the trigger requirements it calculates a region of interest (RoI) defining where in the $\eta - \phi$ detector space the signature has occurred.

The RoI information is sent to the HLT within 2.5μs at a much reduced event rate of 75 kHz. The L2 trigger then uses the full precision sub detector systems within the RoI to further refine the selection. Within an average processing time of 40 ms the L2 trigger sends the remaining information to the event filter, which performs an offline analysis to reduce the rate to a recordable 200 Hz.

3.8. Muon Reconstruction

As muons traverse several of the ATLAS sub-detectors a combination of measurements can be made to reconstruct their kinematics. Muons can be broadly defined as either standalone muons (SA), that characterise the muons using the muon spectrometer only, inner detector tagged muons that only use the inner detector information or combined muons (CB) that use both the inner detector and MS. The highest level of reconstruction efficiency is obtained using combined muons as the inner detector provides the better impact parameter resolution and the MS provides better momentum and position resolution.

3.8.1. Muon Reconstruction Algorithms

Three different muon reconstruction algorithms are available in the ATLAS model, MuId (chain 2), which uses a full re-fit of the track parameters, STACO (chain 1), which utilises a statistical combination of track parameters and Third Chain (chain 3) muons, which use the optimal components of the previous two algorithms.

The standalone muons are reconstructed in the MS by fitting recorded hits in individual chambers with a straight line to form a segment, before linking these segments recorded in the three muon stations to form a track. An extrapolation to the IP is made taking into account the energy loss and possible multiple scatters of the reconstructed muon in the calorimeters. The STACO algorithm determines this energy loss based on the detector material traversed while the MuId algorithm additionally uses measurements made by the calorimeter systems.

The combined muons are constructed by associating a standalone muon to a inner detector track through the use of a χ^2 fit of the track parameters. Vectors of track parameters from the ID and MS are weighted by the their combined covariance matrix to

form the χ^2 match. The χ^2 match can then determine whether the muon is reconstructed as combined muon. The combined track vector is then determined by either a statistical combination of the MS and ID tracks for STACO or by performing a partial refit of the MS and ID tracks for MuId. The MuId fit starts with the ID track and covariance matrix and adds in the MS track, again accounting for energy loss in the calorimeter.

The third chain algorithm uses a combination of the STACO and MuId algorithms into a unified chain. The high mass Drell-Yan analysis described here uses the third chain algorithm muons [20].

3.8.2. Muon Reconstruction and Momentum Resolution

To effectively use muons as a primary signature for a Drell-Yan cross section measurement, both a high reconstruction efficiency and good muon momentum resolution is needed. The reconstruction efficiency is calculated separately for the MS and ID detectors using a 'tag and probe' method described in more detail in section 6.3.1. The efficiencies can then be combined with an additional matching efficiency to determine the combined muon efficiency. The reconstruction efficiencies depend primarily on the η of the muon as shown for the combined muon definition for muons with $p_T > 20$ GeV in figure 3.7. The efficiency is above 98% in all η regions apart from the $\eta = 0$ region which has a a lower efficiency for reasons described in section 3.6. The data MC ratio in figure 3.7 shows that the MC model describes the data almost perfectly with a small 1% deviation in the $\eta = 0$ region [21].

A good muon momentum resolution is needed to determine the mass of a dimuon system. A selection is made to give a high purity of $Z \to \mu\mu$ events and then a template fit is performed to determine the resolution. Figure 3.8 shows the di-muon mass resolution for the STACO definition muons when both of the decay product muons are within an defined η range. In the barrel region the mass resolution is around 1.5 GeV and in the endcap regions the resolution is around 2.0 GeV. There is an observed mis-modelling in the MC for the endcap resolution but these differences are corrected using performance based scale factors described in section 6.3.3.

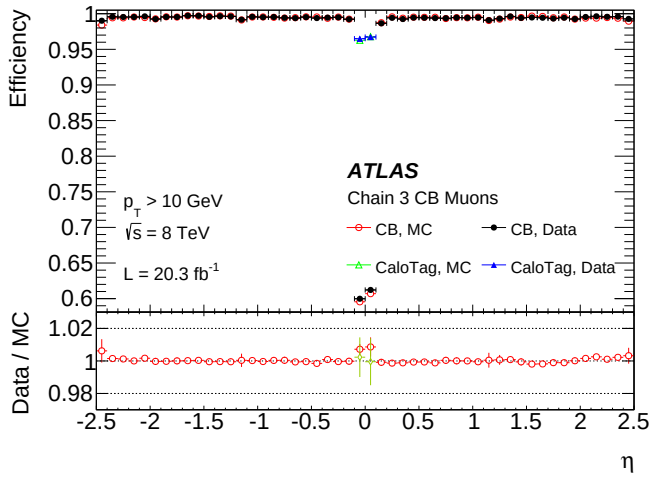

Figure 3.7.: Muon reconstruction efficiency as a function of η, measured using $Z \to \mu\mu$ events, for third chain (chain 3) muons, for different muon reconstruction types. The statistical uncertainties on the efficiencies are represented by the error bars. The lower panel shows the ratio between data and MC predicted efficiencies [21].

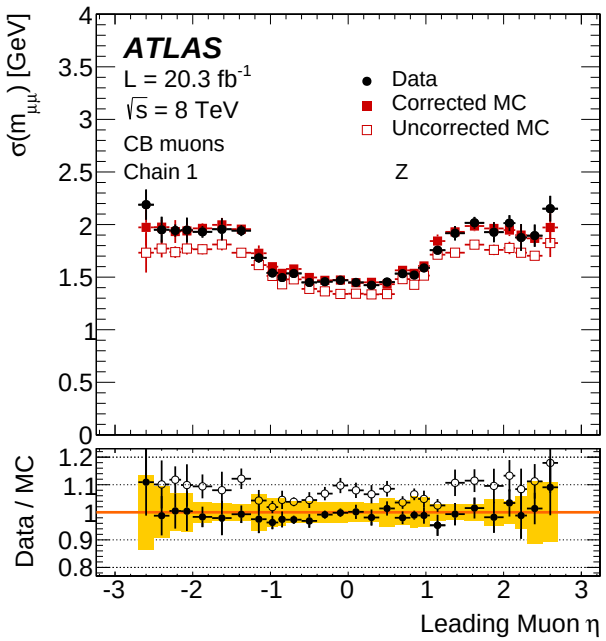

Figure 3.8.: Dimuon mass resolution for CB STACO (chain 1) muons for $Z \to \mu\mu$ events for data and for uncorrected and corrected MC as a function of the η of the leading muon. The upper panel shows the fitted resolution parameter for data, uncorrected MC and corrected MC. The lower panels show the data/MC ratio for both the corrected and uncorrected MC. The shaded area in the lower panels represents the systematic uncertainty on the correction [21].

Chapter 4.

Level-1 Calorimeter Trigger Noise Cuts

In 2012 the centre of mass energy of the LHC collisions was increased to 8 TeV. This increase lead to higher levels of pileup, putting more strain on the ATLAS trigger system. In preparation for the increase in trigger rates in 2012, a study has been carried out investigating a method for reducing the rates of triggers that would be most susceptible to changing pileup conditions. Applying a minimum energy threshold for the L1 Calo to record a measurement would remove more background events and reduce trigger rates. This study investigated what energy threshold should be applied and whether that effected the trigger efficiencies required in certain physic analyses.

To record all the requested types of physics events within the ATLAS detector a number of triggers have to be used during data taking. Each trigger used adds to the rate of information passed on to the next trigger in the chain. Reducing the rates of the individual triggers allows more triggers to be used within the limited bandwidth. For the L1 trigger the total rate transferred to the HLT cannot be greater than 75 kHz. The triggers need to be designed to maximise the efficiency of recording interesting physics events while reducing the rate of the background events not required by physics analyses.

A major component of the L1 trigger decision is provided by the L1 calorimeter trigger. Information from all of the coarse granularity calorimeter systems within the detector are used to help the L1 trigger decision. The analogue readings from the course granularity trigger systems are digitised into ADC counts, which are converted using look-up tables into values of transverse energy (4000 ADC counts is approximately 1 GeV). To reduce the L1 trigger rates, a minimum requirement on the number of ADC counts, or equivalently the amount of energy deposited in the calorimeter, is applied to the L1 calorimeter trigger. These noise suppression cuts provide a lower boundary on the energy that will be recorded

by the L1 trigger decision system. For the 2011 data taking period this noise cut was placed at approximately 1 GeV for the entire detector. The largest flux of particles in the ATLAS detector occurs closest to the beam pipe in the FCal and the electromagnetic endcap inner wheel (EMEC-IW), so it follows that increasing the noise suppression cuts in this region will yield a decrease in the trigger rates. Figure 4.1 shows the position of the FCal and the EMEC-IW in terms of η. For the 2012 data taking period an η dependant noise cut scheme has been determined to reduce the trigger rates.

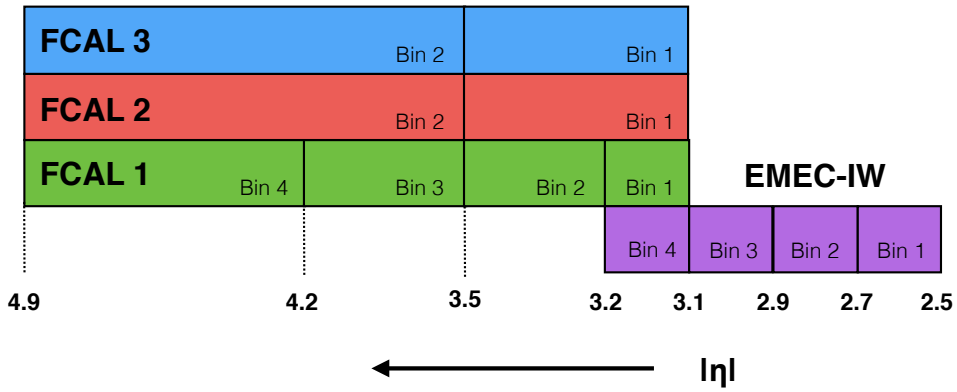

Figure 4.1.: A diagram showing the FCal and EMEC-IW position in terms of η. The boxes represent the different regions of the detector that can have unique noise cuts. The bin numbers correspond to the bin numbers used when calculating alternative binning schemes in figures 4.4, 4.5, 4.6 and 4.12

4.1. Selection

Measuring missing transverse energy E_T^{miss} in the ATLAS detector requires by definition a reading from all parts of the calorimetric systems. Any increase in the noise suppression cuts will have the greatest effect on triggers that depend on the E_T^{miss} of an event. In addition the L1 E_T^{miss} triggers use a considerable amount of the bandwidth afforded to the L1 trigger, so any reduction in rates will improve bandwidth congestion greatly. Four different L1 E_T^{miss} triggers have been used in this performance study as follows:

- L1_XE20, triggers on $E_T^{miss} > 20$ GeV
- L1_XE25, triggers on $E_T^{miss} > 25$ GeV

- L1_XE30, triggers on $E_T^{miss} > 30$ GeV
- L1_XE50, triggers on $E_T^{miss} > 50$ GeV

Testing whether increasing noise cuts effect the efficiency of these triggers requires a study to be carried out on a process that generates true E_T^{miss}. One such process is $W^+(W^-) \rightarrow e^+\nu_e(e^-\bar{\nu_e})$ as the neutrino produced cannot be detected in the ATLAS detector. A selection that enriches the sample in these W decay events would be achieved by looking for an electron with E_T^{miss}. By selecting events triggered by the electron from a data sample, the E_T^{miss} requirement of the triggers can be tested. The selection on the electrons follows guidelines provided by the eGamma performance group and are listed as follows:

- $E_T > 25$ GeV
- $|\eta| < 2.47$ excluding $1.37 < |\eta| < 1.52$ (this a low efficiency region between the barrel and endcap calorimeters)
- Electron object quality cuts. This removes events with calorimeter noise bursts or dead channels [22].
- Electron Tight definition
- $W m_T > 40$ GeV

where E_T is the transverse energy of the electron, W m_T is the transverse mass of the W boson (reconstructed using the four vector of the E_T^{miss} and the electron) and the electron tight definition is set of selections used to identify electrons [22].

Figure 4.2 shows the selected electron η and E_T along with the event E_T^{miss} and W m_T for the analysed 2011 data. The electron η shape is as expected with the gaps in acceptance at $1.37 < |\eta| < 1.52$ and the electron E_T and W m_T distributions show that the selection efficiently pick out the $W \rightarrow e\nu$ events.

4.2. L1Calo Trigger Efficiency

To test the E_T^{miss} triggers on these electron selected events an online E_T^{miss} value determined by the L1 trigger system is compared to an offline value of the E_T^{miss} calculated using the

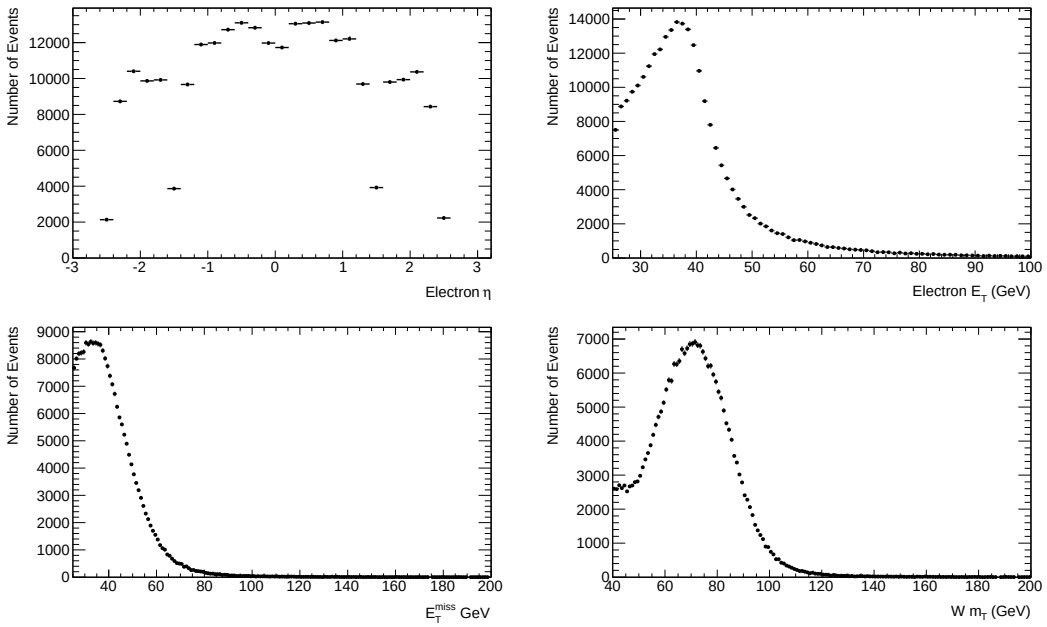

Figure 4.2.: Control distributions showing the selected electron η (top left) and E_T (top right), the E_T^{miss} (bottom left) and W m_T (bottom right). The distributions were made using period K of the 2011 running (explanation of periods see section 5.1).

full high granularity detector systems. The efficiency ϵ of the trigger can then be defined as:

$$\epsilon = \frac{E_T^{miss}(\text{L1 online}) > T}{E_T^{miss}(\text{offline})} \tag{4.1}$$

where T is the threshold of the tested trigger.

The noise cut schemes are tested by reprocessing data samples to create E_T and E_T^{miss} variables that simulate what would be recorded by the L1 calorimeter had the cuts been in place. Applying a single value noise cut to the FCal1, FCal2 and FCal3 of 10000, 22000 and 34000 ADC counts does not effect the efficiency of the E_T^{miss} trigger when compared to the standard 2011 noise cuts value of 4000 ADC counts, as shown in figure 4.3. While these single valued cuts reduce the trigger rate greatly, they may also reduce the efficiency of physics processes with very forward signatures. To reduce the possible impact of these cuts an η and detector dependant scheme has been determined that has higher noise cuts for regions of higher pile-up.

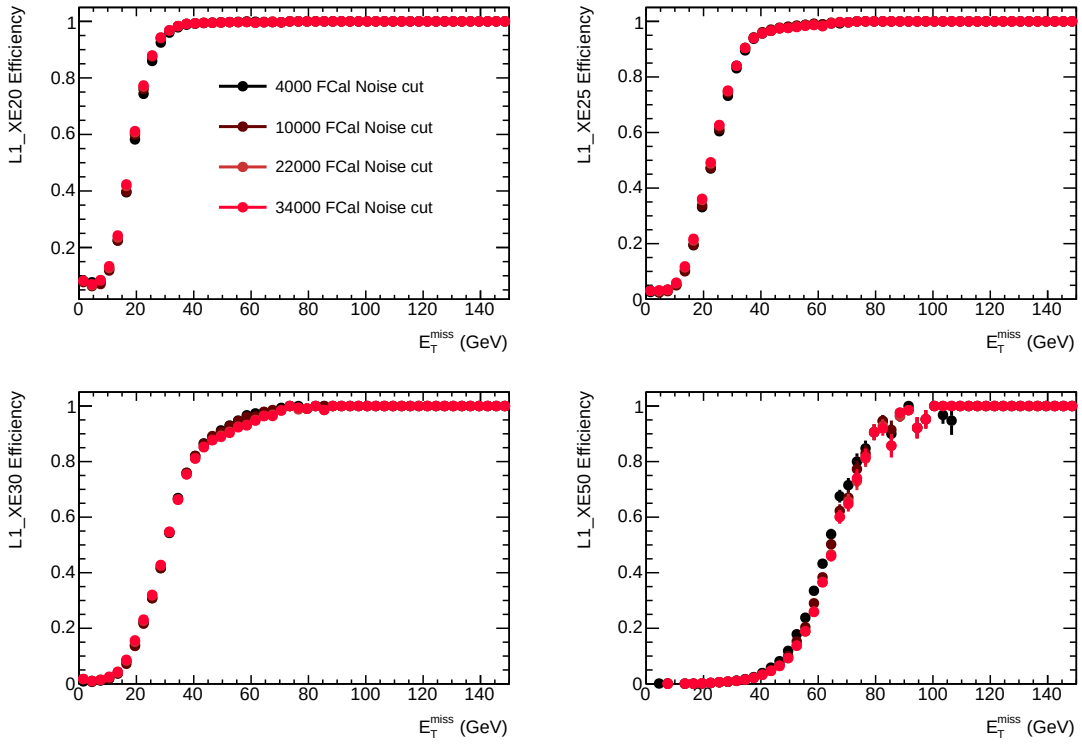

Figure 4.3.: Level one E_T^{miss} trigger efficiencies for trigger thresholds of 20, 25, 30 and 50 GeV using four sets of noise cuts.

The magnitude of the noise cuts required in each part of the FCAL is determined using a sample of data called Zero Bias data. A Zero Bias sample is data that has no interesting physics signatures and as such can be considered background. The initial noise cut scheme labelled $\langle\mu\rangle = 15$ is determined by looking at the FCAL regions with the highest pile up and increasing the noise cut in this region until the trigger rate approximately equals the trigger rate if this region were to be completely removed from the calculation. This process is then repeated for the next highest pileup region and then the next until all of the FCAL compartments have been calculated.

A second noise cut scheme is calculated using an extrapolation of the initial noise cuts to higher pile-up specific conditions. The drifts of the ADC counts recorded by the l1 calo preprocessor during an event are measured and plot relative to the peak ADC counts for the different sub detector η regions. This is shown in the left of figures4.4, 4.5 and 4.6. The RMS of this distribution is measured for different values of $\langle\mu\rangle$ to simulate differing levels of pile-up as shown in the right of figures 4.4, 4.5 and 4.6. Comparing the RMS of the distribution at $\langle\mu\rangle = 15$ to that at $\langle\mu\rangle = 20$ gives a single scale factor that can be applied to the noise cuts in the initial scheme to give the noise cuts for the $\langle\mu\rangle = 20$ scheme.

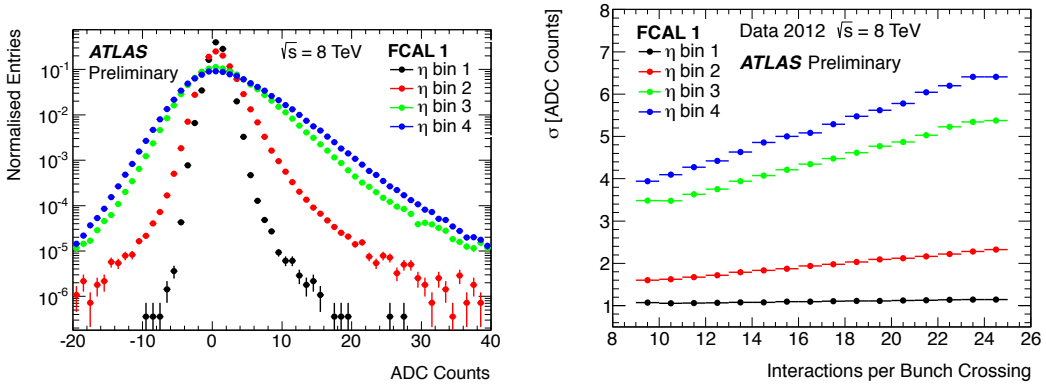

Figure 4.4.: Distribution of the ADC count drifts relative to the peak ADC counts of an event in the four different FCal1 η bins (left). The RMS of the ADC counts drift distribution(left) under different pileup conditions (average interactions per bunch crossing $\langle\mu\rangle$) (right). The bin number correspond to the η regions shown in figure 4.1, $3.1 < |\eta| < 3.2$(bin 1), $3.2 < |\eta| < 3.5$(bin 2), $3.5 < |\eta| < 4.2$(bin 3) and $4.2 < |\eta| < 4.9$(bin 4) [23].

The two noise cut schemes for $\langle\mu\rangle = 15$ and $\langle\mu\rangle = 20$ are shown in figure 4.7 along with additional noise cut schemes studied in the early running of 2012 as discussed in section 4.4. The binning of for the noise cut schemes is displayed graphically in figure 4.1. These noise

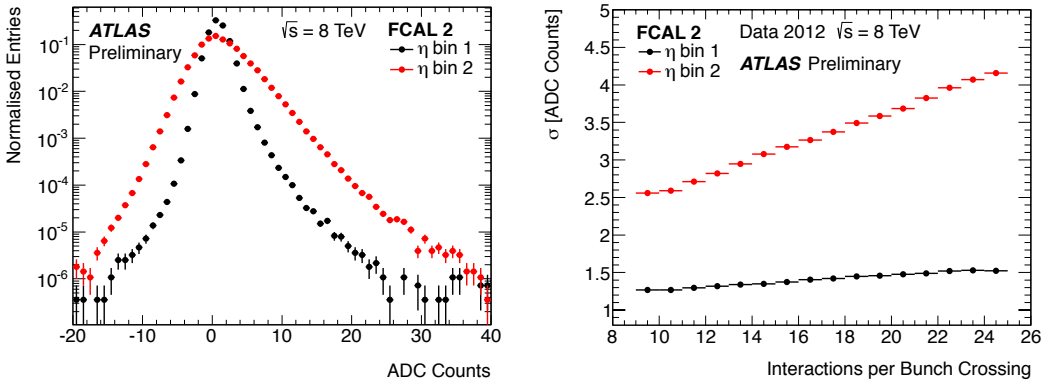

Figure 4.5.: Distribution of the ADC count drifts relative to the peak ADC counts of an event in the two different FCal2 η bins (left). The RMS of the ADC counts drift distribution(left) under different pileup conditions (average interactions per bunch crossing $\langle\mu\rangle$) (right). The bin number correspond to the η regions shown in figure 4.1, $3.1 < |\eta| < 3.5$(bin 1) and $3.5 < |\eta| < 4.9$(bin 2) [23].

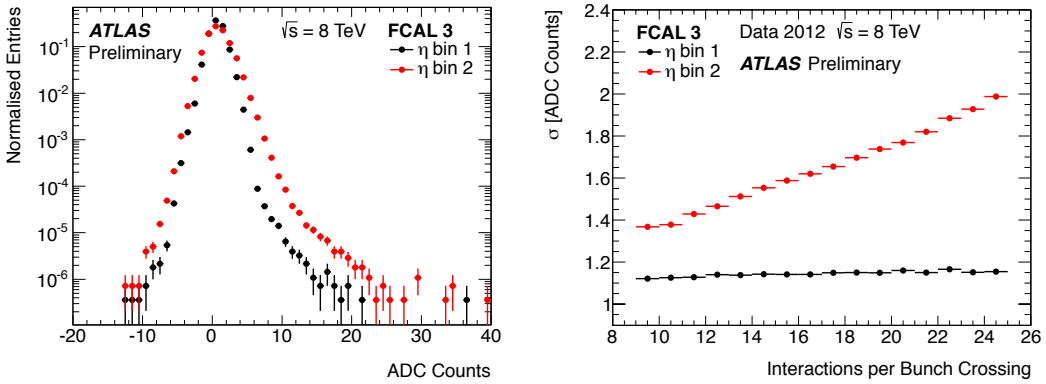

Figure 4.6.: Distribution of the ADC count drifts relative to the peak ADC counts of an event in the two different FCal3 η bins (left). The RMS of the ADC counts drift distribution(left) under different pileup conditions (average interactions per bunch crossing $\langle\mu\rangle$) (right). The bin number correspond to the η regions shown in figure 4.1, $3.1 < |\eta| < 3.5$(bin 1) and $3.5 < |\eta| < 4.9$(bin 2) [23].

cut schemes have again been tested on the four E_T^{miss} using the $W^+(W^-) \rightarrow e^+\nu_e(e^-\bar{\nu}_e)$ process and the efficiencies are shown in figure 4.8. Again the efficiencies are unaffected by the increasing noise cuts for each of the E_T^{miss} thresholds.

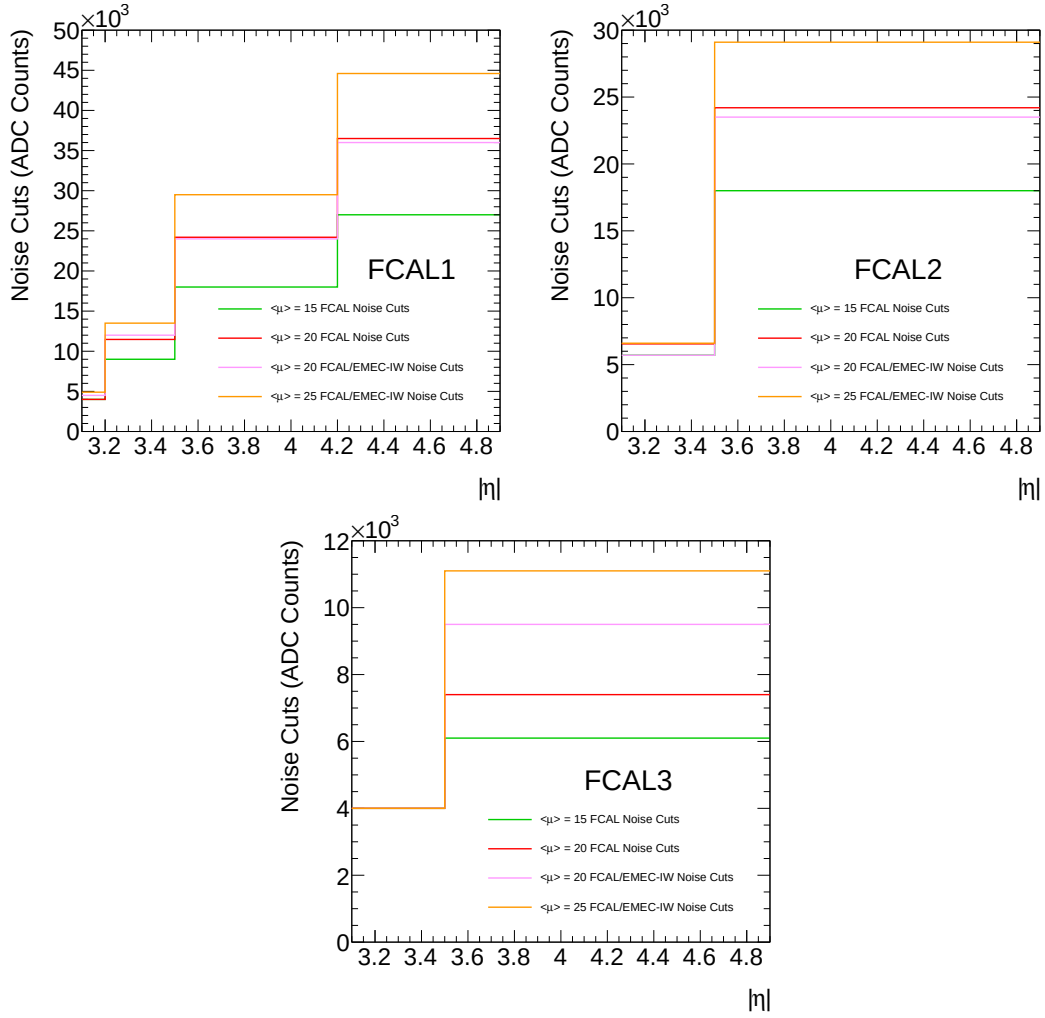

Figure 4.7.: Noise cuts applied in FCal1, FCal2 and FCal3 detectors η regions under the four tested noise cuts schemes.

In addition to testing the E_T^{miss} triggers, jet triggers have been also tested. The forward jet triggers by definition rely heavily on the forward calorimeter system, so will be greatly effected by the noise cuts applied in this region. Efficiencies were again tested using a $W^+(W^-) \rightarrow e^+\nu_e(e^-\bar{\nu}_e)$ signature but this time also requiring a jet for the forward $|\eta| > 3.2$ region with a energy threshold defined by the trigger. The jets stored in the offline and online samples were determined to be the same jet by applying a match condition of $\Delta\phi < 0.3$ (commonly jets would need to be matched in both η and ϕ but as the jets

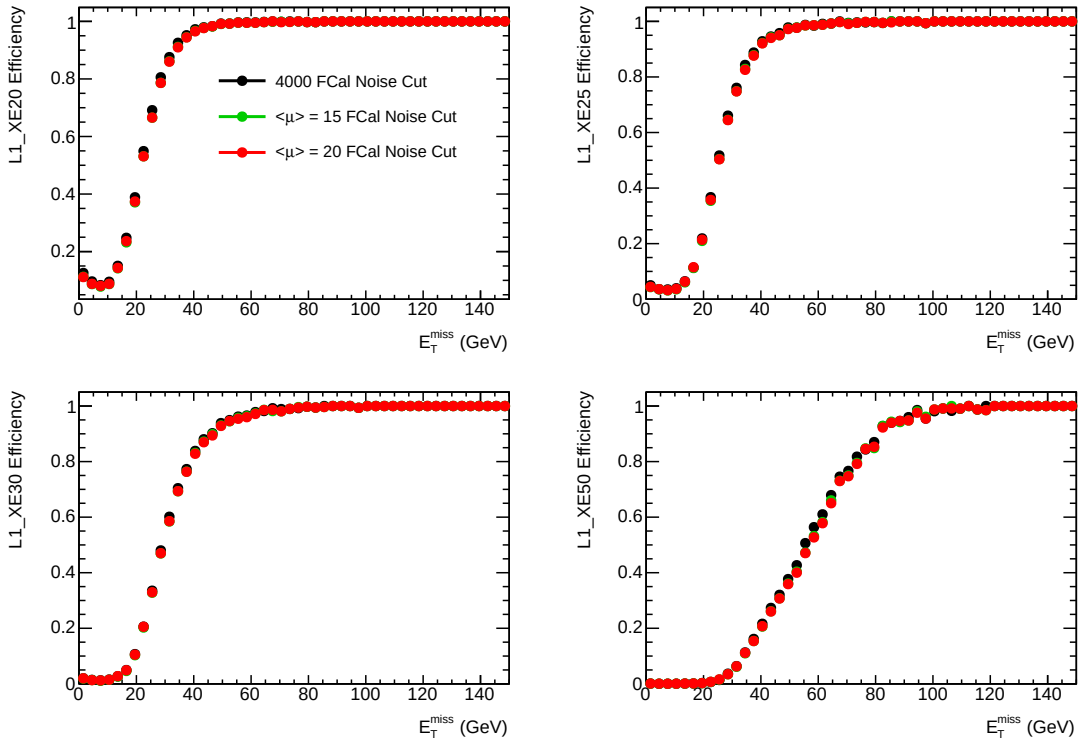

Figure 4.8.: Level one E_T^{miss} trigger efficiencies for trigger thresholds of 20, 25, 30 and 50 GeV comparing two sets of η specific noise cut schemes.

are forward then the η variation is small). Two trigger thresholds have been considered at 30 and 50GeV and the efficiencies are shown in figure 4.9. Here there is a small drop in efficiency in the turn on region but the plateau sees no change in efficiency. As most analyses use data that is in the plateau region of the trigger, these noise cuts will have no additional effect on efficiency.

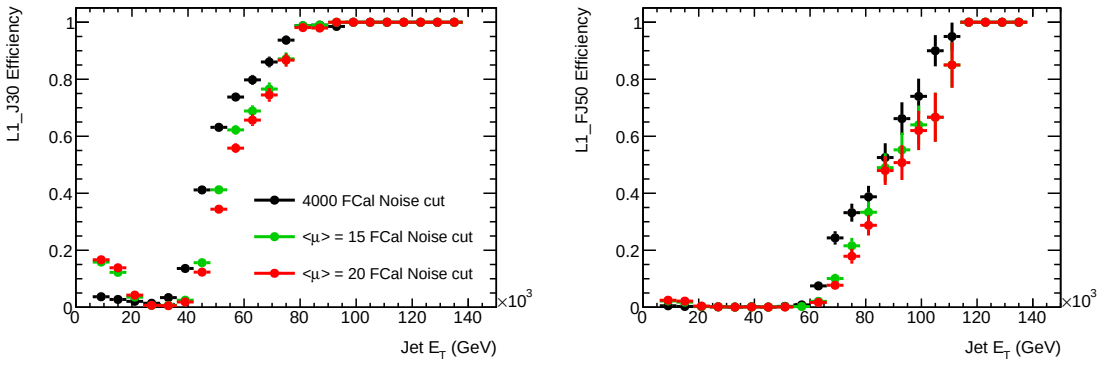

Figure 4.9.: Level one forward jet trigger efficiencies for trigger thresholds of 30 and 50 GeV comparing two sets of η specific noise cut schemes.

4.3. Rate Reduction

The level of rate reduction for the noise cut schemes can be measured using a zero bias data sample with no selection applied. Zero bias data contains events where the trigger triggers on the crossing of filled bunches and no other kinematic requirements. As this selects essentially all events, a heavy prescale needs to be applied to reduce the amount of data to a recordable amount. The zero bias data is made up of almost entirely background processes, so the fewer the number of events passing the threshold, the higher the background rejection. The trigger rates for the four tested E_T^{miss} triggers under varying noise cut scenarios are compared to the 2011 noise cut standard in figure 4.10. The trigger rate for the L1_FJ30 trigger is given in figure 4.11. The trigger rates can be reduced by a factor of 10 of the 2011 rates at a 22000 ADC count flat noise cut for the lower three thresholds and a factor of 5 for the L1_XE50 trigger. This shows that at this point the rate improvements cannot be achieved by increase the noise cuts further. The two η specific noise cut schemes also achieve similar levels of rate reduction while retaining lower noise cuts in some regions of the detector.

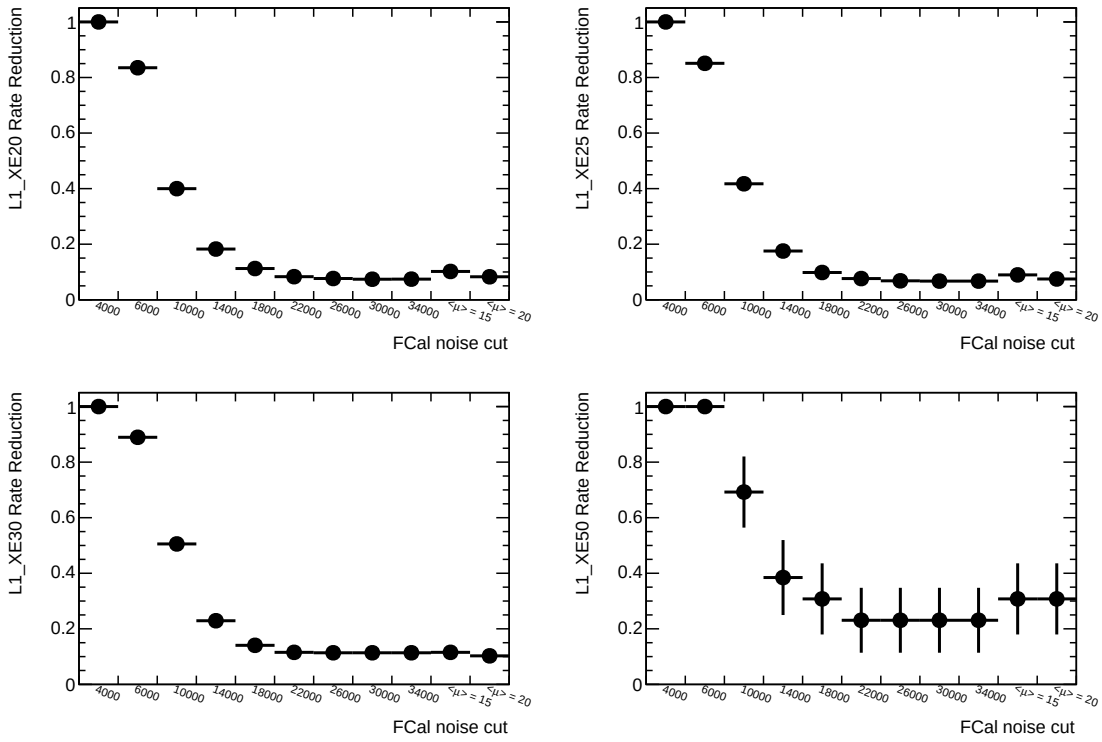

Figure 4.10.: Distribution shows the E_T^{miss} trigger rates (20, 25, 30 and 50 GeV thresholds) for different noise cut schemes relative to the 2011 standard noise cut scheme.

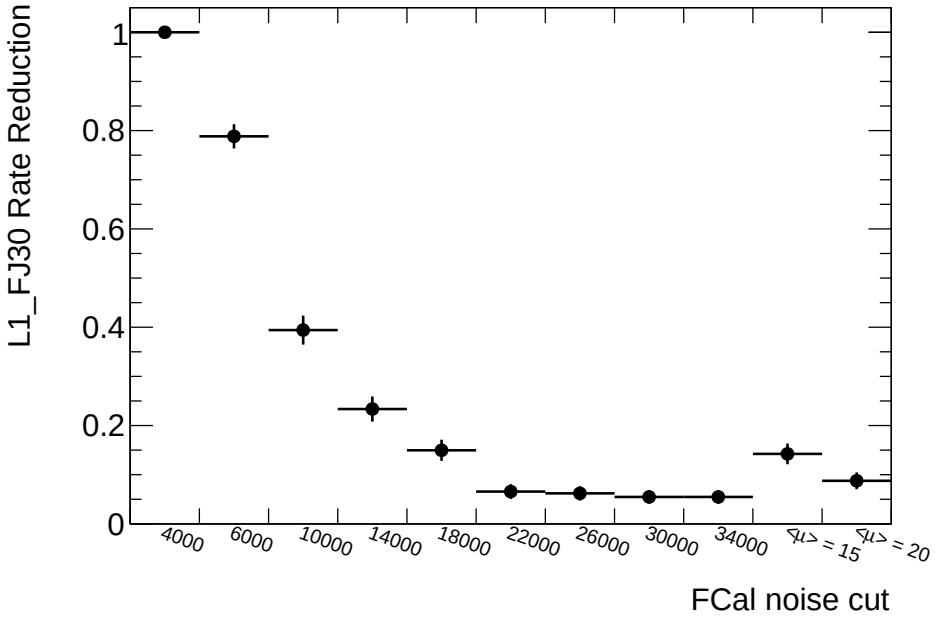

Figure 4.11.: Distribution shows the 30 GeV threshold forward jet trigger rate for different noise cut schemes relative to the 2011 standard noise cut scheme.

4.4. Early 2012 Trigger Efficiencies

Two additional noise cut schemes were determined for the 2012 run after some initial running with the $\langle\mu\rangle = 15$ and $\langle\mu\rangle = 20$ schemes at the start of 2012. These schemes additionally include noise cuts within the electromagnetic calorimeter inner wheel (EMEC-IW) and have been calculated using the same method as used for the $\langle\mu\rangle = 15$ and $\langle\mu\rangle = 20$ schemes shown in figure 4.12. Figure 4.7 shows the two additional schemes noise cuts in the FCal and figure 4.13 shows the additional cuts in the EMEC-IW. The two noise cut schemes labelled $\langle\mu\rangle = 20$ FCAL/EMEC-IW and $\langle\mu\rangle = 25$ FCAL/EMEC-IW have again been tested on the E_T^{miss} triggers in figure 4.14. Again no visible drop off in efficiency is observed.

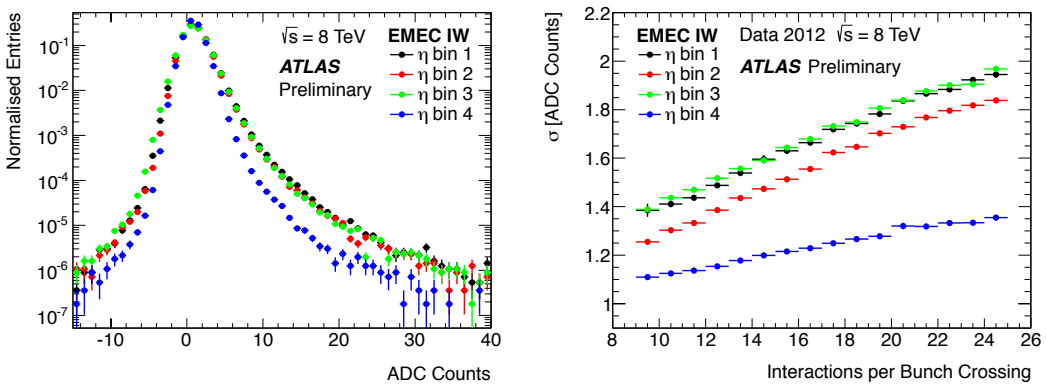

Figure 4.12.: Distribution of the ADC count drifts relative to the peak ADC counts of an event in the four different EMEC-IW η bins (left). The RMS of the ADC counts drift distribution(left) under different pileup conditions (average interactions per bunch crossing $\langle\mu\rangle$) (right). The bin number correspond to the η regions shown in figure 4.1, $2.5 < |\eta| < 2.7$(bin 1), $2.7 < |\eta| < 2.9$(bin 2), $2.9 < |\eta| < 3.1$(bin 3) and $3.1 < |\eta| < 3.2$(bin 4) [23].

The two additional noise cut schemes have also been tested on the L1 jet triggers. Due to the two new noise cut schemes having cuts located in the EMEC-IW wheel ($2.5 < |\eta| < 3.2$) central jet efficiencies have also been tested. As central jets are being tested the offline and online jet matching has to be changed to include $\Delta\eta$ information. A cut of $\Delta R < 0.3$ is used where $\Delta R = \sqrt{(\Delta\phi)^{+}(\Delta\eta)^2}$. The efficiency for the central jet triggers at thresholds of $20, 30, 50$ and 75 GeV are shown in figure 4.15. As expected the small changes to the noise cuts in the inner wheel create no problems with regards to efficiency loss. The forward jet trigger L1_FJ30 has also been tested in this early 2012 running but the small sample size did not allow any conclusions to be made at that time.

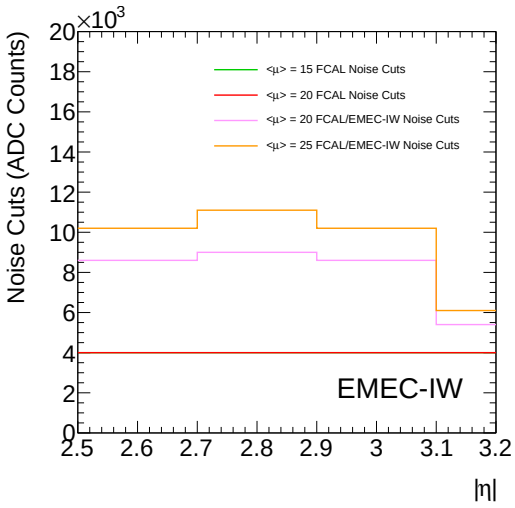

Figure 4.13.: Noise cuts applied in EMEC-IW detector η regions under the four tested noise cuts schemes.

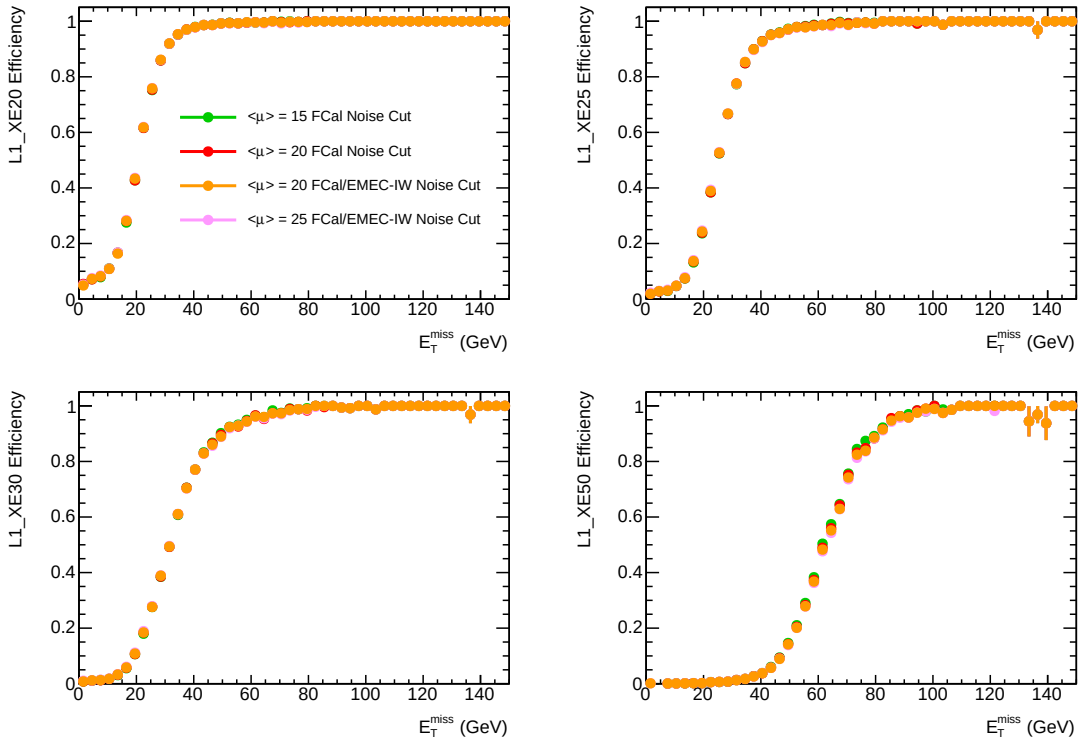

Figure 4.14.: Level one E_T^{miss} trigger efficiencies for trigger thresholds of 20, 25, 30 and 50 GeV comparing four sets of η specific noise cut schemes. The data sample used is from early running in 2012.

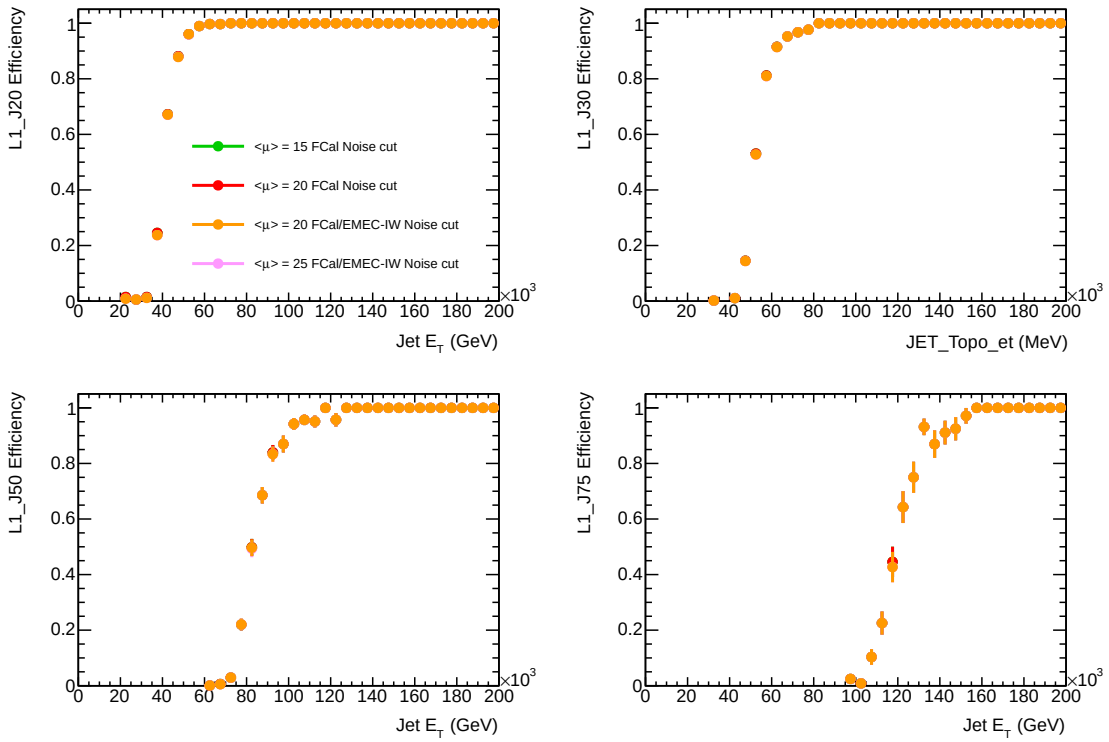

Figure 4.15.: Level one jet trigger efficiencies for trigger thresholds of 20, 30, 50 and 75 GeV comparing four sets of η specific noise cut schemes. The data sample used is from early running in 2012.

Using the information made available by this study the ATLAS detector noise cuts in the FCAL and EMEC-IW were set to the $\langle\mu\rangle = 25$ scheme for the 2012 running. The drop in trigger rates recorded at L1 is shown in figure 4.16. The left hand side of the figure corresponds to the trigger rates during the nominal 2011 running with the standard 2011 noise cuts, the middle of the figure shows the rates for the 2012 running with the new noise cut scheme and the right hand side shows a special high luminosity run performed in 2011 with the 2011 noise cuts. Comparing the L1_XE50 trigger in the left and middle pane at $\langle\mu\rangle = 15$ shows the reduction the noise cuts achieve in trigger rates despite the increased centre of mass energy. Comparing the L1_FJ75 trigger in the middle and right pane at $\langle\mu\rangle = 25$ shows that for the higher pileup conditions the noise cuts reduce the trigger rate by an order of magnitude again despite the increased centre of mass energy.

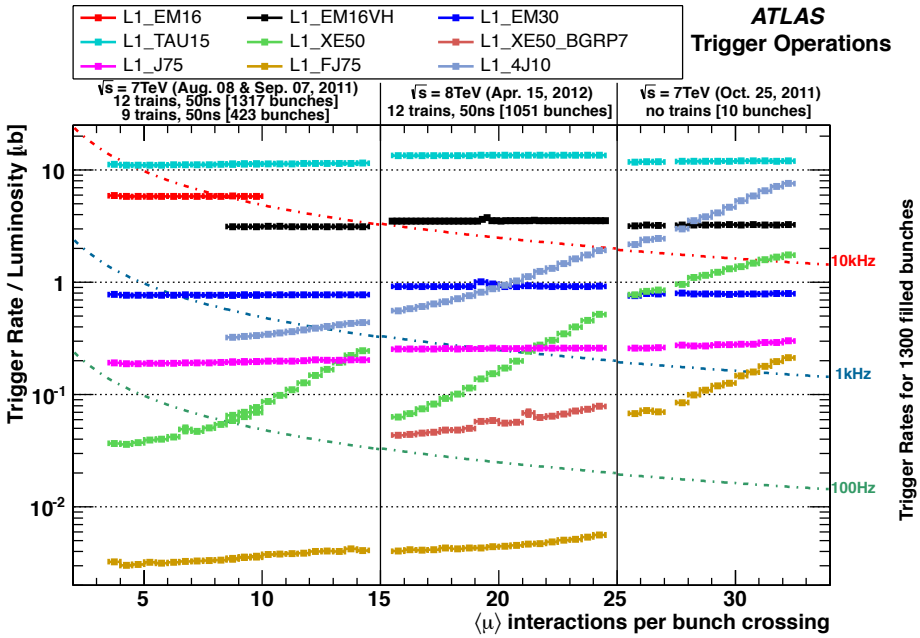

Figure 4.16.: Level-1 Trigger cross-sections (rate/luminosity) for a range of L1Calo triggers. The left panel shows a measurement made in two 7 TeV runs in 2011 using the 2011 standard noise cuts and colliding bunches delivered in 50 ns spaced bunch trains. The middle panel shows a measurement made in a 8 TeV run in 2012 using the $\langle\mu\rangle = 25$ FCAL/EMEC-IW noise cut scheme with again 50 ns bunch spacing. The right panel shows a special high luminosity run at 7 TeV in 2011 using the standard 2011 noise cut scheme with no bunch trains [23].

Chapter 5.

Data and Monte Carlo Samples

This section describes the data and Monte Carlo (MC) samples used in the high mass Drell-Yan analysis. The data sample is taken from the running of the LHC throughout 2012 recording 20.3 fb^{-1} of data. Monte Carlo is used to estimate the contamination of background processes in the signal region as well as calculating the correction factors used for the unfolding of the data.

5.1. Data Sample

In 2012 the LHC increased its centre-of-mass energy from 7 TeV to 8 TeV. This was done to increase the cross section on any potential Higgs signal but additionally had the effect of increasing the amount of recorded data for all analyses. A bunch spacing of 50ns was used throughout the year. The 20.3 fb^{-1} of data was taken throughout 2012 divided into ten periods denoted by the letters A,B,C,D,E,G,H,I,J and L. The periods represent a phase of data taking where there is approximate static detector conditions. Conditions that can change between periods are things such as the triggers that are operating, the detector instantaneous luminosity[1] and the FCal noise cuts discussed in section 4.

[1]High luminosity runs are very important for studying trigger performance under increased pileup.

5.2. Monte Carlo Samples

It is not possible to apply kinematic selections to data that removes all of the background physics processes. These background processes have to be estimated and subtracted from the recorded data. In this analysis both MC prediction and data driven estimations are used to predicted the background. Monte Carlo predictions are also required for the measured physics process so that detector performance can be studied.

The simulation of these processes is done using the Monte Carlo method. The Monte Carlo samples used in particle physics are theoretical predictions of cross sections for a particular process, in which individually simulated collision events are statistically distributed over user defined kinematic phase space, reflecting the kinematic dependance of the calculated cross section.. The samples are processed through various levels of algorithms to simulate the format of real data.

The simulation begins by calculating the matrix element of the hard scattering process, in the case of Drell-Yan this is the $q\bar{q} \rightarrow Z/\gamma^* \rightarrow \mu\mu$ process. Initial and final state gluon radiation contributions are added with the resulting parton showers also included. The method then has to simulate the hadronisation of the partons into colourless hadrons before determining all of the hadron decay products. The remnants of the proton produce similar parton showers and their hadronisation and decay products also need to be added. These decay products are called the underlying event and largely remain in the beam pipe due to the boost of the colliding protons. The event generation is complete when all of the particles have completed the hadronisation step and are in a stable state. These particles are said to be at the hadron level. The four vectors of all of the stable particles are recorded as well as all of the parent daughter information of the intermediate particles. Pileup information is added by separately generating events and adding them to the simulation.

To fully simulate the format of the real data, the detector response has to be accounted for. A detailed description of each aspect of the real life detector has to be simulated in a computer model. The program used to simulate the ATLAS detector is called GEANT4 [24]. It uses the generated hadron level particles four vectors and calculates the particle ionisation in the tracker, the energy deposition in the calorimeters, the decay of the particle and the interaction with the dead material in the detector. The final step of the simulation is to turn these physical aspects of the particle detection into the electronic signal read out by the detector.

The MC can then be reconstructed by the ATLAS software in exactly the same way as the data. This is important as it allows data and MC to be compared without any bias in the reconstruction.

5.2.1. Monte Carlo Generators

Four different MC generators are used in the presented analysis, POWHEG [26] [27] [28], Pythia8 [25], MC@NLO [29] [30] and Herwig++ [31].

The POWHEG and MC@NLO models provide NLO QCD event generation. To complete the computation to the hadron level, hadronisation engines are needed that calculate the parton shower. Interfacing these NLO event generators to hadronisation engines can be difficult as the hadronisation engines will already contain some NLO corrections implemented within their model. A major design issue for these event generators is how to avoids any possible double counting of NLO corrections. The MC@NLO event generator solves this issue by directly subtracting the NLO corrections made by the hadronisation model from the NLO cross section using negative weights. This does however mean that the calculated cross sections are dependant on the hadronisation engine and the negative weights need to be computed correctly. Alternatively the POWHEG event generator computes the hardest radiation first using a technique that only results in positive weight events using the exact NLO matrix elements. This technique does however require interfacing to a hadronisation model with a p_T ordered parton shower.

Pythia8 and Herwig++ are multi purpose generators that can generate events as well as a hadronising the decay products. This means that the generators can provide a MC description at the hadron level either being used in isolation or with alternative event generators or hadronisation models. This is what is done for the Drell-Yan signal MC in this analysis where POWHEG is used as the event generator and Pythia8 is used as the hadronisation model. Pythia8 uses a p_T ordered parton shower allowing the interface to POWHEG but Herwig++ uses an angular ordered parton shower meaning it cannot. The hadronisation models used by Pythia8 and Herwig++ are the lund string [32] and cluster hadronisation [33] models respectively.

To simulate any final state QED radiation (FSR) from the final state leptons an additional program called PHOTOS [34] is used.

5.2.2. Signal and Background Samples

The monte carlo samples used to simulate the background and signal processes are listed in tables 5.1, 5.2, 5.3, 5.4, 5.5 and 5.6. The origin of the backgrounds considered in the analysis are discussed in section 7. To keep MC sample sizes high while reducing the amount CPU time to create them, kinematic cuts called filters are sometimes used at truth level to select events which would likely be outside the detectors acceptance. The efficiency of these selections is called the filter efficiency ϵ_F and is shown in the table. For the MC where a filter is used, the filter definition is given in the table.

Signature	$m_{\mu\mu}$ [GeV]	MC DSID	σ_{MC} [pb] POWHEG	ϵ_F %	N_{evt} [k]
$Z/\gamma^* \to \mu\mu$	60-	129681†	1.110E+03	56.61	49936
$Z/\gamma^* \to \mu\mu$	120-180	129524	9.845E-00	-	4999
$Z/\gamma^* \to \mu\mu$	180-250	129525	1.571E-00	-	1000
$Z/\gamma^* \to \mu\mu$	250-400	129526	5.492E-01	-	600
$Z/\gamma^* \to \mu\mu$	400-600	129527	8.966E-02	-	395
$Z/\gamma^* \to \mu\mu$	600-800	129528	1.510E-02	-	100
$Z/\gamma^* \to \mu\mu$	800-1000	129529	3.750E-03	-	100
$Z/\gamma^* \to \mu\mu$	1000-1250	129530	1.293E-03	-	100
$Z/\gamma^* \to \mu\mu$	1250-1500	129531	3.577E-04	-	100
$Z/\gamma^* \to \mu\mu$	1500-1750	129532	1.123E-04	-	100
$Z/\gamma^* \to \mu\mu$	1750-2000	129533	3.838E-05	-	100

Table 5.1.: Drell-Yan Powheg-pythia8 Monte Carlo samples used in the analysis. The second column gives the mass range in which the Drell-Yan process was simulated, the third the internal ATLAS dataset ID number (DSID). The fourth column lists the MC sample cross section times branching ratio, the fifth column shows the filter efficiency and the sixth column lists the number of events produced. † Note the filter on the Z resonance sample selects two muons with $p_T > 15$ GeV.

Signature	$m^{\dagger}_{\ell\ell}$ [GeV]	MC DSID	σ_{MC} [pb] HERWIG LO	NLO	ϵ_F [%]	N_{evt} [k]
$WW \to \ell X$	-‡	105985	32.501	56.844	38.21	2500
$ZZ \to \ell X$	-‡	105986	4.6915	7.3562	21.15	245
$WZ \to \ell X$	-‡	105987	12.009	21.4721	30.53	1000
$WW \to \mu\nu\mu\nu$	400-1000	180457	0.37894	0.66276	74.75	10
$WW \to \mu\nu\mu\nu$	1000-	180458	0.37896	0.66280	1.11	10
$WZ \to \mu\mu$	400-1000	180459	0.46442	0.83038	0.31	10
$WZ \to \mu\mu$	1000-	180460	0.46444	0.83042	0.01	10
$ZZ \to \mu\mu$	400-1000	180461	0.34574	0.54212	0.14	10
$ZZ \to \mu\mu$	1000-	180462	0.34574	0.54212	0.003	10

Table 5.2.: Diboson Herwig Monte Carlo samples used in the analysis. The second column gives the mass range in which the diboson process was simulated, the third the internal ATLAS dataset ID number (DSID). The fourth and fifth column lists the MC sample cross section times branching ratio for the LO and NLO calculations. The sixth column gives the filter efficiency and the seventh lists the number of events produced.† Note that the selection on $m_{\ell\ell}$ given in this table applies to the two highest p_T leptons in the event at the truth Born level. ‡ Note that these MC samples are created for all the relevant decay channels and the filter simply requires one lepton.

DSID	MC number	σ_{MC} [pb] MC@NLO NLO	NNLO	ϵ_F [%]	N_{evt} [k]
$t\bar{t} \to \ell X$	105200‡	208.13	252.08	54.26	14990
Single Top s-channel	108344	0.56	0.61	-	200
$Wt \to X$	108346	20.67	22.39	-	2000

Table 5.3.: Top MC@NLO Monte Carlo samples used in the analysis. The second column gives the internal ATLAS dataset ID number (DSID). The third and fourth columns lists the MC sample cross section times branching ratio for the NLO and NNLO calculations. The fifth column gives the filter efficiency and the sixth lists the number of events produced. ‡ Note that this MC sample is created for all the relevant decay channels and the filter simply requires one lepton.

Signature	$m_{\tau\tau}$ [GeV]	MC DSID	σ_{MC} [pb] POWHEG	N_{evt} [k]
$Z/\gamma^* \to \tau\tau$	60-	147808	1.109E+03	4995
$Z/\gamma^* \to \tau\tau$	180-250	158731	1.248E-00	150
$Z/\gamma^* \to \tau\tau$	250-400	158732	4.360E-01	150
$Z/\gamma^* \to \tau\tau$	400-600	158733	7.180E-02	150
$Z/\gamma^* \to \tau\tau$	600-800	158734	1.224E-02	150
$Z/\gamma^* \to \tau\tau$	800-1000	158735	3.072E-03	150
$Z/\gamma^* \to \tau\tau$	1000-1250	158736	1.072E-03	150
$Z/\gamma^* \to \tau\tau$	1250-1500	158737	2.997E-04	150
$Z/\gamma^* \to \tau\tau$	1500-1750	158738	9.518E-05	150
$Z/\gamma^* \to \tau\tau$	1750-2000	158739	3.261E-05	150

Table 5.4.: Drell-Yan Powheg-pythia8 Monte Carlo samples used in the ditau channel of the analysis. The second column gives the mass range in which the Drell-Yan process was simulated, the third the internal ATLAS dataset ID number (DSID). The fourth column lists the MC sample cross section times branching ratio and the fifth column lists the number of events produced.

Signature	$m_{\mu\mu}$ [GeV]	MC DSID	σ_{MC} [pb] POWHEG	N_{evt} [k]
$\gamma\gamma \to \mu\mu$	60-200	129662	2.693E+00	500
$\gamma\gamma \to \mu\mu$	200-600	129663	1.216E-01	200
$\gamma\gamma \to \mu\mu$	600-1500	129664	3.495E-03	100
$\gamma\gamma \to \mu\mu$	1500-2500	129665	5.869E-05	100
$\gamma\gamma \to \mu\mu$	2500-	129666	2.297E-06	100

Table 5.5.: Photon induced Pythia8 Monte Carlo samples used in the analysis. The second column gives the mass range in which the photon induced process was simulated, the third the internal ATLAS dataset ID number (DSID). The fourth column lists the MC sample cross section times branching ratio. The fifth column lists the number of events produced.

5.3. Monte Carlo Theory Corrections

The MC are adjusted at the truth level to satisfy the requirements of the analysis. Additional reweighting factors are used to correct for changing pileup conditions, the data

	MC	σ_{MC} [pb] POWHEG		N_{evt}
Signature	DSID	NLO	NNLO	[k]
$W^+ \to \mu\nu$	147801	6891.0	7104.6	200
$W^+ \to \tau\nu$	147802	6890.0	7103.6	100
$W^- \to \mu\nu$	147804	4790.2	4919.5	200
$W^- \to \tau\nu$	147805	4790.9	4920.3	100

Table 5.6.: W Powheg Pythia8 Monte Carlo samples used in the analysis. The second column gives the internal ATLAS dataset ID number (DSID). The third and fourth columns list the MC sample cross section times branching ratio at NLO and NNLO. The fifth column lists the number of events produced.

integrated luminosity and the higher order corrections to the cross section calculation of the MC.

5.3.1. Luminosity Reweighting

Monte Carlo samples that are used to predict the physics processes in the analysis need to be normalised to the amount of data taken by the ATLAS detector. The luminosity scale factor is calculated using the following equation:

$$L_{MC} = \frac{\mathcal{L}_{data}\sigma_{MC}\epsilon_F}{N_{evt}} \tag{5.1}$$

where $\mathcal{L}_{data}$ is the luminosity of the data, σ_{MC} is the cross section of the MC multiplied by the process branching ratio[2] and N_{evt} is the number of events generated by the MC. The MC cross sections and number of events are given in tables 5.2, 5.3, 5.4, 5.5 and 5.6.

5.3.2. Higher Order Corrections

For the high level of precision required by the high mass Drell-Yan measurement, MC that only describe leading order processes are not of sufficient precision. Correction factors that adjust the MC samples cross sections are required to simulate the additional next-to

[2]The branching ratio just gives the fraction of total decays in the particular decay channel.

leading order (NLO) and next-to-next-to leading order (NNLO) terms. The correction terms, called k-factors either scale the LO MC to NNLO or NLO MC to NNLO as follows:

$$k_{NNLO/LO} = \frac{\sigma_{NNLO}}{\sigma_{LO}}, k_{NNLO/NLO} = \frac{\sigma_{NNLO}}{\sigma_{NLO}} \tag{5.2}$$

where σ is the MC cross section. As the higher order processes are heavily dependant on the momentum transfer of the interaction, k-factors for the Drell-Yan process have been parameterised using a dilepton mass dependant function. The function was determined using a NNLO calculation in FEWZ [35] of a di-electron Drell-Yan process and includes NNLO QCD and higher order electroweak effects. As the nominal signal MC sample is produced to NLO by PowhegPythia8 the k-factors used in the analysis are $k_{NNLO/NLO}$ and are shown as a function of mass in figure 5.1. As the k-factors are lepton flavour independent the $Z/\gamma^* \to \tau\tau$ MC also uses the k-factor values shown in figure 5.1. The mass has been chosen as a parameterisation for the k-factor due to the large mass range over which the measurement is made. In principle the k-factors should also incorporate the rapidity information but effect of this variation is expected to be small. The k-factors for the background processes will also depend on the kinematics of the process but there is no parameterised k-factors available so the applied k-factors are single valued. This correction is applied by replacing the LO or NLO cross section values in equation 5.1 with NNLO cross section values.

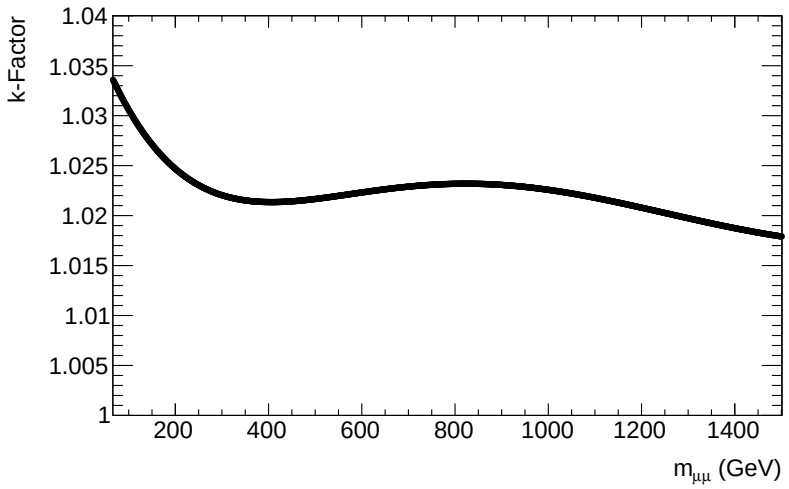

Figure 5.1.: The $k_{NNLO/NLO}$ factor applied to the nominal Drell-Yan MC in terms of dimuon mass.

5.3.3. Pileup Reweighting

The level of pile-up observed in the ATLAS detector depends heavily on conditions of the data runs, such as the bunch spacing or proton density of the bunch. As these values are changed throughout the year of data taking to optimise the amount and quality of data that is recorded, a changing level of pile-up is observed. As the levels of pileup are not static, the pileup in the MC has to be corrected. A standard tool was developed within the ATLAS collaboration that corrects the average number of interactions per bunch crossing ($\langle\mu\rangle$) in MC to that observed in data. A distribution showing the corrected MC compared to data within the reconstruction selection (reconstruction selection is described in section 6.2) is shown in figure 5.2. An equivalent plot for the number of primary reconstructed vertices is also shown in figure 5.2 but the data MC agreement is diminished meaning the out of time pileup is not well described.

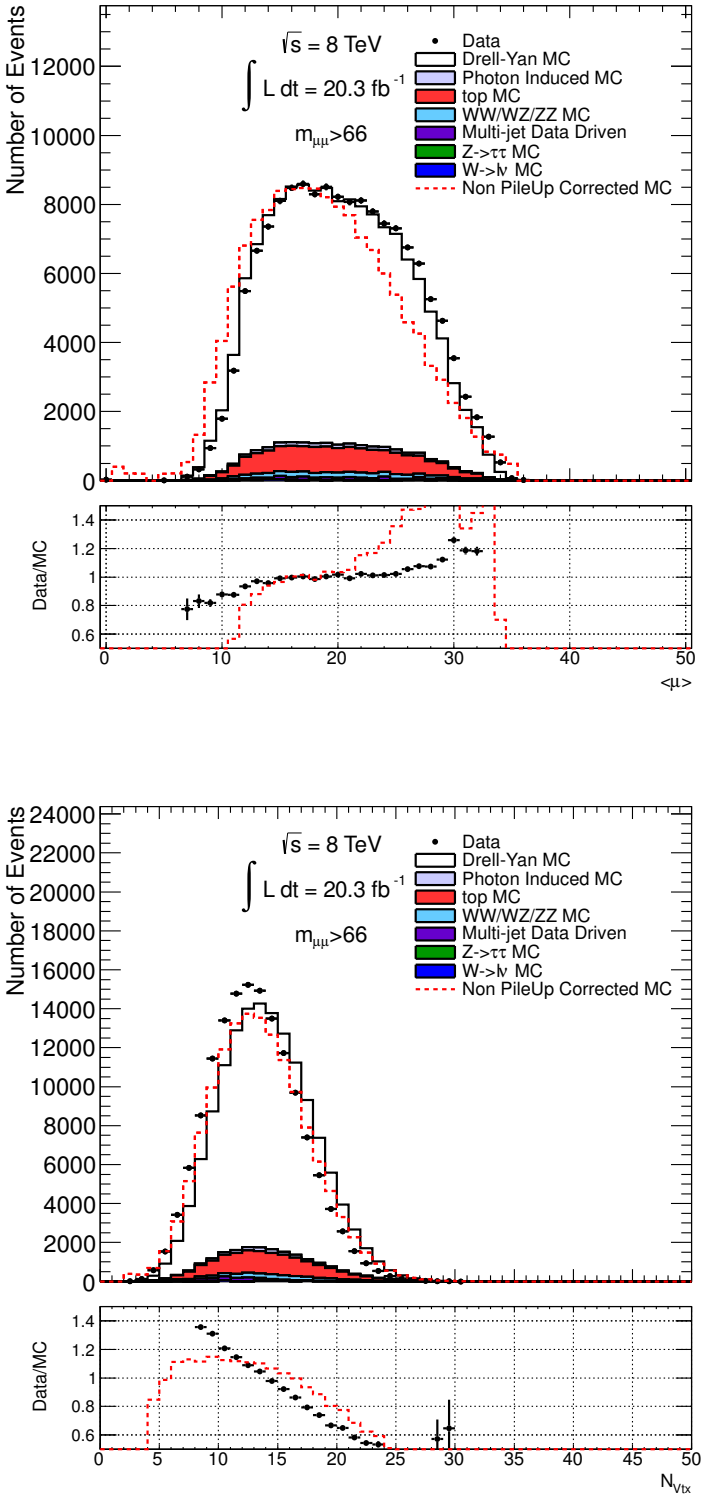

Figure 5.2.: The average number of interactions per bunch crossing $\langle\mu\rangle$ (top) and the number of primary reconstructed vertices N_{Vtx} (bottom).

Chapter 6.

Selection and Muon Performance

This section gives a summary of the nominal selections made for the cross section measurements along with muon perfomance related studies. The source of systematic uncertainties are discussed and summarised in section 9.3.2.

6.1. The Fiducial Volume

The measurement of the Drell-Yan cross section in this analysis has been made to the born level. The born level defines the unfolded truth particle as a particle that has not undergone QED FSR. This is discussed further in chapter 9. The cross section measurement is made in the following fiducial volume:

- $p_T^{\mu 1} > 40$ GeV
- $p_T^{\mu 2} > 30$ GeV
- Muon $|\eta| < 2.5$
- $116 < m_{\mu\mu} < 1500$ GeV

where $p_T^{\mu 1}$ and $p_T^{\mu 2}$ are the p_T of the leading and subleading muon respectively. The dimuon mass range of the fiducial volume is chosen to compliment measurements made of the Drell-Yan cross section in both the low mass region below the Z resonance [36] ($26 < m_{\mu\mu} < 66$ GeV) and on the Z resonance [37] ($66 < m_{\mu\mu} < 116$ GeV). The η range of the fiducial volume exceeds the η range accessible by the combined muon definition ($|\eta| < 2.4$) but is required for combinations with the electron channel. The extrapolation

to the fiducial volume can be achieved without large levels of uncertainty due to the small size of the extrapolation. The p_T requirements have again been selected with the equivalent electron channel measurement in mind as there are no electron triggers with $p_T < 30$ GeV.

For the 2D double differential mass and $\Delta\eta_{\mu\mu}$ measurement there is also a fiducial selection of $\Delta\eta_{\mu\mu} < 3$. This has been implemented due to the electron measurement requiring a $\Delta\eta_{\mu\mu}$ reconstruction level selection of $\Delta\eta_{\mu\mu} < 3.5$ that is used reduce backgrounds.

6.2. Reconstruction Level Selection

Selections are placed on the data to provide a good background rejection while maintaining a high signal efficiency. $Z/\gamma^* \to \mu\mu$ candidates are defined by the following selections.

- Event passes the ATLAS data quality good runs list.
- Event rejected if the LAr Error is present.
- Either EF_mu24i_tight or EF_mu36_tight single muon triggers fired.
- Event has ≥ 2 combined third chain algorithm muons passing the following selections.
  - Muon is of third chain medium plus definition.
  - Muon passes muon combined performance quality cuts.
  - $p_T > 30$ GeV
  - $|\eta| < 2.4$
  - $|z_0| < 10$ mm
  - Isolation requirement, $I_{\mu\mu} = \Sigma p_T^{(\Delta R=0.2)}/p_T < 0.1$
- Event additionally has one muon with
  - $p_T > 40$ GeV
  - Muon must have an opposite sign charge (OS) to one of the selected muons.

The selections made are largely inline with recommendations made by the ATLAS muon combined performance (MCP) group and are explained in the following:

- **ATLAS Good Runs List:** The good runs list (GRL) is provided by the data quality group to help remove any data that has been taken when known errors have been recorded due to the detector configuration or operational error. Each run is split into roughly two minute long lumi blocks where the detector performance is recorded. If there is a detector performance issue such as dead channels or voltage spikes within an individual lumi block then this lumi block can be removed from the good runs lists. For the analysis described here a GRL is used that allows measurement of wide range of standard model precision measurements[1].

- **LAr Error:** During the data taking there are noise bursts in the liquid argon calorimeter. A flag is recorded in the data so these events can be removed individually.

- **Triggers:** The triggers, EF_mu24i_tight and EF_mu36_tight required in the selection are single muon triggers with cuts of $p_T > 24$ and $p_T > 36$ GeV respectively. In addition the EF_mu24i_tight trigger has an isolation requirement of $I_{\mu\mu} < 0.12$ explained below in equation 6.2. The trigger efficiencies are discussed in relation to calculating MC scale factors in section 6.3.5.

- **Third Chain Medium Plus Definition:** For the third chain algorithm muons the definition of a CB muon is looser than those used in the STACO and MuId algorithms. For the STACO and MuId algorithm there is a selection on a variable that measures the energy loss in the calorimeters in relation to the momentum measurements in the ID and MS. As there is no such selection for the third chain algorithm muons additional muons that originate from decays of particles in flight may be measured. To counter this difference additional requirements are applied to the muons under the umbrella term of the medium plus requirements. Applying this selection tightens the requirements for a third chain muon to those used for the STACO and MuId muons.

- **Impact Parameter $z0$:** Cosmic rays in the form of proton and atomic nuclei can penetrate the earth's upper atmosphere and produce a cascade of secondary particles such as muons as they travel through the atmosphere. Due to the high sensitivity of the ATLAS detector some of these muons that reach the detector can be reconstructed as Drell-Yan candidates. To remove any cosmic events from the measurement, an impact parameter cut is used to limit the measurement to muons produced close to the primary z vertex position.

[1] GRL used in the analysis is called data12_8TeV.periodAllYear_DetStatus-v61-pro14-02_DQDefects-00-01-00_PHYS_StandardGRL_All_Good

The two impact parameters that are commonly used in ATLAS measurements are the d_0 and z_0 variables. These values give the distance between the closest approach of the muon track and the primary vertex position. The d_0 variable gives the transverse distance in the x-y plane and the z_0 variable gives the longitudinal distance along the z axis. An additional variable d_0^{sig} that is related to d_0 is also defined as follows:

$$d_0^{sig} = \frac{d_0}{\sigma(d_0)} \tag{6.1}$$

where $\sigma(d_0)$ is the measurement uncertainty on d_0 originating from the determination of the track and z vertex position. The impact parameter selection chosen by this analysis is $|z_0| < 10$mm. This selection was chosen to be consistent with a Z resonance Drell-Yan analysis [37]. The cut is loose enough to maintain a high signal efficiency with appropriate scale factors calculated as discussed in section 6.3.4.

A cosmic muon fakes two opposite sign muons by travelling through the detector towards the beam axis and then away from the beam axis. This change of direction relative to the beam axis means the two fake reconstructed muons have opposite charge. Due to the fact the two reconstructed muons are in fact the same cosmic muon, the variable $\eta_\mu^1 + \eta_\mu^2$ describing the sum of the η of the two reconstructed muons will be very close to unity. The $\eta_\mu^1 + \eta_\mu^2$ distributions for a data sample with or without the z_0 cut are shown in figure 6.1. Figure 6.2 is a zoomed version of figure 6.1, showing the important $\eta_\mu^1 + \eta_\mu^2 = 0$ region.It can be seen from the plot that the z_0 selection has the desired effect of removing the cosmic events.

- **Muon Quality Cuts:** The MCP group within ATLAS provides a set of selections that remove muons that are poorly reconstructed [21]. The set of selections require certain numbers of hits within the ID detector when compared to any dead sensors or flags regarding any reduced detector performance. The ID muon quality requirements are as follows:
  - Number of Pixel Hits + Number of Crossed Dead Pixel Sensors > 0.
  - Number of SCT Hits + Number of Crossed Dead SCT Sensors > 4.
  - Number of Pixel Holes + Number of SCT Holes < 3.
  - A successful TRT extension defined as appropriate hits n_{TRT}^{hits}, in the eta acceptance of the TRT described in section 3.4. An unsuccessful TRT extension can be

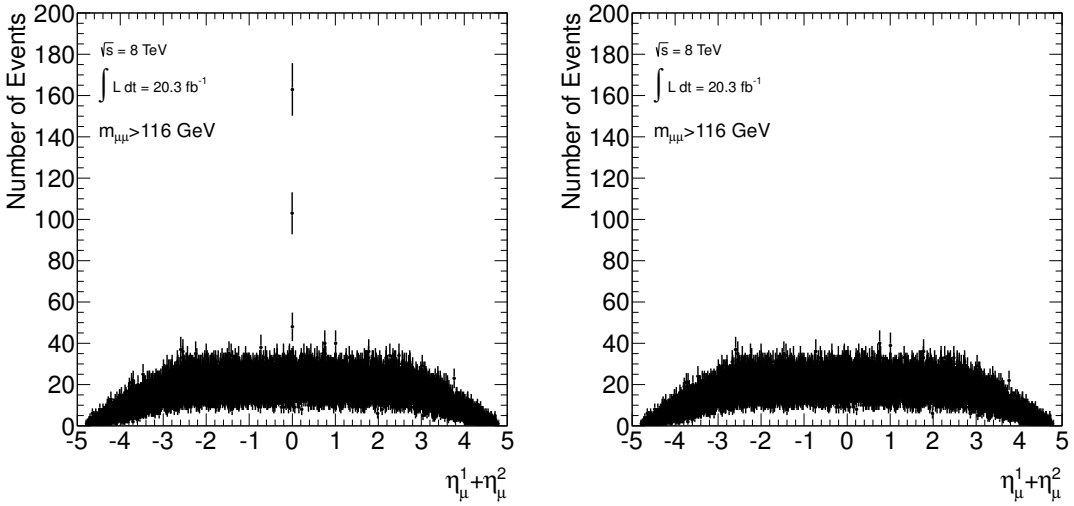

Figure 6.1.: The $\eta_\mu^1 + \eta_\mu^2$ distributions for a data sample with $m_{\mu\mu} > 116$ GeV for a selection including the $|z_0| < 10$ mm cut(right) and without the cut (left).)

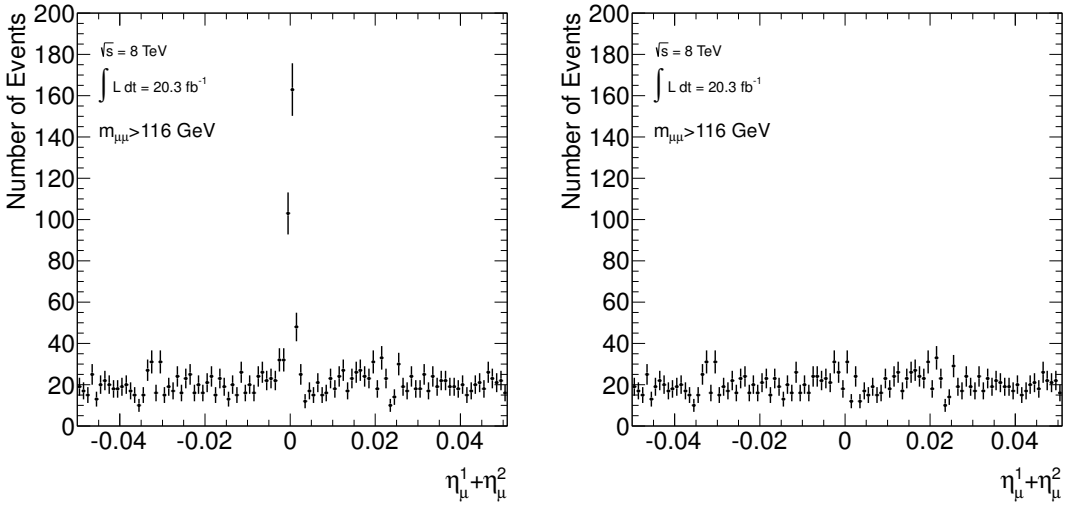

Figure 6.2.: The $\eta_\mu^1 + \eta_\mu^2$ distributions zoomed around $\eta = 0$ for a data sample with $m_{\mu\mu} > 116$ GeV for a selection including the $|z_0| < 10$ mm cut(right) and without the cut (left).)

described by either no hits or a set of hits that are assigned as outliers, $n_{TRT}^{outliers}$. If $n = n_{TRT}^{hits} + n_{TRT}^{outliers}$, then the cut is defined as:

  - For $0.1 < |\eta| < 1.9$, require $n > 5$ and $n_{TRT}^{outliers} < 0.9n$.

- **Isolation Requirement:** A track isolation requirement is implemented to avoid background contamination from jets formed from hadronic decays. Muons originating

from a Z or γ^* decay are expected to be isolated whereas muons originating from jets will have nearby tracks. The isolation condition is defined by a ratio of the p_T of additional objects within a cone of radius $R = 0.2$, ($\Sigma p_T^{R=0.2}$) to the p_T^{μ} of the hard muon. Isolation variable can then be given by:

$$I_{\mu\mu} = \frac{\Sigma p_T^{R=0.2}}{p_T^{\mu}} \tag{6.2}$$

It must be noted that the isolation cut of $I_{\mu\mu} < 0.1$ is a harsher cut than the isolation requirement from the EF_mu24i_tight trigger. The isolation selection used in this analysis has been chosen to be consistent with recommendations from the MCP group. Figure 6.3 shows the signal efficiency versus background rejection for different isolation cuts and cone sizes, calculated using MC. While alternative isolation selections would provide better background rejections the nominal selection was chosen to keep the signal efficiency high.

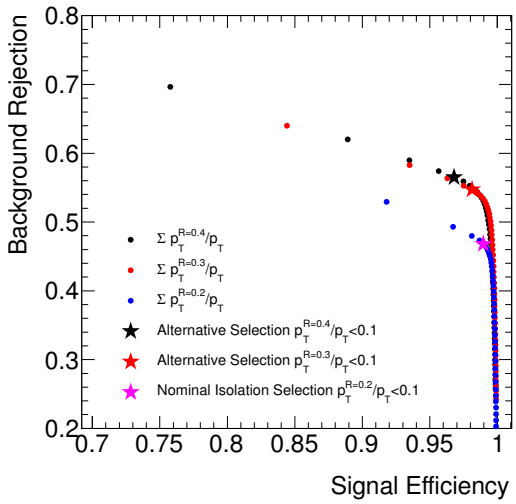

Figure 6.3.: Signal Efficiency versus the background rejection, both as fractions for three different isolation cone sizes. Two alternative isolation selections are shown with the nominal selection.

6.3. Muon Performance

Corrections are applied to the MC to account for any differences between data and simulation in the determination of the muon reconstruction, trigger and isolation efficiencies.

Recommendations from the MCP group have been used where appropriate. The MCP group packages used by the analysis are as follows:

- Muon Momentum Scale - MuonMomentumCorrections-00-09-08-02
- Muon Reconstruction Efficiencies - MuonEfficiencyCorrections-02-01-19-01
- Muon Trigger Efficiencies - TrigMuonEfficiency-00-02-48, used only for comparison to a dedicated study described in this chapter.

Corrections are typically determined using the tag and probe method as described in the section below.

Figure 6.4 shows the the average muon p_T in the dimuon mass bins for Drell-Yan MC. The expected nature of the increasing average p_T with increase dimuon mass is observed but it can also be noted that the higher the dimuon mass the larger the spread of the muon p_T, as shown by the error bars, which represent the RMS of the p_T of the muons in that bin.

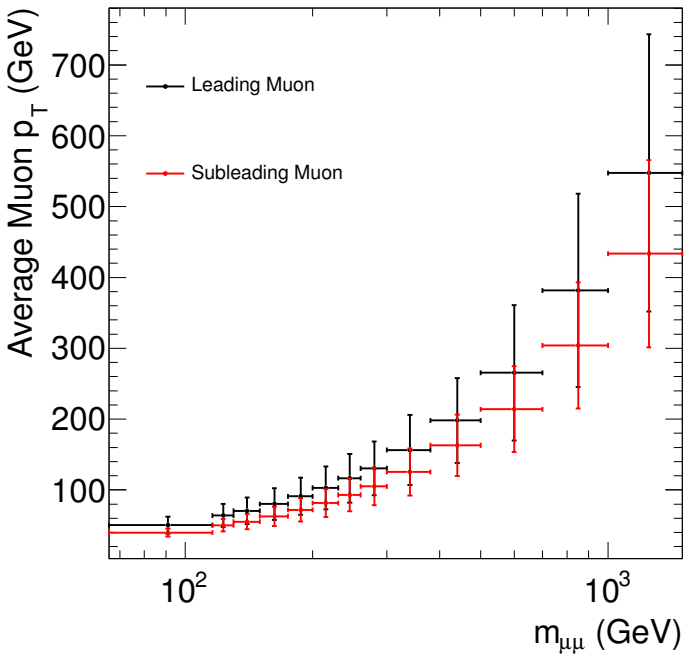

Figure 6.4.: Average muon p_T for the leading and subleading muon in the 1D dimuon mass bins for signal Drell-Yan MC.

6.3.1. The Tag and Probe Method

The tag and probe method is a data driven technique used to determine the efficiency of a selection. Two muons originating from the decay of the same particle (typically a Z boson but other processes such as J/Ψ meson decays can be used) have a high level of correlation that allow you to infer the properties of one from the other. A 'tag' muon is defined by a series of tight selections ensuring the purity of the $Z \to \mu\mu$ events and a 'probe' muon is used investigate the efficiency in question. Comparing efficiencies of data and MC samples gives correction scale factors that can be applied to the MC to correct for this mismodelling. The tag and probe method is used by the ATLAS MCP group to provide scale factors for the trigger and muon reconstruction efficiencies. In addition the tag and probe method is used in this analysis to calculate dedicated scale factors for the trigger and isolation efficiencies described in sections 6.3.4 and 6.3.5.

6.3.2. Muon Momentum Scale and Resolution

To correct mis-modelling of the muon momentum scale and resolution in the ATLAS detector, scale factors are determined by the MCP group [38]. The MC detector level muon transverse momentum is corrected, resulting in improved data MC agreement. The effect of the muon momentum scale change on muon p_T is shown in figure 6.5. The muon momentum scale is adjusted by between 0.01 and 0.25 GeV for muons with $p_T < 300$ GeV. The p_T resolution of the muons described by the MC is also smeared to match results obtained from data and is shown in figure 6.6.

6.3.3. Muon Reconstruction Scale Factors

Muon reconstruction scale factors are calculated to account for any MC mismodelling in the reconstruction of muons within the ATLAS detector [21]. The muon reconstruction efficiencies are calculated by the MCP group using a tag and probe method. As the MS and ID independently reconstruct the muons, a combined muon reconstruction efficiency can be calculated as a combination of the MS reconstruction efficiency, the ID reconstruction efficiency and an efficiency related to the matching between the two. A combined muon is used as the tag muon and then either the MS efficiency is measured by requiring the probe muon to have an ID track or the ID efficiency is measured by requiring the probe to

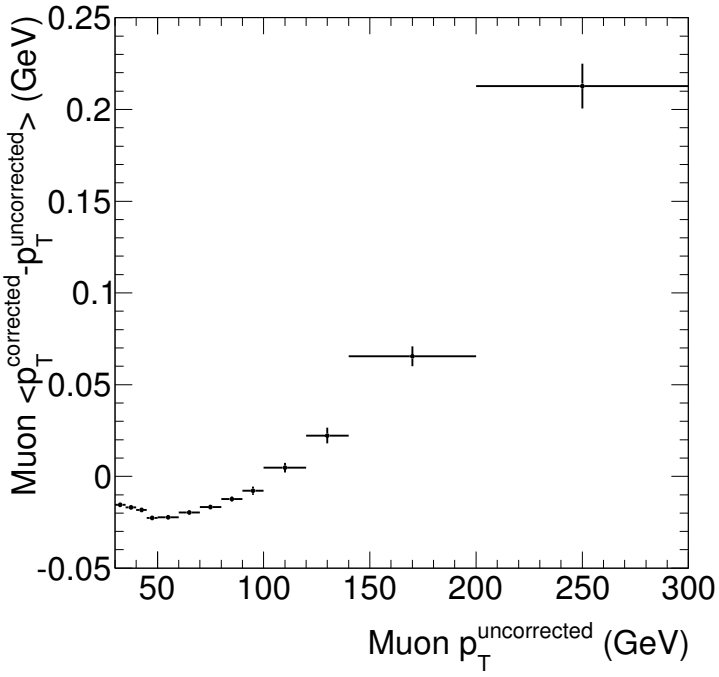

Figure 6.5.: Average difference between the muon scale corrected p_T and uncorrected p_T in each uncorrected muon p_T bin for signal Drell-Yan MC. The y-axis error bars represent the RMS of values that deviate from the mean value in that bin.

have a MS track. The matching efficiency is calculated by requiring the probe muon has a calorimeter tagged track. The scale factors are calculated by taking the data MC ratio of the efficiencies and are parameterised two dimensionally in terms of η-ϕ

The average muon reconstruction scale factors for the reconstruction level selection are shown as a function of η and p_T in figure 6.7. The MC describes the data well with the largest deviations below 1%. Included in the plots are the systematic and statistical uncertainty shifts used to calculate the effect the muon reconstruction has on the cross section results. Again these shifts are very small showing the muon reconstruction SFs are under good control. The systematics considered by the MCP are listed as follows:

- A background contamination systematic.
- A MS ID matching systematic.
- A systematic regarding how the granularity of the bins allows differences in the efficiencies due to the data and MC not having the exact same distribution of probes over the η-ϕ region.

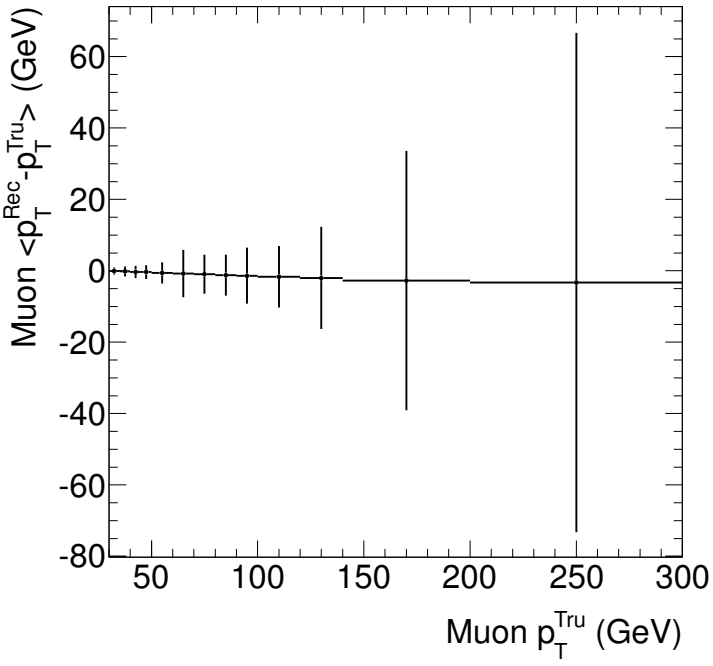

Figure 6.6.: Average resolution of the muon p_T in each p_T bin defined by the reconstructed muon for signal Drell-Yan MC. The y-axis error bars represent the RMS of deviations from the mean value in that bin.

- A systematic accounting from any biases originating from the tag and probe selection.
- A systematic for muons with p_T higher than the range of the study.

The statistical part of this uncertainty provided by the study and shown in figure 6.7 can be propagated to the cross section measurement using the toy MC method as described in section 9.3.1.

6.3.4. Isolation and Impact Parameter Scale Factor

Corrections to the MC isolation efficiencies are determined using a standard tag and probe method. Additionally the loose impact parameter cut applied in the measurement is absorbed into the isolation scale factor. Selections on the tag and probe are made to ensure a high purity of $Z \to \mu\mu$ events. In each event all muons are considered as either a tag or probe muon if the selection criteria are met. The selections made on the tag and probe are as follows:

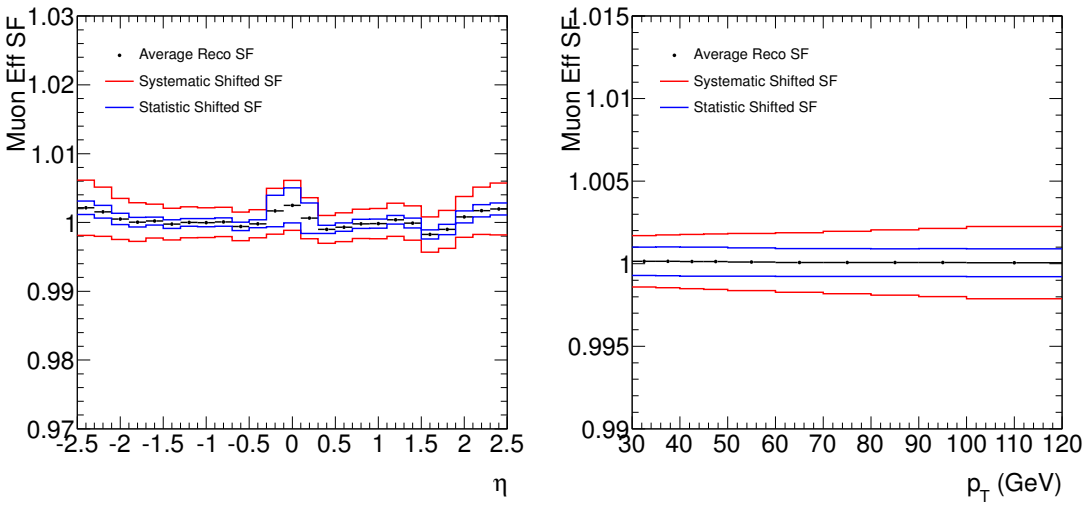

Figure 6.7.: Distributions showing the average muon reconstruction scale factor when a muon is in a particular η(left) or p_T(right) bin in the full analysis selection. As each event selects a leading and subleading muon there are two entries in the plots. The red and blue lines show the systematic and statistical shifted scale factors.

Tag Muon:

- Third chain medium plus definition muon.
- $p_T > 25$ GeV
- $|z_0| < 3$ mm
- $I_{\mu\mu} < 0.1$
- MCP quality cuts

Probe Muon:

- Third chain medium plus definition muon.
- $p_T > 20$ GeV
- MCP quality cuts

Combined Tag and Probe System:

- $\Delta m_Z = |m_Z - m(tag, probe)| < 10$ GeV

where m_Z is the PDG value of the Z boson mass [1]. The η and p_T spectra in data and MC are shown separately for tag and probe muons in figure 6.8. Electroweak background

contamination is predicted by MC and then subtracted from the data. The multi-jet background is predicted using a modified ABCD method described in section 7.1.2. The MC underestimates the normalisation by 4% and this is discussed in section 8. The shape of the η spectra are well described by MC but there is a small discrepancy in the shape of the p_T spectra at higher p_T shown in section 8 figure 6.8. This is likely to be due to mismodelling of the dimuon p_T spectrum. The invariant mass spectrum of the tag and probe muon system is shown in figure 6.9 and confirms the purity of $Z \to \mu\mu$ events by reproducing the Z mass lineshape. The total background contamination in the analysis phase space is below 0.4%.

An event with the appropriate tag and probe muons can be used to determine the isolation efficiency by comparing the number of probe muons that pass and fail the nominal isolation requirement of $I_{\mu\mu} < 0.1$ and impact parameter cut $|z_0| < 10$ mm. To avoid bias in the selection both muons are considered as a tag and a probe. The isolation efficiency is observed to depend most strongly on p_T and only weakly on η as shown in figure 6.10. Therefore the scale factor is parameterised as a function of p_T with an assigned systematic uncertainty originating from the weak η dependence.

Three sources of systematic uncertainty are considered, a background contamination systematic, an event topology systematic and an η dependence systematic. Each source of uncertainty is described in the following.

The uncertainty from the level of background contamination in the tag and probe samples is determined by adjusting the selection. The selection changes that are considered are listed as follows:

- Tag Muon $I_{\mu\mu} < 0.26$
- Tag and Probe $\Delta m_Z = |m_Z - m(tag, probe)| < 15$ GeV
- Tag Muon $p_T > 40$ GeV

The total uncertainty in each p_T bin is taken as the RMS of the deviations the alternative selection scale factors have from the nominal selection scale factor. The RMS is taken since each variation is not an independent source of systematic uncertainty but rather the variations to the selection all affect the level of multi-jet background contamination. The effect the selection has on the efficiencies is shown in figure 6.10. The difference between the efficiencies is small apart from at low p_T where the changes to selection will adjust the level of multi-jet background contamination in the sample.

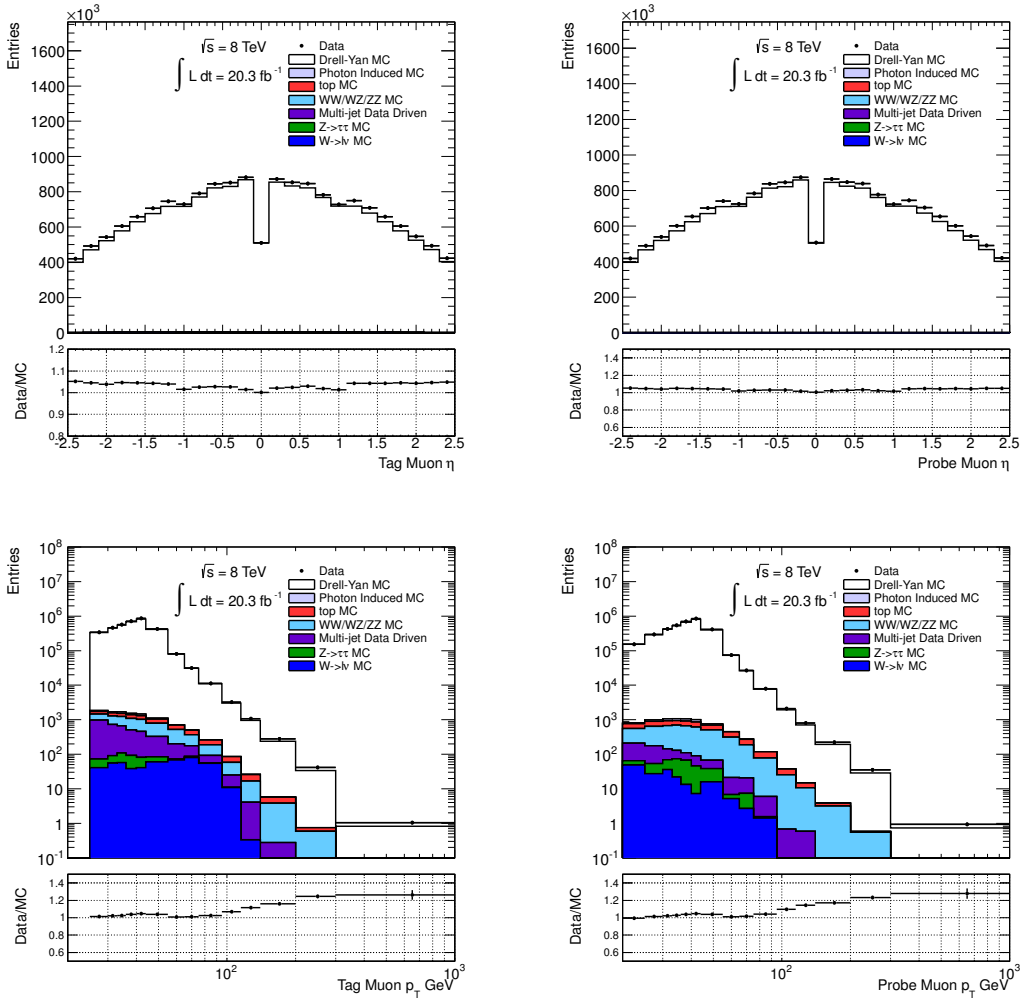

Figure 6.8.: The η and p_T spectra of the tag (left) and probe (right) muons. The lower pad shows the ratio of the data and MC prediction.

A systematic uncertainty related to the topology of the tag and probe muons is considered by recalculating the isolation efficiencies with the addition of a selection on the absolute difference in tag and probe ϕ denoted by $\Delta\phi$. The selection $\pi - \Delta\phi < 2$ is used for this systematic uncertainty consideration. The cut is not considered in the nominal selection because while it has a good background rejection, it also rejects the boosted topologies that result in higher p_T muons. Due to this kinematic limit, this source of systematic uncertainty can only be calculated for muons with $p_T < 115$ GeV. The statistical errors on the calculated isolation scale factors dominate in this region meaning the topology systematic is considered negligible at high p_T. The isolation efficiencies

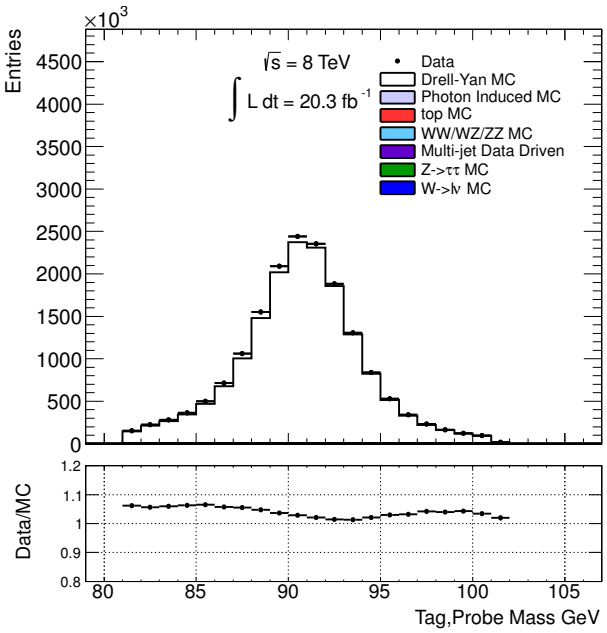

Figure 6.9.: The tag and probe dimuon invariant mass distribution. The backgrounds are shown but are negligible. The lower pad shows the ratio of the data and MC prediction.

calculated with the $\Delta\phi$ cut are shown in figure 6.10. The systematic uncertainty is taken to be the deviation this alternative selection has on the scale factor in each muon p_T bin.

Figure 6.10 also shows the variation of the isolation efficiencies and scale factors with respect to muon η. A small variation with respect to η is observed in the scale factors. A systematic uncertainty is assigned to this variation by calculating the average scale factor across the η range and then averaging the magnitude of the deviations in each bin with respect to the average scale factor. This single value uncertainty of 0.017% is then applied to the full p_T range.

The total uncertainty is calculated as the quadratic sum of the background systematic, topology systematic, η variation systematic and statistical uncertainty and is shown in figure 6.11. Figure 6.12 shows the isolation scale factors used in the measurement. The isolation efficiencies are well described by MC, leading to small scale factor corrections of less than 0.4% for the full p_T range. The largest corrections are seen at $p_T < 30$ GeV, where the multi-jet background contamination is at its largest, and $p_T > 150$ GeV where the statistical uncertainty is dominant. This nature is evident from figure 6.11.

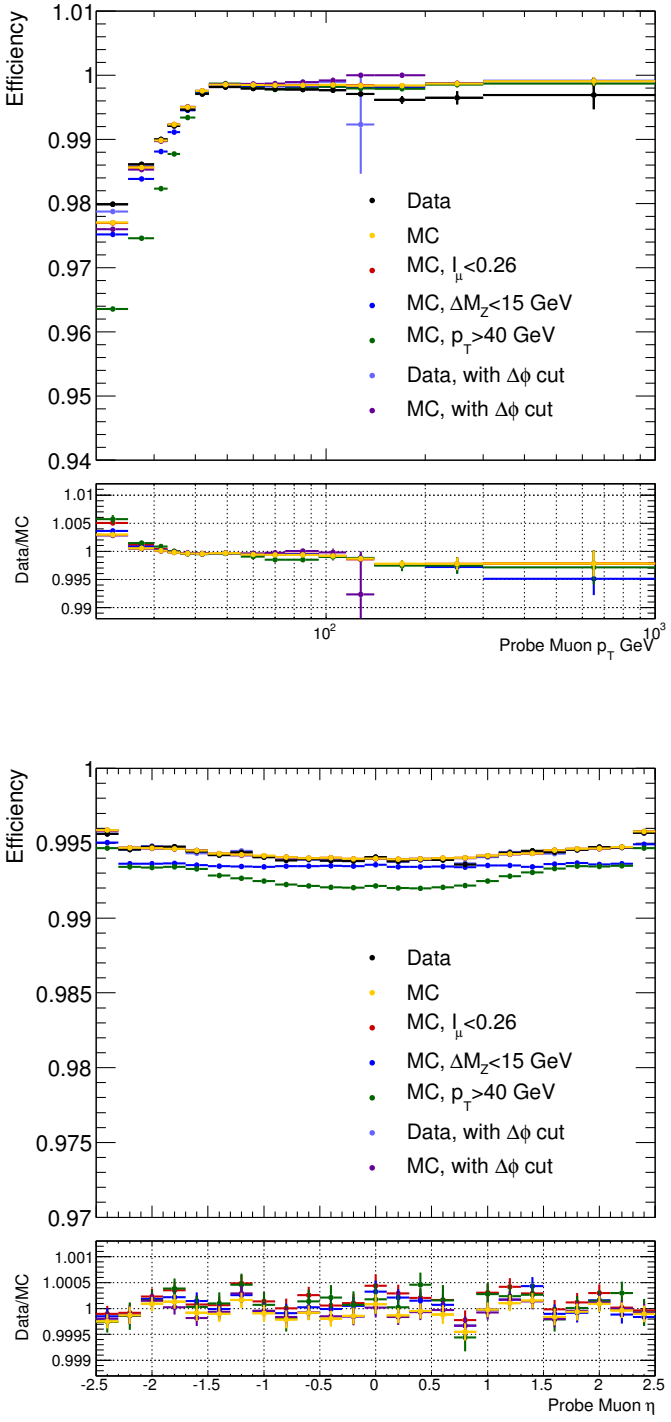

Figure 6.10.: The isolation efficiencies are presented in terms of muon p_T(top) and muon η(bottom). The lower pad shows the ratio of the data and MC prediction, which is equivalent to the isolation scale factor. Additional the plots show the effect the alternative selections have on the efficiency.

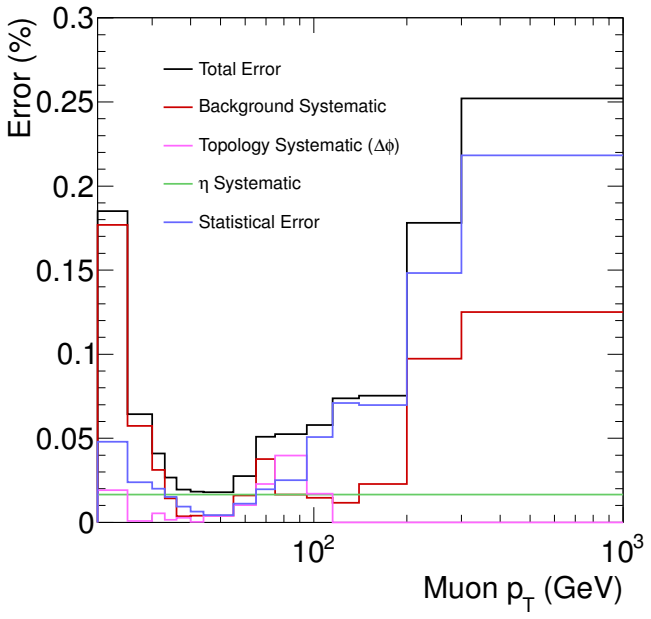

Figure 6.11.: The relative contributions of the considered systematic uncertainties on the isolation scale factors. The black line corresponds to the total uncertainty and the coloured lines correspond to the systematic and statistical uncertainties considered.

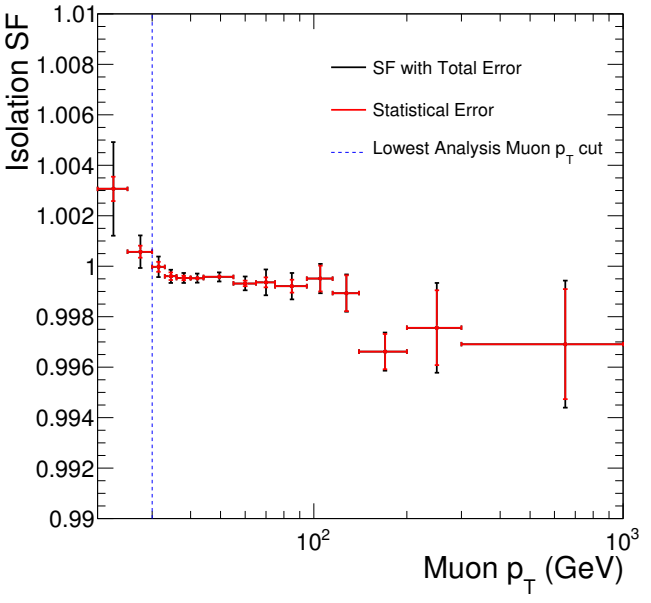

Figure 6.12.: The isolation scale factors with associated systematic and statistical uncertainties. The dashed line shows the lowest muon p_T cut applied in the nominal selections for the cross section measurements.

6.3.5. Trigger Scale Factors

Corrections to the MC trigger efficiencies are provided by the muon trigger signature group for STACO and MUID algorithm muons with systematic uncertainties considered too conservative for a precision cross section measurement [39]. Therefore a dedicated evaluation of the trigger efficiencies for this measurement using third chain muons has been carried out and described in the following section. A tag and probe method similar to that used in the determination of the isolation efficiency scale factors has been used to calculate the trigger efficiency scale factors. The selections made on the tag and probe muons are the same as those used by the muon trigger signature group in the determination of the standard muon trigger efficiency scale factors. The selections made on the tag and probe are as follows:

Tag Muon:

- Medium definition Third Chain Muon
- $p_T > 25$ GeV
- $|z_0| < 3$ mm
- $I_{\mu\mu} < 0.1$
- MCP quality cuts
- EF_mu24i_tight or EF_mu36_tight triggers fired. A ΔR match between the triggered muon and the tag muon is applied.

Probe Muon:

- Medium definition Third Chain Muon
- $p_T > 20$ GeV
- $I_{\mu\mu} < 0.1$
- MCP quality cuts

Combined Tag and Probe System:

- $|\Delta d_0(tag, probe)| < 10$ mm
- $|\Delta z_0(tag, probe)| < 20$ mm

- $\Delta m_Z = |m_Z - m(tag, probe)| < 10$ GeV

The η and p_T spectra in data and MC are shown for the tag and probe muons in figure 6.13. The level of agreement between data and MC is similar to that found in the isolation efficiency scale factor determination.

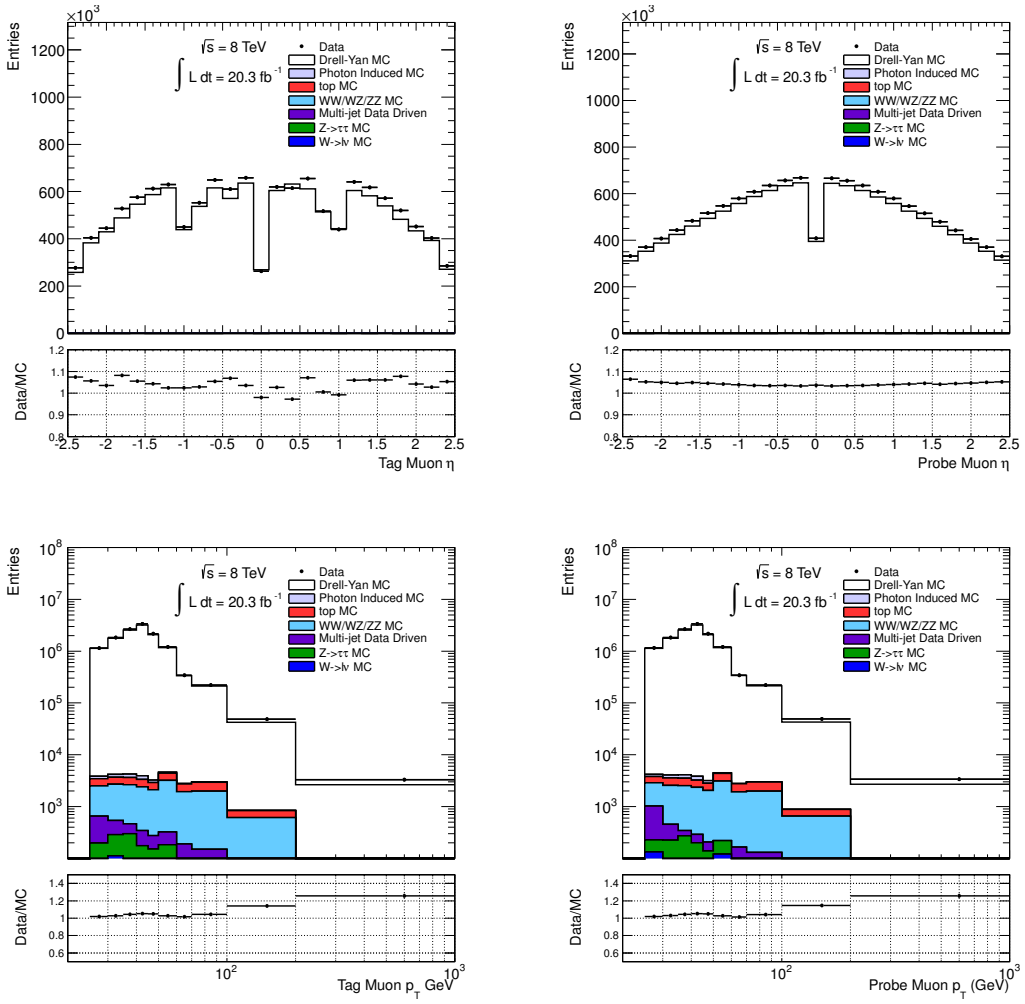

Figure 6.13.: The η and p_T spectra of the tag (left) and probe (right) muons. The lower pad shows the ratio of the data and MC prediction.

The triggers used in the analysis are the EF_mu24i_tight trigger, which has a threshold of $p_T > 24$ GeV and a HLT track isolation cut of $I_{\mu\mu}^{\Delta R=0.2} < 0.12$ and the EF_mu36_tight, which has a threshold of $p_T > 36$ GeV but without any isolation cut applied. By ensuring that the tag muon fired on either of the tested triggers, the probe muon is free to pass or fail the triggers allowing a measurement of the trigger efficiency to be made. As with the

isolation efficiencies the electroweak background is predicted using MC and the multi-jet background is calculated using a modified ABCD method described in section 7.1.2.

The ATLAS muon triggers are defined by the p_T cut applied to the muons. Above this threshold the p_T dependence of the trigger efficiencies is small. The largest variation in the trigger efficiencies comes as a result of the varing detector subsystems and their respective perfomance. For these reasons the trigger efficiency scale factors have been parameterised by the η and ϕ variables with an additional systematic uncertainty added to account for any residual p_T dependence. Due to the nature of the toriodal magnetic field produced by the detector combined with a non perfect distribution of working trigger towers, there is a observed charge dependence seen in the trigger efficiency scale factors shown in figure 6.14. The double ratio of positive to negative muon efficiencies and data to MC efficiencies is defined by the formula:

$$R_D = \left(\frac{\epsilon^-_{data}}{\epsilon^+_{data}}\right) / \left(\frac{\epsilon^-_{MC}}{\epsilon^+_{MC}}\right) \tag{6.3}$$

where ϵ^-_{data} and ϵ^+_{data} are the data trigger efficiencies for the positive and negative muons and ϵ^-_{MC} and ϵ^+_{MC} are the MC trigger efficiencies for the positive and negative muons. Figure 6.15 shows the double ratio in terms of η and ϕ. The deviations from unity shown are much larger than statistical fluctuations in the trigger efficiencies, which can be seen for data and MC in figures 6.24 and 6.25. To account for this difference all of the positively charged anti-muons and negatively charged muons have been treated separately with trigger efficiency distributions calculated for each.

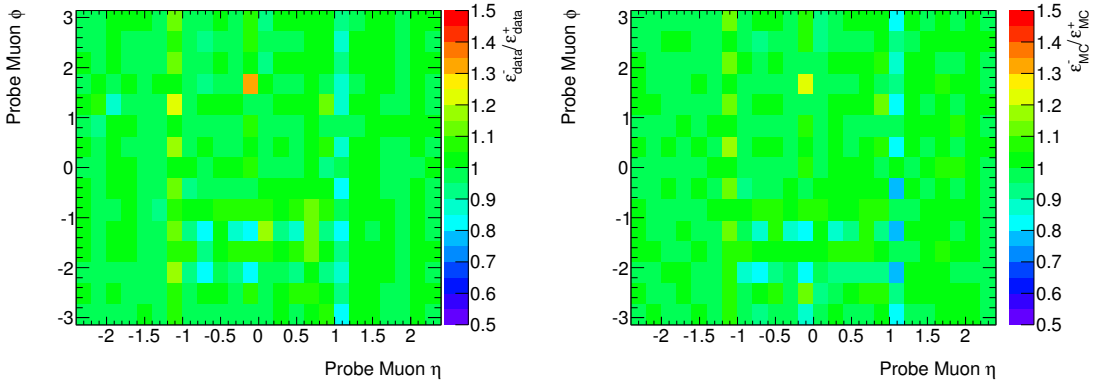

Figure 6.14.: Distributions showing the ratio of positive to negative muon trigger efficiencies in data (left) and MC (right).

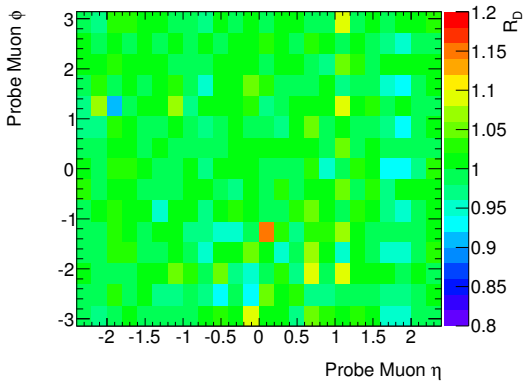

Figure 6.15.: Double ratio R_D of positive to negative muons trigger efficiencies and data to MC trigger efficiencies.

As only one muon is needed to trigger in any given event, a combination of the single muon efficiencies in data and MC are used to build up a MC event weight for events with multiple muons to correct the MC to the measured data efficiency. The trigger event weight W_{trig} for each event is calculated using the following formula:

$$W_{trig} = \frac{1 - \prod_{i=1}^{N}(1 - \epsilon^{i}_{data}(\eta, \phi))}{1 - \prod_{i=1}^{N}(1 - \epsilon^{i}_{MC}(\eta, \phi))} \tag{6.4}$$

where the data and MC trigger efficiencies ϵ are calculated over all the N muons in an event. As a result of the scale factors having a dependence on the number of muons in the event, data and MC trigger efficiencies are needed to calculate an event by event weight rather than single muon scale factors as seen in the isolation efficiency determination. The single muon trigger efficiency is shown for data and MC in figures 6.16 and 6.17.

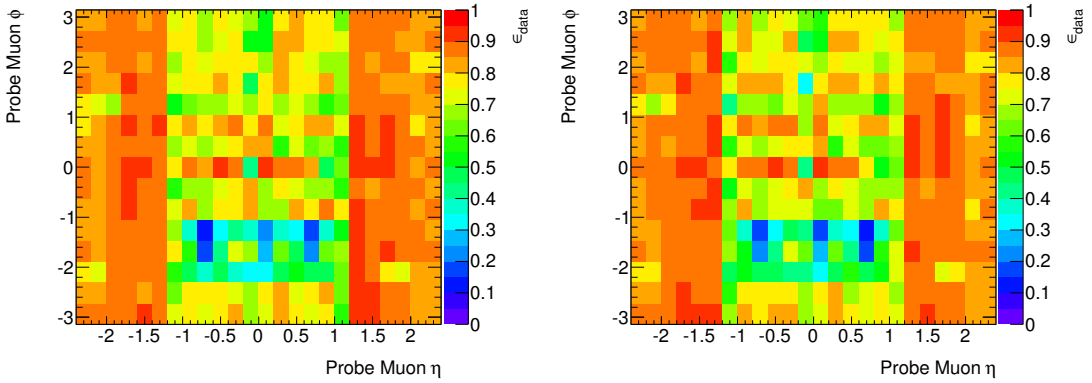

Figure 6.16.: Trigger efficiencies in data in terms of $\eta - \phi$ for negatively charged (left) and positively charged (right) muons.

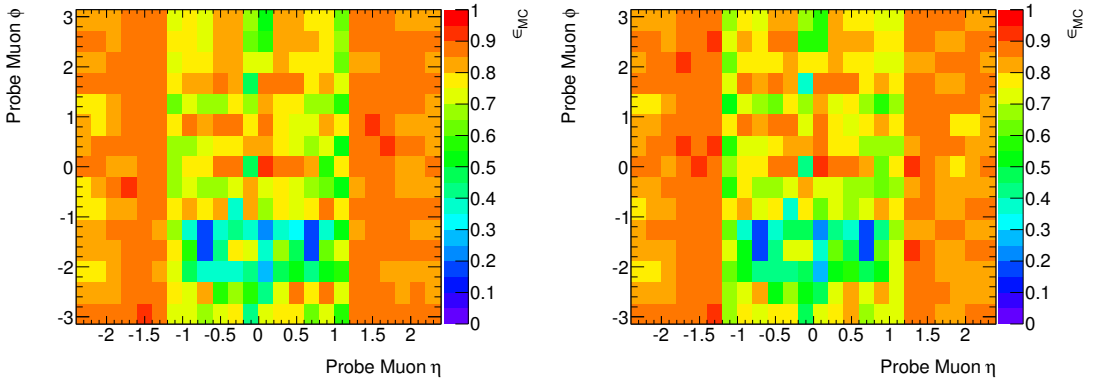

Figure 6.17.: Trigger efficiencies in Drell-Yan MC in terms of $\eta - \phi$ for negatively charged (left) and positively charged (right) muons.

Three sources of systematic uncertainty have been considered for this measurement, a background contamination systematic, an event topology systematic and a residual p_T dependence systematic.

The effect the level of background contamination has on the trigger efficiencies is measured by changing the nominal tag and probe selections as follows:

- Tag muon $p_T > 27.5(+10\%)$ GeV
- Tag and probe muons $I_{\mu\mu} < 0.09(-10\%)$
- Tag and probe $\Delta M_Z < 15(+50\%)$ GeV

The background contamination systematic is then taken as the RMS of the deviations of each of these three selections from the efficiency calculated using the nominal selection in each $\eta - \phi$ bin. The absolute uncertainty originating from the background contamination systematic on the SF of a MC event with a single muon is shown in figure 6.18. It is important to note that for events with more than one muon (as with the nominal analysis) there is a higher trigger efficiency than the single muon case as both muons can trigger, leading to a smaller uncertainty.

The $Z/\gamma^* \rightarrow \mu\mu$ events heavily favour back to back topologies meaning that the majority of the tag and probe efficiency calculation comes from this one topology. Any variation on the trigger efficiency with respect to the event topology is determined by recalculating the efficiencies with a constraint on the absolute difference in ϕ of the tag and probe muons of $\pi - \Delta\phi > 0.1$. The kinematic phase space removed by applying

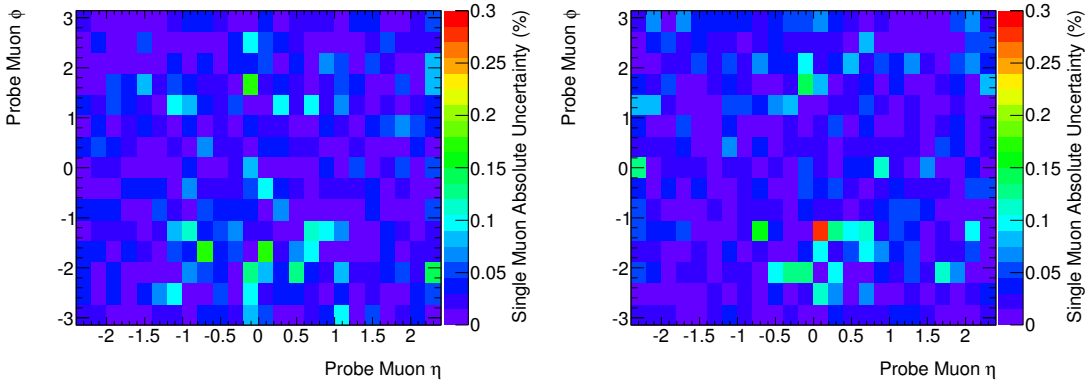

Figure 6.18.: Absolute background contamination uncertainty on a SF for an MC event with a single muon in percent for negatively charged (left) and positively charged (right) muons.

this selection is shown in figure 6.19. The deviation of the topology restricted selection from the nominal selection in each $\eta - \phi$ bin is taken as the uncertainty. The absolute uncertainty originating from the event topology systematic on the SF of a MC event with a single muon is shown in figure 6.20.

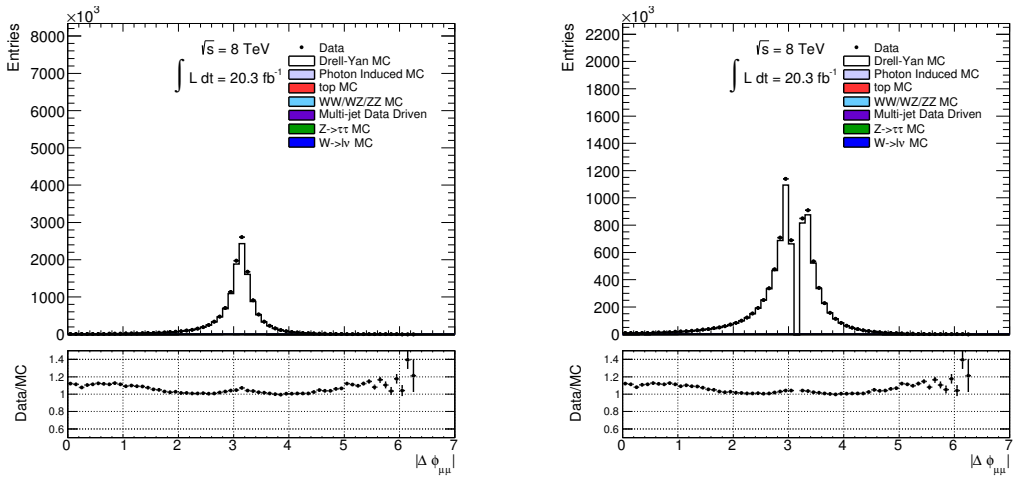

Figure 6.19.: $\Delta\phi$ distributions before (left) and after (right) the $\Delta\phi$ cut used for calculating the event topology systematic

To calculate the p_T dependence of the trigger efficiencies a two step process has been employed. Firstly trigger efficiencies are calculated for both data and MC in terms of $\eta - \phi$. These efficiencies are then used to calculate scale factors that are applied to the probe muon in the second part of the process. Applying these scale factors removes the

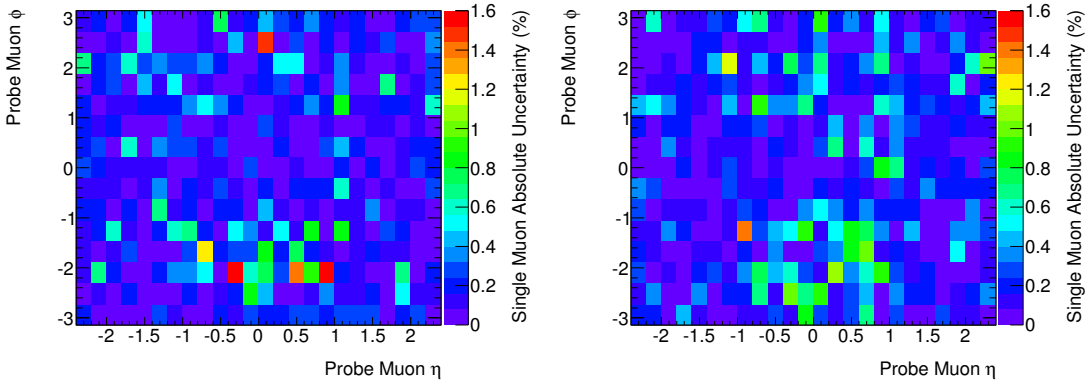

Figure 6.20.: Absolute event topology uncertainty on a SF for an MC event with a single muon in percent for negatively charged (left) and positively charged (right) muons.

$\eta - \phi$ dependence that is caused by the varying detector subsystems and leaves the residual p_T dependence. As the p_T dependence is small, muon and anti-muon p_T distributions have been combined to avoid bias from the relatively large statistical fluctuations at high p_T. The p_T dependence systematic is determined by the maximum deviation over the $25 < p_T < 100$ GeV region and is found to be 0.5% and 0.7% for the barrel and endcap regions respectively. The $p_T > 100$ GeV region has low statistics but is consistent with the maximum deviation seen in the lower p_T region. Therefore the systematic uncertainty at low p_T is applied in the $p_T > 100$ GeV region. The η-ϕ trigger efficiencies in terms of p_T are shown in figure 6.21. As the p_T dependence of the trigger efficiencies is weak, no correction is applied in this variable.

A source of systematic uncertainty that has been considered but not included is the pileup dependence on the trigger efficiencies. As the trigger can fire on muons that are produced via in-time pileup, the number of reconstructed primary vertices, N_{Vtx}, in an event will have some relation to the trigger efficiencies. Unfortunately the N_{Vtx} variable is not modelled well by the MC as shown in figure 5.2. The pileup reweighting procedure discussed in section 5.3.3 corrects the MC prediction of the average number of interactions per bunch crossing $\langle\mu\rangle$ to data, resulting in a much better data MC agreement seen in this variable in figure 5.2. The trigger efficiencies have been measured for these two variables to assess the pileup dependence. The same iterative process used for calculating the p_T dependence systematic is used to measure this effect. Calculated η-ϕ trigger scale factors are applied to the probe muon and the residual pileup dependence is measured. Trigger efficiencies in terms of N_{Vtx} and $\langle\mu\rangle$ for events where the probe muon is located in the barrel ($|\eta| < 1.05$) and endcap ($|\eta| > 1.05$) regions are given in figures 6.22 and 6.23. This

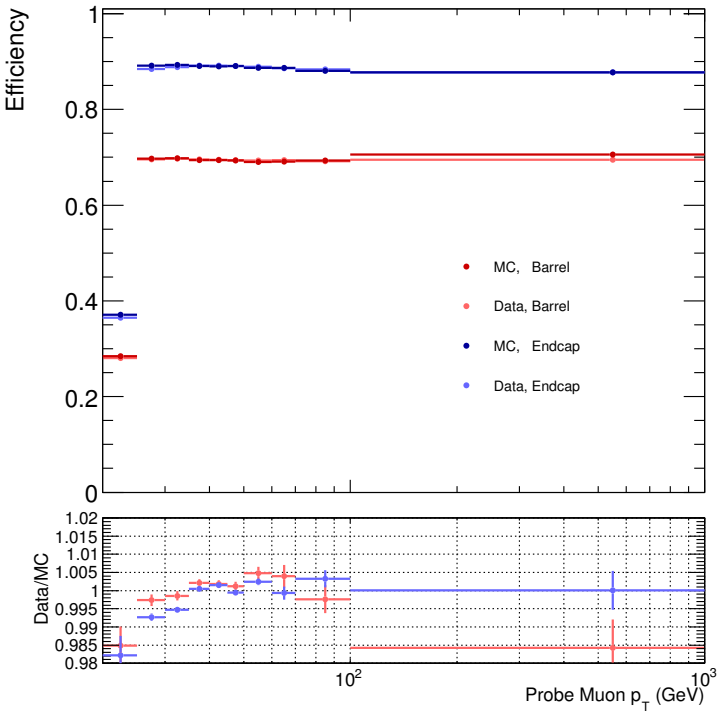

Figure 6.21.: Muon trigger efficiencies in terms of p_T after η-ϕ SFs have been applied to the probe muon. The lower panel gives the data to MC ratio and this shows the residual p_T dependence. To keep a sufficient level of statistics the positive and negative muons have been combined.

source of systematic is not included in the full systematics uncertainty as the background contamination systematic should include any effects resulting from a changing pileup conditions.

The total systematic uncertainty on the trigger efficiencies is calculated separately for the data and MC as the quadratic sum of the background systematic, the topology systematic and the p_T dependence systematic. The statistical uncertainty on the efficiencies is shown in figures 6.24 and 6.25 and is propagated through the final cross sections using the toy MC method described in section 9.3.1. The p_T dependence systematic is calculated using the single muon scale factors and so is only applied in the ϵ_{MC} part of equation 6.4, whereas for the topology and background contamination systematics both data and MC efficiencies are shifted by the calculated uncertainties.

Figure 6.26 shows the average trigger SF recorded in each $\eta - \phi$ bin, both for the trigger scale factors calculated in this analysis for third chain algorithm muons as well as those calculated by the muon trigger signature group for MuId algorithm muons. A ratio of the scale factors calculated for this analysis to those calculated by the muon trigger signature group is shown in figure 6.27. The two sets of scale factors agree to within 5% for the complete phase space apart from three bins that deviate by 7% and one bin that deviates by 16%. While the different algorithms would be expected to have some level of difference in trigger efficiencies, the broad level of agreement validates the analysis method discussed. The calculated trigger scale factors remain within 5% of unity for the majority of the detector volume with two bins in which the scale factor corrects by 15% and 20%. Using the scale factors presented in this analysis reduce the trigger systematic uncertainty by a factor of six when compared to the scale factors calculated by the muon trigger signature working group. The trigger systematic uncertainty on the single differential fiducial cross section is shown in table 6.1 using both the muon trigger signature groups scale factors and the scale factors calculated in this dedicated analysis.

Mass Bin (GeV)	MTSG SFs (%)	HMDY SFs (%)
$66 < m_{\mu\mu} < 116$	0.49	0.08
$116 < m_{\mu\mu} < 130$	0.52	0.08
$130 < m_{\mu\mu} < 150$	0.54	0.08
$150 < m_{\mu\mu} < 175$	0.56	0.09
$175 < m_{\mu\mu} < 200$	0.58	0.09
$200 < m_{\mu\mu} < 230$	0.59	0.09
$230 < m_{\mu\mu} < 260$	0.60	0.09
$260 < m_{\mu\mu} < 300$	0.60	0.10
$300 < m_{\mu\mu} < 380$	0.61	0.10
$380 < m_{\mu\mu} < 500$	0.60	0.09
$500 < m_{\mu\mu} < 700$	0.59	0.09
$700 < m_{\mu\mu} < 1000$	0.58	0.07
$1000 < m_{\mu\mu} < 1500$	0.63	0.08

Table 6.1.: Uncertainty on the 1D cross section measurement when either the muon trigger signature group (MTSG) scale factors and associated uncertainties are used or the scale factors from the described analysis (HMDY) are used.

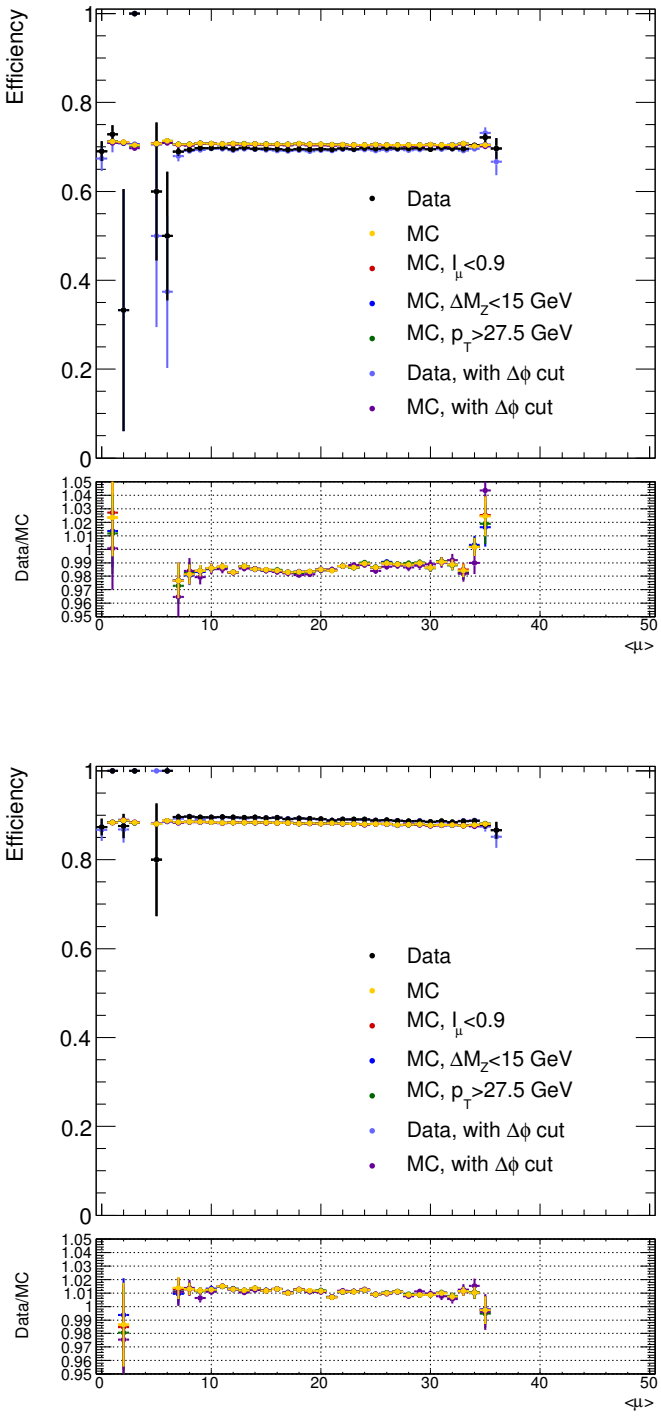

Figure 6.22.: The trigger efficiencies for the data and MC in the barrel region(top) and endcap region(bottom) in terms of $\langle\mu\rangle$. Included are trigger efficiencies calculated using the changing selections used in the determination of the background contamination and event topology systematics. The lower pad shows the potential trigger scale factor in this variable.

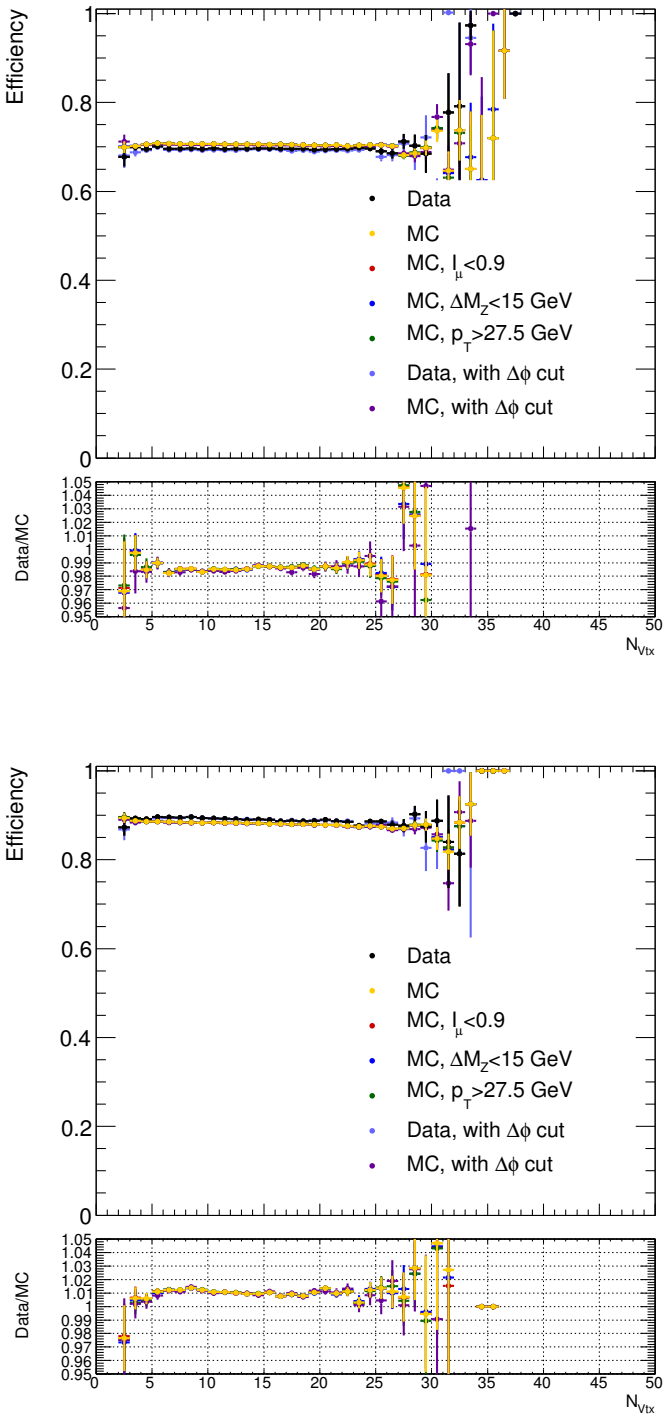

Figure 6.23.: The trigger efficiencies for the data and MC in the barrel region(top) and endcap region (bottom) in terms of N_{Vtx}. Included are trigger efficiencies calculated using the changing selections used in the determination of the background contamination and event topology systematics. The lower pad shows the potential trigger scale factor in this variable.

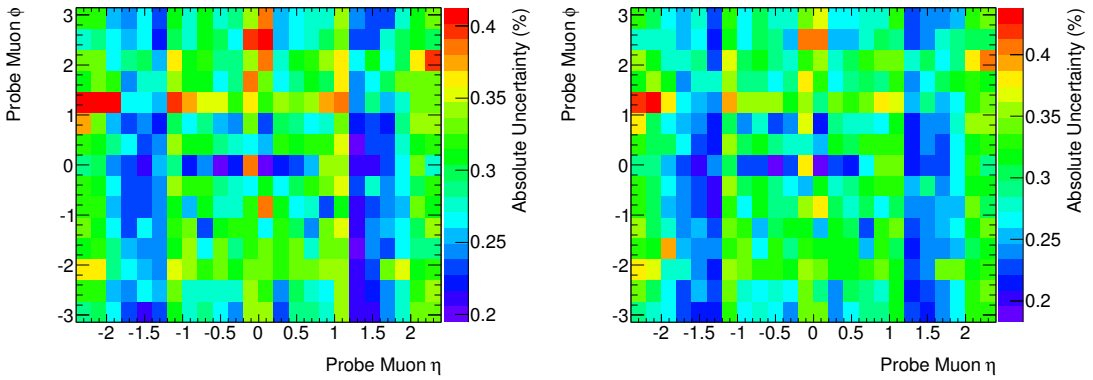

Figure 6.24.: Absolute statistical uncertainty on the trigger efficiencies in data for negatively charged (left) and positively charged (right) muons.

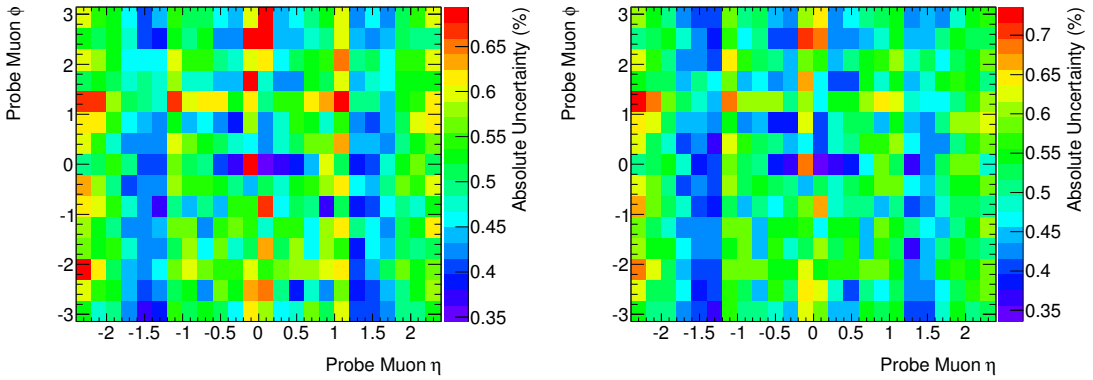

Figure 6.25.: Absolute statistical uncertainty on the trigger efficiencies in MC for negatively charged (left) and positively charged (right) muons.

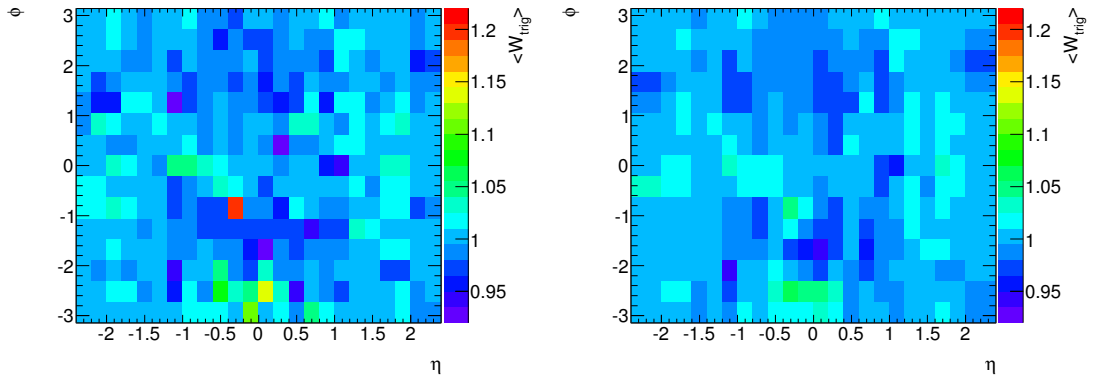

Figure 6.26.: Average trigger SF for events that pass the full analysis selection using the trigger efficiencies calculated for third chain algorithm muons in the method described in the text (left) and the muon trigger signature groups calculation of the MUID algorithm trigger efficiencies (right).

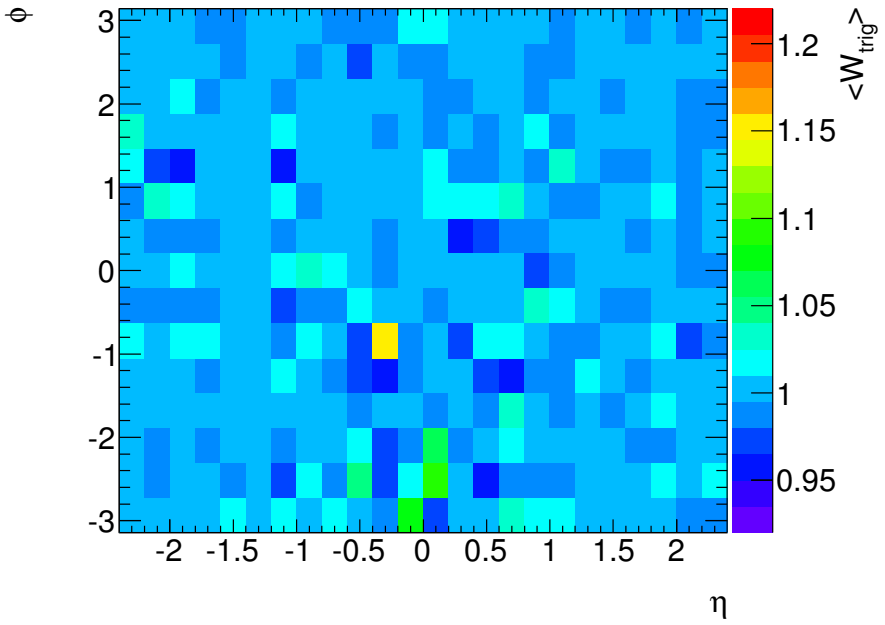

Figure 6.27.: Ratio of the average trigger SF for events that pass the full analysis selection using the trigger efficiencies calculated for third chain algorithm muons to those calculated using the muon trigger signature group scale factors for the MUID algorithm muons.

Chapter 7.

Background Estimation

To measure the cross section of the Drell-Yan process, the background contamination needs to be estimated and subtracted from the data events. Background processes that manifest in the fiducial volume and are considered in this analysis are listed as followed.

- $\boldsymbol{Z/\gamma^* \to \tau\tau}$**:** This process contaminates the signal region when the tau particles decay into muon and muon neutrinos through the process $\tau^+(\tau^-) \to \mu^+\nu_\mu(\mu^-\bar{\nu_\mu})$.
- $\boldsymbol{WW/WZ/ZZ}$ **Diboson background:** As with the decay of the single Z boson. Multiple muons can be produced as the W and Z bosons decay through the processes $Z \to \mu^-\mu^+$ and $W^- \to \mu^-\bar{\nu_\mu}$.
- $\boldsymbol{t\bar{t}}$ **and single top decays:** The heavy top particles decay mostly into b quarks and W bosons. Muons can be produced either from jets produced by the b and W or by the leptonic W decay $W^- \to \mu^-\bar{\nu_\mu}$.
- $\boldsymbol{W \to \mu\nu}$**:** Along with the muon produced in the hard scatter, additional muons can be produced by jets originating from initial state radiation.
- $\boldsymbol{W \to \tau\nu}$**:** As with $Z \to \tau\tau$ background the tau particles can decay into muons with the additional muons again produced from jets.
- **QCD multi-jet backgrounds:** These backgrounds include processes in which jets of quarks produce muons in the decay products.

The high lepton p_T cuts of the measurement result in the multi-jet background comprising predominately of heavy flavour production. Due to the large uncertainties associated with the heavy flavour MC, the multi-jet background is estimated using a data driven method.

Electroweak background processes are estimated by MC. Figures 7.1, 7.2 and 7.3 show the fractional contribution of each background to the total MC prediction in the cross section variables studied. Photon induced dimuon production ($\gamma\gamma \to \mu\mu$, abbreviated as PIP) is also predicted to contribute in the analysis phase space. This process is considered part of the signal and is included in the cross section measurements.

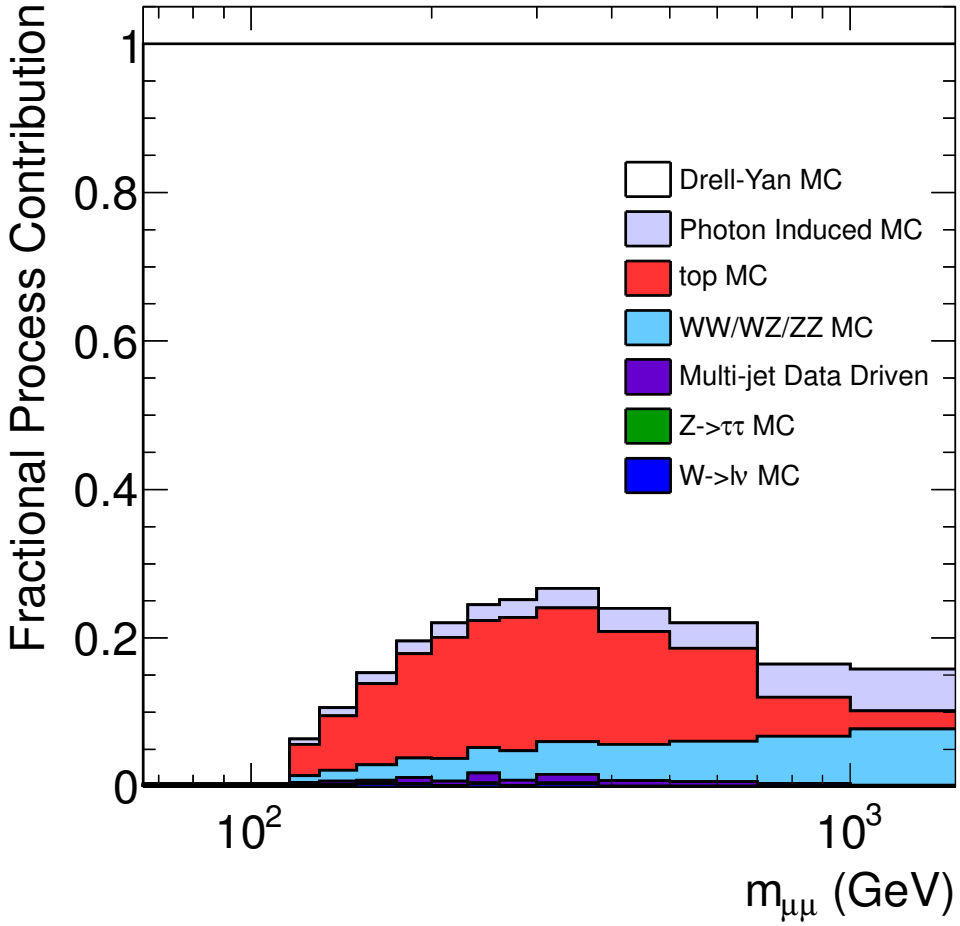

Figure 7.1.: The fractional contribution each backgrounds has to the total background and signal prediction displayed in a stack histogram.

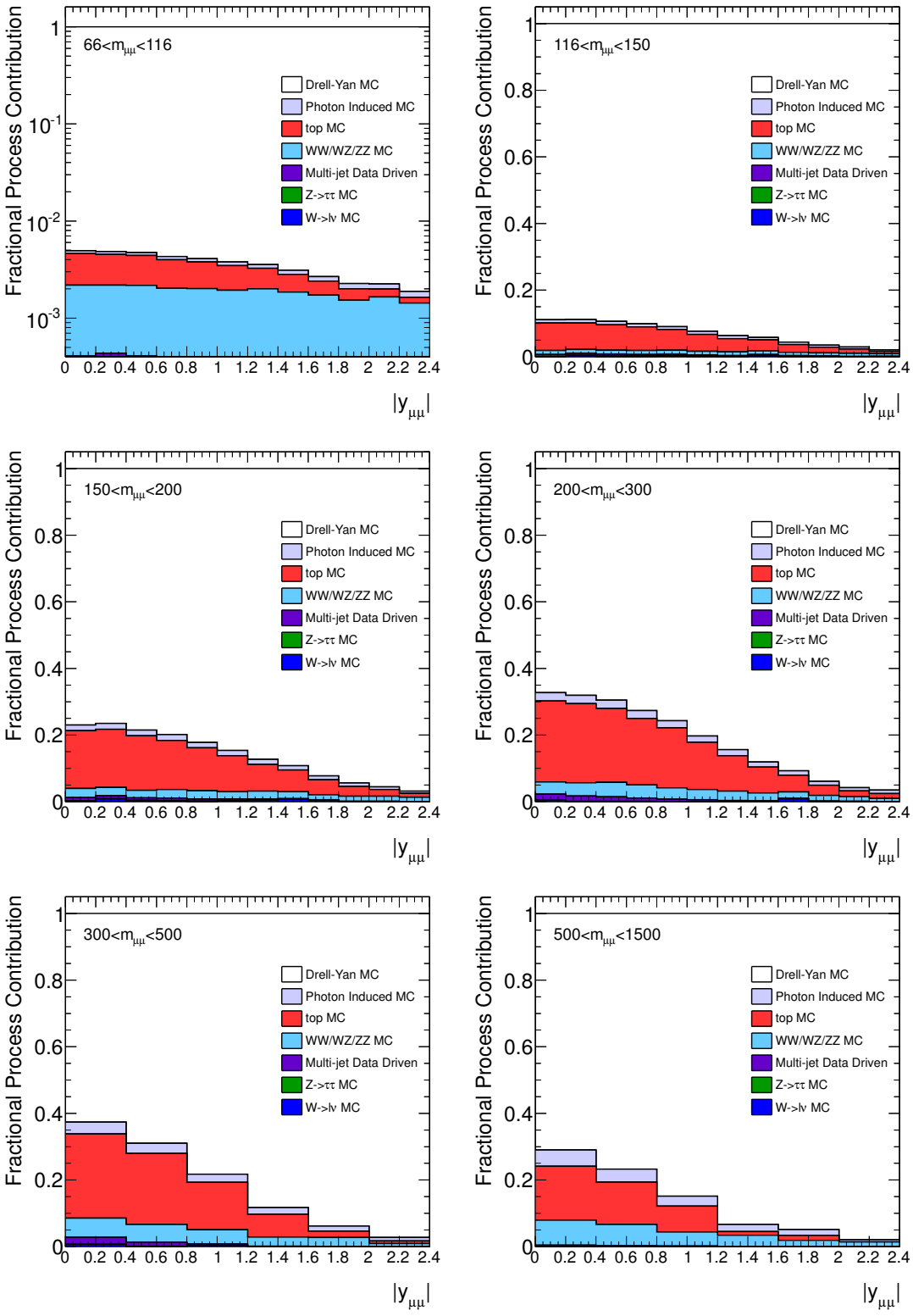

Figure 7.2.: The fractional contribution each backgrounds has to the total background and signal prediction displayed in a stack histogram.

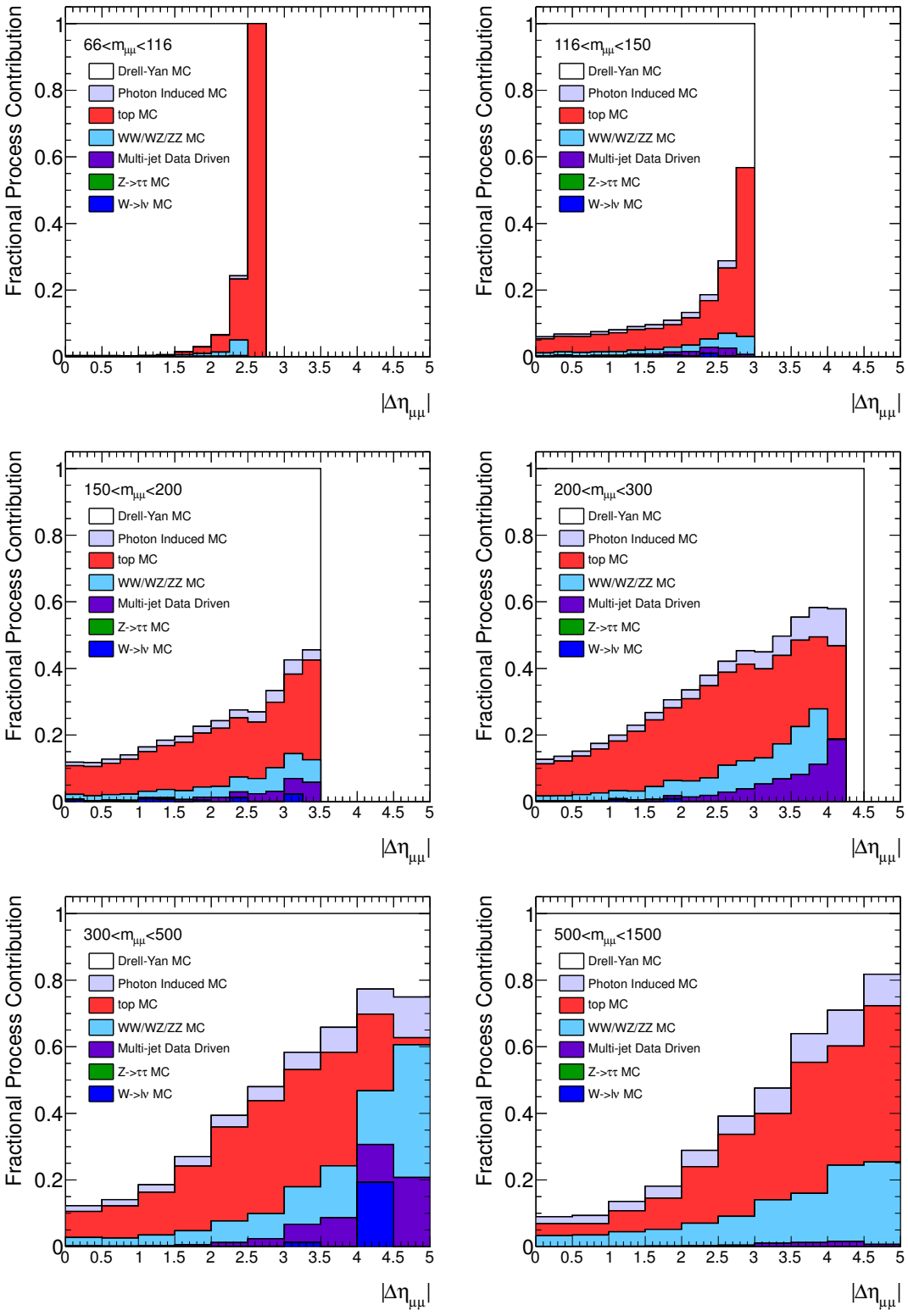

Figure 7.3.: The fractional contribution each backgrounds has to the total background and signal prediction displayed in a stack histogram.

7.1. Multi-jet Background Estimation

Two alternative methods of estimating the multi-jet processes by data driven techniques are described in this section. Section 7.1.1 describes a method that was used in an alternative 2011 $\sqrt{s} = 7$ TeV Drell-Yan measurement that centres on the Z resonance region [37]. Expertise gained from this study such as the use of control regions and extrapolation into the signal region have been used when developing the multi-jet estimation method used in the $\sqrt{s} = 8$ TeV high mass Drell-Yan analysis described in section 7.1.2. Further details on the $\sqrt{s} = 7$ TeV measurement is given in appendix A.

7.1.1. Isolation Template Fit Method

The isolation template fit method provides an estimate for the multi-jet background by attempting to model the complete muon isolation spectrum. This is achieved by defining a control region using isolation requirements on one muon and assuming that the isolation spectrum of the other muons within a pure multi-jet sample are uncorrelated. In a multi-jet dominated control region the full isolation spectrum is fitted by a combination of two templates: a Pythia heavy flavour b, c multi-jet Monte Carlo, and a data same-sign selection. In this method the data same-sign accounts for any mismodelling in the shape of the isolation spectrum by the Monte Carlo as well as any light flavour multi-jet contribution. The template fit gives the fractions of data SS and multi-jet MC that make up the multi-jet estimation in the control region. These fractions are assumed to be the same in the control region as in the full analysis selection region. The full multi-jet estimation in the analysis region is then calculated by multiplying the data SS and multi-jet MC in the the full analysis selection by the fractions calculated in the control region. This process is repeated for the three mass regions studied by the analysis, $46 < m_{\mu\mu} < 66$, $66 < m_{\mu\mu} < 116$ and $116 < m_{\mu\mu} < 150$ GeV.

The multi-jet dominated region is chosen to limit the amount of electroweak background contamination but leave enough data and multi-jet Monte Carlo to provide enough statistical precision for the template fit. This was chosen by applying the full analysis selection but changing the isolation and d_0^{sig} cuts on one muon only (here denoted as the tag muon). An isolation variable similar to that described in section 6.2 is defined as

$$I_{\text{tag}}^{R=0.4} = \Sigma p_T^{R=0.4} / p_T \tag{7.1}$$

where the tag subscript can be replaced by either 'probe' for an isolation requirement on the probe muon or '$\mu\mu$' for a requirement on both muons. The isolation and d_0^{sig} cuts can then be defined for the tag muon as $I_{tag}^{R=0.4} < 0.2$ and $d_0^{sig}(tag) > 2.0$.

Multi-jet events dominate this region as muons from jets commonly have large energy depositions close to the muon track. The choice of which muon to use as the tag is made a random to avoid bias in muon p_T, η, etc. The other muon in the event (here denoted as the probe muon) has the full selection applied but without an isolation or d_0^{sig} cut. With these criteria the isolation is only marginally correlated between the tag and probe muon, therefore the isolation spectrum of the probe muon can be used as an unbiased estimate of the shape of the multi-jet isolation spectrum.

In the three analysis mass regions the isolation spectrum for the probe muon in OS data (N_{data}^{OS}) is fitted with two templates, one coming from the SS data (N_{data}^{SS}) and the other from the OS b, c multi-jet Monte Carlo ($N_{QCD,MC}^{OS}$). To avoid double counting the SS contributions in data, the SS b,c multijet Monte Carlo ($N_{QCD,MC}^{SS}$) is subtracted from the Monte Carlo template. These two templates are fitted to the OS data using a likelihood fit using the TFractionFitter tool within in the ROOT framework [40]. This gives the relative fractions of the b, c Monte Carlo and SS data used to fit the data and is shown in the equation below.

$$N_{data}^{OS} = f_1 \cdot \mathcal{N} \cdot (N_{QCD,MC}^{OS} - N_{QCD,MC}^{SS}) + f_2 \cdot N_{data}^{SS} \tag{7.2}$$

where $\mathcal{N}$ is a normalisation factor defined in equation 7.3.

To avoid any electroweak contamination, the relevant Monte Carlos predictions are subtracted from $N_{QCD,MC}^{OS}$, $N_{QCD,MC}^{SS}$, N_{data}^{SS} and N_{data}^{OS} before performing the fit. The electroweak Monte Carlo predicts the electroweak contribution to be contained to the most isolated bin in all the three mass regions. Figure 7.4 shows the result of the two component template fit to the probe muon isolation spectrum and the agreement is around 10% for the low mass region and Z peak regions and is around 20% for the high mass region.

In order to predict the QCD multi-jet background in the signal region an additional normalisation factor $\mathcal{N}$ is determined for the b, c Monte Carlo. The normalisation condition is expressed in the equation below and determined in the non-isolated region, $I_{\mu\mu}^{R=0.4} > 0.2$ and $d_0^{sig} > 2.0$

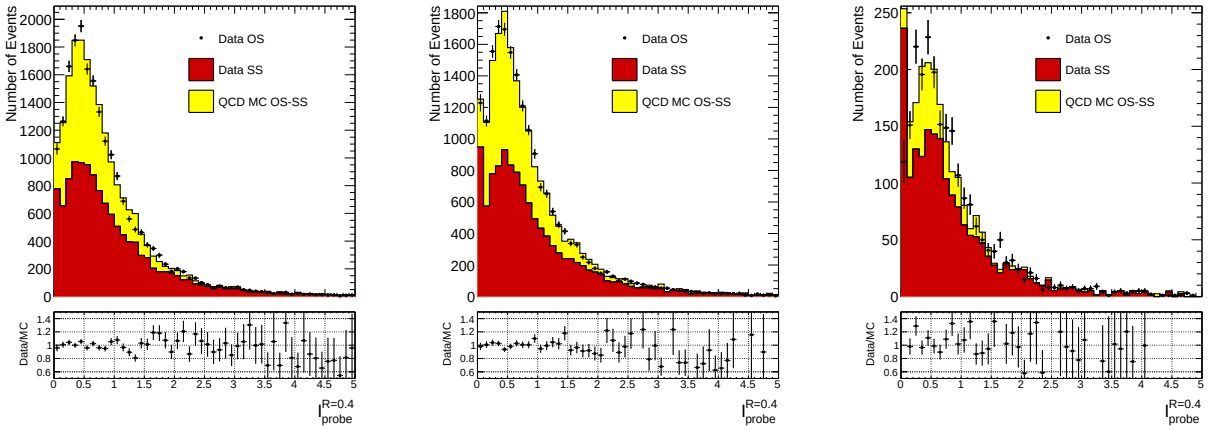

Figure 7.4.: Isolation spectra of one muon in the event when the other has had a harsh anti-isolation and large $d_0^{sig}(tag)$ cut applied. The two templates have then been fit to the data OS. The isolation spectra are shown for mass regions $46 < m_{\mu\mu} < 66$ GeV(left), $66 < m_{\mu\mu} < 116$ GeV(middle) and $116 < m_{\mu\mu} < 150$ GeV(right)

	$46 < m_{\mu\mu} < 66\,GeV$	$66 < m_{\mu\mu} < 116\,GeV$	$116 < m_{\mu\mu} < 150\,GeV$
$f_{qcd} \pm \delta f_{qcd}$	0.254 ± 0.026	0.009 ± 0.001	0.277 ± 0.054

Table 7.1.: Percent fractions of estimated multi-jet events to data for in the mass regions of the Z inclusive cross-section measurement. Only statistical uncertainties from the fits are reported.

$$\frac{N_{data}}{[\mathcal{N} \cdot f_1 \cdot (N^{OS}_{QCD,MC} - N^{SS}_{QCD,MC})] + [f_2 \cdot N^{SS}_{data}]} = 1 \tag{7.3}$$

The templates provide a good description of the isolation variable over the full mass range to within about 10% and can be seen in figure 7.5. The method is limited by the statistics of the Monte Carlo and the SS data specially at large $m_{\mu\mu}$. Results showing the fraction of estimated multi-jet events to data events (f_{qcd}) is given in table 7.1. In the Z inclusive analysis a variety of multi-jet estimation techniques including this method were employed and a weighted average was taken [37].

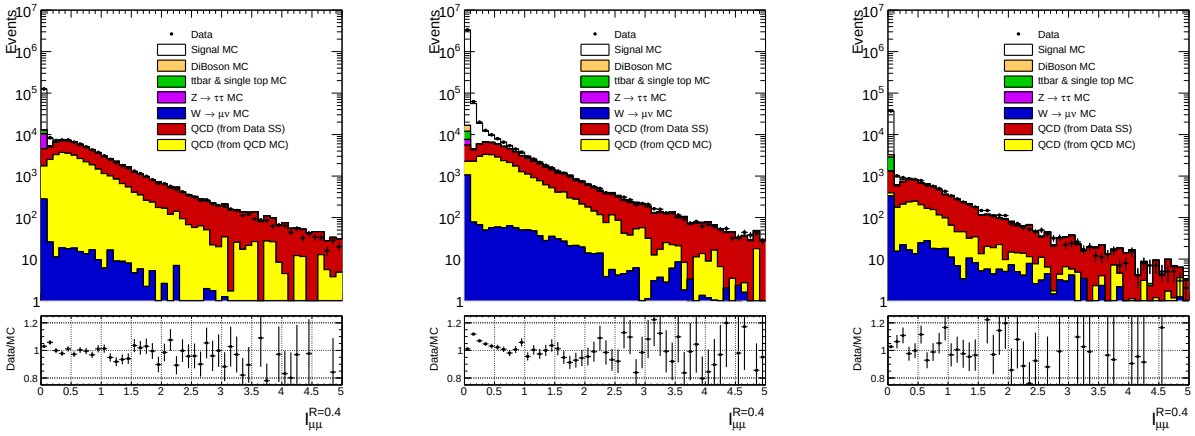

Figure 7.5.: Isolation spectra for events with the full analysis selection apart from the isolation requirement in the mass regions $46 < m_{\mu\mu} < 66$ GeV(left), $66 < m_{\mu\mu} < 116$ GeV(middle) and $116 < m_{\mu\mu} < 150$ GeV(right). The QCD multi-jet estimation from the isolation method is shown.

7.1.2. High Mass Drell-Yan Multi-jet Estimation

For the high mass Drell-Yan analysis the multi-jet background is estimated using a three step data-driven technique. A modified ABCD method is used to estimate the multi-jet background in each $m_{\mu\mu}$ bin. The ABCD method uses three control regions (B, C and D) and the relation between them to predict the background in the signal region (A). Two variables with a weak correlation are chosen so that the following relation holds:

$$\frac{N_A}{N_B} = \frac{N_C}{N_D} \tag{7.4}$$

where N_A, N_B, N_C and N_D are the number of events in regions A, B, C and D. The estimation made by the modified ABCD method is extrapolated into higher mass bins where the method loses predictive power due to limited statistical precision. For the 2D measurement the shape of the $|y_{\mu\mu}|$ and $|\Delta\eta_{\mu\mu}|$ multi-jet background is predicted using a non-isolated control region.

The kinematic regions for the modified ABCD method are defined as for the full analysis selection with the following isolation and muon charge requirements.

- Region A: $I_{\mu\mu} < 0.1$ for both muons with opposite charge(OS) (signal region).
- Region B: $I_{\mu\mu} < 0.1$ for both muons with same charge(SS).

- Region C: $I_{\mu\mu} > 0.1$ for both muons with opposite charge.
- Region D: $I_{\mu\mu} > 0.1$ for both muons with same charge.

The variables used in the modified ABCD method have been chosen to enrich multi-jet events outside the signal region. Muons produced from multi-jet events have a close proximity to other objects originating from the jet leading to a low level of isolation. In addition the muons originating from heavy flavour jets can produce both same sign and opposite sign lepton pairs depending on the meson decay chain. Contamination from electroweak backgrounds in the method is countered by subtracting appropriate MC predictions from the regions B, C and D.

The ABCD method relies on the two background discriminating variables having minimal correlation. To show the correlation of the two variables, the muon isolation spectra for regions C(OS) and D(SS) are normalised to unit area and the ratio of the two is compared. The ratios show a difference in shape, however the relationship between these two shapes is observed to be very well behaved as shown in figures 7.6, 7.7 and 7.8. To account for this discrepancy in the OS and SS isolation spectra in the method an additional correction factor F_{ABCD} can be implemented. The factor F_{ABCD} is calculated by fitting the OS SS ratios with a first order polynomial and extrapolating this fit into the centre of the signal isolation region at $I_{\mu\mu} = 0.05$. Figures 7.6, 7.7 and 7.8 show the isolation spectrum and the fitted ratio for the 1D and 2D $m_{\mu\mu}$ binning. At higher masses the statistics in region C and D are too low in each bin for the correction factor to be calculated, so the bins in the region $300 < m_{\mu\mu} < 1500$ GeV are merged. The estimated number of multi-jet events in the signal region N^A_{QCD} is then predicted using the equation:

$$N^A_{QCD} = (N^B_{Data} - N^B_{EW,MC}) \cdot \frac{(N^C_{Data} - N^C_{EW,MC})}{(N^D_{Data} - N^D_{EW,MC})} \cdot F_{ABCD} \tag{7.5}$$

where N^B_{Data}, N^C_{Data}, and N^D_{Data} are the number of data events in region B, C and D and $N^B_{EW,MC}$, $N^C_{EW,MC}$, and $N^D_{EW,MC}$ are the number of MC predicted electroweak events in regions B, C and D.

The value of F_{ABCD} remains approximately constant for the $m_{\mu\mu}$ range, so a weighted average is used. The systematic uncertainty is taken as the RMS of the deviations between each $m_{\mu\mu}$ bin and the weighted average. Figure 7.9 shows the F_{ABCD} factor as a function of $m_{\mu\mu}$.

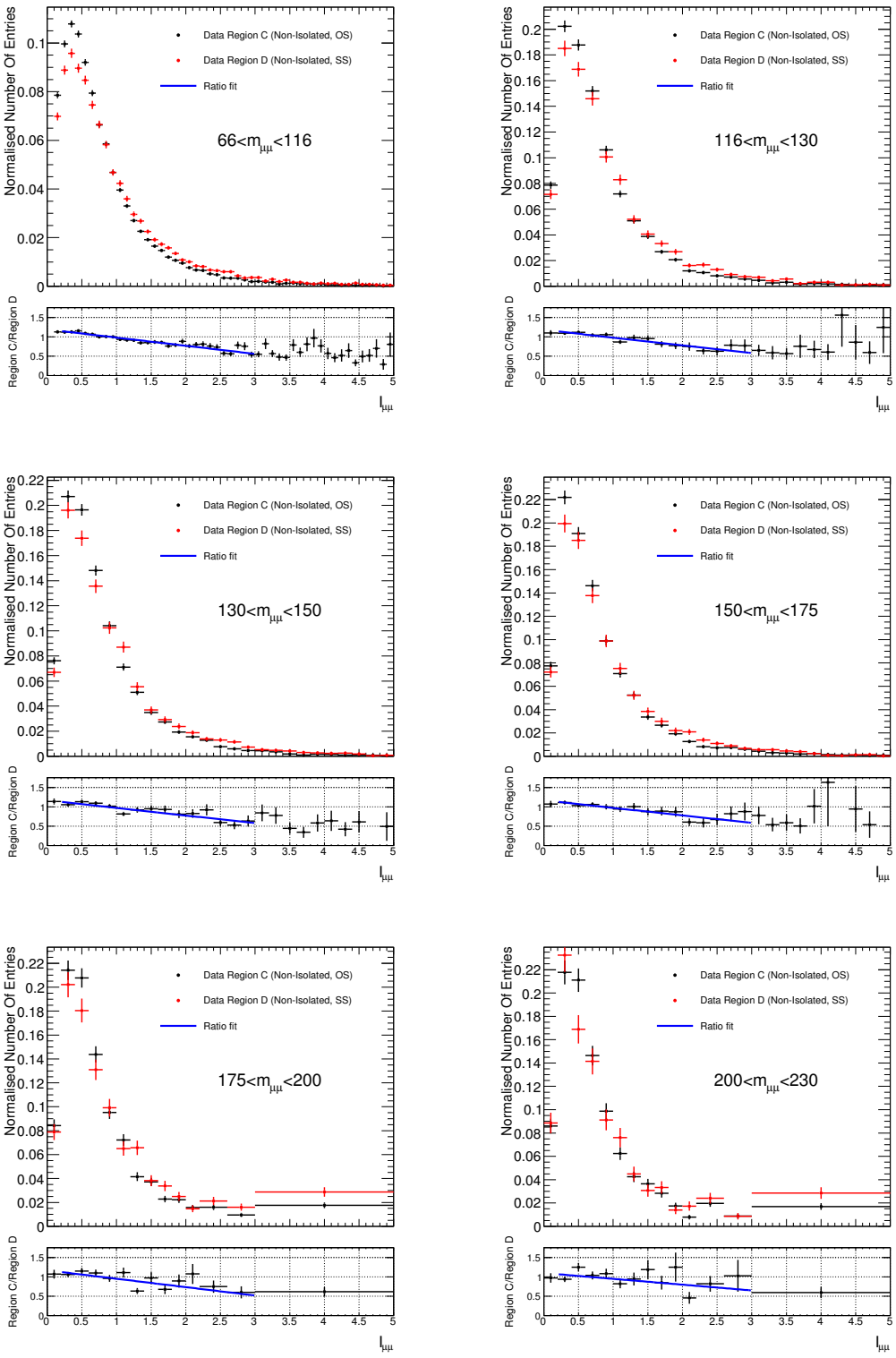

Figure 7.6.: Isolation spectra shape comparisons for regions C and D in the 1 dimensional binning. The extrapolation of the blue fit into the isolated signal region bin gives the F_{ABCD} factor.

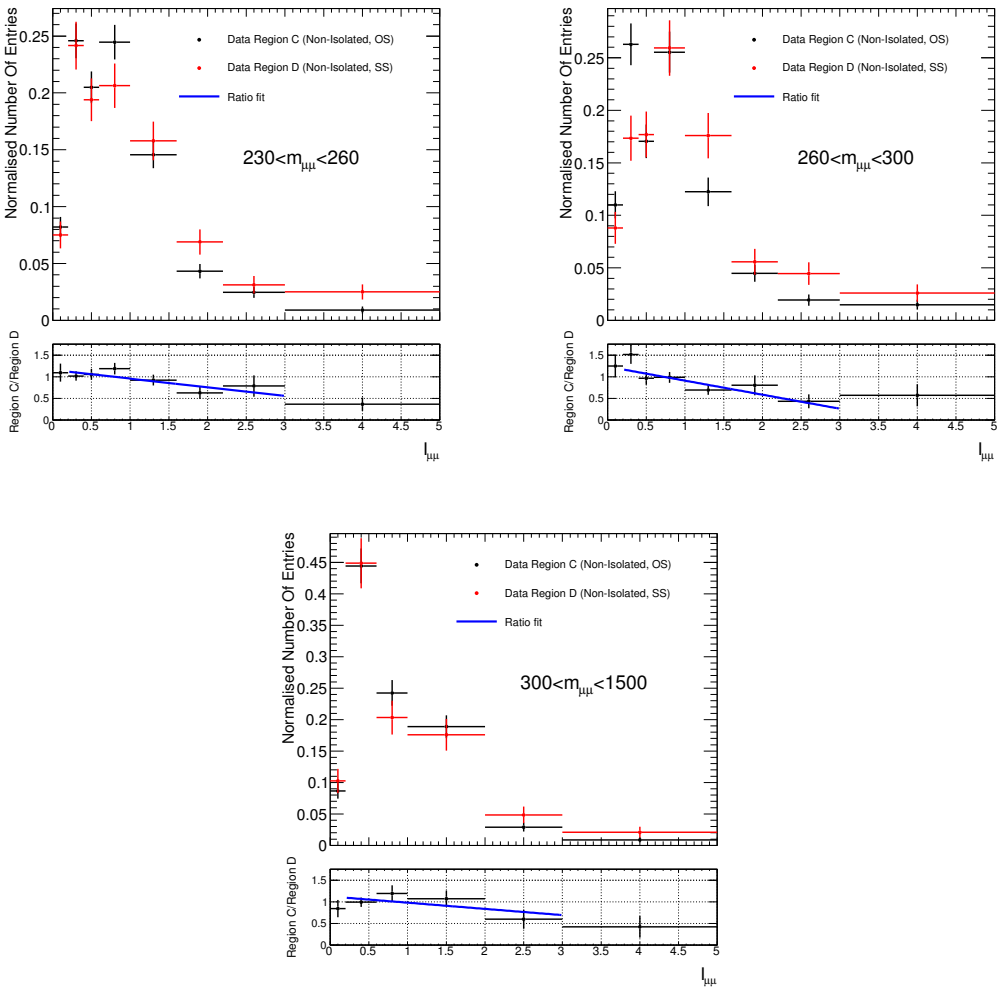

Figure 7.7.: Isolation spectra shape comparisons for regions C and D in the 1 dimensional binning. The extrapolation of the blue fit into the isolated signal region bin gives the F_{ABCD} factor. The bottom right plot represents the region where $m_{\mu\mu}$ bins have been merged into a single bin.

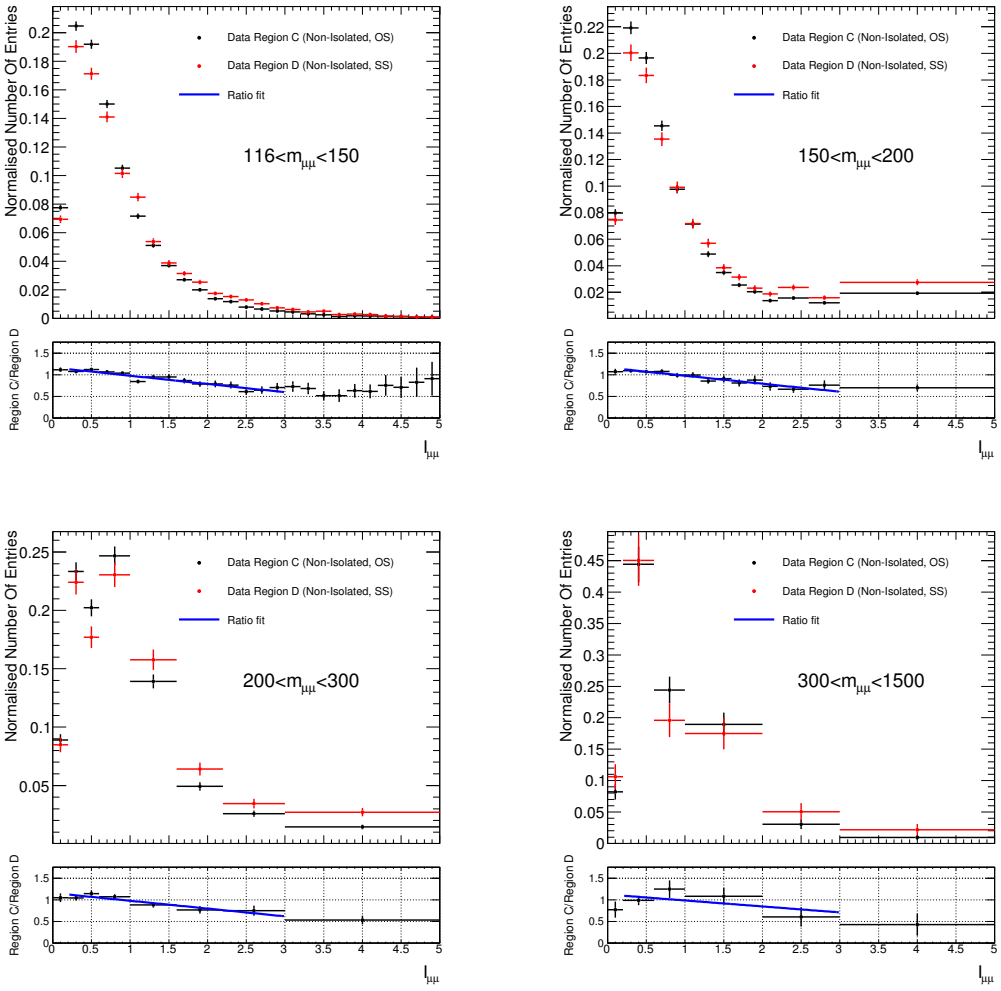

Figure 7.8.: Isolation spectra shape comparisons for regions C and D in the 2 dimensional binning. The extrapolation of the blue fit into the isolated signal region bin gives the F_{ABCD} factor. The bottom plot represents the region where $m_{\mu\mu}$ bins have been merged into a single bin.

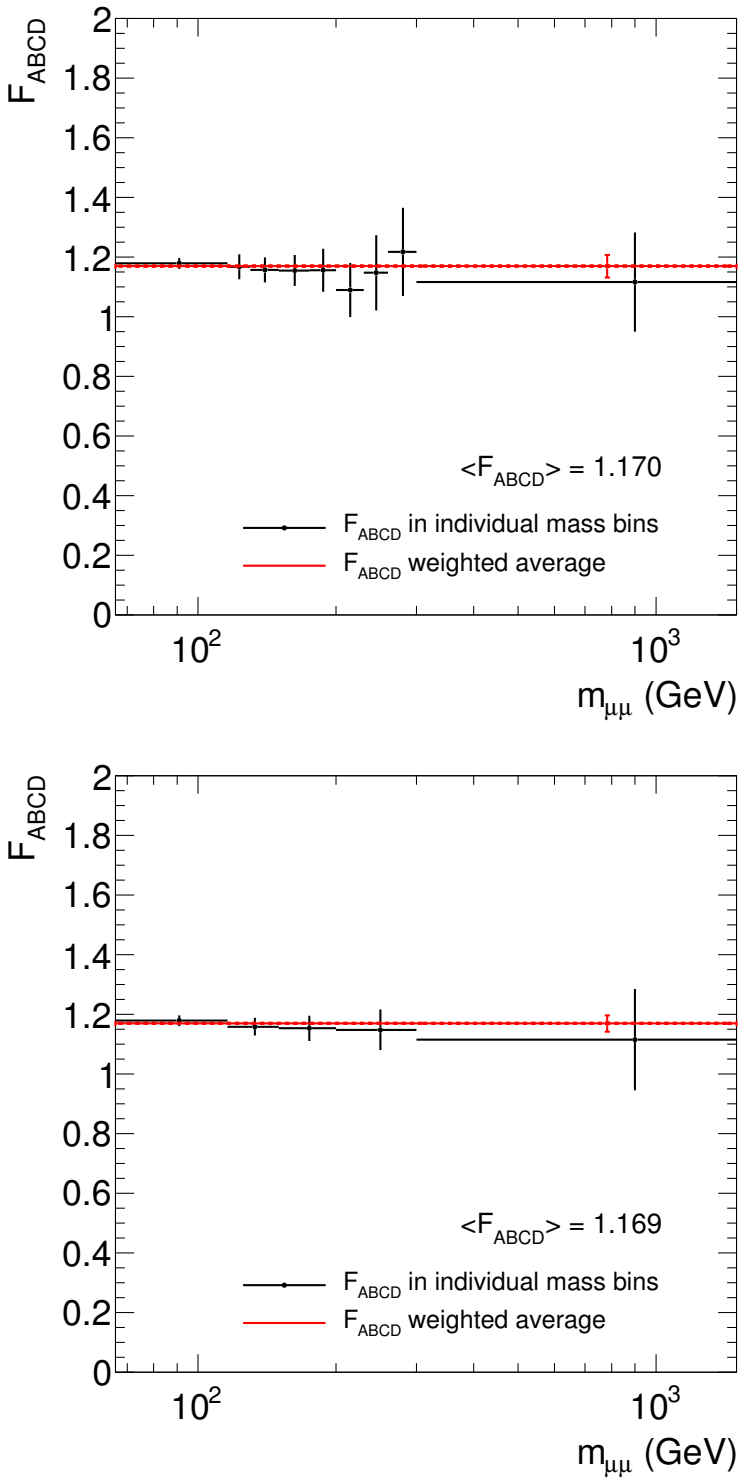

Figure 7.9.: Correction factor F_{ABCD} calculated in each one dimensional (left) and two dimensional (right) binning schemes. The red point represents the weighted average of the F_{ABCD} factor calculated over the complete $m_{\mu\mu}$ range. The y-axis error bars on this point show the RMS of the deviations of the F_{ABCD} factor calculated in each bin with respect to the weighted average.

Tables 7.2 and 7.3 show the observed data and predicted electroweak contamination in each $m_{\mu\mu}$ bin for the modified ABCD method as well as the F_{ABCD} factor and the final estimated multi-jet background. The large number of electroweak background events in region B can be seen in the table and is dominated by the diboson processes. At higher masses either no multi-jet events are predicted or there are too few SS isolated region B events to make an accurate estimation. To make a multi-jet prediction in the $m_{\mu\mu} > 500$ GeV region, two functions are fitted to the predicted number of multi-jet events and extrapolated into the high mass region. The two functions chosen for the fit are:

- $y = Ax^B x^{Clog(x)} \rightarrow$ a dijet function.
- $y = \frac{A}{(x+B)^C} \rightarrow$ an inverse monomial function.

The functions chosen have been used in a ATLAS dilepton search analysis to describe falling backgrounds at high masses [41]. The fits are shown in figure 7.10. The prediction in this $m_{\mu\mu} < 500$ GeV region is taken as the average value of the two fits. To extrapolate the systematic uncertainty into this higher mass region the electroweak sample in region B is increased and decreased by one standard deviation of its predicted normalisation uncertainty as discussed in section 7.2 and the extrapolation repeated. The largest deviation this electroweak adjusted prediction has from the central extrapolation value is taken as the uncertainty. This provides a very conservative estimate of the systematics, however the statistical uncertainty on the cross section in this region is dominant.

	Data and Electroweak (EW) Events in Region							Predicted
$m_{\mu\mu}$ Bin (GeV)	Data B	EW B	Data C	EW C	Data D	EW D	F_{ABCD}	Multi-jet
$66 < m_{\mu\mu} < 116$	576.00	318.18	60019.00	699.53	29682.00	283.34	1.175	606.88
$116 < m_{\mu\mu} < 130$	154.00	73.71	10801.00	51.06	5607.00	50.21	1.170	181.21
$130 < m_{\mu\mu} < 150$	163.00	92.03	9825.00	48.68	5035.00	45.48	1.148	162.23
$150 < m_{\mu\mu} < 175$	131.00	90.84	6654.00	28.46	3608.00	29.36	1.156	86.75
$175 < m_{\mu\mu} < 200$	101.00	56.09	3382.00	19.45	1924.00	15.31	1.157	92.31
$200 < m_{\mu\mu} < 230$	70.00	45.13	2186.00	12.30	1197.00	8.79	1.082	53.07
$230 < m_{\mu\mu} < 260$	57.00	27.17	1096.00	6.39	576.00	7.98	1.138	66.75
$260 < m_{\mu\mu} < 300$	37.00	23.42	688.00	4.58	395.00	5.19	1.219	27.77
$300 < m_{\mu\mu} < 380$	42.00	26.11	459.00	1.18	223.00	3.44	1.125	38.65
$380 < m_{\mu\mu} < 500$	19.00	13.49	110.00	-0.07	64.00	0.26	1.125	11.10
$500 < m_{\mu\mu} < 700$	5.00	5.10	27.00	0.02	12.00	0.00	1.125	3.51
$700 < m_{\mu\mu} < 1000$	3.00	2.06	2.00	0.00	0.00	0.00	1.125	0.53
$1000 < m_{\mu\mu} < 1500$	0.00	0.49	0.00	0.00	0.00	0.00	1.125	0.05

Table 7.2.: The table lists the number of data or MC predicted electroweak (EW) background events in each region defined by the modified ABCD method for the 1D binning scheme. The F_{ABCD} factor calculated in each mass bin is given apart from the highest five $m_{\mu\mu}$ bins where the data has been merged to improve statistics. The final column shows the estimated number of multi-jet events calculated using the weighted average F_{ABCD} factor. For the highest three $m_{\mu\mu}$bins the extrapolation of the multi-jet prediction is given in the final column. A negative value is shown for a bin in the electroweak region C column due to the $t\bar{t}$ background having some events with negative MC generator weights.

	Data and Electroweak (EW) Events in Region							Predicted
$m_{\mu\mu}$ Bin (GeV)	Data B	EW B	Data C	EW C	Data D	EW D	F_{ABCD}	Multi-jet
$66 < m_{\mu\mu} < 116$	576.00	318.18	60019.00	699.53	29682.00	283.34	1.175	606.90
$116 < m_{\mu\mu} < 150$	317.00	165.74	20626.00	99.74	10642.00	95.69	1.157	343.46
$150 < m_{\mu\mu} < 200$	232.00	146.92	10036.00	47.91	5532.00	44.67	1.154	180.67
$200 < m_{\mu\mu} < 300$	164.00	95.73	3970.00	23.28	2168.00	21.95	1.144	146.48
$300 < m_{\mu\mu} < 500$	61.00	39.60	569.00	1.11	287.00	3.71	1.120	50.04
$500 < m_{\mu\mu} < 1500$	8.00	7.65	29.00	0.02	12.00	0.00	1.120	1.42

Table 7.3.: The table lists the number of data or MC predicted electroweak (EW) background events in each region defined by the modified ABCD method for the 2D binning scheme. The final column shows the estimated number of multi-jet events calculated using the weighted average F_{ABCD} factor. For the highest $m_{\mu\mu}$bin the extrapolation of the multi-jet prediction is given in the final column.

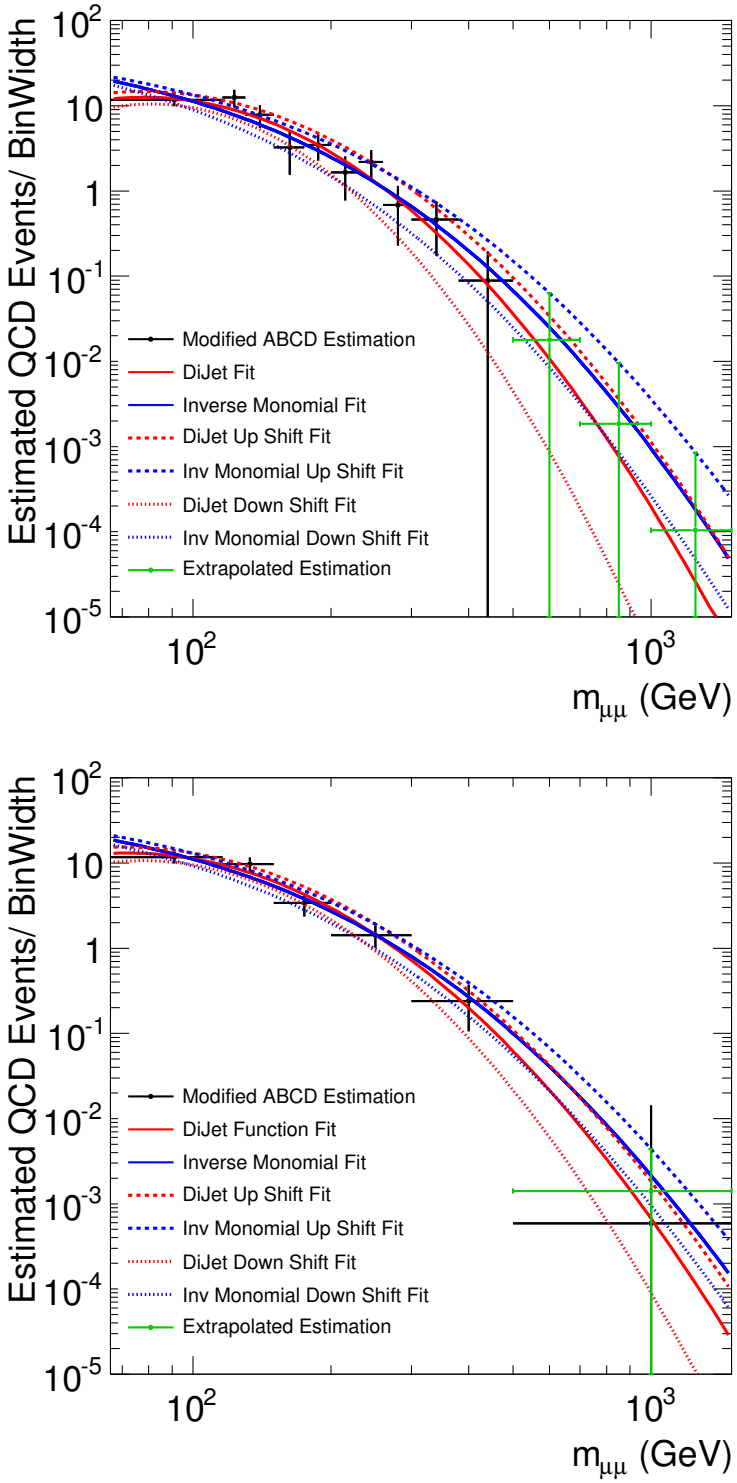

Figure 7.10.: Estimated number of multi-jet events in each one dimensional (left) and two dimensional (right) binning scheme. The red and blue lines show the dijet and inverse monomial fits. The green points represent the average of the two fits and the value taken as the multi-jet prediction in this region. Also displayed is the systematic variations of the extrapolation calculated by varying the electroweak background contamination by one standard deviation.

The modified ABCD method provides an estimate of the total number of multi-jet events in each $m_{\mu\mu}$ bin. For the 2D measurement, the rapidity and $\Delta\eta$ dependence of the multi-jet background has to be determined. To measure the shape of the multi-jet background, a control region is defined in which both muons have $I_{\mu\mu} > 0.1$. Requiring this anti-isolation condition enriches the multi-jet events, allowing the rapidity and $\Delta\eta$ shapes to be predicted. The electroweak contamination is removed by subtracting appropriate MC predictions and is found to be below 5% for the $m_{\mu\mu} > 66$ GeV analysis region. To determine whether the level of background remaining in the selection has an effect on the predicted multi-jet shapes, the anti-isolation requirement was tightened to $0.1 < I_{\mu\mu} < 0.2$, $0.2 < I_{\mu\mu} < 0.4$ and $I_{\mu\mu} > 0.6$ and shapes compared. The effect of tightening the selections on the predicted multi-jet rapidity and $\Delta\eta$ shapes are shown in figures 7.11 and 7.12. The shapes shown in the plots are normalised to the number of events predicted by the modified ABCD method. The shapes of the rapidity and $\Delta\eta$ spectra change little with respect to the tightening isolation conditions. The uncertainty associated with this determination of the rapidity and $\Delta\eta$ shape is calculated as the RMS of the deviations of the tightening selections with respect to the nominal $I_{\mu\mu} > 0.1$ anti-isolation selection. In the highest $500 < m_{\mu\mu} < 1500$ GeV mass bin there are no events, so the shape is taken from the $300 < m_{\mu\mu} < 500$ GeV bin under the assumption that the both the rapidity and $\Delta\eta$ shapes of the multi-jet background will only vary within the large uncertainty in this region.

The total number of multi-jet events in the 2D binning schemes is calculated by multiplying either the rapidity or $\Delta\eta$ shape by the normalisation calculated by the modified ABCD method. Figures 7.13 and 7.14 show the estimated multi-jet rapidity and $\Delta\eta$ spectra respectively. Overall the multi-jet background contribution varies from 1% to 0.01% over the full $m_{\mu\mu} > 66$ GeV range with an uncertainty varying between 20% at lower $m_{\mu\mu}$ and 100% in the $380 < m_{\mu\mu} < 500$ GeV bin. The increased uncertainty at higher $m_{\mu\mu}$ is due to the lack of events in the SS isolated region B used in the modified ABCD method. Figures 7.15 and 7.16 show the source of systematic uncertainty when calculating the normalisation using the modified ABCD method. The large uncertainties at higher masses are due to the conservative extrapolation of the systematics, however for the cross section measurement the statistical uncertainty dominates in this region.

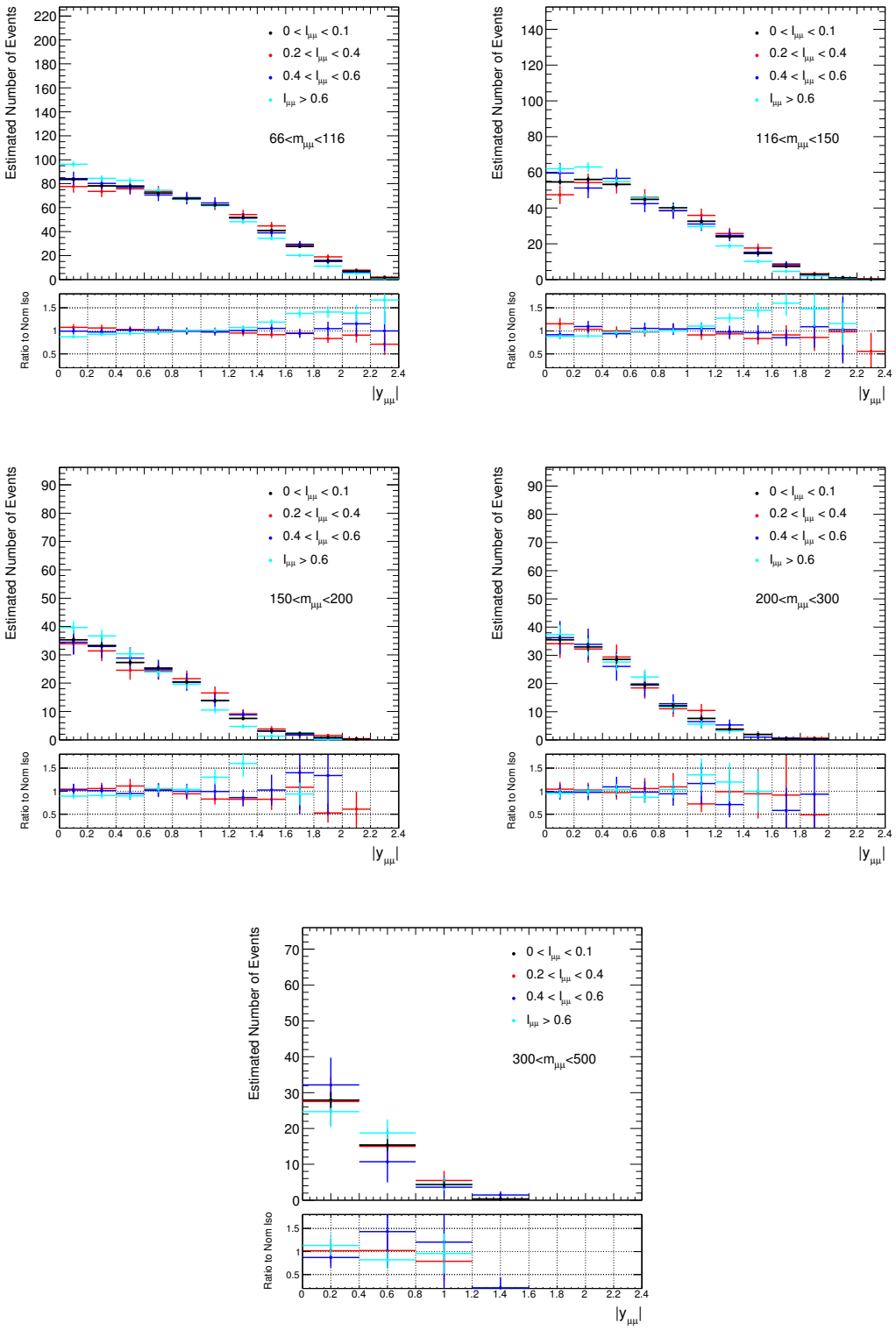

Figure 7.11.: Rapidity shapes of four varying anti-isolation requirements normalised to the number of events predicted by the modified ABCD method in each mass bin. For the $500 < m_{\mu\mu} < 1500$ GeV bin the shape is taken from the $300 < m_{\mu\mu} < 500$ GeV region.

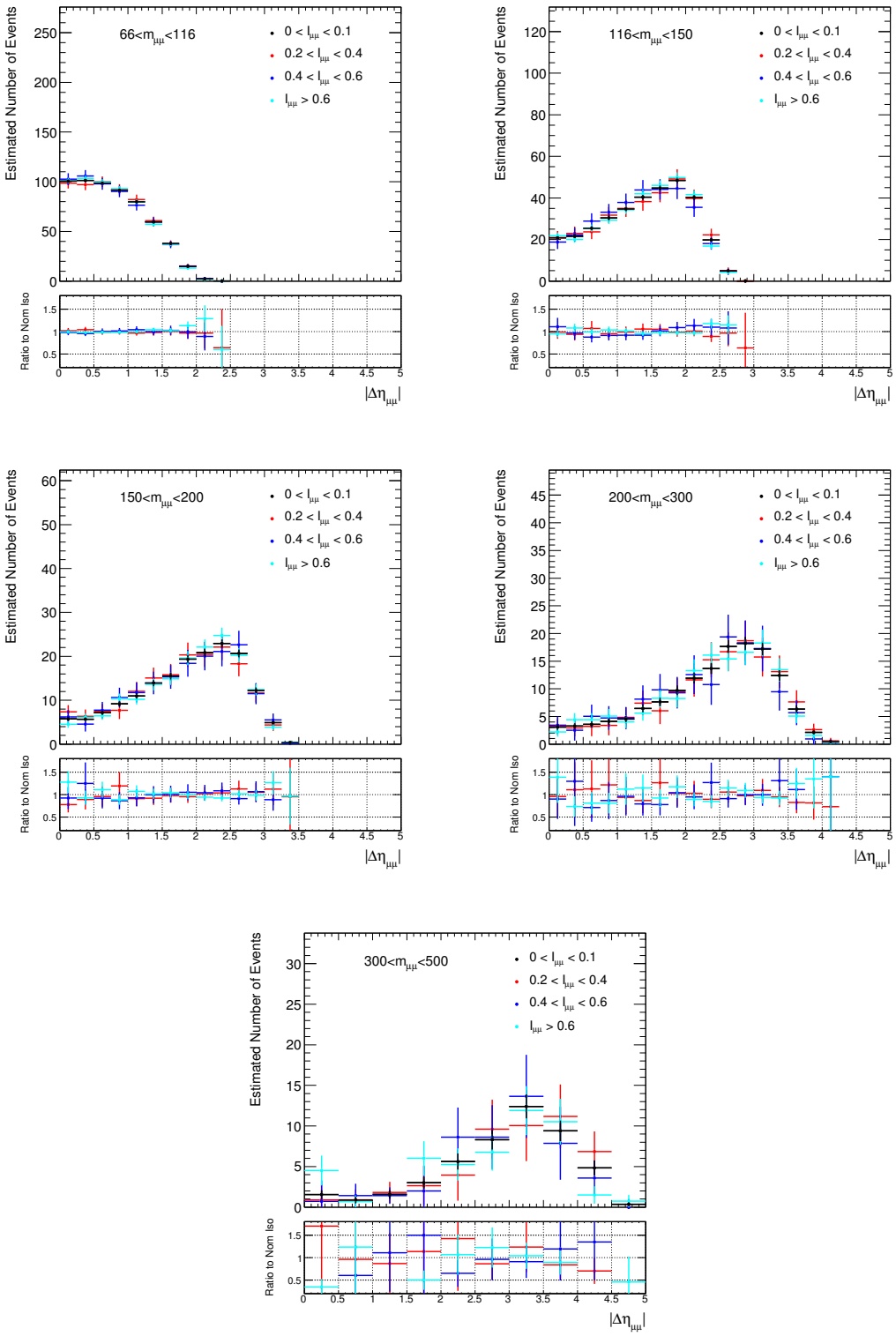

Figure 7.12.: $\Delta\,\eta$ shapes of four varying anti-isolation requirements normalised to the number of events predicted by the modified ABCD method in each mass bin. For the $500 < m_{\mu\mu} < 1500$ GeV bin the shape is taken from the $300 < m_{\mu\mu} < 500$ GeV region.

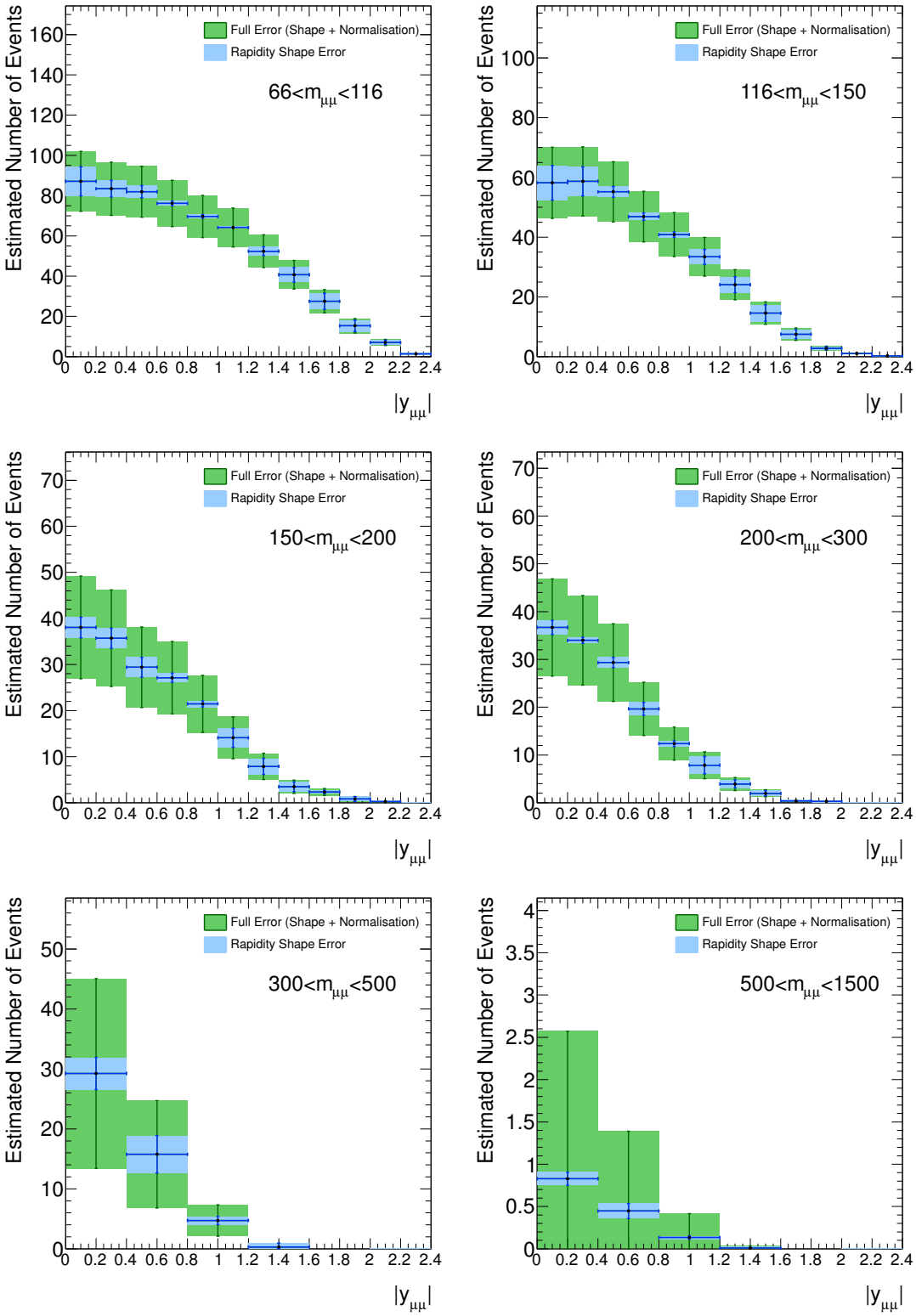

Figure 7.13.: Estimated number of multi-jet events. Blue error bars show the error derived from the estimated multi-jet rapidity shape and the green error bars include the error from the modified ABCD method in each mass bin. For the $500 < m_{\mu\mu} < 1500$ GeV bin the shape is taken from the $300 < m_{\mu\mu} < 500$ GeV region.

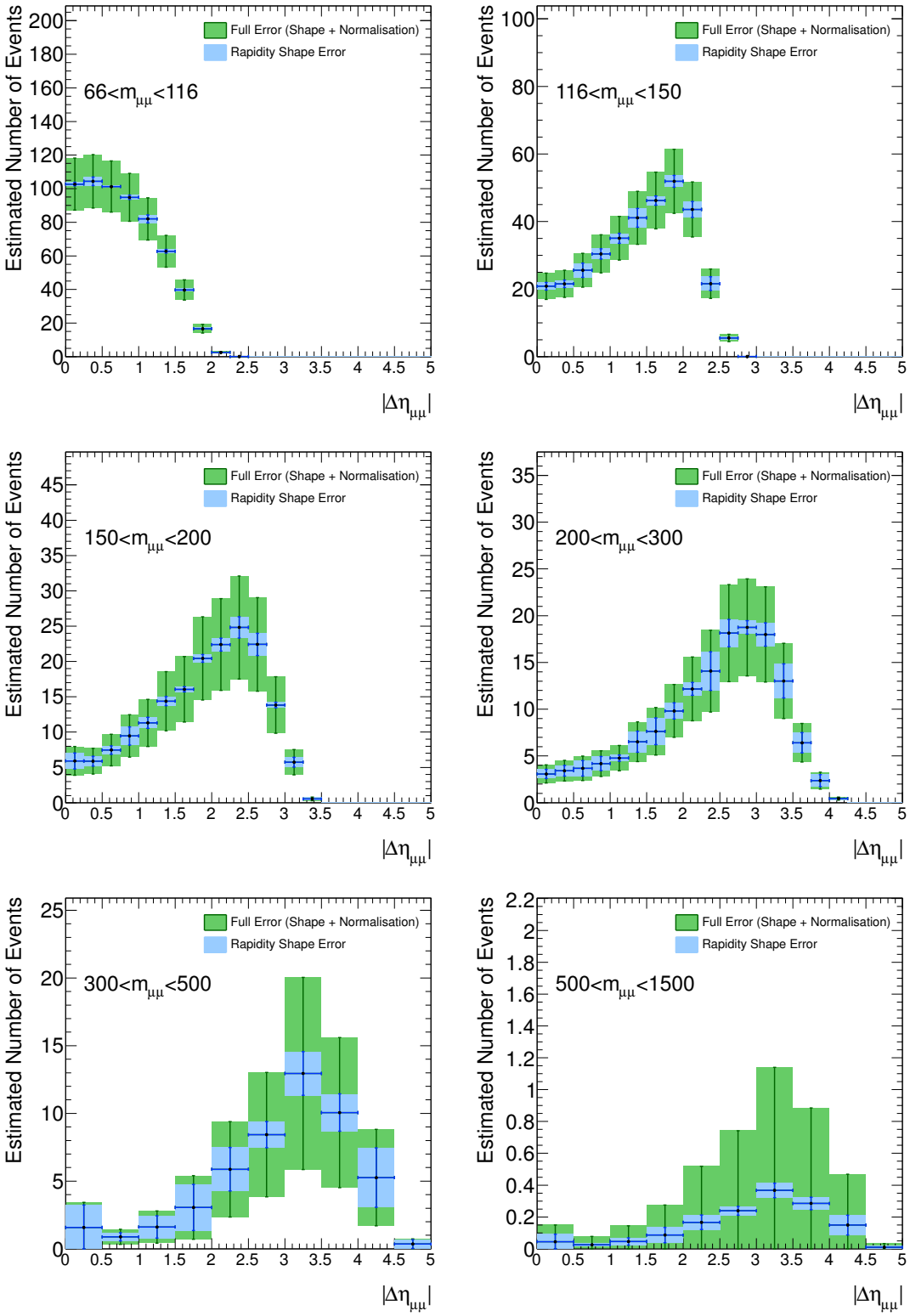

Figure 7.14.: Estimated number of multi-jet events. Blue error bars show the error derived from the estimated multi-jet rapidity shape and the green error bars include the error from the modified ABCD method in each mass bin. For the $500 < m_{\mu\mu} < 1500$ GeV bin the shape is taken from the $300 < m_{\mu\mu} < 500$ GeV region.

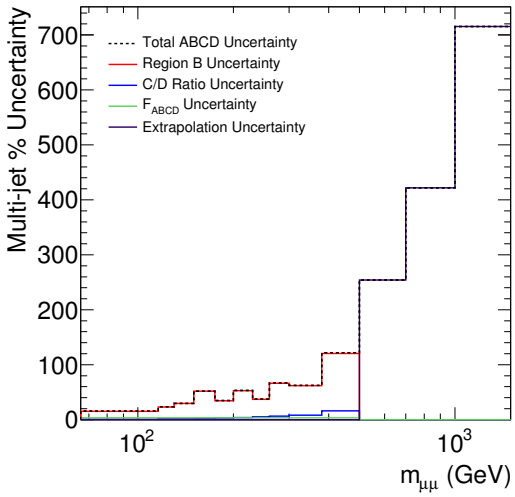

Figure 7.15.: The source of uncertainty in the 1D mass binning scheme. The region B uncertainty originates from the electroweak subtraction in this region, the C/D ratio is the statistical uncertainty from the C and D regions and the F_{ABCD} uncertainty is the uncertainty on the fit of the region C and D isolation spectra. The uncertainty in the extrapolated region is taken as the envelope of fits to electroweak background adjusted estimation in the non extrapolated region.

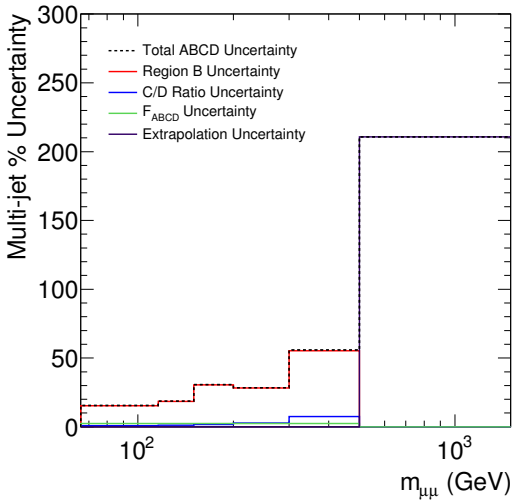

Figure 7.16.: The source of uncertainty in the 2D mass binning scheme. The region B uncertainty originates from the electroweak subtraction in this region, the C/D ratio is the statistical uncertainty from the C and D regions and the F_{ABCD} uncertainty is the uncertainty on the fit of the region C and D isolation spectra. The uncertainty in the extrapolated region is taken as the envelope of fits to electroweak background adjusted estimation in the non extrapolated region.

7.2. Electroweak Background

Electroweak background processes are estimated using MC simulation with leading order matrix elements for the diboson and W backgrounds and NLO for the $t\bar{t}$ and single top backgrounds. A correction to NNLO is made by applying a k-factor to the cross section of the MC sample as shown in tables 5.3, 5.2 and 5.6. For the $Z/\gamma^* \to \tau\tau$ background the k-factors shown in figure 5.1 are used as these k-factors are independent of lepton flavour. The uncertainty associated with the correction to NNLO and determination of the sample cross section is taken to be 5% for the diboson, $W \to \mu\nu$, $W \to \tau\nu$ and $Z/\gamma^* \to \tau\tau$ backgrounds and 6% for the $t\bar{t}$ and single top production backgrounds [7–9, 42–51].

The top backgrounds are the largest background in the analysis as shown in figure 7.1. The normalisation of the top background MC can be checked by looking at a region in which the process dominates and measuring the data MC ratio. The top particle most often decays into the W and b particles. The leptonic decay of these particles are more likely to produce isolated muons than a hadronic decay and as such are much more likely to occur in the analysis selection. The leptonic decay of these particles will contain a neutrino, which is not directly detectable by the ATLAS detector. This results in a higher value of E_T^{miss} than in Drell-Yan events. The E_T^{miss} variable is shown in the 2D binning scheme mass bins in figure 7.17. There is a better than 10% level of agreement in the top background rich region of $E_T^{miss} > 50$ GeV and $116 < m_{\mu\mu} < 500$ GeV, which is consistent with the 6% cross section and k-factor uncertainty assigned to this background in this measurement.

A data driven estimate of the $t\bar{t}$ background could be made using a similar method to that described for the multi-jet estimation in section 7.1.2. A control region rich in $t\bar{t}$ events could be made by requiring both high E_T^{miss} and an electron muon pair rather than the muon pair required in the analysis region. The electron muon pair selection will be rich in $t\bar{t}$ events because when the top particle decays it can decay into both electrons and muons and while the muons may be selected from one of the top decays an electron can be picked up from the other. This is in contrast to the Z decay where either muon or electron pairs are produced in isolation. While this method would provide a good data driven estimate of the $t\bar{t}$ background, it has not been studied in this analysis due to the good agreement seen between MC and data at high E_T^{miss}. The number of background events in each 1D and 2D binning scheme bin is given along with the unfolding factors in appendix C.

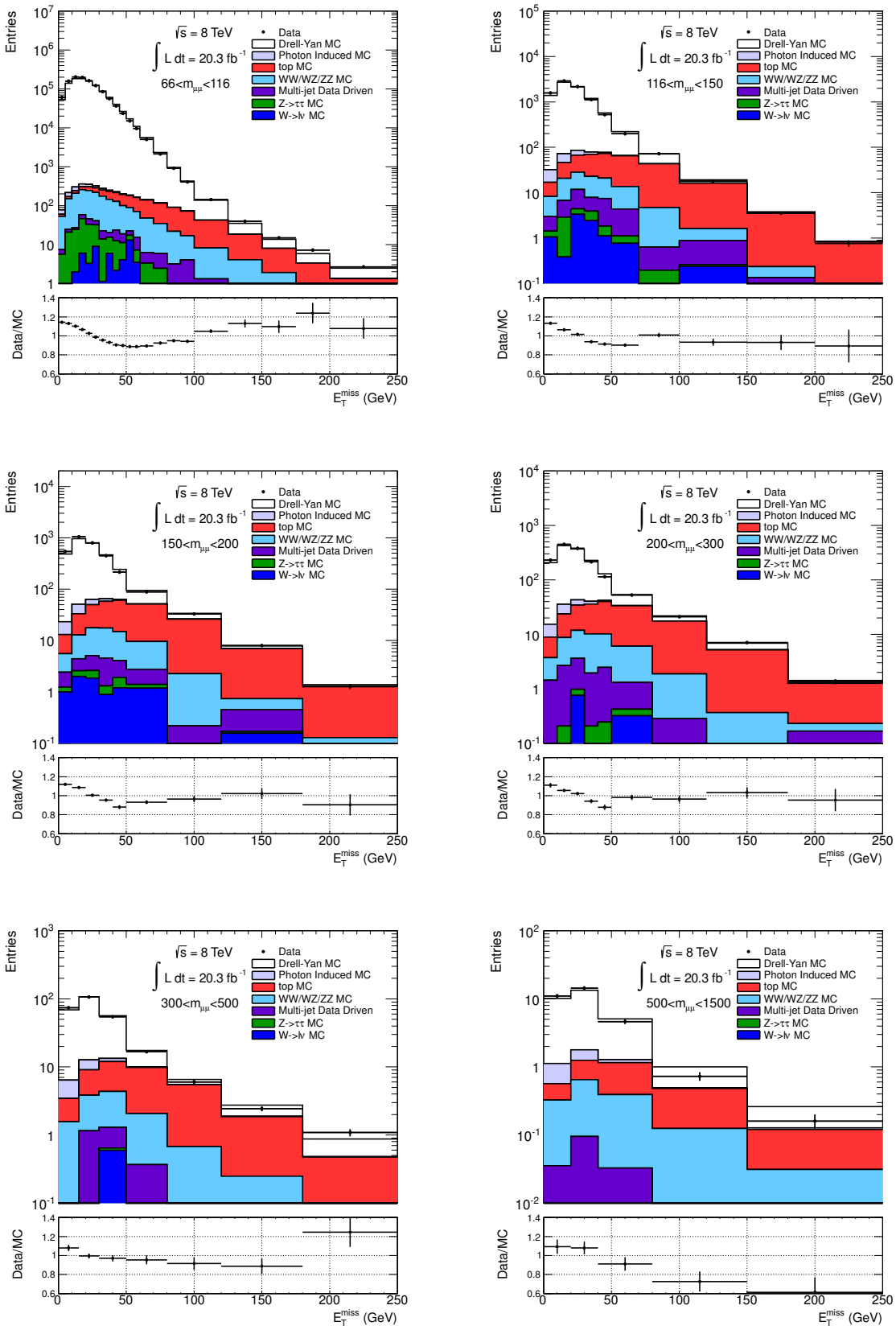

Figure 7.17.: Missing transverse energy E_T^{miss} in the 2D analysis dimuon mass bins.

Chapter 8.

Control Distributions

Once correction factors for any known mismodelling of the MC or detector response are made, the data MC agreement can be checked in the control plots. Having a good agreement between data and MC in well understood kinematic distributions is important, as this shows that the analysis scale factors and background estimations are well described.

A difference in normalisation between the data and MC is observed all of the kinematic distributions but is especially noticeable in the dimuon mass distribution shown in figure 8.1. The difference between data and theory is 3% in the Z resonance region and then falls into agreement as the mass increases. The data MC ratio in the 2D mass binning scheme is shown in table 8.1. This discrepancy between data and MC is also observed in the parallel Drell-Yan dielectron channel analysis and is discussed in appendix E.

Distributions showing the leading and subleading muon p_T, η and ϕ for events with $m_{\mu\mu} > 116$ GeV are shown in figures 8.2 and 8.3. As the η and ϕ distributions are governed by the layout and performance of the sub detector systems, the better than 10% data theory agreement shows that the detector is modelled well by the MC. The p_T distribution for $m_{\mu\mu} > 116$ GeV also shows a good level of agreement in the statistics rich low p_T region.

The dimuon control plots for $m_{\mu\mu}$, $p_T^{\mu\mu}$, $y_{\mu\mu}$ and $\Delta\eta_{\mu\mu}$ are shown in figures 8.1, 8.4, 8.5 and 8.6. The $p_T^{\mu\mu}$ distribution is limited to events with $m_{\mu\mu} > 116$ GeV and shows a small discrepancy at low p_T likely due to a slight mismodelling in the Drell-Yan MC. A study that investigates the possible effect this discrepancy has on the fiducial cross sections is described in appendix B. The two variables $y_{\mu\mu}$ and $\Delta\eta_{\mu\mu}$ in which the 2D analysis

measurement is made have a data MC agreement of better than 10% for all but the most statistically limited regions.

The muon control plots showing the p_T, η and ϕ distributions for the mass region $66 < m_{\mu\mu} < 116$ GeV are shown in figures 8.8 and 8.9. The dimuon control plots for this mass region are shown in figures 8.7 and 8.10.

The muon control plots showing the p_T, η and ϕ distributions for the mass region $m_{\mu\mu} < 300$ GeV are shown in figures 8.11 and 8.12. The dimuon control plots for this mass region are shown in figure 8.13.

The number of events remaining after each reconstruction level selection applied is shown for data and MC in cutflow table 8.2. For the MC listed in the table all of the scale factors discussed in section 6.3 have been applied. The multi-jet estimation is not included in this table as there is only an prediction for the analysis region and not before the selections are applied.

Mass Bin (GeV)	data/MC
$66 < m_{\mu\mu} < 116$	1.031
$116 < m_{\mu\mu} < 150$	1.019
$150 < m_{\mu\mu} < 200$	1.014
$200 < m_{\mu\mu} < 300$	1.006
$300 < m_{\mu\mu} < 500$	0.990
$500 < m_{\mu\mu} < 1500$	0.985

Table 8.1.: Data MC ratio in the 2D binning scheme. The MC includes the multi-jet background estimated using a data driven technique.

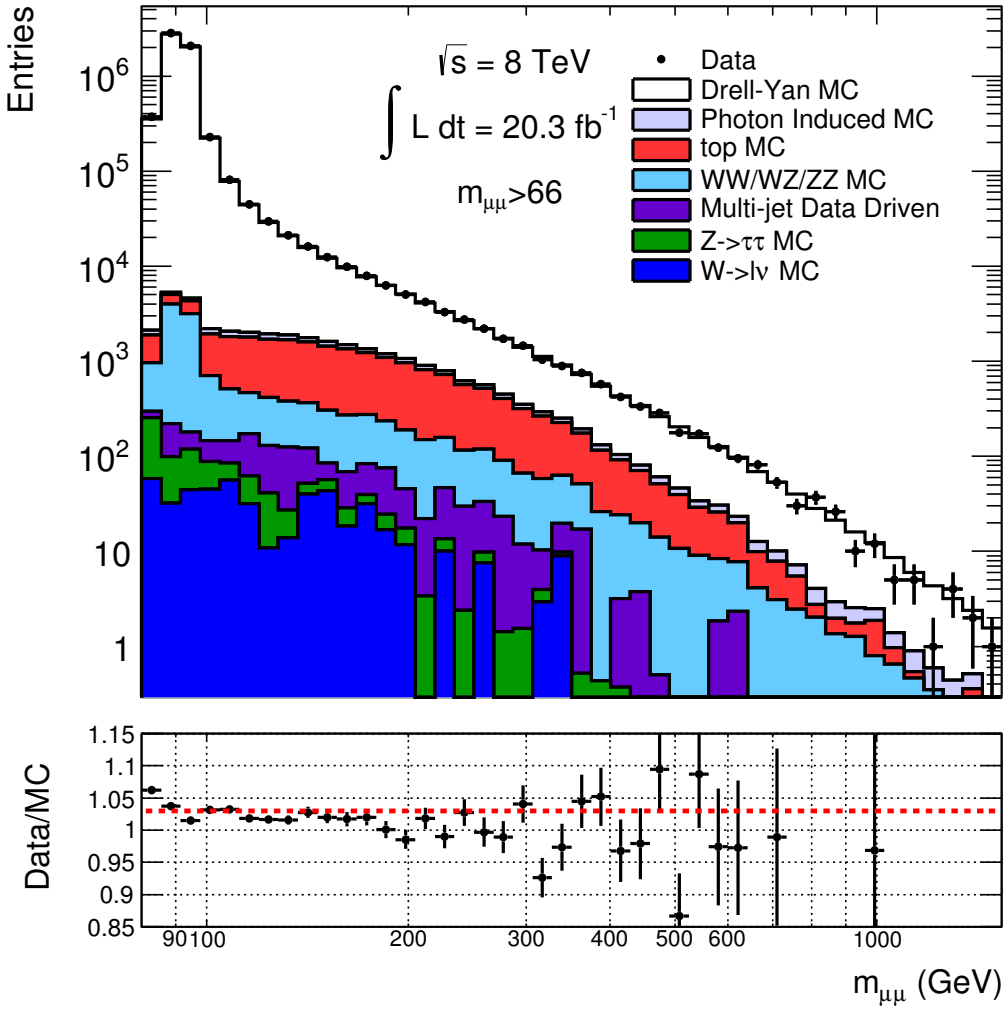

Figure 8.1.: Dimuon invariant mass ($m_{\mu\mu}$) distribution after full event selection and detector response corrections applied. The dashed red line gives the data MC ratio for the $80 < m_{\mu\mu} < 1500$ GeV region.

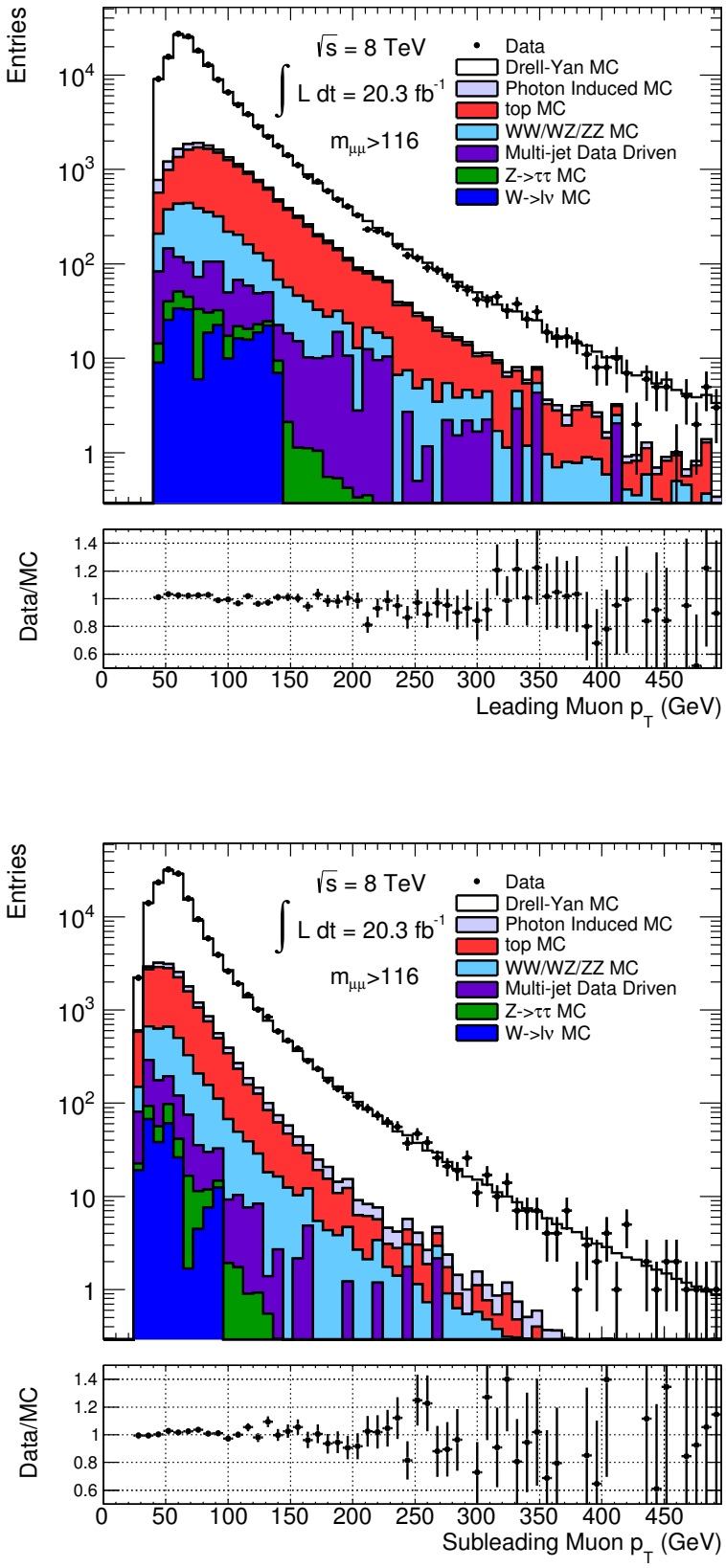

Figure 8.2.: Leading (top) and subleading (bottom) muon p_T distributions for $m_{\mu\mu} > 116$ GeV after full event selection and detector response corrections applied.

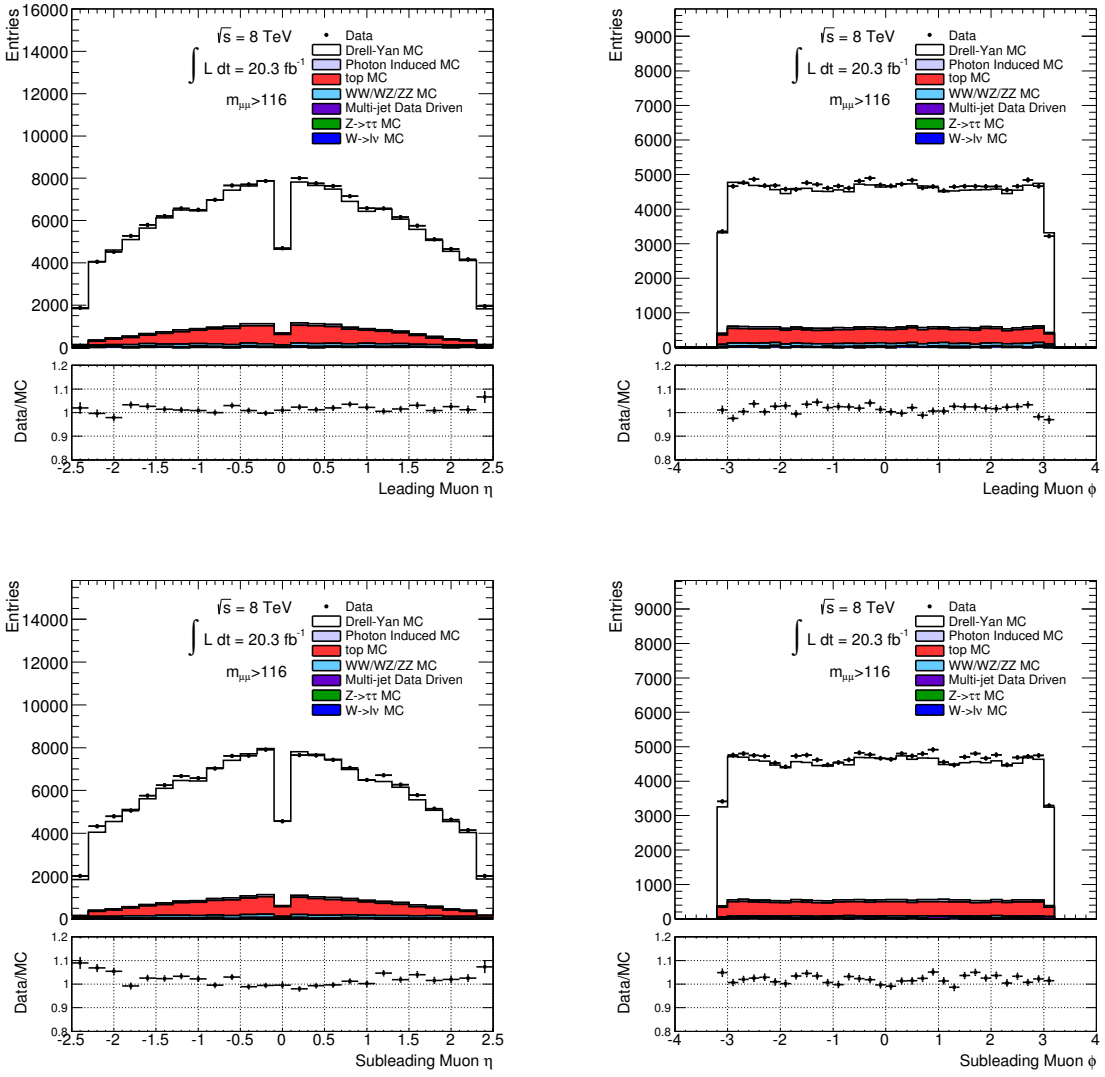

Figure 8.3.: Leading (upper row) and subleading (lower row) muon η (left) and ϕ (right) distributions for $m_{\mu\mu} > 116$ GeV after full event selection and detector response corrections applied.

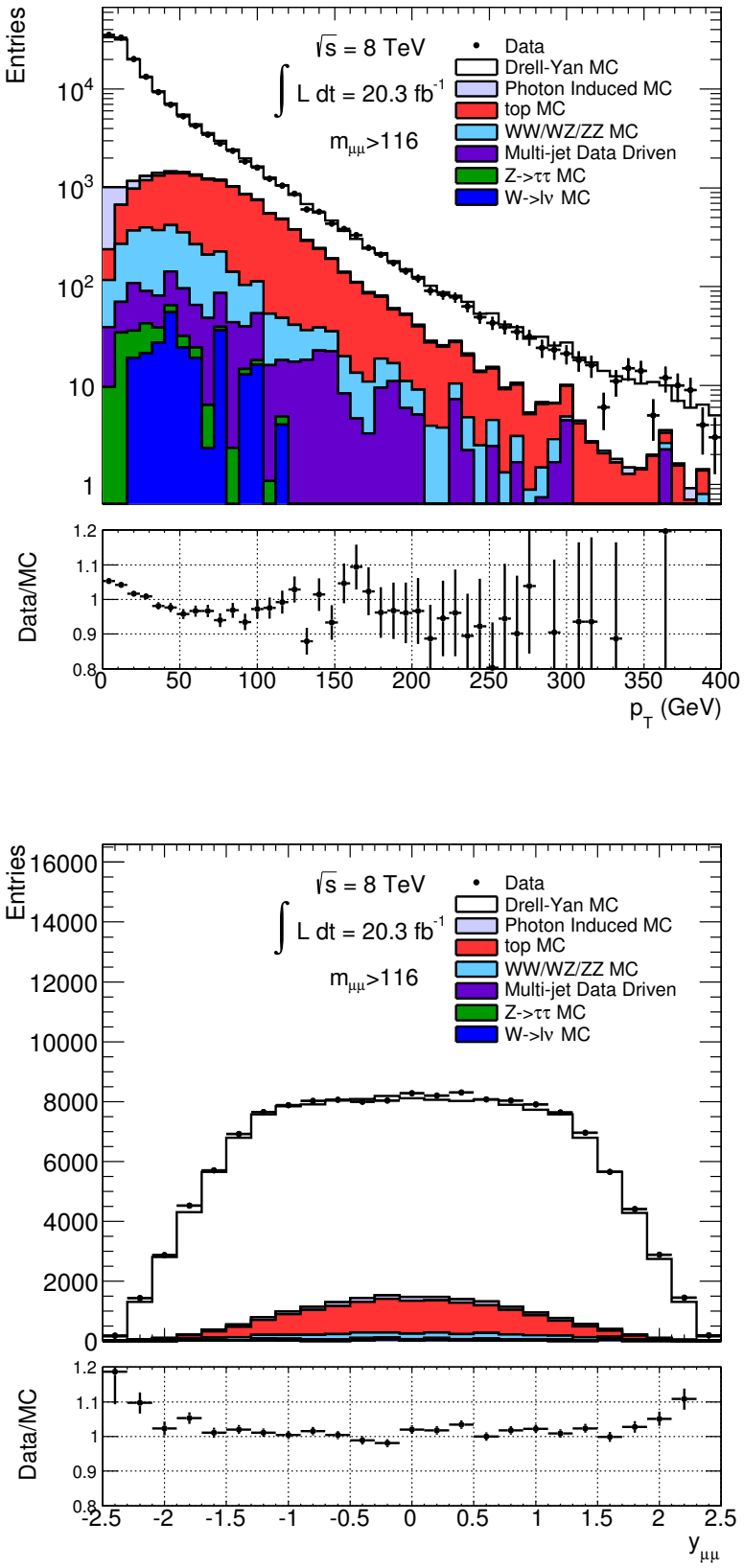

Figure 8.4.: Dimuon p_T (top) and $y_{\mu\mu}$ (bottom) distributions for $m_{\mu\mu} > 116$ GeV after full event selection and detector response corrections applied.

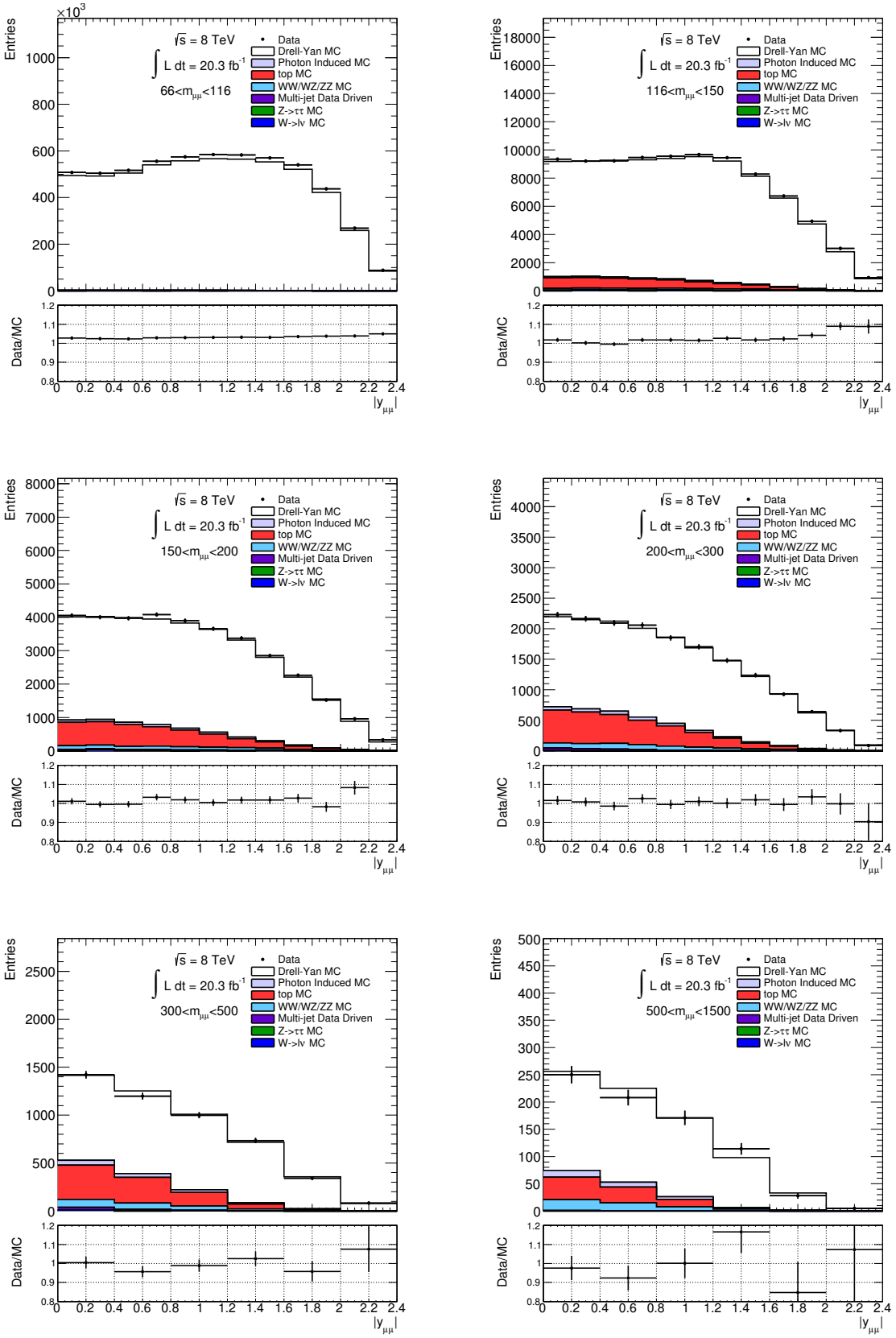

Figure 8.5.: Dimuon $y_{\mu\mu}$ distributions for the 2D $m_{\mu\mu}$ binning scheme after full event selection and detector response corrections applied.

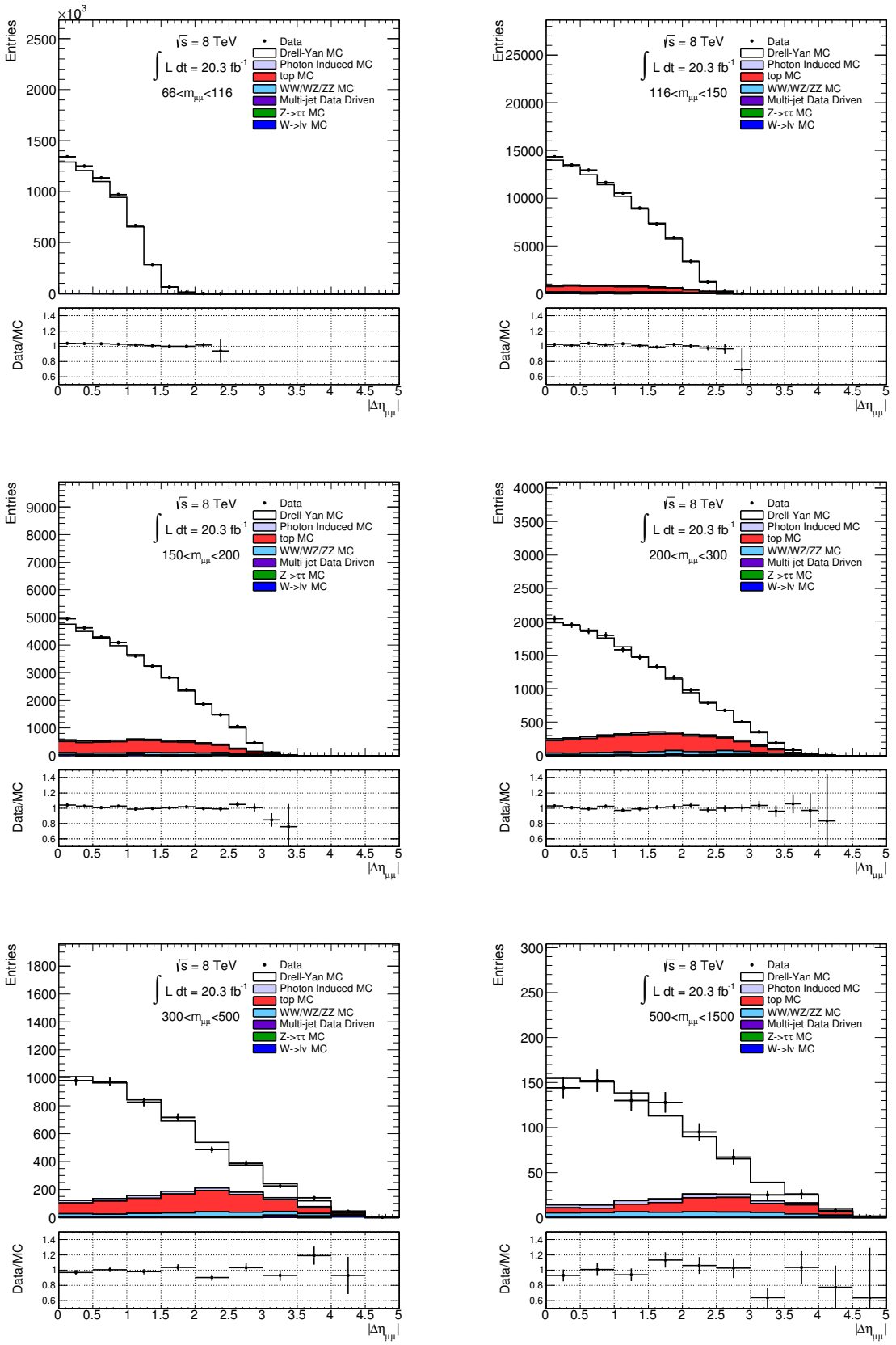

Figure 8.6.: Muon $\Delta\eta$ distributions for the 2D $m_{\mu\mu}$ binning scheme after full event selection and detector response corrections applied.

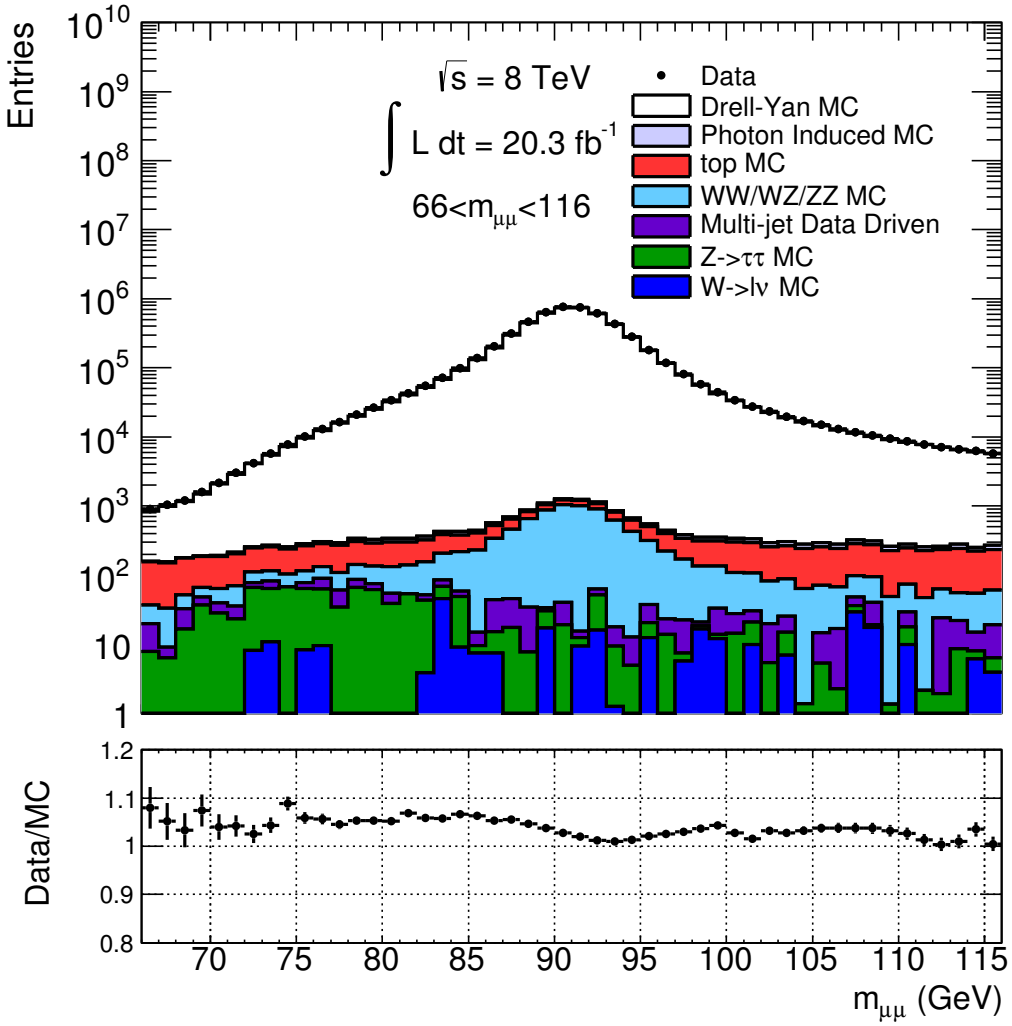

Figure 8.7.: Dimuon invariant mass ($m_{\mu\mu}$) distribution after full event selection and detector response corrections applied ($66 < m_{\mu\mu} < 116$ GeV).

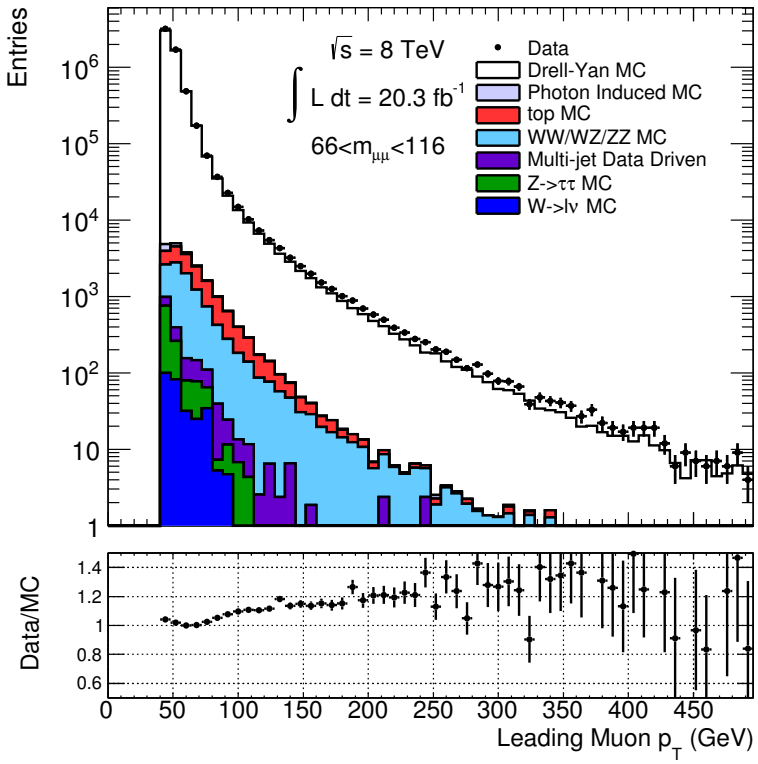

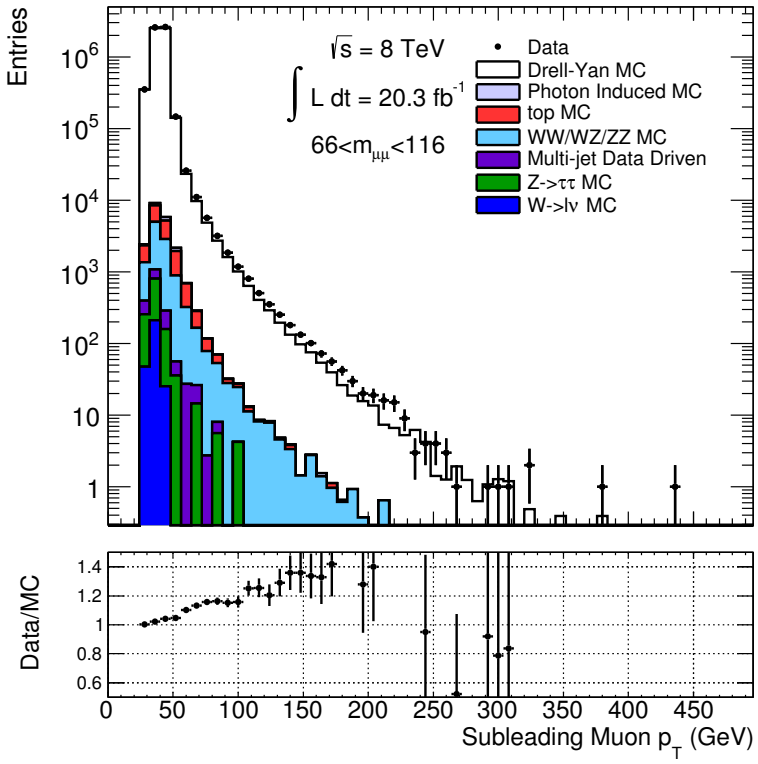

Figure 8.8.: Leading (top) and subleading (bottom) muon p_T distributions for $66 < m_{\mu\mu} < 116$ GeV after full event selection and detector response corrections applied.

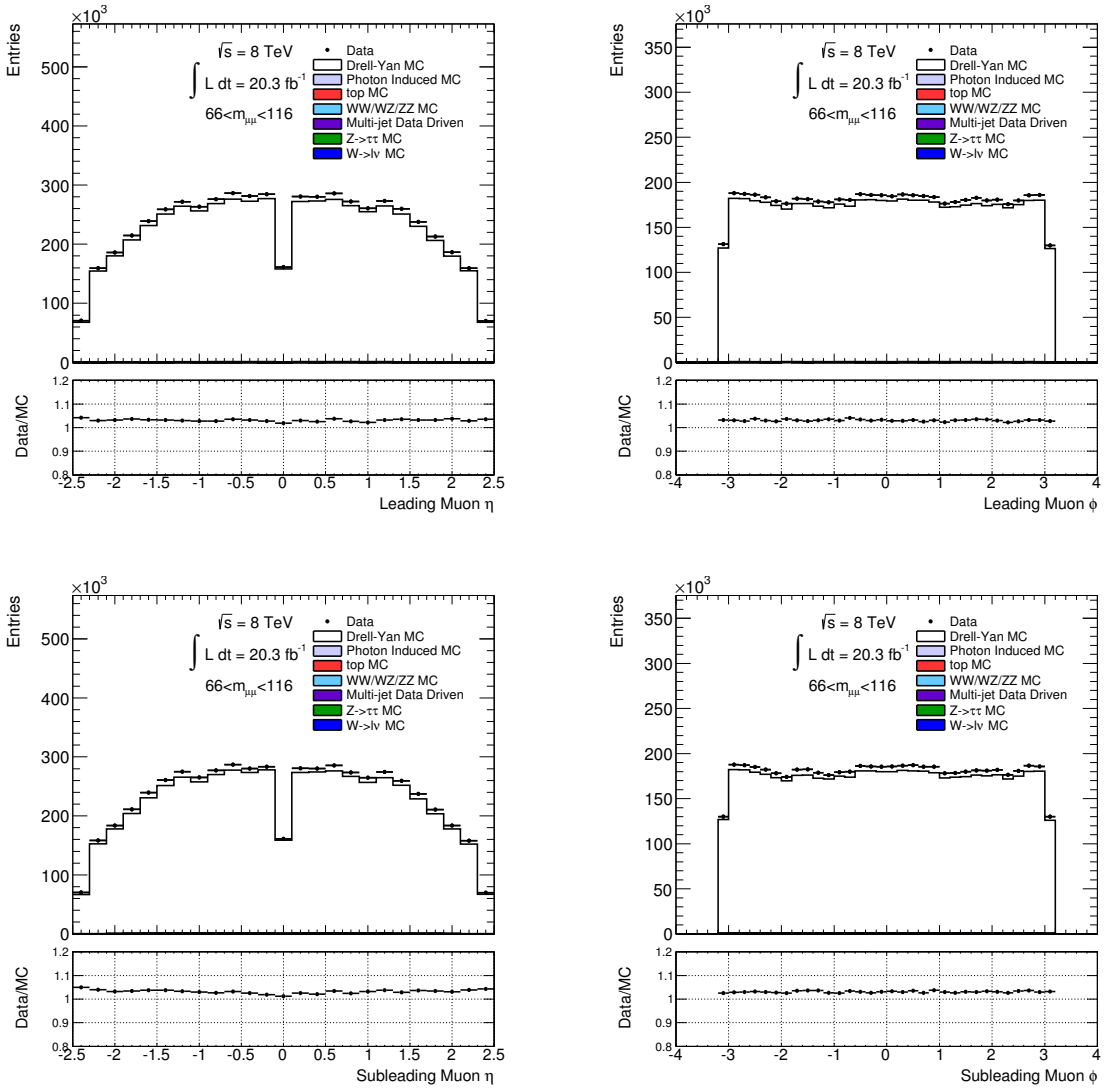

Figure 8.9.: Leading (upper row) and subleading (lower row) muon η (left) and ϕ (right) distributions for $66 < m_{\mu\mu} < 116$ GeV after full event selection and detector response corrections applied.

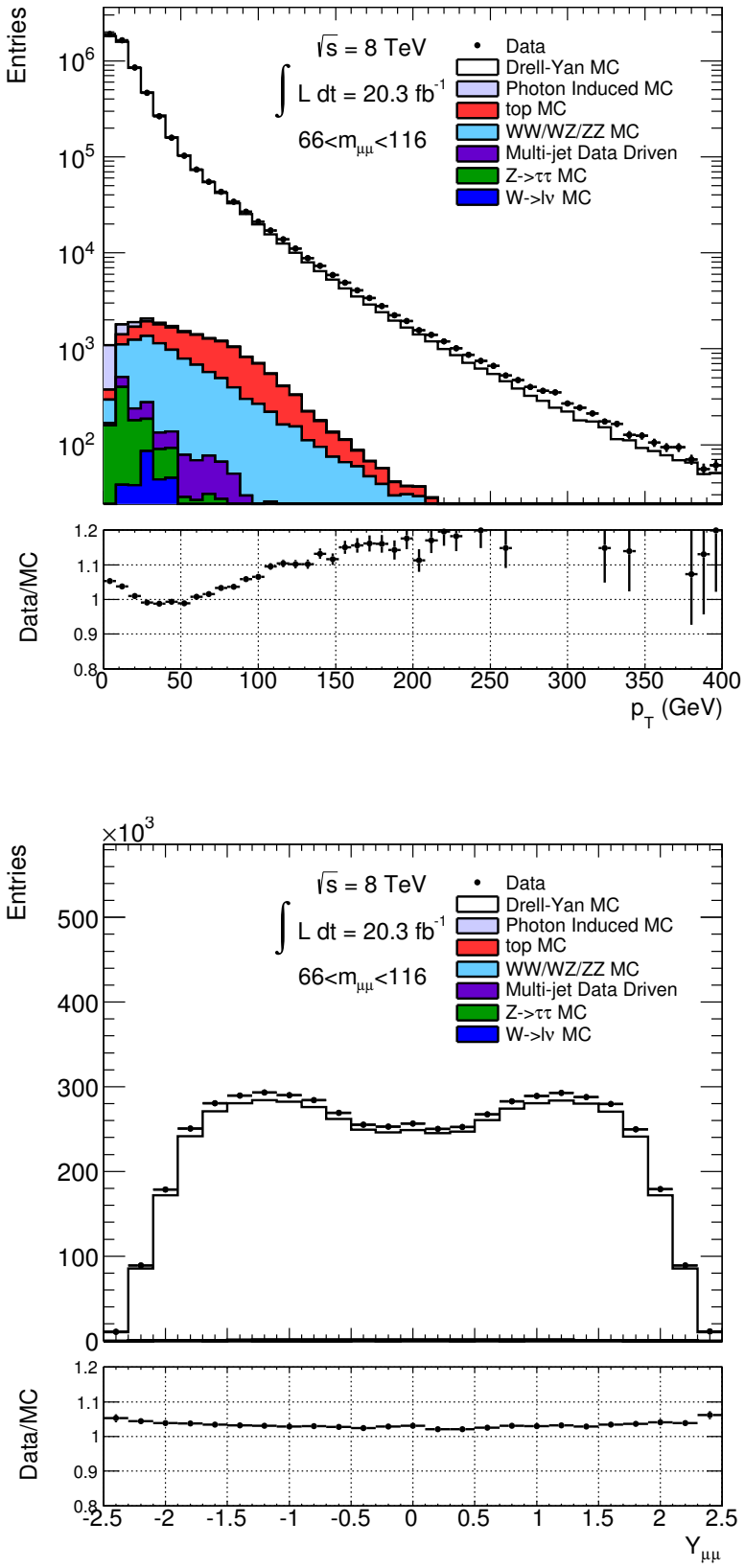

Figure 8.10.: Dimuon p_T (top) and $y_{\mu\mu}$ (bottom) distributions for $66 < m_{\mu\mu} < 116$ GeV after full event selection and detector response corrections applied.

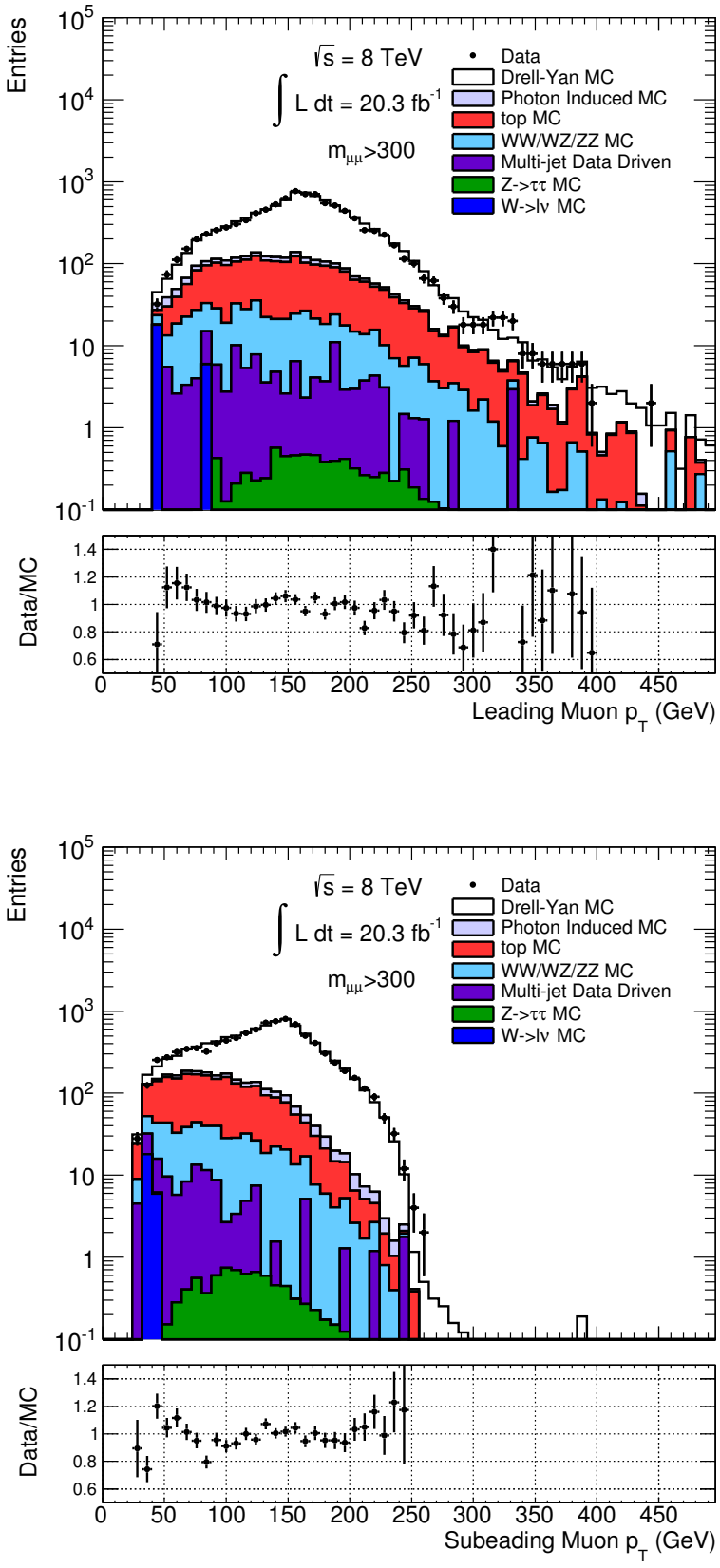

Figure 8.11.: Leading (top) and subleading (bottom) muon p_T distributions for $m_{\mu\mu} > 300$ GeV after full event selection and detector response corrections applied.

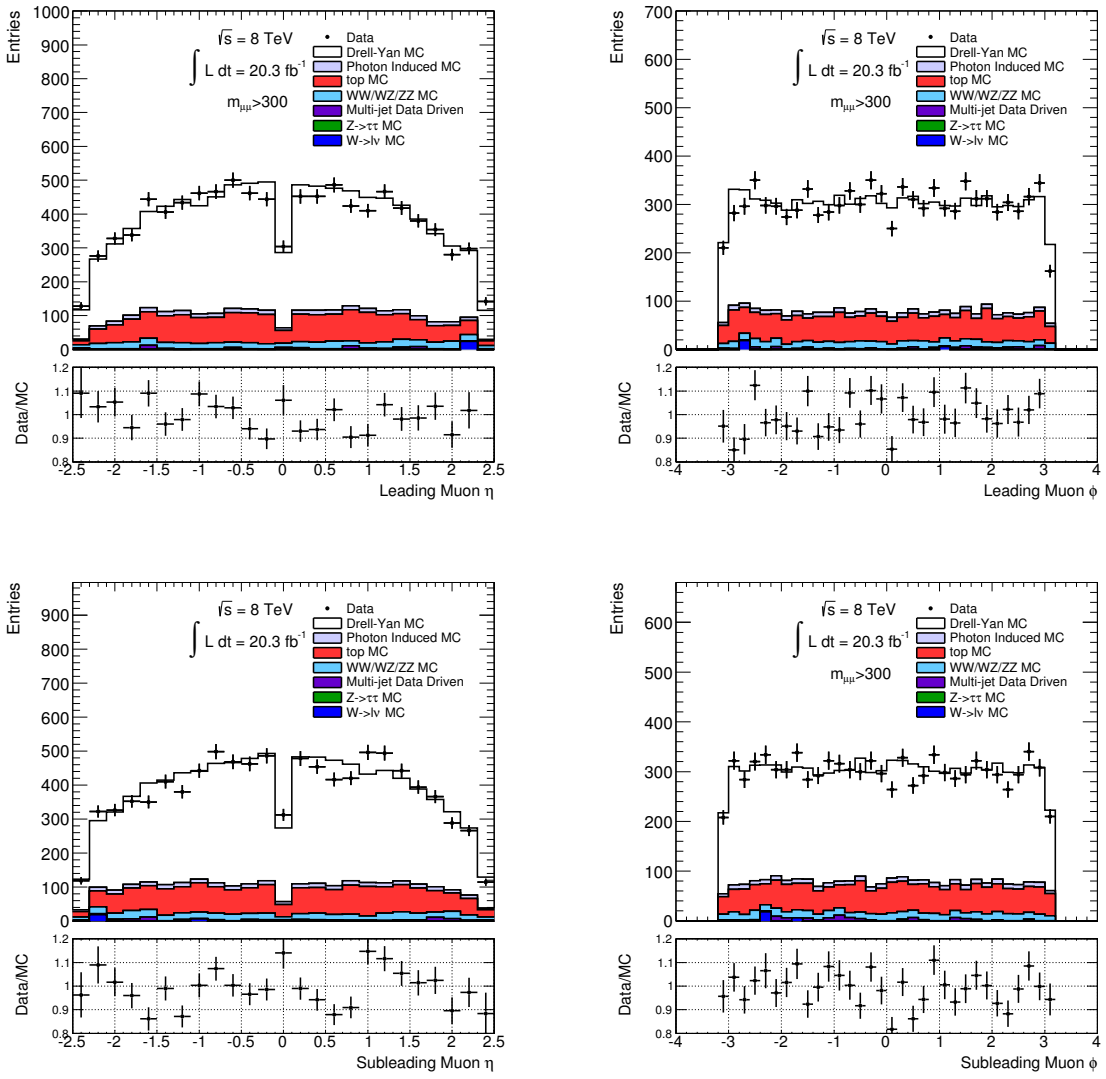

Figure 8.12.: Leading (upper row) and subleading (lower row) muon η (left) and ϕ (right) distributions for $m_{\mu\mu} > 300$ GeV after full event selection and detector response corrections applied.

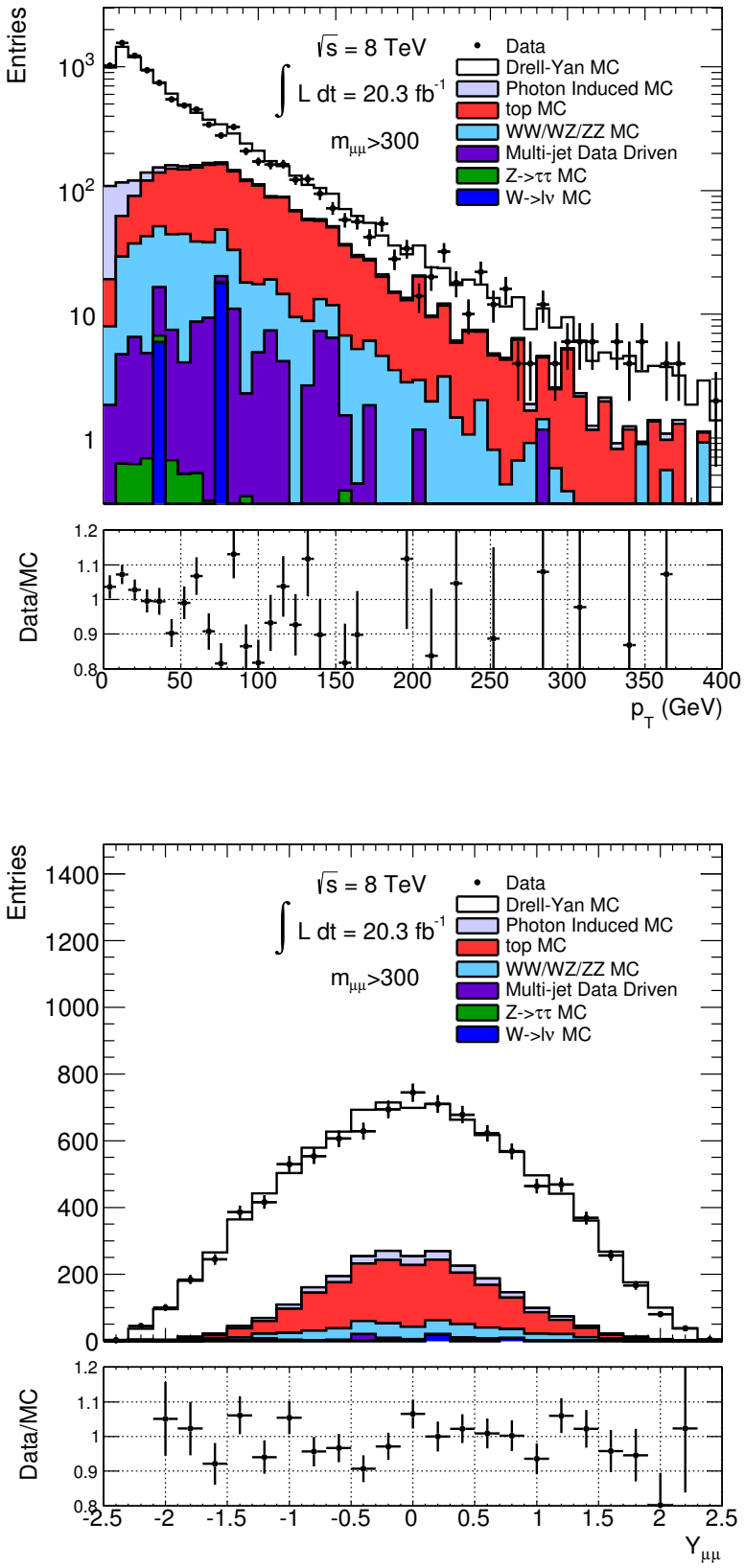

Figure 8.13.: Dimuon p_T (top) and $y_{\mu\mu}$ (bottom) distributions for $m_{\mu\mu} > 300$ GeV after full event selection and detector response corrections applied.

channel	Data		Drell-Yan		PIP		Top		WW/WZ/ZZ		$Z \to \tau\tau$		$W \to l\nu$	
selection	events	ϵ_{abs} [%]	events	ϵ_{abs} [%]	events	ϵ_{abs} [%]	events	ϵ_{abs} [%]	events	ϵ_{abs} [%]	events	ϵ_{abs} [%]	events	ϵ_{abs} [%]
Preselection	147648799	100.00	12007583	100.00	344939	100.00	1250250	100.00	228106	100.00	1752475	100.00	51818414	100.00
Trigger	112379340	76.11	11169801	93.02	47457	13.76	704265	56.33	145542	63.80	498744	28.46	36109795	69.69
Number Of Muons	29490310	19.97	10924314	90.98	40605	11.77	278423	22.27	41661	18.26	111541	6.36	4082993	7.88
MCP req	27049311	18.32	10344284	86.15	38617	11.20	265478	21.23	38516	16.89	102623	5.86	3498280	6.75
z_0	22147811	15.00	10263773	85.48	36181	10.49	238326	19.06	31822	13.95	77771	4.44	995911	1.92
η	20996647	14.22	9691251	80.71	34419	9.98	232427	18.59	30139	13.21	73484	4.19	861824	1.66
Base p_T	7414705	5.02	6896297	57.43	5767	1.67	39779	3.18	13235	5.80	3368	0.19	4967	0.01
Isolation	7125921	4.83	6833879	56.91	5621	1.63	26134	2.09	12928	5.67	3287	0.19	618	0.00
Lead p_T	5908466	4.00	5669040	47.21	3935	1.14	24653	1.97	12153	5.33	1484	0.08	569	0.00
OS	5907356	4.00	5668978	47.21	3935	1.14	24455	1.96	11902	5.22	1484	0.08	520	0.00
$m_{\mu\mu} > 66$	5877901	3.98	5665348	47.18	3470	1.01	21012	1.68	11574	5.07	1125	0.06	520	0.00
$m_{\mu\mu} > 116$	147193	0.10	126759	1.06	1814	0.53	12700	1.02	2626	1.15	134	0.01	237	0.00
$m_{\mu\mu} > 300$	5555	0.00	4209	0.04	163	0.05	914	0.07	266	0.12	4	0.00	11	0.00
$m_{\mu\mu} > 500$	778	0.00	629	0.01	29	0.01	85	0.01	45	0.02	0	0.00	0	0.00

Table 8.2.: A cutflow table that shows the number of events that pass each reconstruction level selection as listed in section 6.2. The MC values have all the muon performance SFs applied.

Chapter 9.

Drell-Yan Cross Section

The cross section measurements have been made using a bin-by-bin unfolding technique due to the high bin purity seen in both the 1D and 2D binning schemes. This section describes the justification for the unfolding techniques used as well as the methodology for calculating the cross sections. The three analysis cross sections that are measured are calculated using the following formulae:

$$\frac{d\sigma}{dm_{\mu\mu}} = \frac{N - B}{\mathcal{L} \cdot C_{DY} \cdot \Gamma_m} \tag{9.1}$$

$$\frac{d^2\sigma}{dmd|y_{\mu\mu}|} = \frac{N - B}{\mathcal{L} \cdot C_{DY} \cdot \Gamma_m \cdot \Gamma_y} \tag{9.2}$$

$$\frac{d^2\sigma}{dmd|\Delta\eta_{\mu\mu}|} = \frac{N - B}{\mathcal{L} \cdot C_{DY} \cdot \Gamma_m \cdot \Gamma_{\Delta\eta}} \tag{9.3}$$

where N is the number of data events, B is the estimated background, $\mathcal{L}$ is the integrated luminosity of the data used, C_{DY} is an unfolding correction factor and Γ_m, Γ_y and $\Gamma_{\Delta\eta}$ are the bin widths for the single differential mass measurement, the double differential mass and rapidity measurement and the double differential mass and $\Delta\eta$ measurement respectively.

The definition of the cross section measured depends on the definition of the truth particles that the data is unfolded to. Three different definitions of the truth muons can be

defined depending on how the QED FSR is handled. Born level muons are muons before any QED FSR, bare level muons are muons after any QED FSR and dressed level muons are combination of the two where a $\Delta R < 0.1$ cone is applied around the bare muons and any QED FSR is resumed into the muon definition.

The muon definition can be chosen as appropriate for each analysis. The born muon definition is the fundamental hard scattering process without QED FSR and can be easily compared to theory. The bare muon definition is closer to the raw experimentally observed data and doesn't suffer from any uncertainty from the unfolding with regards to QED FER model. The dressed muon definition is primarily used for comparison to electron channel results, where the electron is detected in a calorimeter that sums the adjacent QED FSR as part of the particle detection.

The cross sections measured in this analysis use the born muon definition. All generator quantities mentioned in this chapter are at the born level. To unfold to the bare and dressed level either the generator quantities have to be changed to the bare or dressed level or MC can be used to calculate a scale factor to correct the born level cross sections to the required muon definitions.

9.1. Purity and Stability

Determining the cross section within the fiducial volume described in section 6.1 requires a correction accounting for the difference between the reconstruction and fiducial level selections. This correction needs to account for any events that have migrated from their generated bins to other analysis bins. In addition because the detector doesn't have a perfect detector efficiency some of the generated events will not be reconstructed at all and this needs to be accounted for. The level of bin migrations is heavily dependant on the detector resolution and specifically the detector resolution relative to the size of the bins. If the detector resolution is small relative to the size of the bins then the random fluctuations in the reconstructed variable will not be large enough to move the event to a different bin. The fraction of events generated in a bin to those reconstructed in a bin is given by the acceptance as follows:

$$A^i = \frac{N^i_{rec}}{N^i_{gen}} \tag{9.4}$$

where i is the bin index, N^i_{rec} is the number of events reconstructed in bin i and N^i_{gen} is the number of events generated in bin i. The level of bin migration in the analysis can be gauged by measuring the number of events that are reconstructed and generated in the same bin. The purity gives a value of how many events in each reconstructed bin were generated in the same bin in the definition as follows:

$$P_i = \frac{\text{Events generated and reconstructed in a bin}_i}{\text{Events reconstructed in a bin}_i} \tag{9.5}$$

A corollary value, the stability, describes how many events have left the bin in which they were generated:

$$S_i = \frac{\text{Events generated and reconstructed in a bin}_i}{\text{Events generated in a bin}_i} \tag{9.6}$$

The purity and stability are calculated for the high mass Drell-Yan analysis using the Drell-Yan MC listed in table 5.1. Figures 9.1, 9.2 and 9.3 show the purity and stability in the analysis binning schemes for the dimuon mass, dimuon rapidity, and $\Delta\eta$ variables respectively. Using the preceding equations it can be noted that the acceptance can be built from the stability and purity $A = P/S$.

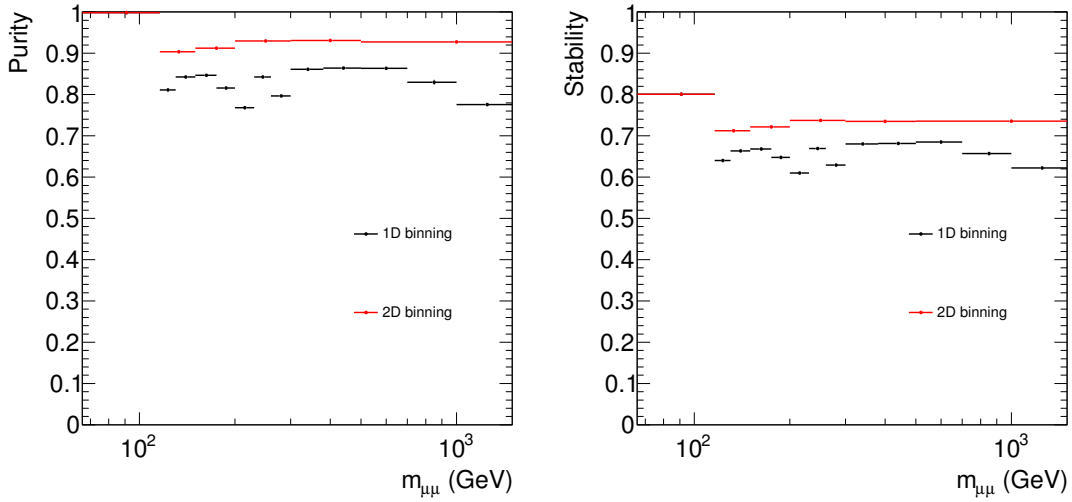

Figure 9.1.: The purity (left) and stability (right) in the 1D and 2D mass binning scheme using PowhegPythia Drell-Yan MC.

The purity in dimuon mass is over 75% for the 1D binning scheme and over 90% for the 2D coarser binning scheme. Purities of over 85% are observed for almost all of the rapidity binning and over 90% for almost all of the $\Delta\eta$ binning. The few bins with lower purities

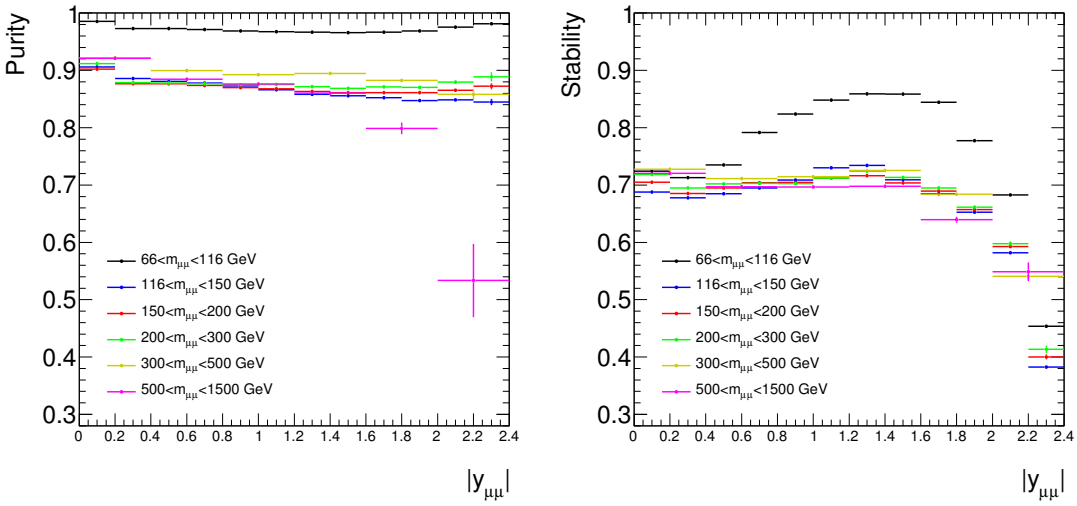

Figure 9.2.: The purity (left) and stability (right) in the 2D mass and rapidity binning scheme using PowhegPythia Drell-Yan MC.

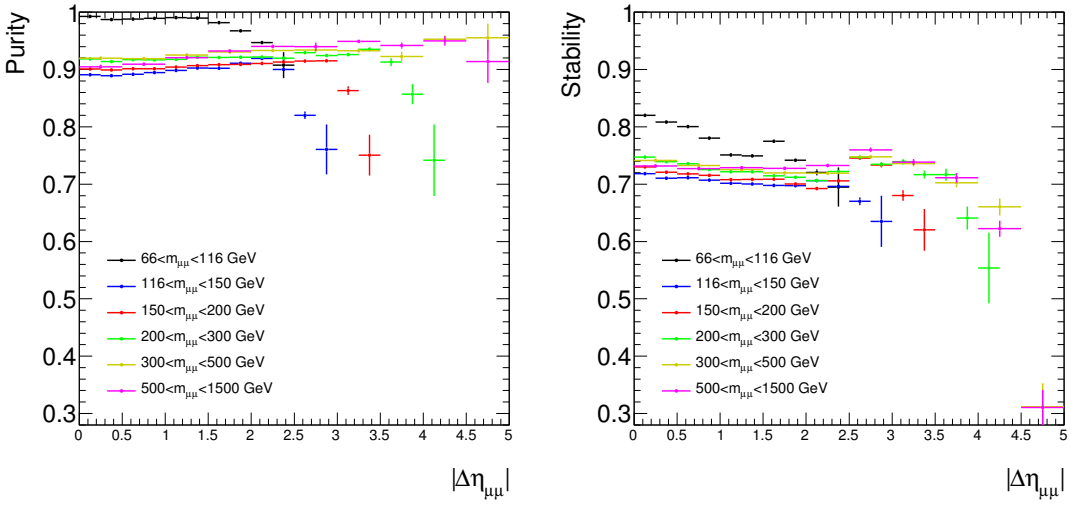

Figure 9.3.: The purity (left) and stability (right) in the 2D mass and $\Delta\eta$ binning scheme using PowhegPythia Drell-Yan MC.

are at the edge of the kinematic limit and as such have fewer events recorded leading to a lower purity. The shape of the Z resonance peak within the $66 < m_{\mu\mu} < 116$ GeV bin results in a relatively high stability and purity as there are fewer events populating the bin edge regions.

The purity observed in the high mass Drell-Yan is very high due to the size of the bin widths used when compared to the detector resolution. Higher bin migration is observed in

dimuon mass than in the rapidity and $\Delta\eta$ variables due to the detectors excellent angular resolution. The resolution of the dimuon rapidity and muon $\Delta\eta$ are shown in figures 9.5 and 9.6. Variables $m^{gen}_{\mu\mu}$, $|y^{gen}_{\mu\mu}|$ and $|\Delta\eta^{gen}_{\mu\mu}|$ give the generator level quantities and variables $m^{rec}_{\mu\mu}$, $|y^{rec}_{\mu\mu}|$ and $|\Delta\eta^{rec}_{\mu\mu}|$ give the reconstructed level values. The error bars shown in the figures represent the RMS of the entries within each bin.

The Drell-Yan MC used to produce the resolution plots also contains muons not originating from the $Z/\gamma^* \to \mu\mu$ hard scattering process. In some events these muons may be reconstructed as one of the selected muons, leading to a large difference in kinematics between the generator level muon and the selected reconstructed muon. This would result in an overestimate of the detector resolution. To combat this a $\Delta R < 0.2$ selection is applied between the generated and reconstructed muons.

It can be seen from the figures that for both the rapidity and $\Delta\eta$ variables the bin size is always at least 5 times the size of the RMS of the data resulting in the low bin migration seen in the purity distributions. Figure 9.4 shows the dimuon mass resolution. The dimuon mass resolution is not as good as the $|y_{\mu\mu}|$ and $|\Delta\eta_{\mu\mu}|$ resolution but the bin sizes are relatively large. For the all of the mass bins apart from the low statistics $1000 < m_{\mu\mu} < 1500$ GeV bin the RMS of the data doesn't exceed half the size of the bin.

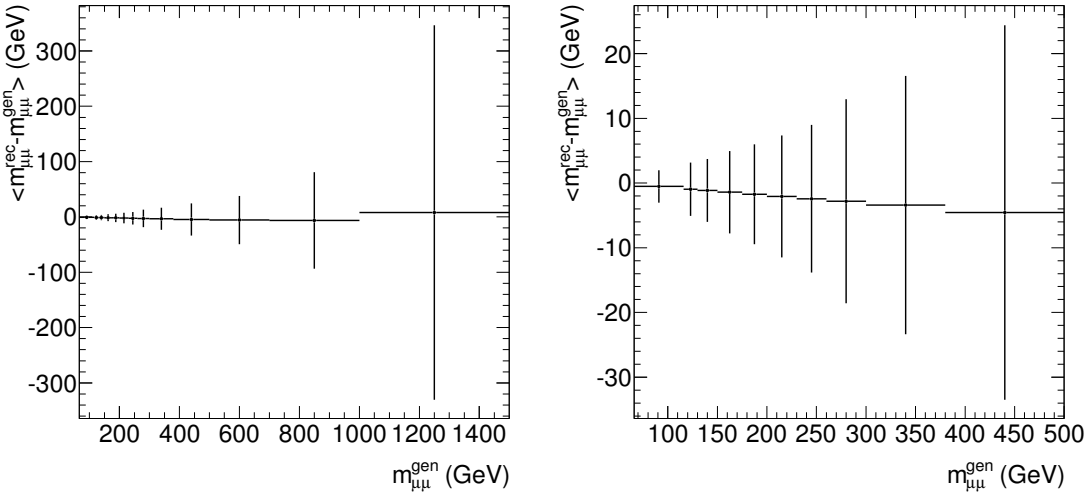

Figure 9.4.: Average ATLAS dimuon mass resolution as simulated by Drell-Yan MC in the complete mass range $66 < m_{\mu\mu} < 1500$ GeV (left) and zoomed in on the lower mass range $66 < m_{\mu\mu} < 500$ GeV (right). The error bars represent the RMS of the entries within each bin.

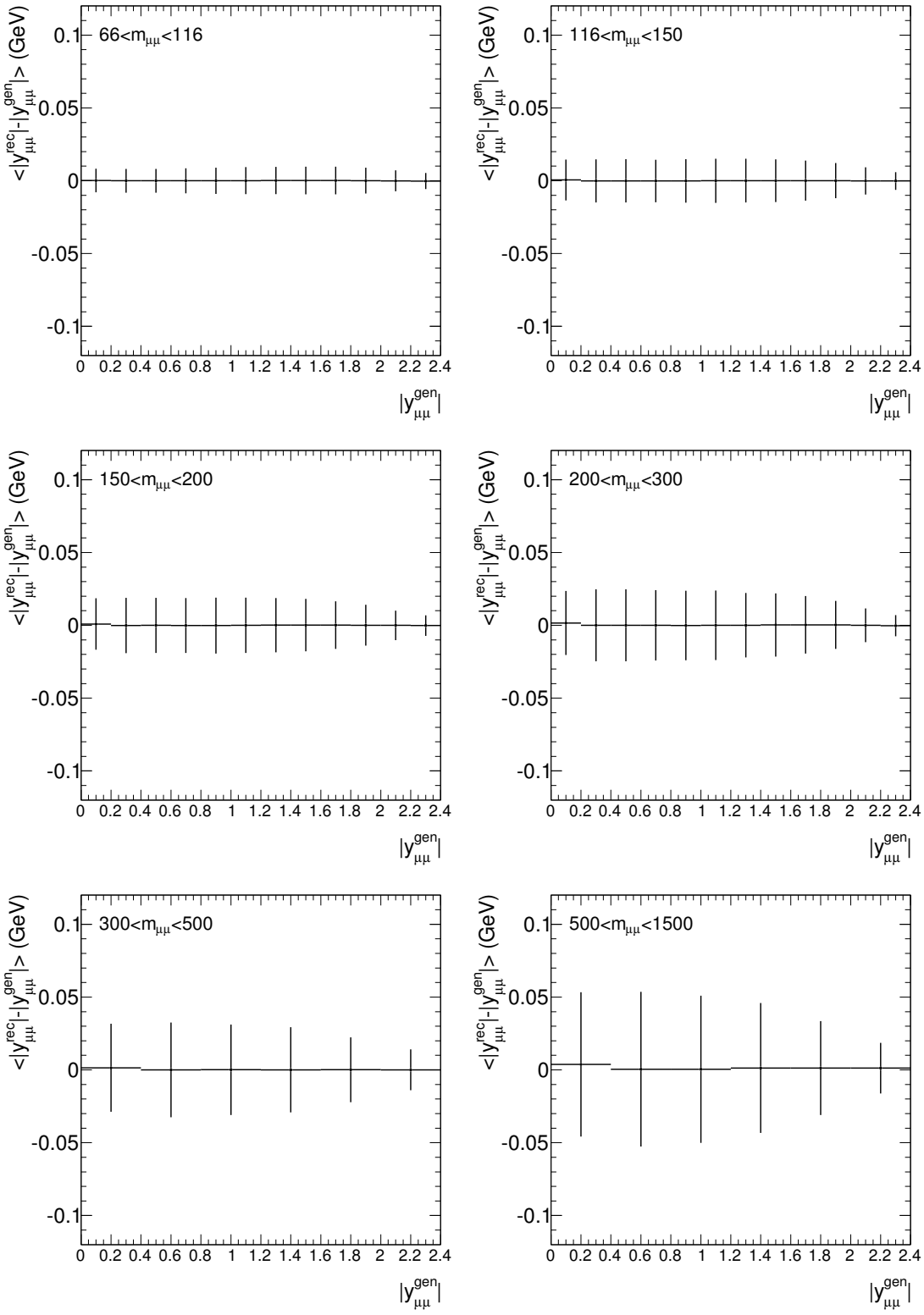

Figure 9.5.: Average ATLAS dimuon rapidity resolution as simulated by Drell-Yan MC in the 2D binning scheme for mass and rapidity. The error bars represent the RMS of the entries within each bin.

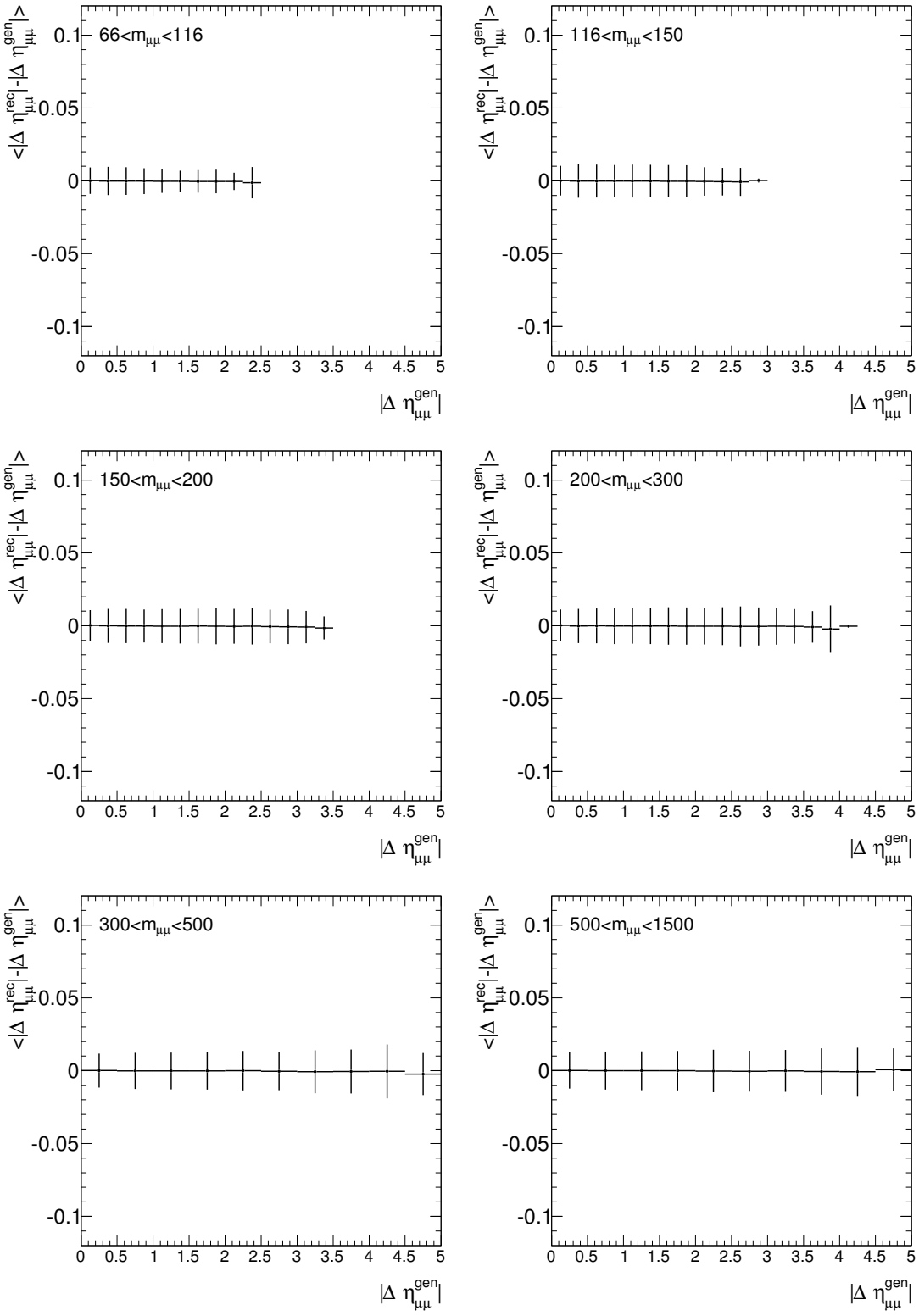

Figure 9.6.: Average ATLAS dimuon rapidity resolution as simulated by Drell-Yan MC in the 2D binning scheme for mass and $\Delta\eta$. The error bars represent the RMS of the entries within each bin.

9.2. Unfolding

The measurement of a physics process in a detector is subject to the resolution of that detector and any internal biases and distortions in the apparatus. For comparisons with theory, the data collected needs to be corrected back to a truth level state where the detectors distortions and biases are accounted for and removed. This process of correcting reconstruction level data to the truth level is called unfolding. In addition to correcting for the detector effects it is also useful to unfold to a common fiducial volume accessible by different analyses for comparison. For the high mass Drell-Yan analysis a common fiducial volume had to be chosen that allows for a measurement in the dimuon and dielectron channels. The common fiducial volume selected in this analysis is given in section 6.1.

The signal MC (Drell-Yan and PIP) is used to calculate the corrections to truth level by comparing the MC at the reconstruction and generation level selections. The exact bin migrations can then be given by the smearing matrix:

$$R_{ij} = \frac{\text{Probability(observed in bin j and true value bin i)}}{\text{Probability(true value bin i)}} \tag{9.7}$$

where R_{ij} gives the probability that the reconstruction level measurement is in bin i and the event was generated in bin j. The relationship between the truth and reconstruction level distributions can then be given as:

$$D_j = \sum_i R_{ij} T_i \tag{9.8}$$

where D_j is the reconstruction events in bin j and T_i is the generated truth level events in bin i. The inverse of the response matrix can be applied to the reconstructed data to recover the true distribution as follows.

$$T_i = \sum_j R_{ij}^{-1} D_j \tag{9.9}$$

It can be observed from equation 9.7 that the diagonal elements (where $i = j$) of the response matrix are just the stability introduced in equation 9.6. The response matrices for the three analysis cross section measurements are shown in figures 9.7, 9.8 and 9.9. The distributions clearly show that the response matrices are dominated by their diagonal

elements and this can be expected from the purity and stabilities shown in figures 9.1, 9.2 and 9.3.

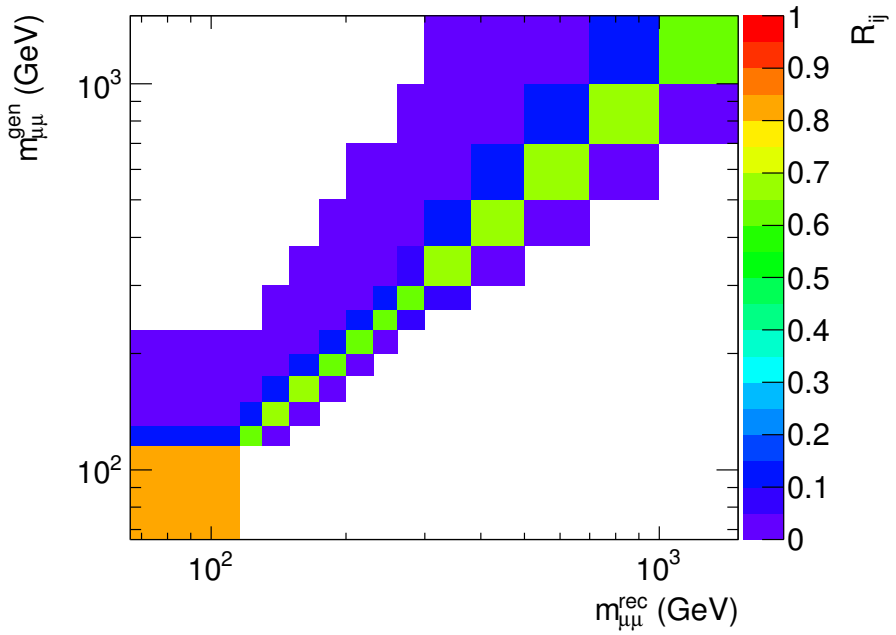

Figure 9.7.: Response matrix for the single differential dimuon mass measurement.

Due to the off diagonal elements being small, a simplified 1D version of the response matrix can be taken from the diagonal elements. Unfolding in 1D this way is called bin-by-bin unfolding and defines the correction value in each bin as:

$$C^i_{DY} = \frac{N^{rec}_i}{N^{gen}_i} \tag{9.10}$$

where N^{rec}_i is the number of events reconstructed in bin i and N^{gen}_i is the number of events generated in bin i. The detector resolution compared to the bin size is almost perfect but with the small but non zero off diagonal elements there will be a systematic uncertainty. This systematic uncertainty is measured by comparing the results obtained by bin-by-bin unfolding to that obtained using a method that uses the complete response matrix described in section 9.2.1.

In addition to any systematic uncertainty in the bin-by-bin method there will be an associated statistical uncertainty based the limited number of events in the signal MC. To calculate an uncertainty on C_{DY}, N_{rec} and N_{gen} have to be split into independent variables. The events recorded in a bin are either events that have been generated and reconstructed

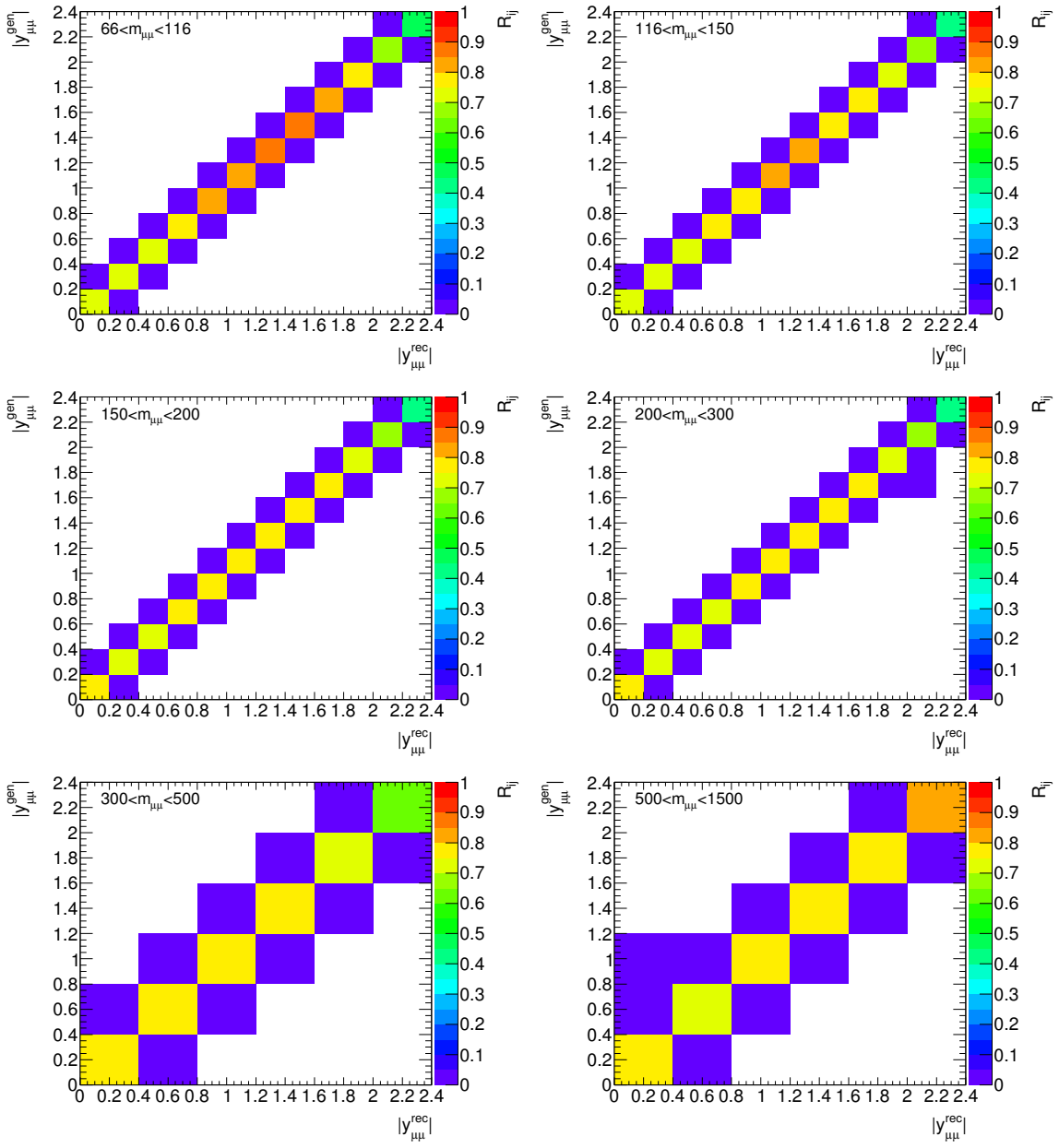

Figure 9.8.: Response matrix for the double differential dimuon mass and rapidity measurement.

in the same bin or events that have been generated in a different bin to the reconstructed bin. The C_{DY} factor can then be redefined as:

$$C_{DY} = \frac{N^{rec}_{stay} + N^{rec}_{come}}{N^{gen}_{stay} + N^{gen}_{leave}} \tag{9.11}$$

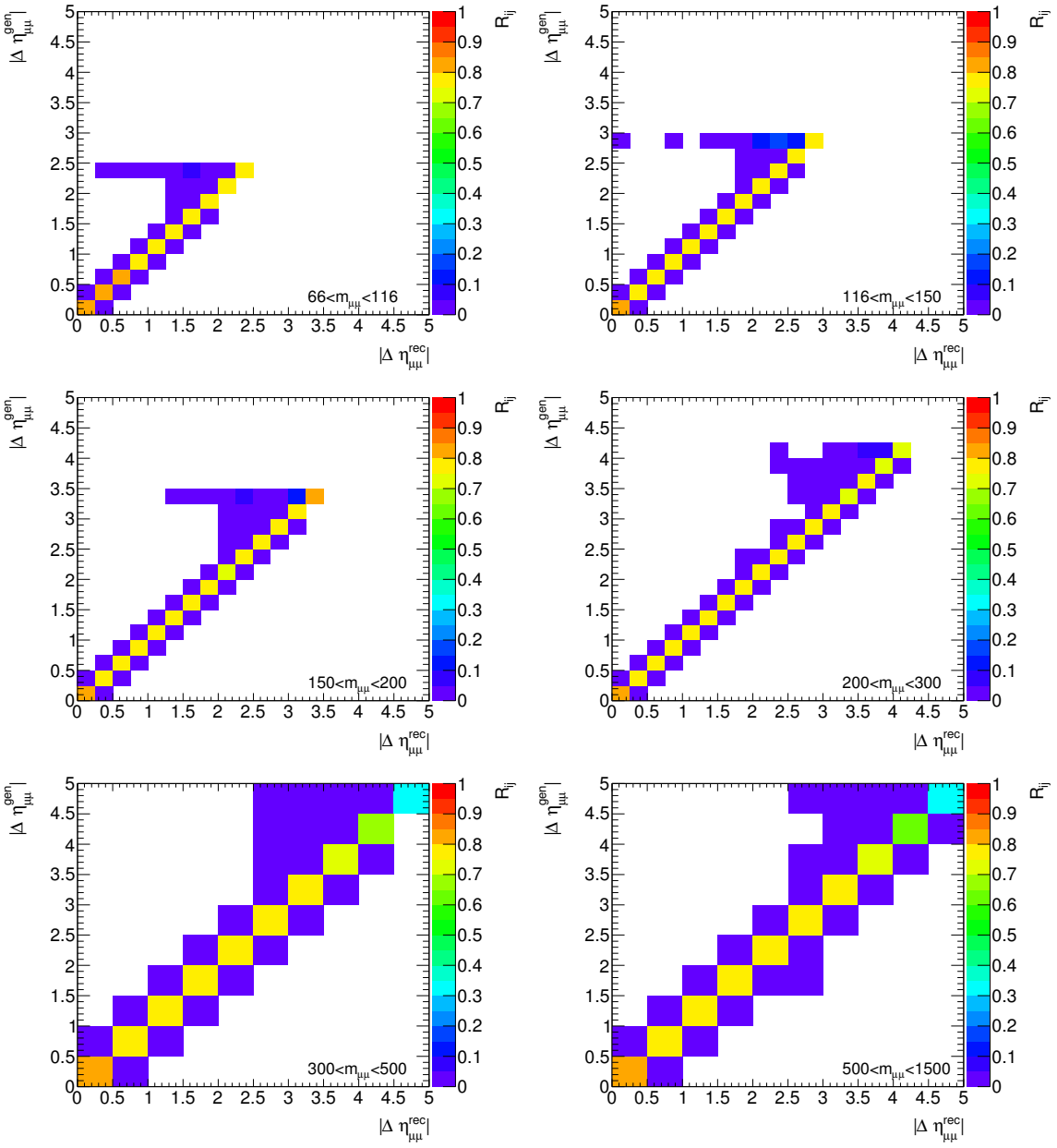

Figure 9.9.: Response matrix for the double differential dimuon mass and muon $\Delta\eta$ measurement.

where N_{stay} is the number of events that have been generated and then reconstructed in the same bin, N_{come} is the number of events that have come into the bin and N_{leave} is the number of events that have left the bin. The weights applied to the reconstructed events contain all of the same weights as the generator level with the addition of weights applied to correct for the trigger, isolation and muon reconstruction. These additional weights

are to a good approximation equal to unity as shown in figures 6.26,6.12 and 6.7, so the assumption $N^{rec}_{stay} = N^{gen}_{stay} = N_{stay}$ can be made. Propagating the relative uncertainties, as shown in the following reference [52], the total statistical uncertainty on C_{DY} can be expressed as:

$$(\Delta C_{DY})^2 = \frac{(N^{gen} - N^{rec})^2}{(N^{gen})^4}(\Delta N_{stay})^2 + \frac{1}{(N^{gen})^2}(\Delta N^{rec}_{come})^2 + \frac{(N^{rec})^2}{(N^{gen})^4}(\Delta N^{gen}_{leave})^2 \quad (9.12)$$

The C_{DY} factor for the high mass Drell-Yan analysis is given figures 9.10, 9.11 and 9.12. Figure 9.10 in addition shows the C_{DY} factor if the PIP MC is not included. As the PI contribution is small this factor has a small effect of below 1.3% for the entire analysis phase space.

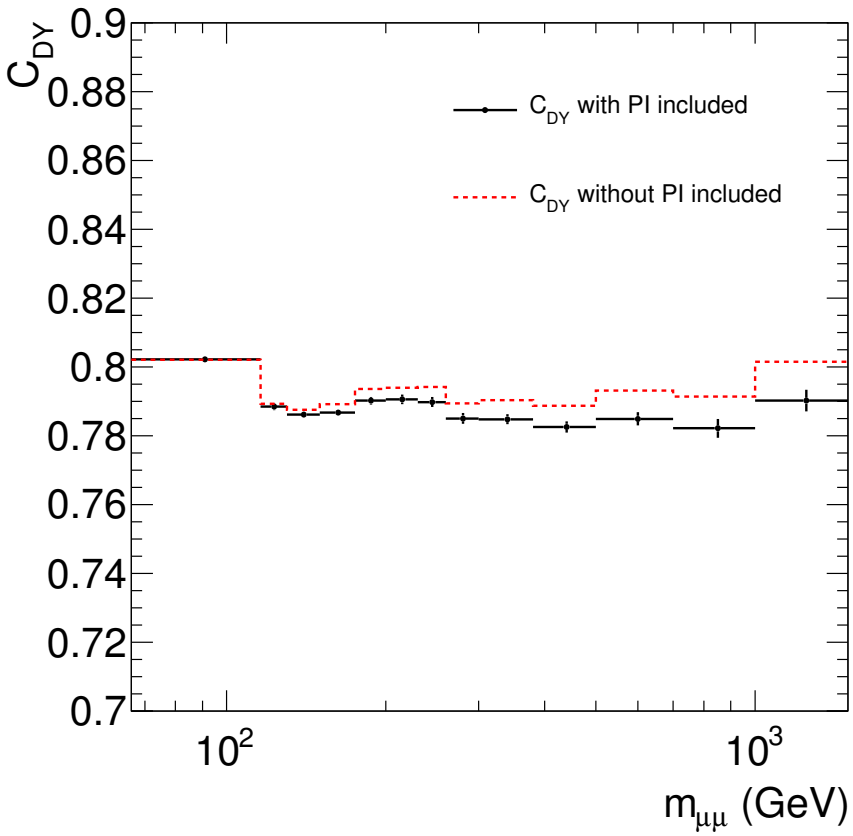

Figure 9.10.: Bin-by-bin unfolding factor C_{DY} for the single differential measurement.

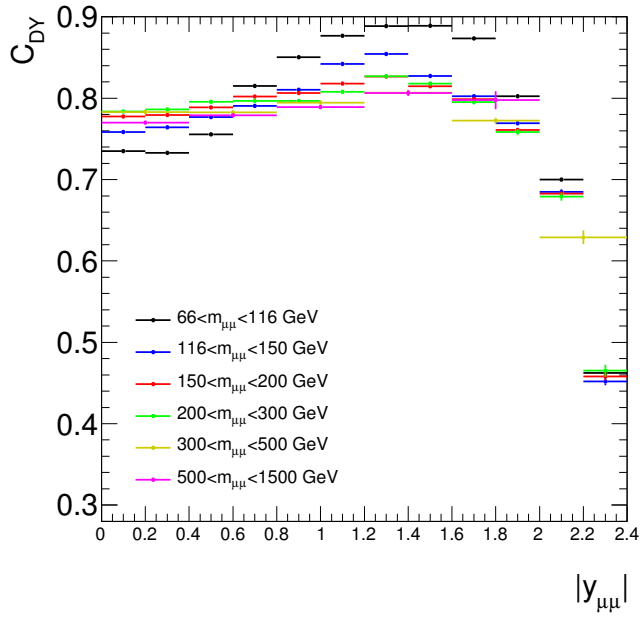

Figure 9.11.: Bin-by-bin unfolding factor C_{DY} for the double differential mass and rapidity measurement.

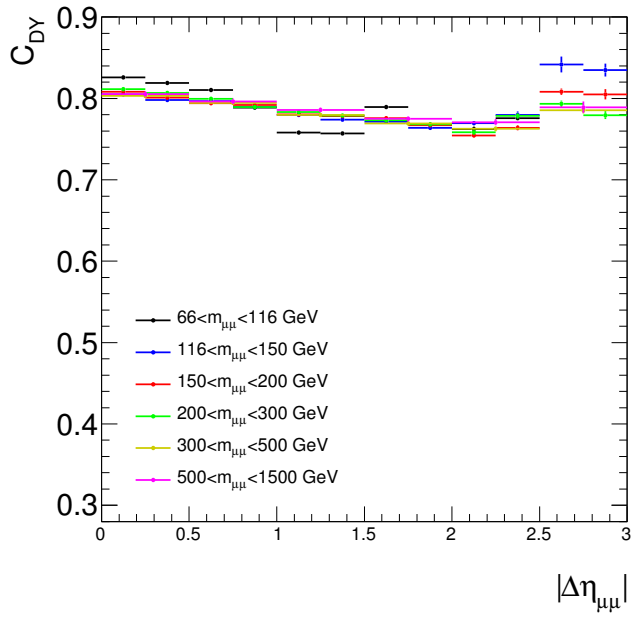

Figure 9.12.: Bin-by-bin unfolding factor C_{DY} for the double differential mass and $\Delta\eta$ measurement.

9.2.1. Alternative Unfolding Comparison

As discussed in the previous section, applying a bin-by-bin unfolding neglects the effect of large bin migrations and correlations occurring between adjacent bins. The assumption is that the low level of bin migrations will leave this systematic bias negligible. An additional unfolding technique has been studied to measure any effect on the fiducial cross section.

The alternative unfolding method used in this analysis is an unfolding technique based on Bayes theorem [53]. Bayes theorem can be derived from a sample space S containing two subsets A and B with conditional probability (on condition that $P(B) \neq 0$) of:

$$P(A|B) = \frac{P(A \cap B)}{P(B)} \tag{9.13}$$

The reverse of this equation must also hold:

$$P(B|A) = \frac{P(B \cap A)}{P(A)} \tag{9.14}$$

If the two subsets A and B are independent then:

$$P(A \cap B) = P(A)P(B) \tag{9.15}$$

and then it follows from equation 9.13 that $P(A|B) = P(A)$ and $P(B|A) = P(B)$. Bayes theorem can then given:

$$P(A|B) = \frac{P(B|A)P(A)}{P(B)} \tag{9.16}$$

If the sample space S is a sum of several independent subsets A_i then the law of total of probability:

$$P(B) = \sum_i P(B|A_i)P(A_i) \tag{9.17}$$

can be combined with equation 9.16 to rewrite Bayes theorem as:

$$P(A_i|B_j) = \frac{P(B_j|A_i)P(A_i)}{\sum_k P(B_j|A_k)P(A_k)} \tag{9.18}$$

where the sample space is also a sum of several independent subsets B_j. The equation applied experimentally just means that the probability of the B outcome in bin j being a result of the A cause in bin i is proportional to the product of the probability of A_i and the probability that A_i will cause B_j. If n B events are observed then the relation to the cause A can be written as:

$$n(A_i) = n(B_j)P(A_i|B_j) \tag{9.19}$$

where this equation mirrors exactly equation 9.9 with the inverse of the response matrix R_{ij} being equivalent to $P(A_i|B)$. Equation 9.18 can now be written in terms of the reconstruction and truth level quantities as follows:

$$R_{ij}^{-1} = P(T_i|D_j) = \frac{P(D_j|T_i)P_0(T_i)}{\sum_k P(D_j|T_k)P_0(T_k)} \tag{9.20}$$

where $P_0(T_i)$ is the prior probability of the truth event occurring in bin i. The denominator of the equation is just a normalisation factor so one can draw the conclusion:

$$R_{ij}^{-1} \propto P(D_j|T_i)P_0(T_i) = R_{ij}P_0(T_i) \tag{9.21}$$

which means the unfolding can be achieved with the calculable response matrices given the prior probabilities. This however has the same problem as the bin-by-bin unfolding as the truth level prior probability will have a large effect on the unfolded distributions. To combat this bias an iterative process is applied whereby the result of applying the bayesian unfolding T_i (also called the posterior probability) is used to replace the prior probability of the next iteration.

The iterative Bayesian unfolding has been applied using the RooUnfold package [54] and the fiducial cross sections are compared to the bin-by-bin method in figures 9.13, 9.14 and 9.15. As expected due to the low bin migrations, the difference between bin-by-bin unfolding and iterative bayesian unfolding is small and well below the statistical uncertainty on the data. For the largest mass mass bin in the single differential measurement there is a 10% deviation between the two methods but as this bin has only a handful of events this effect is likely largely statistical. Any systematic uncertainty on the cross section measurement coming from the unfolding technique is considered negligible and not included.

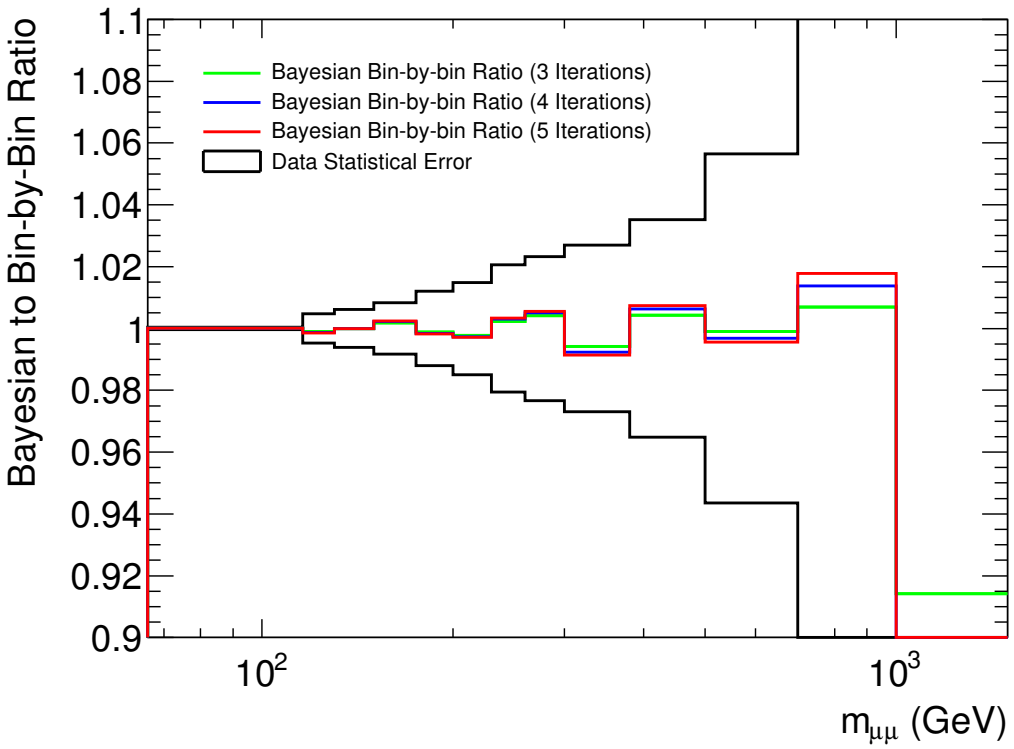

Figure 9.13.: Ratio between the final cross section unfolded with the standard bin by bin unfolding method and a bayesian unfolding method.

9.3. Cross Section Uncertainties

Uncertainties on the measured cross section arise from the determination of performance SFs, estimation of the backgrounds and theory based corrections and unfolding. The systematic uncertainties arising from the determination of performance scale factors are calculated by shifting the per event scale factors by the calculated uncertainty and observing the effected on the fiducial cross section. Shifting the scale factors can effect both the C_{DY} factor and the estimated background B given in the cross section equations 9.1, 9.2 and 9.3. The systematic uncertainty arising from the background contamination is determined by shifting the total level of background up and down by the associated uncertainties and again observing the effect on the fiducial cross section. The value of each systematic uncertainty is calculated as an average as follows:

$$\Delta\sigma_i = \frac{|\sigma_i - \sigma_i^+| + |\sigma_i - \sigma_i^-|}{2} \tag{9.22}$$

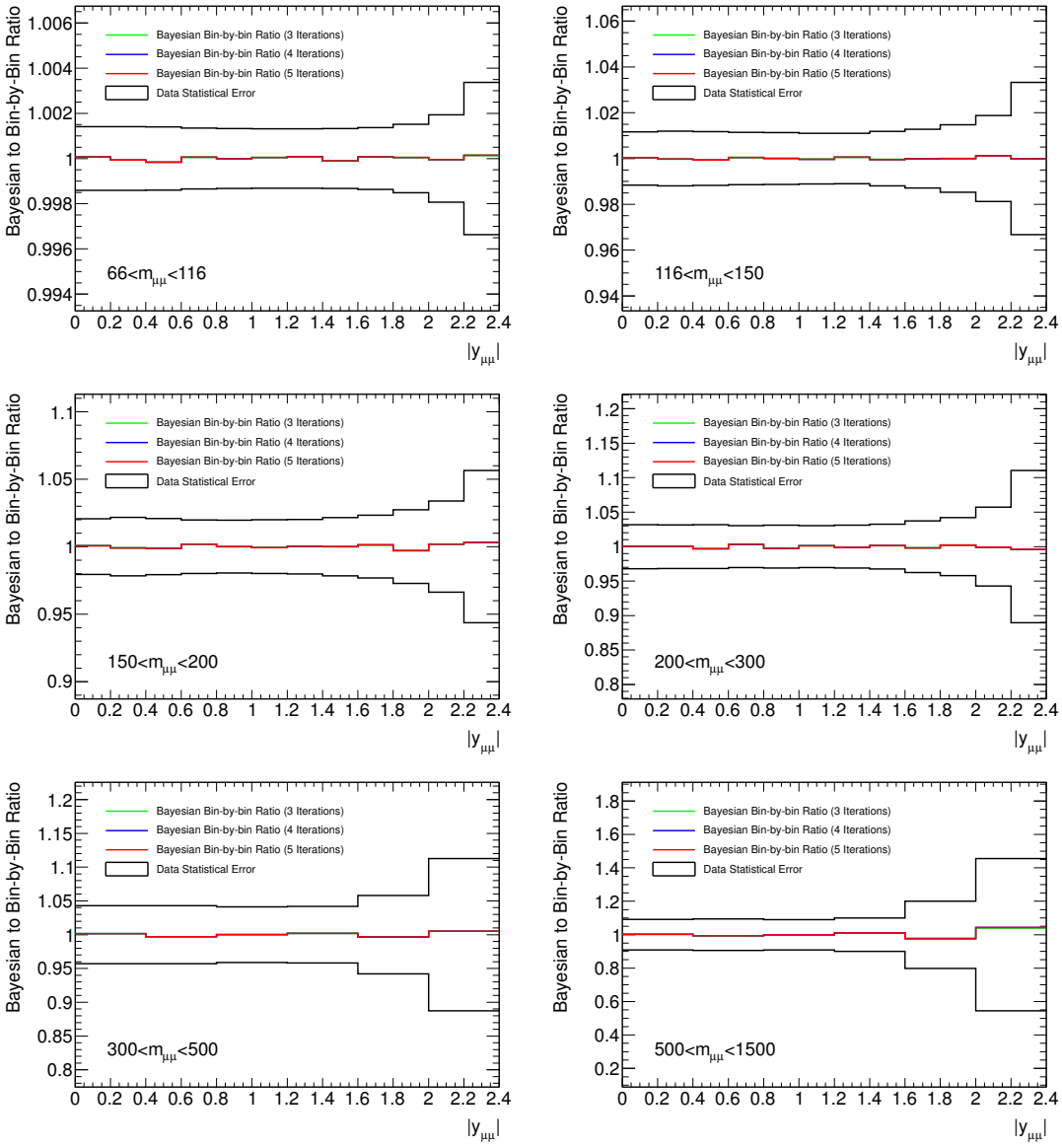

Figure 9.14.: Ratio between the final cross section unfolded with the standard bin by bin unfolding method and a bayesian unfolding method.

where σ_i is the central fiducial cross section, σ_i^+ is the upward shifted cross section and σ_i^- is the downward shifted cross section in bin i. The theory based uncertainties are considered by comparing the effect different MC models and unfolding techniques have on the fiducial cross section.

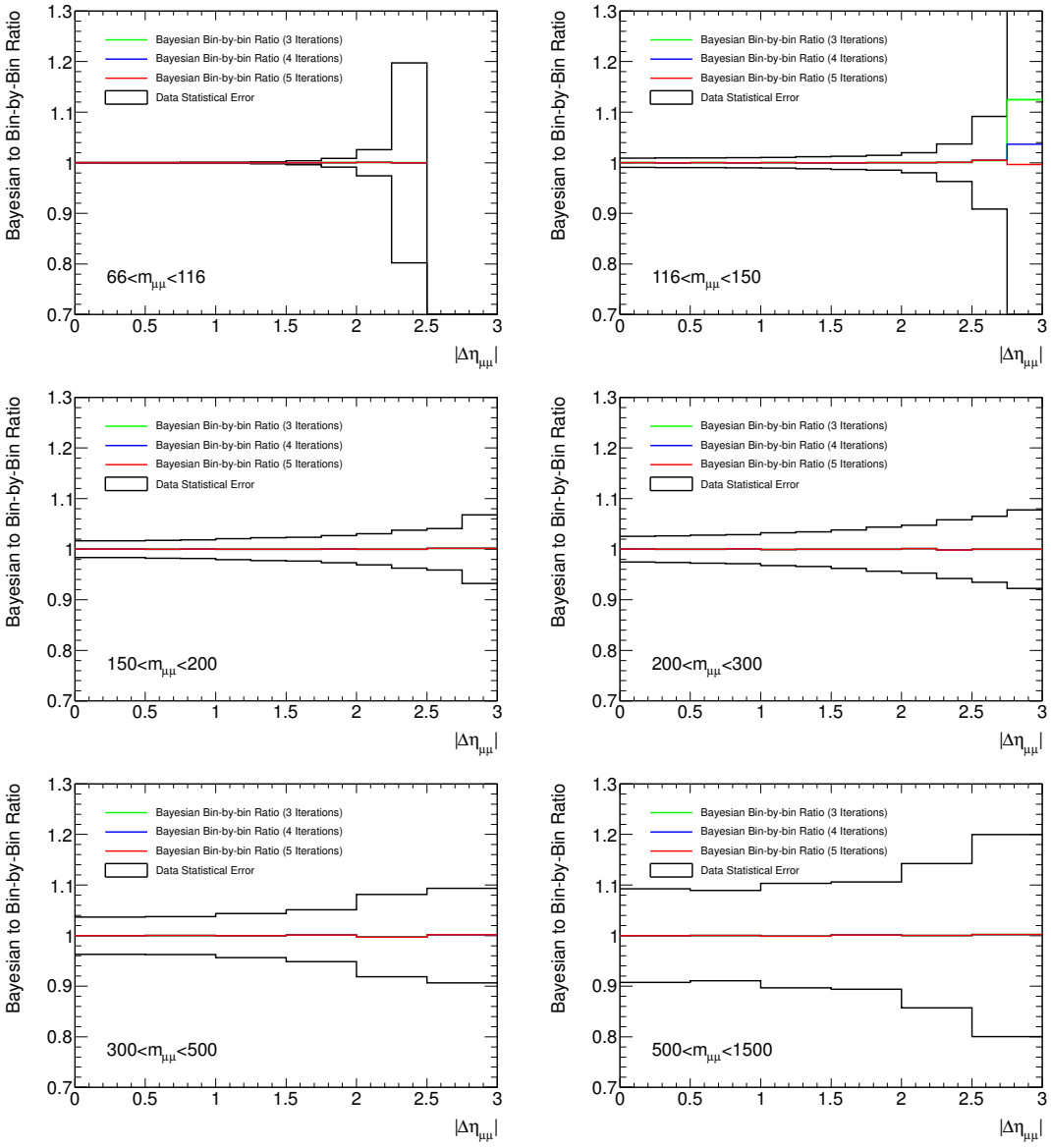

Figure 9.15.: Ratio between the final cross section unfolded with the standard bin by bin unfolding method and a bayesian unfolding method.

The standard statistical uncertainty in each bin i of a distribution is given by:

$$\Delta_i^{stat} = \sqrt{N_i} \tag{9.23}$$

where N_i is the population of bin i. However this relationship only holds when the weights applied to the entries in this distribution are unity as in the case for data. For the MC the weights applied by the muon performance SFs have to be considered and the equation

becomes:

$$\Delta_i^{stat} = \sqrt{\sum_j (w_i^j)^2} \tag{9.24}$$

where w_i^j is the jth weight in bin i and the sum is over all of the weights j within bin i. Statistical uncertainties in distributions that are used to create performance SFs or estimate backgrounds are propagated to create statistically shifted SFs and backgrounds. Observing the effect these shifted results have on the fiducial cross section allows a statistical uncertainty to be determined. For the trigger and muon reconstruction SF a more rigorous approach to determining statistical uncertainties is used called the toy MC method. This is described in section 9.3.1. The total uncertainty on the cross sections is calculated as a quadratic sum of all of the systematic and statistical uncertainties.

9.3.1. Toy MC Method

The trigger efficiency and muon reconstruction efficiency scale factors are parameterised in terms of η-ϕ-charge and as such have some regions where there is only a few events in each two dimensional bin. Using the SF shifting method described above can result in large statistical uncertainties on the fiducial cross section. As statistical uncertainties are uncorrelated an additional more rigorous method is used to calculate the statistical component of the uncertainties called the toy MC method. The toy MC method creates N_{toy} toy SFs that are randomly created along a gaussian distribution centred on the central SF, with the statistical uncertainty calculated from equation 9.24 used as the gaussian width. A distribution showing the difference between the toy MC SFs W^i and the central SF W^0 for one single event is shown in for the trigger and reconstruction SFs in figure 9.16. This one event shows that the difference between the toy SFs and the central value is very small and this behaviour is mirrored throughout the analysis phase space. This method correctly propagates the statistical component of the systematic uncertainties ensuring no correlation between bins.

The toy SFs when applied to the MC produce N_{toy} fiducial cross sections which are then compared to the cross section obtained from the central value SFs. The RMS of the toy cross sections is then taken as the statistical uncertainty on the cross section. The RMS of the SFs in the single event shown in figure 9.16 are very small and this behaviour is duplicated in the uncertainty on the fiducial cross section.

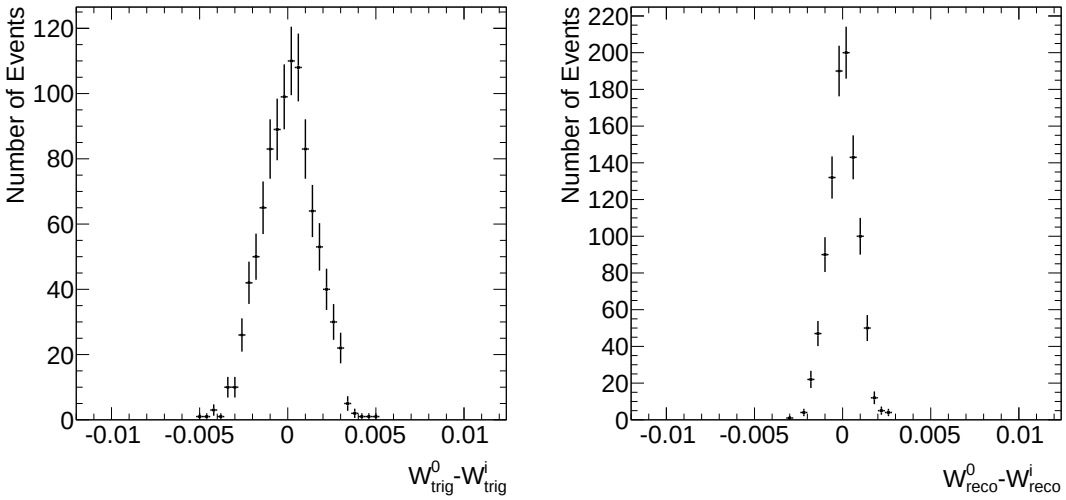

Figure 9.16.: Distriubutions show the difference between the toy MC SF and the central value for the trigger(left) and reconstruction (right) SFs for one individual Drell-Yan MC event. A total of 1000 toys were used to make this plot.

9.3.2. Systematic Uncertainties

The systematic uncertainties considered in this analysis are listed below. Figures 9.17, 9.18 and 9.19 show the systematic uncertainty in percent on the cross section in the single differential, double differential dimuon mass and rapidity and double differential dimuon mass and muon $\Delta\eta$ measurements.

- **Trigger:** The trigger SFs used in the analysis are calculated in a dedicated performance study described in section 6.3.5. Sources of systematic uncertainties that are considered include a background contamination systematic, event topology systematic and a p_T dependence systematic. The difference between cross sections calculated using the nominal and shifted SFs is used to calculate the systematic uncertainty using equation 9.22. The statistical part of the uncertainty is determined using the toy MC method described in section 9.3.1 The systematic part of the trigger uncertainty is 0.1% or below for the kinematic range. The statistical part of the uncertainty is negligible, contributing less 0.01% uncertainty.

- **Muon Reconstruction:** The muon reconstruction efficiencies are provided by the MCP group and are calculated using a tag and probe method. The efficiencies are determined in the MS and ID detectors separately and then are combined to provide muon reconstruction scale factors as described in section 6.3.3. Shifted scale factors

are also provided and can be used to calculate the systematic uncertainty on the cross section. The statistical part of the uncertainty is calculated using the toy MC method. The systematic part of the muon reconstruction uncertainty is one of the larger uncertainties ranging from 0.4% at lower mass to around 1.0% at higher masses. The statistical part of the muon reconstruction uncertainty is negligible at below 0.02%.

- **Isolation:** The isolation scale factors are determined in terms of muon p_T using a tag and probe method. Uncertainties regarding the background contamination, event topology and muon η variation are considered and described in section 6.3.4. Shifted scale factors are determined using a combination of these uncertainties with the effect on the cross section giving the total isolation systematic uncertainty. The systematic and statistical uncertainties are combined for this particular uncertainty and the total uncertainty is below 0.3% for $m_{\mu\mu} < 300$ GeV rising to 0.5% at the very highest dimuon masses.

- **MS and ID Resolutions:** The MS and ID resolution systematics are provided by the muon combined performance group and are calculated by adjusting the muon momentum smearing for the muon spectrometer and inner detector parts individually. These systematics are below 0.2% in the higher statistic region of lower dimuon mass and more central rapidity and $\Delta\eta$. The systematic can reach 0.8% in the kinematically less favourable regions.

- **Momentum Scale:** The muon momentum scale corrections, described in section 6.3.2 have an associated systematic that is provided by the muon combined performance group. This systematic is below 0.3% for all but the larger rapidity and $\Delta\eta$ bins.

- **Electroweak Background:** The electroweak backgrounds are predicted using MC. The associated theoretical uncertainties on the cross section and k-factors of the samples are estimated to be 5% for the electroweak backgrounds and 6% for the $t\bar{t}$ and single top production backgrounds [7–9, 42–51]. The statistical uncertainty from the finite size of the MC samples is also included in this error but is subdominant. This is the analysis largest systematic and contributes up to 2.0% in the 2D analysis in the region $150 < m_{\mu\mu} < 500$ GeV.

- **Multi-jet Estimation:** The multi-jet estimation is predicted using a data driven method described in section 7.1.2. For the one dimensional dimuon mass measurement

the systematic comes purely from the normalisation factor calculated using the ABCD method. For the two dimensional measurements there is an additional systematic arising from the multi-jet rapidity or $\Delta\eta$ shape determination. The associated statistical uncertainties are combined with the systematics. For the $m_{\mu\mu} > 500$ GeV region the multi-jet estimation is made as an extrapolation of the lower mass region. The uncertainty in this region is calculated by adjusting the dominant electroweak background subtraction systematic by one standard deviation and observing the effect on the extrapolation. The multi-jet estimation provides one of the larger systematics but is below 1.0% for $m_{\mu\mu} < 300$ GeV and reaches up to 2.6% at the statistically limited higher mass region.

- **Drell-Yan Signal MC Statistic:** The uncertainty from the limited number of simulated events for the signal MC when determining the C_{DY} factor. The uncertainty calculation is explained in section 9.2. This systematic is below 0.4% for all regions where the signal is not kinematically limited.

- **Drell-Yan Signal MC k-Factor:** The NNLO k-Factors are taken from a dilepton mass dependent function that corrects NLO Powheg Pythia8 Drell-Yan MC to a calculation of using FEWZ MSTW2008. The associated systematic uncertainty is found to be negligible.

- **Drell-Yan MC Boson p_T Reweighting:** The Z/γ^* p_T spectrum is not well described by the Drell-Yan signal MC, as shown in figures 8.4, 8.10 and 8.13. This results in a poor description of the muon p_T seen in figures 8.2, 8.8 and 8.11. This mismodelling could effect the cross section through changes to the shape of the C_{DY} unfolding factors. The signal MC was reweighted to match the Z/γ^* p_T spectrum of the data and the C_{DY} factor recalculated. The effect on the cross section was found to be below 0.1% for almost the entire phase space with a few fluctuations above this value in regions of low statistics. Therefore the associated systematic is considered negligible and not included in the uncertainty calculation. Further details on this study are shown in appendix B.

- **Unfolding:** The bin-by-bin unfolding method used in this analysis is compared to an iterative Bayesian unfolding technique provided by the RooUnfold package as explained in section 9.2.1. As the effect of the unfolding technique on the cross section is negligible, this systematic is not included in the total uncertainty.

- **Generator:** To account for any MC model dependences when calculating the C_{DY} factor used for the unfolding, an additional Drell-Yan MC can be compared to the nominal Drell-Yan sample. At this time alternative MC samples are unavailable for the dimuon channel but preliminary conclusions can be drawn from the equivalent dielectron Drell-Yan analysis (the same fiducial selection is used) [55]. The alternative MC compared uses MC@NLO for the matrix element calculation and Herwig++ for the parton shower and QED FSR models. The ratio of the C_{DY} factor calculated using the alternative MC to that calculated using the nominal MC is shown in figures 9.20, 9.21 and 9.22, for the single differential, double differential dilepton mass and rapidity, and double differential dilepton mass and $\Delta\eta$ measurements respectively. The figures show that for the dielectron analysis changing the matrix element, parton shower and QED FSR model has no effect on the C_{DY} factor to within the statistical uncertainties and as such the generator systematic can be neglected. The differences between the models in terms of the matrix element calculation and parton shower are largely lepton flavour independent, so the same conclusion can be drawn for these components of the dimuon channel generator systematic. The QED FSR component of the systematic in the two channels will differ only in the lepton mass effects. The PHOTOS QED FSR model used in this analysis has been validated against SANC [56] and found to have a systematic uncertainty of less than 0.2% [57]. The generator systematic is not currently included in the total uncertainty of the measurement pending a more dedicated study.

- **Luminosity:** The uncertainty on the determination of the luminosity is given as 2.8% by ATLAS for 2012. This is determined using the same method as that described in Ref. [58] but using data obtained from beam separation scans in November 2012. This uncertainty is not included in the plots and by convention not included in the total uncertainty quoted in the tables.

For the single differential measurement the largest systematic uncertainties originate from the background estimations. The electroweak backgrounds predicted by MC dominate the uncertainties for the $m_{\mu\mu} < 500$ GeV region. The distribution on the right of figure 9.17 shows the individual background contributions to the total electroweak background. The systematic component of the top MC systematic dominates for the $m_{\mu\mu} < 500$ GeV region where the electroweak is the largest systematic. For the $m_{\mu\mu} > 500$ GeV region the multi-jet estimation is the largest systematic and this originates from the extrapolation of

the estimation described in section 7.1.2. However the statistical uncertainty on the data is much larger than the systematic components in the $m_{\mu\mu} > 380$ GeV region.

For the double differential measurements the largest uncertainty in the $66 < m_{\mu\mu} < 116$ GeV bin originates from the muon reconstruction efficiency. The good level of statistics within this bin as well as the fact that most performance SFs are calculated in this bin result in the total uncertainty being below 0.5% for the full rapidity region and the central $\Delta\eta$ region. For the $200 < m_{\mu\mu} < 500$ GeV region the electroweak background systematic is the largest as seen in the 1D measurement. In the highest mass bin the statistical uncertainty on the data again dominates.

Tables listing the uncertainties shown in figures 9.17, 9.18 and 9.19 are shown in appendix C.

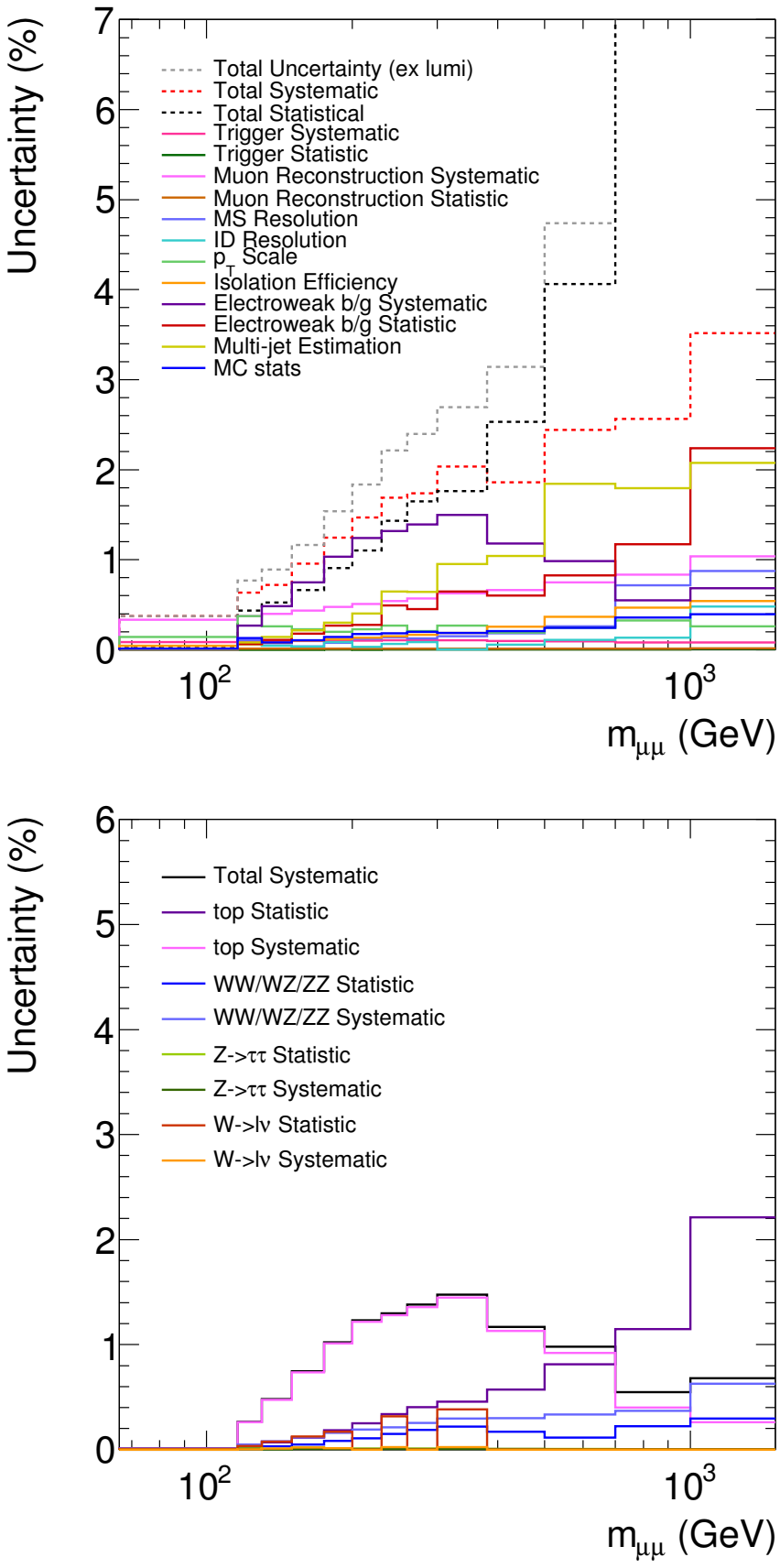

Figure 9.17.: The relative size of the considered systematic uncertainties on the 1 dimensional cross section measurement (left) and the breakdown of the MC background contributions to the electroweak background systematic (right).

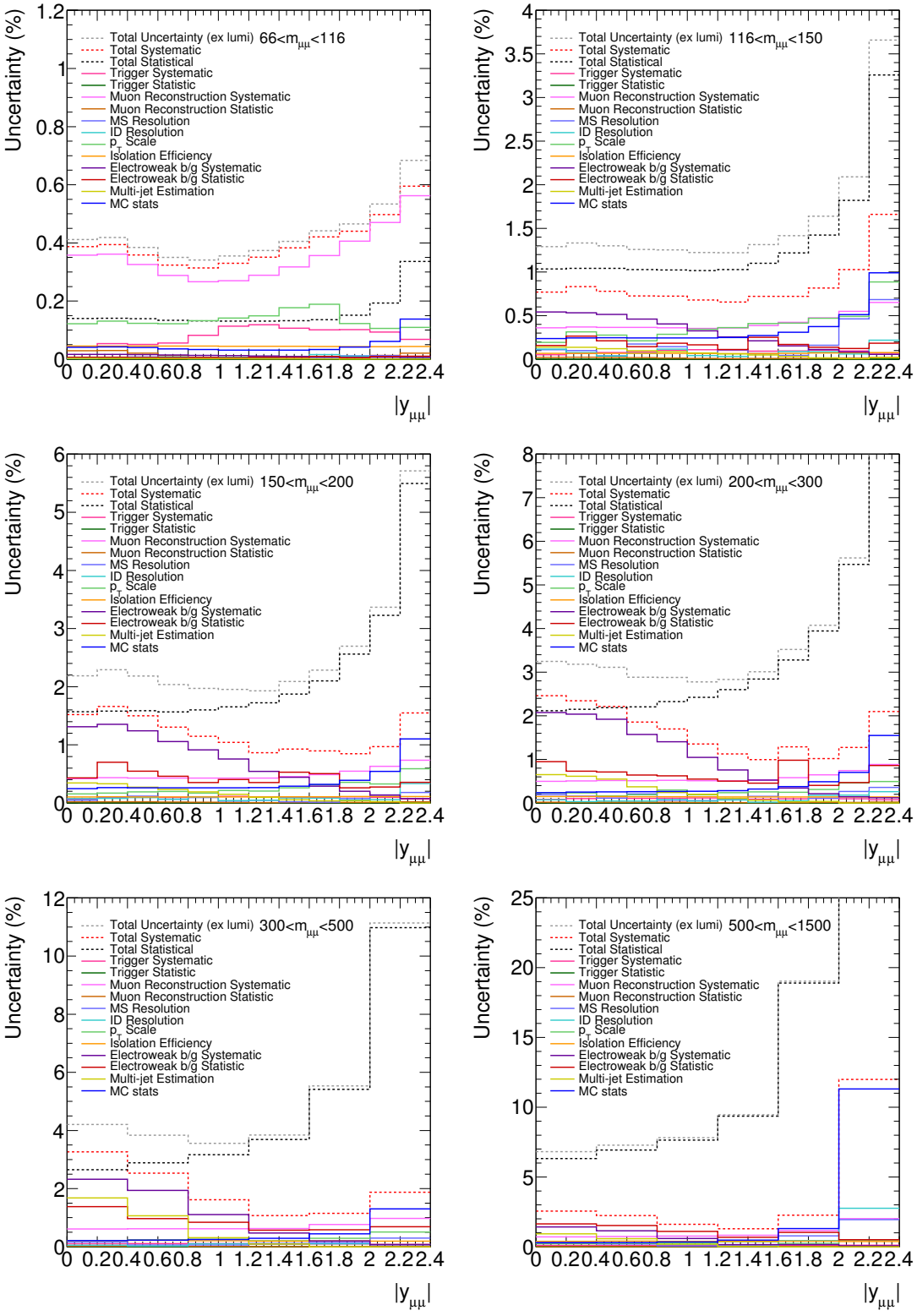

Figure 9.18.: The relative size of the considered systematic uncertainties on the 2 dimensional $|y_{\mu\mu}|$ cross section measurement.

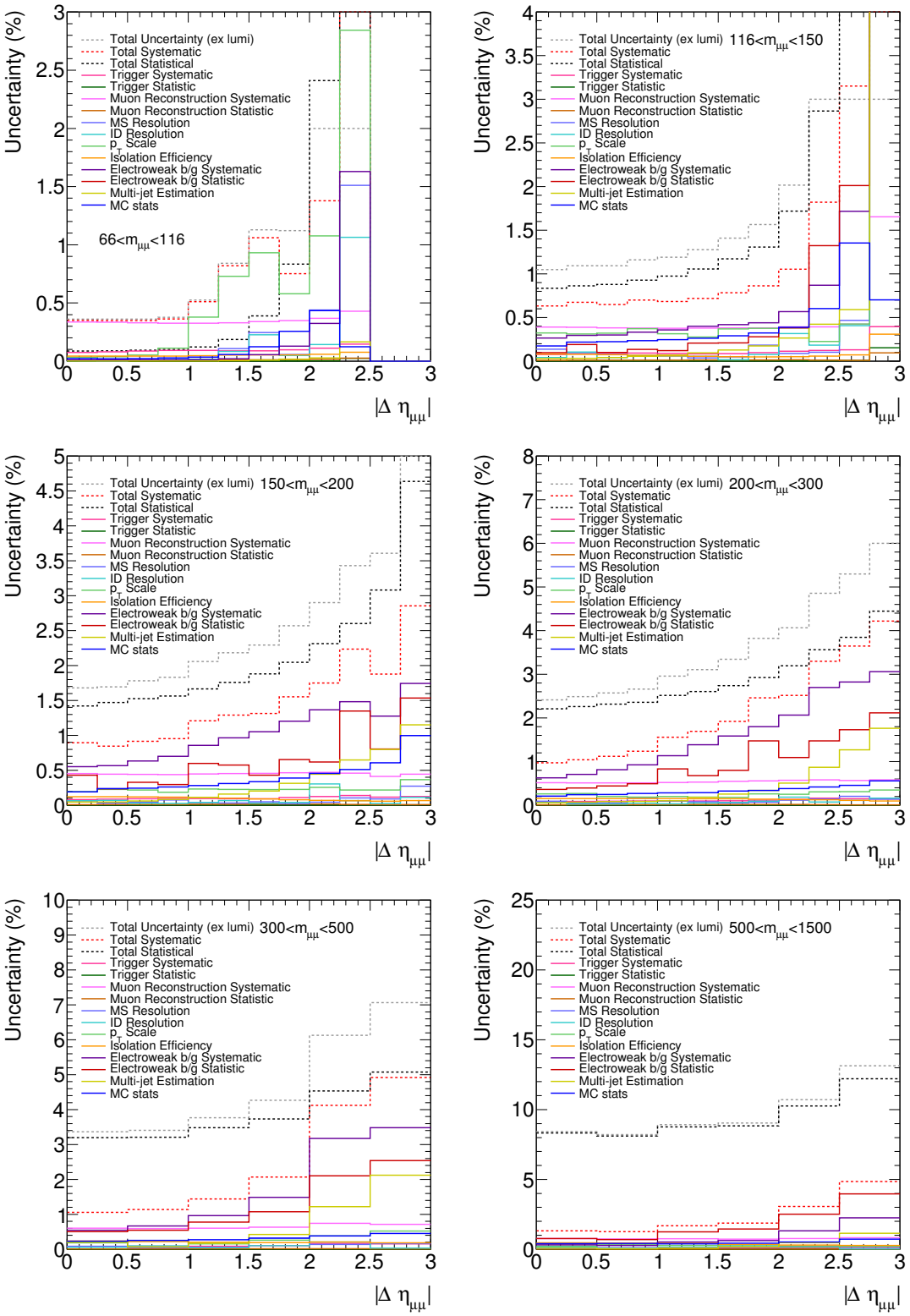

Figure 9.19.: The relative size of the considered systematic uncertainties on the 2 dimensional $|\Delta\eta|$ cross section measurement.

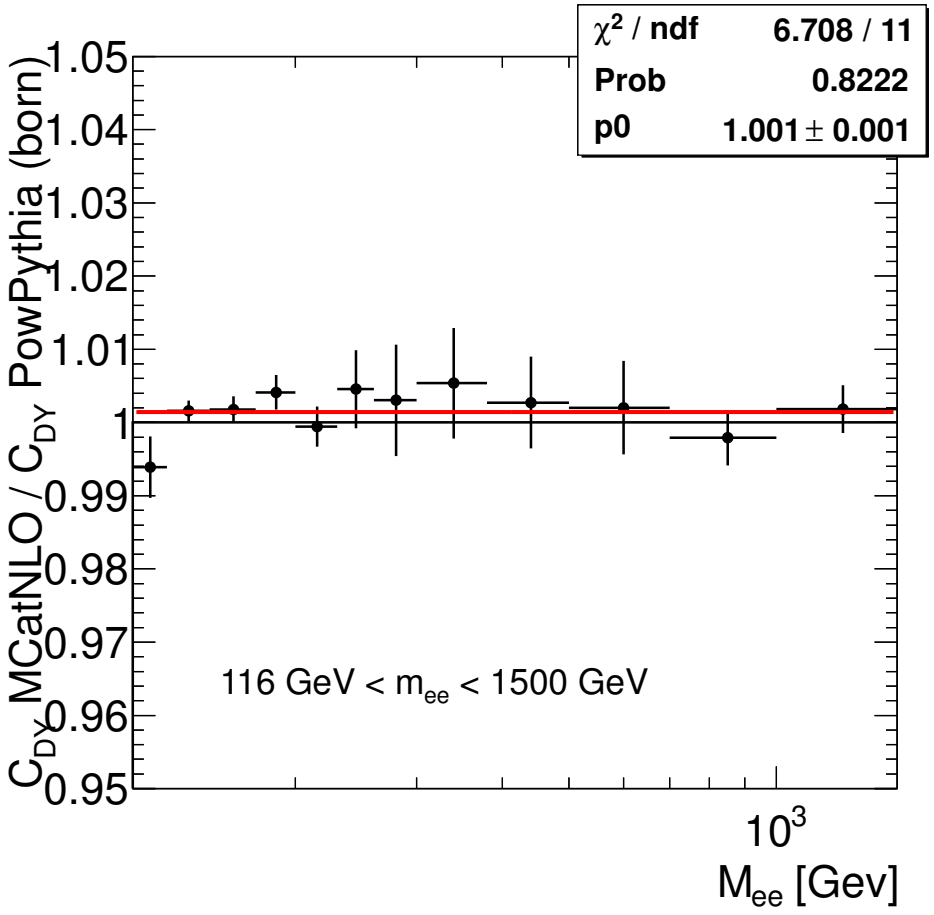

Figure 9.20.: Ratio between C_{DY} calculated with the alternative MC@NLO Herwig++ Drell-Yan MC to C_{DY} calculated with the nominal Powheg Pythia Drell-Yan MC for an equivalent dielectron analysis [55]. The red line shows the average ratio over the shown range.

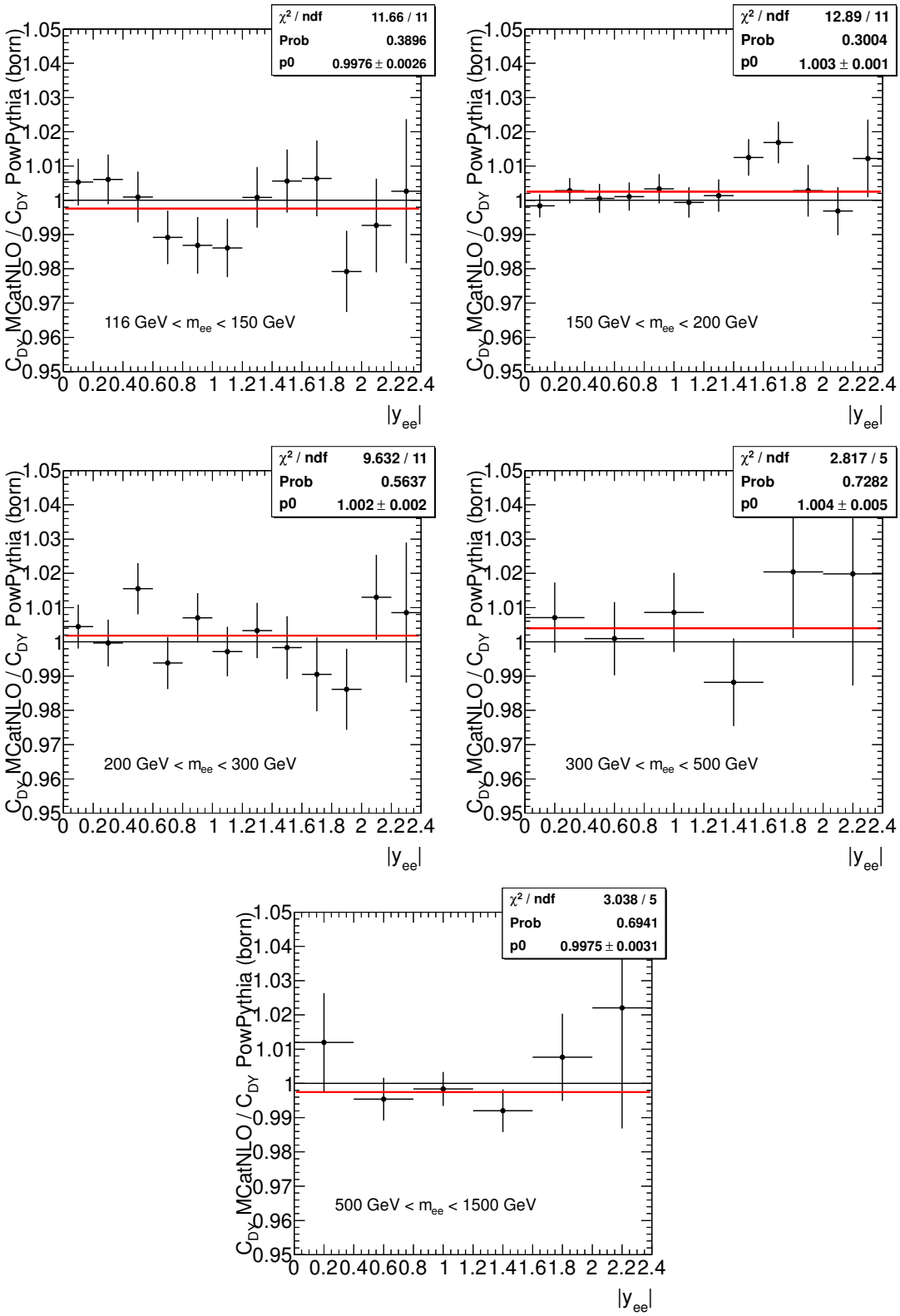

Figure 9.21.: Ratio between C_{DY} calculated with the alternative MC@NLO Herwig++ Drell-Yan MC to C_{DY} calculated with the nominal Powheg Pythia Drell-Yan MC for an equivalent dielectron analysis [55]. The red line shows the average ratio over the shown range.

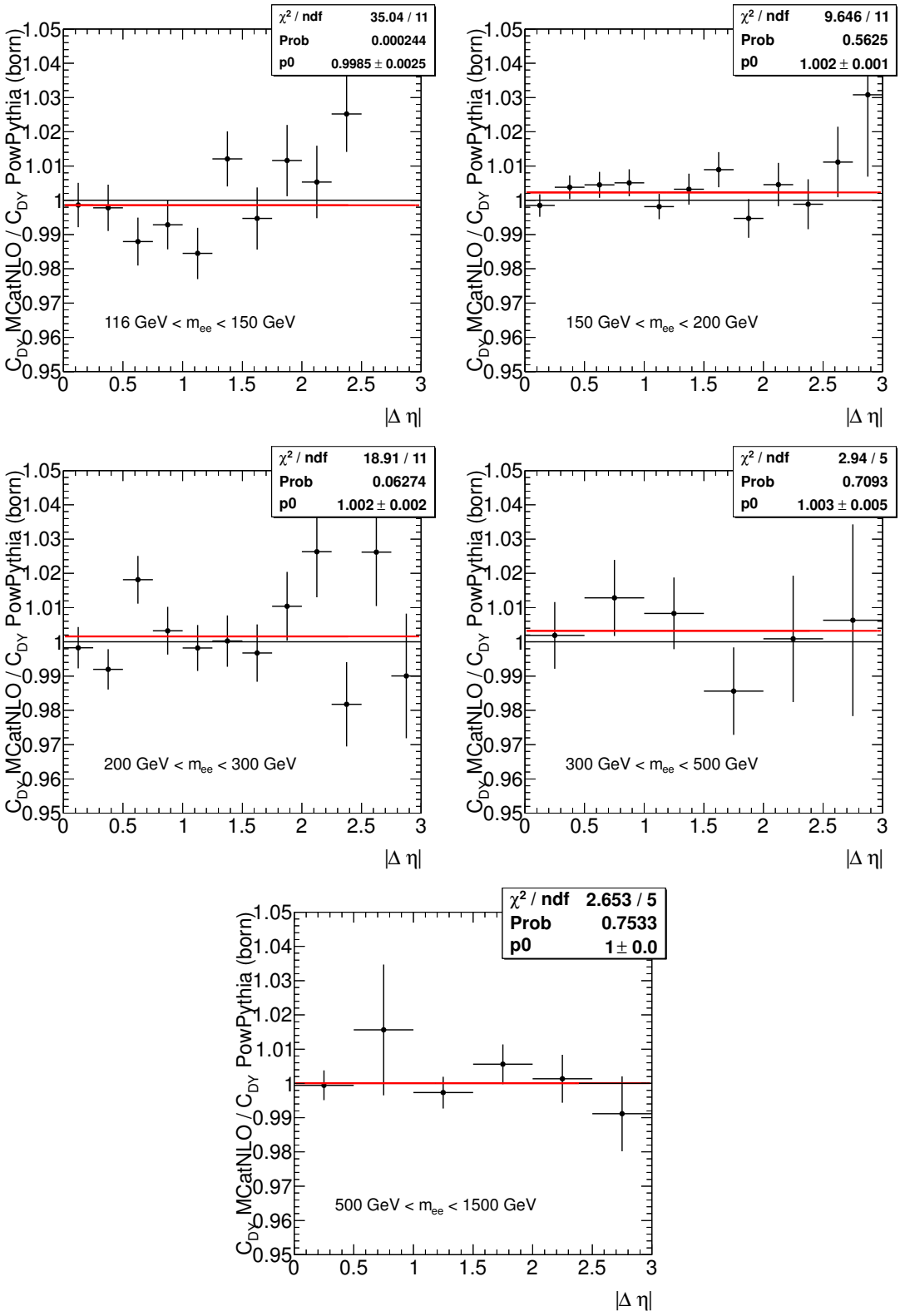

Figure 9.22.: Ratio between C_{DY} calculated with the alternative MC@NLO Herwig++ Drell-Yan MC to C_{DY} calculated with the nominal Powheg Pythia Drell-Yan MC for an equivalent dielectron analysis [55]. The red line shows the average ratio over the shown range.

9.4. Theoretical Predictions

The cross section results are compared to theoretical predictions made to NNLO in QCD by FEWZ [35]. The FEWZ program has be chosen as it allows computation of a NNLO prediction with applied kinematic limits. The photon induced contribution (Δ^{PI}) has also been predicted to NNLO using FEWZ and is observed to contribute between 2-3% on the cross sections. In addition to the NNLO prediction, higher order electroweak corrections (Δ^{HOEW}) are included to NLO. The HOEW corrections provide a description of the electroweak loop processes, the QED initial state radiation (ISR) and the interference between QED ISR and FSR. One part of the HOEW corrections that is not included is the corrections from the QED FSR. This part is already included in the signal MC using PHOTOS as described in section 5.2.1. The FSR models used in PHOTOS and using the SANC [56] program are shown to be in good agreement, validating the PHOTOS model.

The HOEW corrections are made using a electroweak parameterisation scheme G_μ that defines the electroweak theory in terms of precision variables such as α and the masses of the W and Z bosons. Calculations using SANC show that changes to this parameterisation scheme have a small effect on the corrections. The HOEW corrections are a small effect, reaching a maximum of 5% on the cross section at higher masses.

The PDF set used for the FEWZ calculation is CT10 NNLO PDF [8] and the uncertainties quoted are all at the 68% confidence limit. The renormalisation and factorisation scales are dynamically set to the dimuon mass of the interaction $\mu_R = \mu_F = m_{\mu\mu}$. The uncertainty originating from the choice of scale is predicted by adjusting the μ_R and μ_F scales within the range $0.5 \leq \mu_R/\mu_F \leq 2$ and taking the envelope of the results.

The dimuon high mass Drell-Yan analysis has been built with the dielectron channel in mind. In the dielectron channel the Z resonance region is not included as the multi-jet background estimation technique does not work in this region. As such the theoretical prediction have only been produced for $m_{\mu\mu} > 116$ GeV [59].

The Drell-Yan NNLO + NLO HOEW theoretical predictions for the differential fiducial cross sections are shown in tables in appendix D. The photon induced contributions to the cross sections are also shown in appendix D.

9.5. Fiducial Cross Sections and Conclusions

The Drell-Yan and photon induced fiducial cross sections are shown for the single differential, double differential dimuon mass and rapidity and double differential dimuon mass and muon $\Delta\eta$ measurements in figures 9.23, 9.24 and 9.25 respectively. Tables showing the cross section values are in appendix C. As seen with the control plots there is a normalisation difference between the data and theory.

The single differential measurement shown in figure 9.23 shows that this normalisation discrepancy varies around 2-3% for the complete dimuon mass range. The shape of the dimuon mass cross section is consistent with theory with a deviation in the highest mass bin likely due to low statistics at the edge of the kinematic limit. The total uncertainty (excluding the luminosity uncertainty) remains below 2.5% for the $m_{\mu\mu} < 300$ GeV region. The systematic and statistical uncertainties are below 2% in this region and that compares to a systematic and statistical uncertainty of around 5% for the 2011 7 TeV high mass Drell-Yan equivalent analysis [12].

For the double differential measurements again a normalisation issue is again seen but the shapes of the data and theory agree very well for the high statistic region of $m_{\mu\mu} < 300$ GeV and agree within the expected statistical fluctuations for the $300 < m_{\mu\mu} < 1500$ GeV region. There is one region with a slight data theory disagreement in the double differential dimuon mass and rapidity measurement. The deviation occurs at $|y_{\mu\mu}| > 2.0$ and in the mass range $116 < m_{\mu\mu} < 200$ GeV. This origin of this deviation is currently not none and under investigation.

For the double differential dimuon mass and rapidity measurement a total uncertainty of below 2.7% for the central rapidity in the $m_{\mu\mu} < 300$ GeV region is obtained. In the $66 < m_{\mu\mu} < 116$ GeV bin the total uncertainty is below 0.5%, which compares to a precision of around 2% for a combined dimuon and dielectron 2010 7 TeV Z inclusive ATLAS measurement [60].

Improvement on the precision of the measurement could be achieved by reevaluating the muon reconstruction scale factors. The muon reconstruction scale factors have been produced centrally by ATLAS and as such the systematic determination has been approached conservatively. Using a method similar to that used in the determination of the trigger scale factors could yield improved systematics.

Estimating the top background using a data driven method could also improve systematics. Currently the largest systematic in the analysis in the $m_{\mu\mu}$ region is the top background systematic. A data driven method similar to that used in determination of the multi-jet background could control this background further and help understand the associated systematic.

While the primary aim of the high mass Drell-Yan analysis is to provide information for constraining PDFs, a measurement has been made on double differential dimuon mass and $\Delta\eta$ cross section. The goal of this measurement is to provide information on the photon induced processes that is included within the signal of this analysis. The sensitivity within the analysis for the photon induced processes is not optimised but the cross sections can provide a basis for future dedicated photon induced processes studies. The photon induced process sensitivity can be achieved in the high mass region if the muon p_T selection is lowered [13]. A preliminary study where the measurements fiducial muon p_T selection is reduced to $p_T > 25$ GeV is given in appendix F. A further improvement on sensitivity could be achieved if the cross sections were measured triple differentially in terms of dimuon mass, p_T and an angular variable such as rapidity or $\Delta\eta$

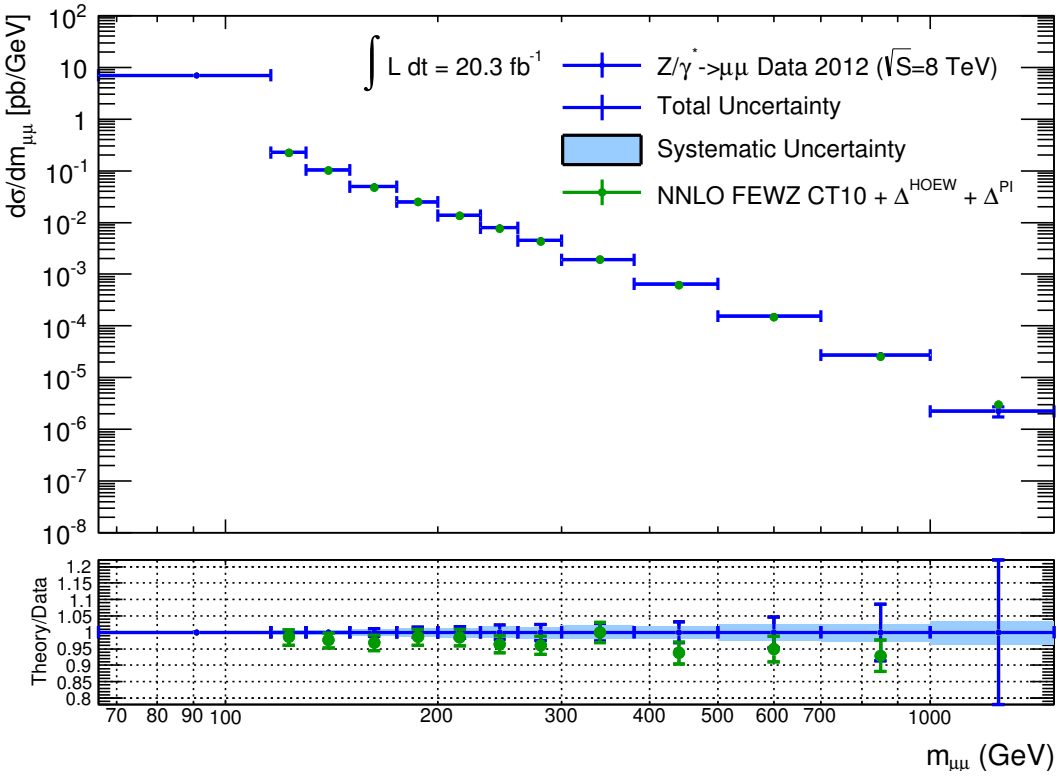

Figure 9.23.: The single differential Drell-Yan dimuon channel fiducial cross section compared to NNLO theory, which includes NLO higher order electroweak corrections (Δ^{HOEW}) and the photon induced contribution (Δ^{PI}). The shaded errors on the data show the systematic uncertainty and the error bars show the total uncertainty. The lower plot shows the ratio of theory to data. The shown experimental uncertainties do not include an overall 2.8% normalisation uncertainty due to the luminosity determination.

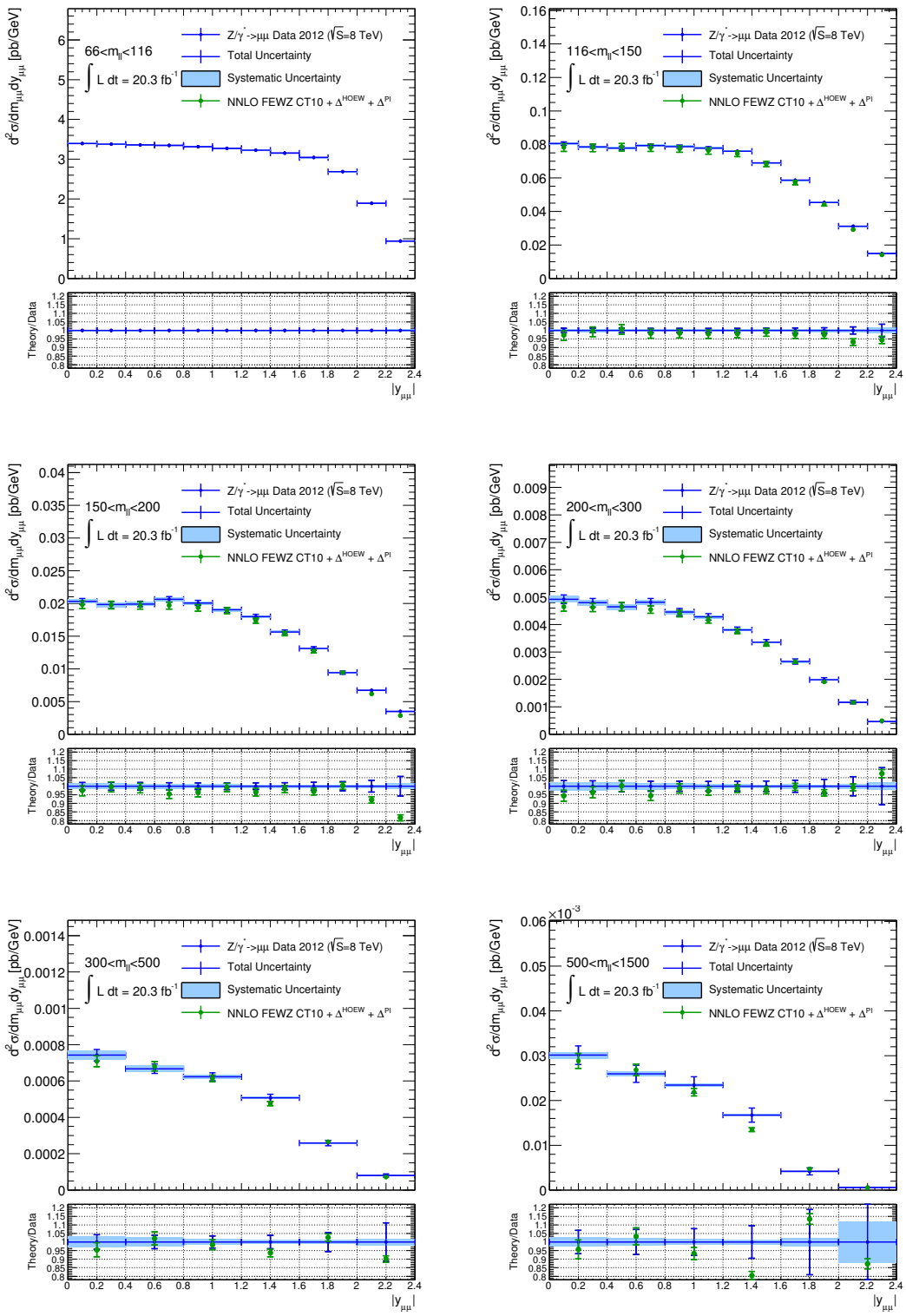

Figure 9.24.: The double differential mass and rapidity Drell-Yan dimuon channel fiducial cross section compared to NNLO theory, which includes NLO higher order electroweak corrections (Δ^{HOEW}) and the photon induced contribution (Δ^{PI}). The shaded errors on the data show the systematic uncertainty and the error bars show the total uncertainty. The lower plot shows the ratio of theory to data. The shown experimental uncertainties do not include an overall 2.8% normalisation uncertainty due to the luminosity determination.

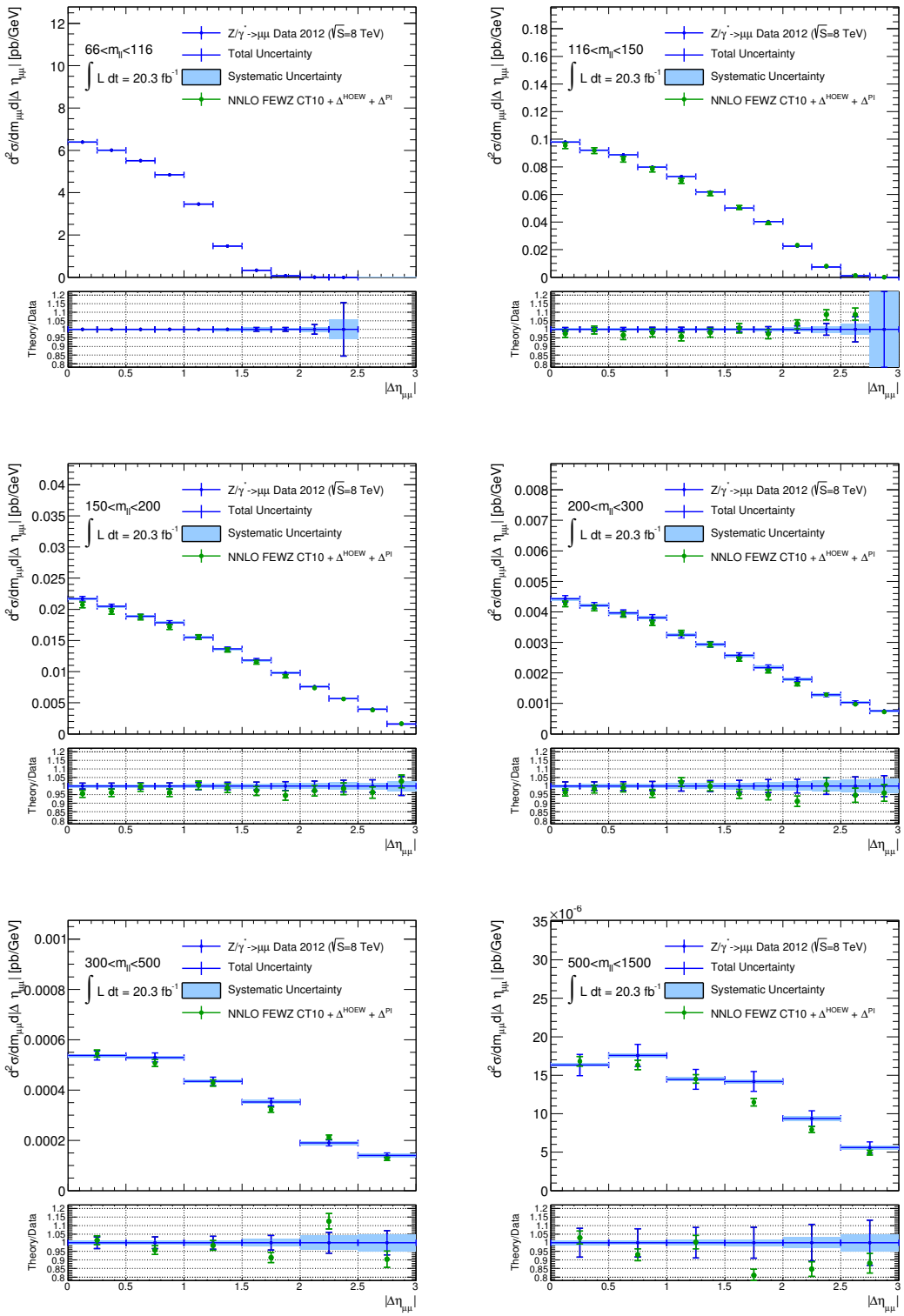

Figure 9.25.: The double differential mass and $\Delta\eta$ Drell-Yan dimuon channel fiducial cross section compared to NNLO theory, which includes NLO higher order electroweak corrections (Δ^{HOEW}) and the photon induced contribution (Δ^{PI}). The shaded errors on the data show the systematic uncertainty and the error bars show the total uncertainty. The lower plot shows the ratio of theory to data. The shown experimental uncertainties do not include an overall 2.8% normalisation uncertainty due to the luminosity determination.

Appendix A.

Z inclusive $\sqrt{s} = 7$ TeV analysis

The QCD multi-jet estimation described in section 7.1.1 has been performed for an Z inclusive Drell-Yan analysis in the dimuon mass window $46 < M_{ll} < 150$ [37]. Similarly to the high mass Drell-Yan analysis described in the rest of the thesis, the goal of this analysis is to precisely measure a double differential cross section in terms of mass and rapidity. The Z inclusive analysis uses $5fb^{-1}$ of 2011 ATLAS data with centre-of mass energy of 7TeV. The selections used for this analysis are listed as followed:

- Appropriate GRL
- The first reconstructed primary vertex has ≥ 3 tracks
- Trigger EF_mu18 for periods D to I and then EF_mu18_medium for J to M.
- Events with only two combined STACO muons that pass the following requirements
  - MCP quality cuts
  - $|z_0| < 10$ mm
  - $p_T > 20$ GeV
  - $|\eta| < 2.4$
  - Isolation, $\Sigma p_T^{(\Delta R=0.4)}/p_T < 0.1$

The Z inclusive analysis measures the double differential cross section in three broad dimuon invariant mass bins of $46 < m_{\mu\mu} < 66$, $66 < m_{\mu\mu} < 116$ and $116 < m_{\mu\mu} < 150$ GeV. The higher two mass bins correspond to the lowest two mass bins for the high mass Drell-Yan measurement presented here, although at a different $\sqrt{s}$.

Appendix B.

Boson p_T Reweighting

The Powheg Pythia Drell-Yan MC does not describe the Z/γ^* p_T spectrum well, as shown in figures 8.4, 8.10 and 8.13. This mismodelling results in a poor description of the muon p_T spectrum shown in figures 8.2, 8.8 and 8.11. As the Drell-Yan MC is relied upon to calculate the C_{DY} unfolding factors, any effect this mismodelling has on the fiducial cross sections must be measured.

An estimate of the effect on the cross section can be made by reweighting the MC Z/γ^* p_T shape to that seen in data. As the shape of the Z/γ^* p_T spectrum depends on the dimuon mass of the event, weights have been calculated separately for the $66 < m_{\mu\mu} < 116$, $116 < m_{\mu\mu} < 300$ and $m_{\mu\mu} > 300$ GeV regions. As this effect is a truth level effect, the weights are applied at the truth level using the truth Z/γ^* mass and p_T. The resulting corrected Z/γ^* p_T spectra are shown in figure B.1. Compared to the uncorrected distributions shown in figures 8.4, 8.10 and 8.13, a good improvement is seen especially in the statistics rich $66 < m_{\mu\mu} < 116$ GeV bin. An improvement is also seen in the muon p_T plots shown in figure B.2.

The effect on the cross section can then be measured by comparing the boson p_T corrected ($\sigma_{\text{boson pt corrected}}$) and uncorrected ($\sigma_{\text{uncorrected}}$) cross sections. The ratio of the corrected and uncorrected cross sections are shown for the single differential measurement in figure B.3, the double differential dimuon mass and rapidity measurement in figure B.4 and the double differential dimuon mass and $\Delta\eta$ measurement in figure B.5. The error bars shown give the statistical and total uncertainty on the nominal uncorrected measurement. For the single differential measurement all of the values show a less than 0.1% shift apart from the $260 < m_{\mu\mu} < 300$ GeV bin where 0.2% shift is observed. As the ratio shows no systematic trend this point is likely to be a statistical fluctuation. The

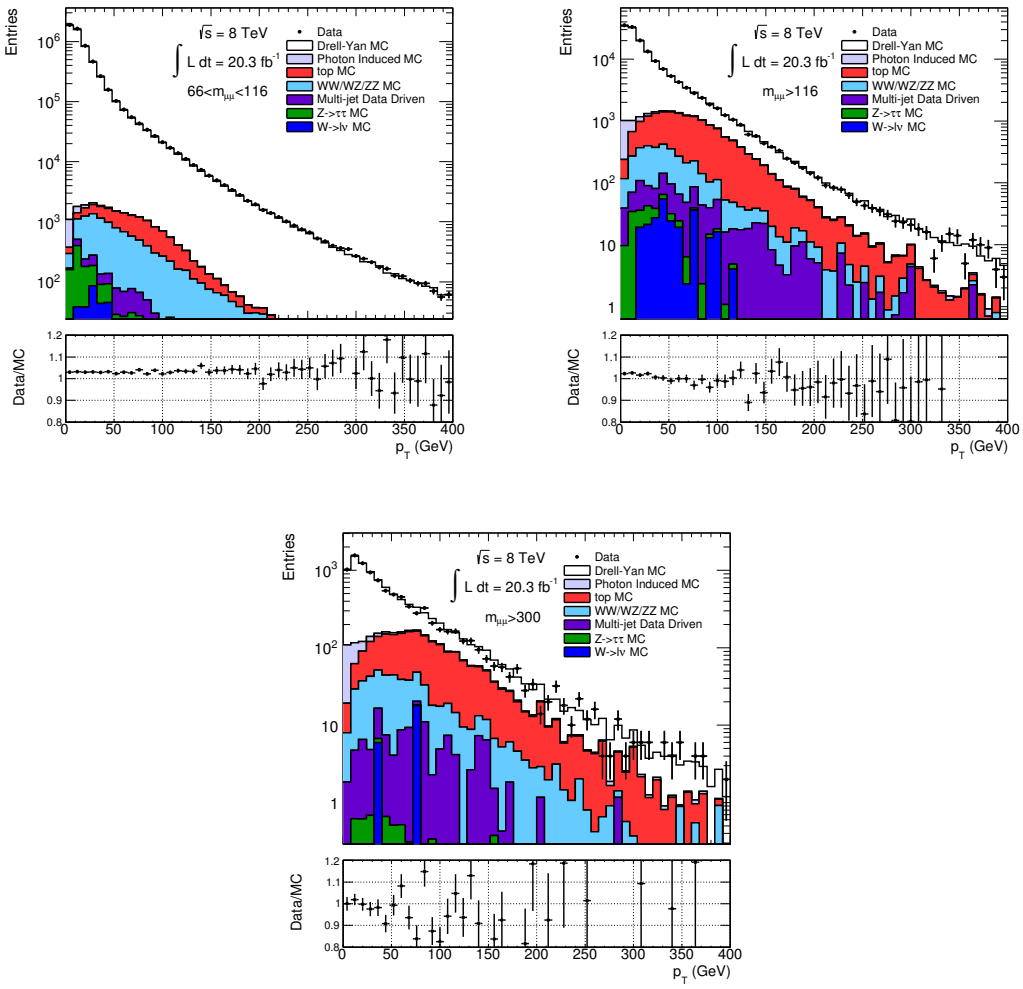

Figure B.1.: Dimuon p_T distributions for the $66 < m_{\mu\mu} < 116$ (top left), $m_{\mu\mu} > 116$ (top right) and $m_{\mu\mu} > 300$ GeV regions after full event selection and detector response corrections are applied including a reweighting of the Drell-Yan MC based on the truth Z/γ^* p_T.

double differential measurements again show shifts of less than 0.1% for almost the entire phase space apart from a few larger shifts where the statistics are very poor. As the deviations seen with this correction are small, this uncertainty has been neglected for the full uncertainty measurement in the nominal measurement.

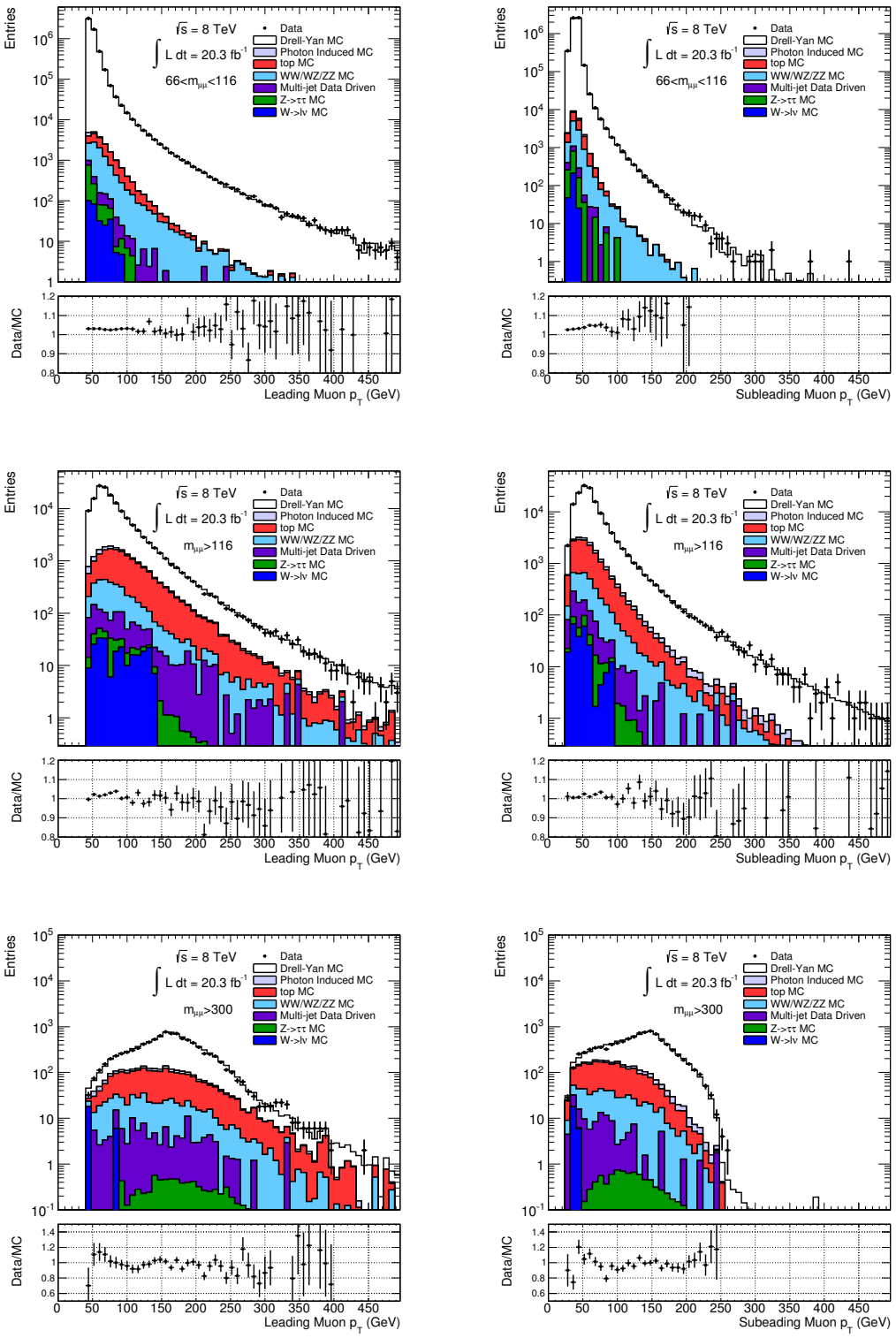

Figure B.2.: Muon p_T distributions for the $66 < m_{\mu\mu} < 116$ (top row), $m_{\mu\mu} > 116$ (middle row) and $m_{\mu\mu} > 300$ (bottom row) GeV regions after full event selection and detector response corrections are applied including a reweighting of the Drell-Yan MC based on the truth Z/γ^* p_T for the leading (left) and subleading (right) muon.

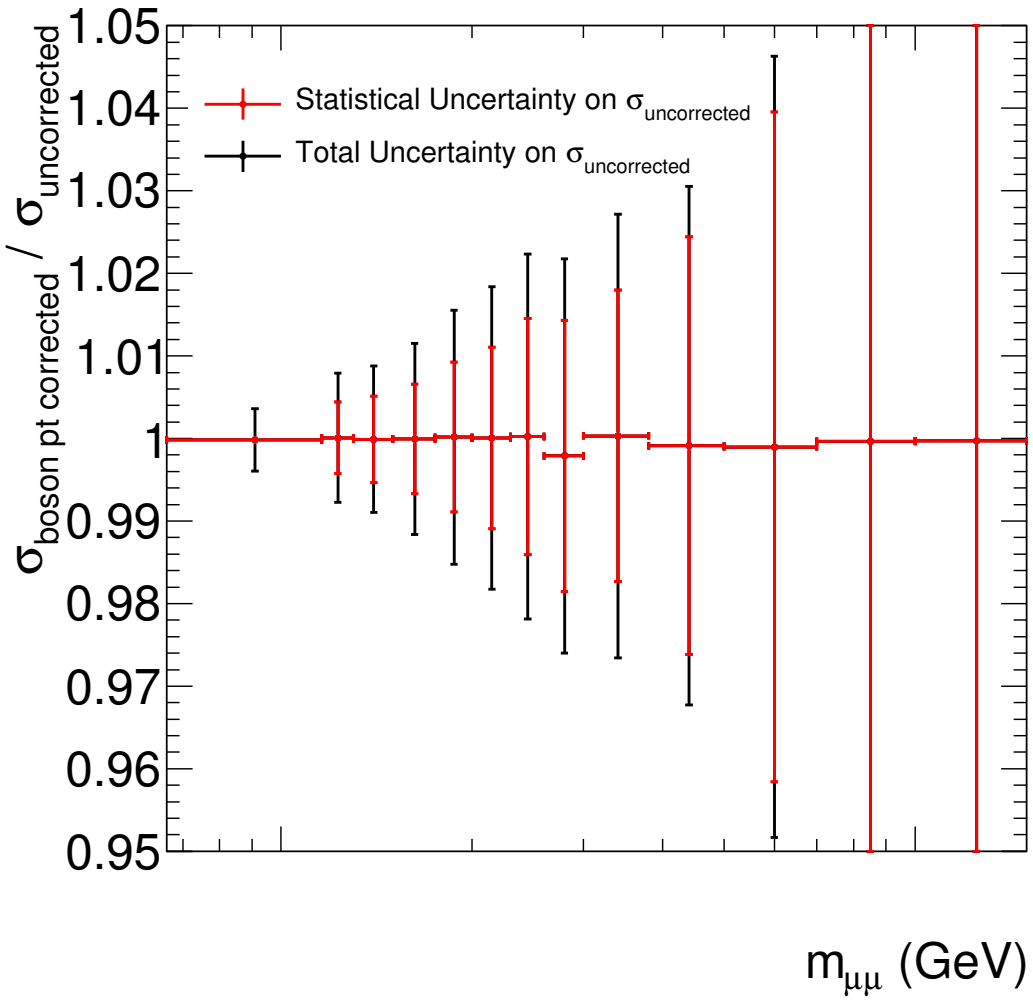

Figure B.3.: Ratio of the single differential fiducial cross sections when boson p_T reweighting has been applied to the nominal cross section when no correction is applied. The error bars show the uncertainties from the nominal cross section measurement.

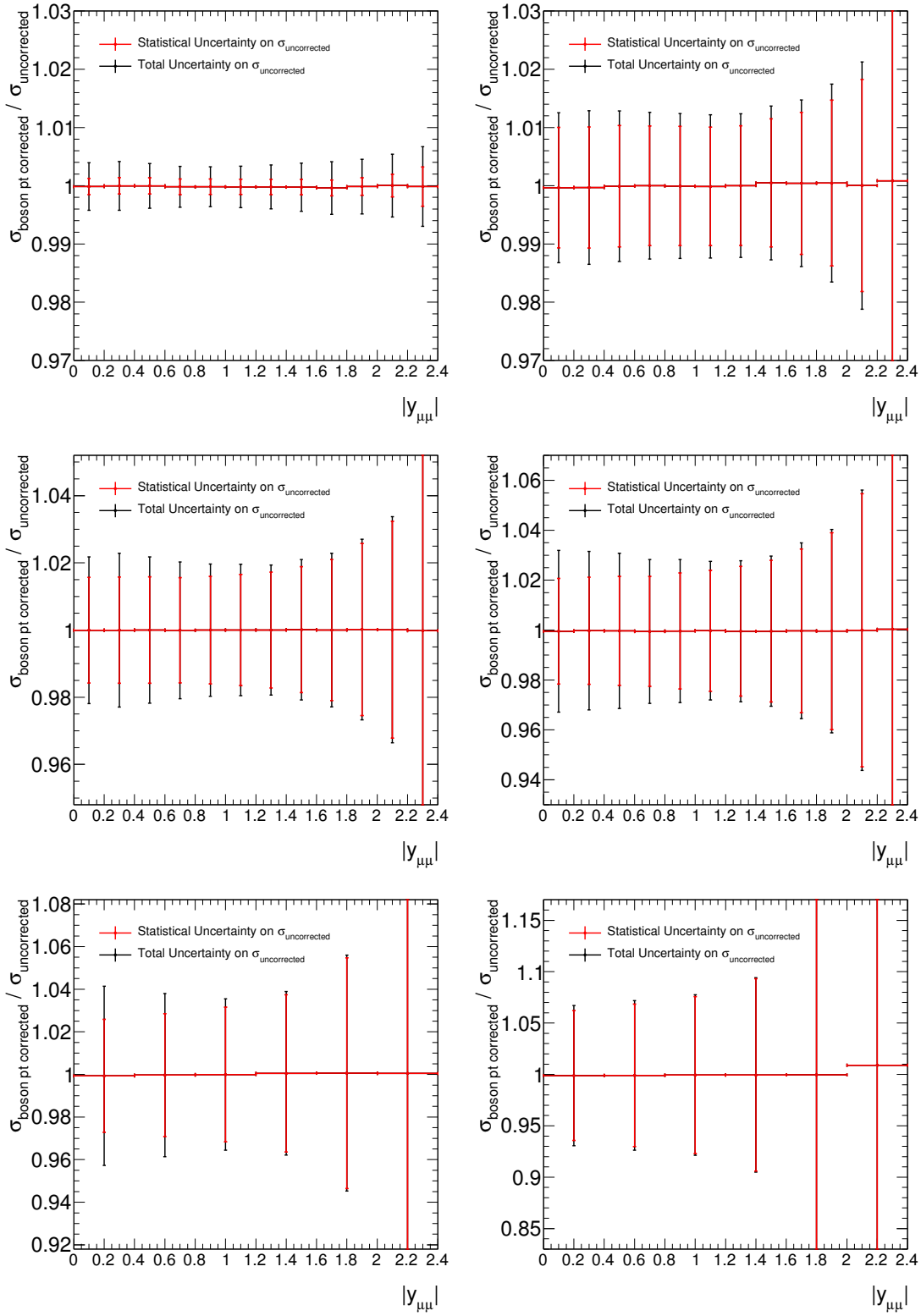

Figure B.4.: Ratio of the double differential dimuon mass and rapidity fiducial cross sections when boson p_T reweighting has been applied to the nominal cross section when no correction is applied. The error bars show the uncertainties from the nominal cross section measurement.

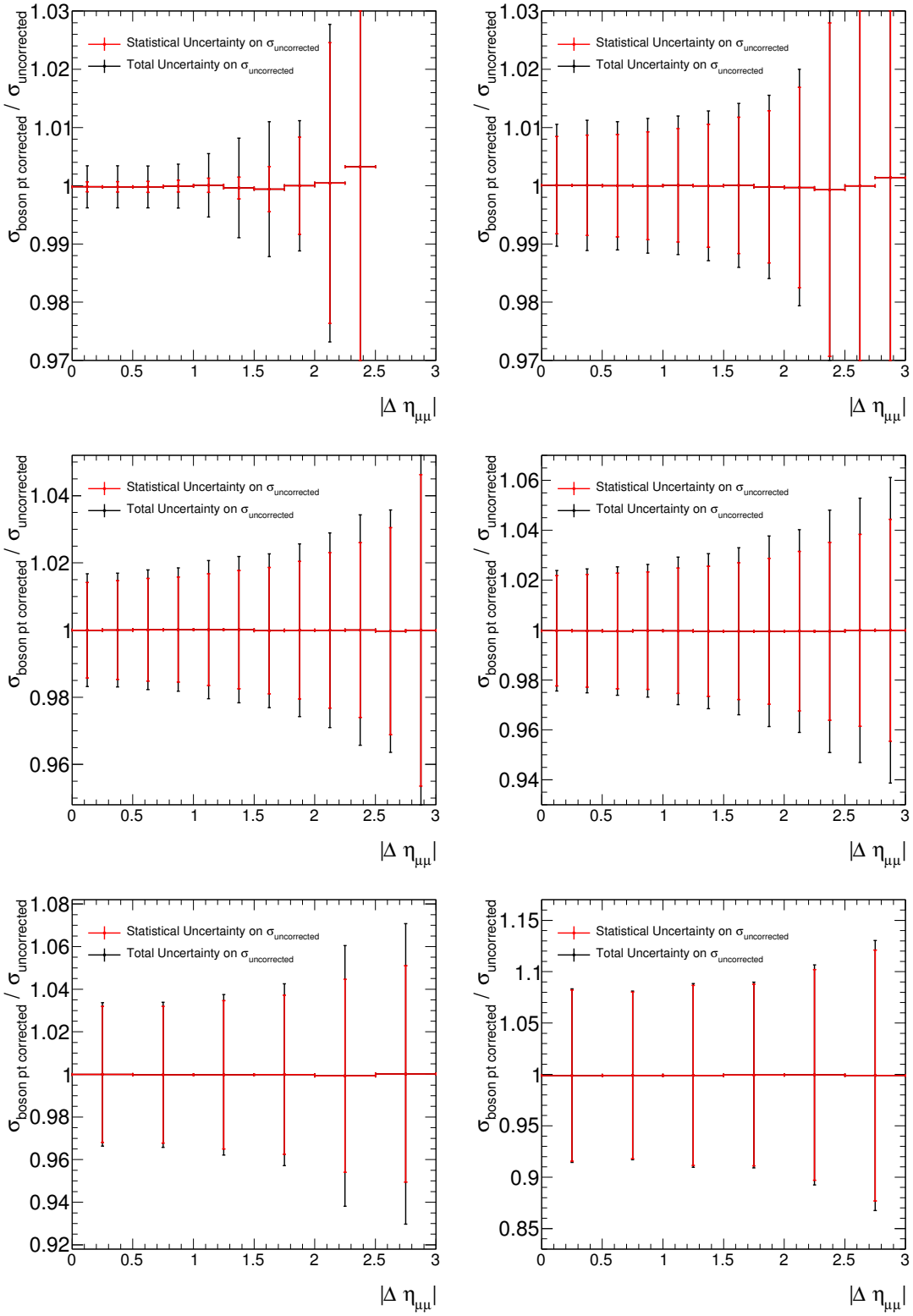

Figure B.5.: Ratio of the double differential dimuon mass and $\Delta\eta$ fiducial cross sections when boson p_T reweighting has been applied to the nominal cross section when no correction is applied. The error bars show the uncertainties from the nominal cross section measurement.

Appendix C.

Tables Of Recorded Results

The number of recorded data events, bin-by-bin unfolding factors and estimated backgrounds are listed for the single differential measurement in table C.1, for the double differential mass and rapidity measurement in tables C.2 and C.3 and the double differential mass and $\Delta\eta$ measurement in tables C.4 and C.5.

The fiducial cross sections are listed for the single differential measurement in table C.6, for the double differential dimuon mass and rapidity measurement in tables C.7 and C.8, and for the double differential dimuon mass and $\Delta\eta$ measurements in tables C.9 and C.10

$m_{\mu\mu}$ bin (GeV)	N_{data}	C_{DY}	B_{top}	$B_{diboson}$	$B_{multi-jet}$	$B_{Z/\gamma^* \to \tau\tau}$	$B_{W \to l\nu}$
$66 < m_{\mu\mu} < 116$	5730708	0.802177	1656	8946	586	990	282
$116 < m_{\mu\mu} < 130$	53304	0.788458	374	487	174	48	36
$130 < m_{\mu\mu} < 150$	36536	0.786201	394	517	156	26	66
$150 < m_{\mu\mu} < 175$	22788	0.786747	329	467	81	25	76
$175 < m_{\mu\mu} < 200$	12185	0.790193	202	323	86	13	28
$200 < m_{\mu\mu} < 230$	8256	0.790549	161	252	49	8	0
$230 < m_{\mu\mu} < 260$	4882	0.789810	102	163	65	4	17
$260 < m_{\mu\mu} < 300$	3682	0.785059	86	145	27	3	0
$300 < m_{\mu\mu} < 380$	3217	0.784796	86	146	37	2	11
$380 < m_{\mu\mu} < 500$	1560	0.782591	47	74	10	1	0
$500 < m_{\mu\mu} < 700$	606	0.784937	20	33	3	0	0
$700 < m_{\mu\mu} < 1000$	149	0.782157	6	9	0	0	0
$1000 < m_{\mu\mu} < 1500$	21	0.790227	1	2	0	0	0

Table C.1.: Table shows the number of recorded data events (N_{data}), the bin-by-bin unfolding factor (C_{DY}) and the number of background events (B) in the 1D mass binning scheme.

$m_{\mu\mu}$ bin (GeV)	$\lvert y_{\mu\mu}\rvert$ bin	N_{data}	C_{DY}	B_{top}	$B_{diboson}$	$B_{multi-jet}$	$B_{Z/\gamma^*\to\tau\tau}$	$B_{W\to l\nu}$
$66 < m_{\mu\mu} < 116$	$0 < \lvert y_{\mu\mu}\rvert < 0.2$	507932	0.735	1191	877	83	96	19
$66 < m_{\mu\mu} < 116$	$0.2 < \lvert y_{\mu\mu}\rvert < 0.4$	504402	0.733	1160	861	78	107	27
$66 < m_{\mu\mu} < 116$	$0.4 < \lvert y_{\mu\mu}\rvert < 0.6$	516486	0.756	1136	896	78	103	16
$66 < m_{\mu\mu} < 116$	$0.6 < \lvert y_{\mu\mu}\rvert < 0.8$	555749	0.815	1067	921	72	70	23
$66 < m_{\mu\mu} < 116$	$0.8 < \lvert y_{\mu\mu}\rvert < 1.0$	574266	0.850	983	939	67	94	24
$66 < m_{\mu\mu} < 116$	$1.0 < \lvert y_{\mu\mu}\rvert < 1.2$	584175	0.877	865	953	62	62	20
$66 < m_{\mu\mu} < 116$	$1.2 < \lvert y_{\mu\mu}\rvert < 1.4$	582976	0.889	707	912	51	126	40
$66 < m_{\mu\mu} < 116$	$1.4 < \lvert y_{\mu\mu}\rvert < 1.6$	570019	0.889	527	842	40	113	28
$66 < m_{\mu\mu} < 116$	$1.6 < \lvert y_{\mu\mu}\rvert < 1.8$	540033	0.874	358	736	27	76	60
$66 < m_{\mu\mu} < 116$	$1.8 < \lvert y_{\mu\mu}\rvert < 2.0$	437719	0.802	204	559	15	57	11
$66 < m_{\mu\mu} < 116$	$2.0 < \lvert y_{\mu\mu}\rvert < 2.2$	268516	0.700	89	337	7	70	9
$66 < m_{\mu\mu} < 116$	$2.2 < \lvert y_{\mu\mu}\rvert < 2.4$	88435	0.462	17	107	1	11	0
$116 < m_{\mu\mu} < 150$	$0 < \lvert y_{\mu\mu}\rvert < 0.2$	9344	0.758	753	114	54	4	0
$116 < m_{\mu\mu} < 150$	$0.2 < \lvert y_{\mu\mu}\rvert < 0.4$	9213	0.764	729	105	56	7	32
$116 < m_{\mu\mu} < 150$	$0.4 < \lvert y_{\mu\mu}\rvert < 0.6$	9229	0.777	708	112	53	4	12
$116 < m_{\mu\mu} < 150$	$0.6 < \lvert y_{\mu\mu}\rvert < 0.8$	9471	0.791	656	115	44	5	0
$116 < m_{\mu\mu} < 150$	$0.8 < \lvert y_{\mu\mu}\rvert < 1.0$	9556	0.810	582	117	40	5	18
$116 < m_{\mu\mu} < 150$	$1.0 < \lvert y_{\mu\mu}\rvert < 1.2$	9669	0.842	481	109	32	6	9
$116 < m_{\mu\mu} < 150$	$1.2 < \lvert y_{\mu\mu}\rvert < 1.4$	9452	0.855	370	103	24	4	0
$116 < m_{\mu\mu} < 150$	$1.4 < \lvert y_{\mu\mu}\rvert < 1.6$	8280	0.827	266	88	14	17	22
$116 < m_{\mu\mu} < 150$	$1.6 < \lvert y_{\mu\mu}\rvert < 1.8$	6731	0.802	156	63	7	11	3
$116 < m_{\mu\mu} < 150$	$1.8 < \lvert y_{\mu\mu}\rvert < 2.0$	4941	0.769	80	43	2	3	3
$116 < m_{\mu\mu} < 150$	$2.0 < \lvert y_{\mu\mu}\rvert < 2.2$	3013	0.685	35	25	1	2	0
$116 < m_{\mu\mu} < 150$	$2.2 < \lvert y_{\mu\mu}\rvert < 2.4$	941	0.452	6	6	0	0	0
$150 < m_{\mu\mu} < 200$	$0 < \lvert y_{\mu\mu}\rvert < 0.2$	4056	0.778	694	112	35	4	5
$150 < m_{\mu\mu} < 200$	$0.2 < \lvert y_{\mu\mu}\rvert < 0.4$	4004	0.779	700	101	33	3	32
$150 < m_{\mu\mu} < 200$	$0.4 < \lvert y_{\mu\mu}\rvert < 0.6$	3973	0.789	654	91	27	3	12
$150 < m_{\mu\mu} < 200$	$0.6 < \lvert y_{\mu\mu}\rvert < 0.8$	4078	0.802	583	101	25	4	9
$150 < m_{\mu\mu} < 200$	$0.8 < \lvert y_{\mu\mu}\rvert < 1.0$	3899	0.806	493	96	20	7	0
$150 < m_{\mu\mu} < 200$	$1.0 < \lvert y_{\mu\mu}\rvert < 1.2$	3656	0.818	392	80	13	3	9
$150 < m_{\mu\mu} < 200$	$1.2 < \lvert y_{\mu\mu}\rvert < 1.4$	3373	0.826	264	78	7	2	6
$150 < m_{\mu\mu} < 200$	$1.4 < \lvert y_{\mu\mu}\rvert < 1.6$	2849	0.815	183	56	3	3	19
$150 < m_{\mu\mu} < 200$	$1.6 < \lvert y_{\mu\mu}\rvert < 1.8$	2268	0.799	98	32	2	1	9
$150 < m_{\mu\mu} < 200$	$1.8 < \lvert y_{\mu\mu}\rvert < 2.0$	1525	0.761	45	23	0	1	0
$150 < m_{\mu\mu} < 200$	$2.0 < \lvert y_{\mu\mu}\rvert < 2.2$	961	0.683	18	13	0	0	0
$150 < m_{\mu\mu} < 200$	$2.2 < \lvert y_{\mu\mu}\rvert < 2.4$	331	0.458	3	3	0	0	0

Table C.2.: Table shows the number of recorded data events (N_{data}), the bin-by-bin unfolding factor (C_{DY}) and the number of background events (B) in the 2D rapidity mass binning scheme for the lowest three $m_{\mu\mu}$ bins.

$m_{\mu\mu}$ bin (GeV)	$\lvert y_{\mu\mu}\rvert$ bin	N_{data}	C_{DY}	B_{top}	$B_{diboson}$	$B_{multi-jet}$	$B_{Z/\gamma^*\to\tau\tau}$	$B_{W\to l\nu}$
$200 < m_{\mu\mu} < 300$	$0 < \lvert y_{\mu\mu}\rvert < 0.2$	2230	0.784	536	81	35	2	10
$200 < m_{\mu\mu} < 300$	$0.2 < \lvert y_{\mu\mu}\rvert < 0.4$	2165	0.786	514	85	32	2	0
$200 < m_{\mu\mu} < 300$	$0.4 < \lvert y_{\mu\mu}\rvert < 0.6$	2095	0.796	474	91	28	1	0
$200 < m_{\mu\mu} < 300$	$0.6 < \lvert y_{\mu\mu}\rvert < 0.8$	2059	0.797	401	79	19	2	0
$200 < m_{\mu\mu} < 300$	$0.8 < \lvert y_{\mu\mu}\rvert < 1.0$	1851	0.797	332	63	12	1	0
$200 < m_{\mu\mu} < 300$	$1.0 < \lvert y_{\mu\mu}\rvert < 1.2$	1704	0.808	239	52	7	1	0
$200 < m_{\mu\mu} < 300$	$1.2 < \lvert y_{\mu\mu}\rvert < 1.4$	1480	0.827	157	41	3	1	0
$200 < m_{\mu\mu} < 300$	$1.4 < \lvert y_{\mu\mu}\rvert < 1.6$	1240	0.818	94	29	1	0	0
$200 < m_{\mu\mu} < 300$	$1.6 < \lvert y_{\mu\mu}\rvert < 1.8$	930	0.795	46	18	0	0	7
$200 < m_{\mu\mu} < 300$	$1.8 < \lvert y_{\mu\mu}\rvert < 2.0$	643	0.758	19	11	0	0	0
$200 < m_{\mu\mu} < 300$	$2.0 < \lvert y_{\mu\mu}\rvert < 2.2$	334	0.679	6	5	0	0	0
$200 < m_{\mu\mu} < 300$	$2.2 < \lvert y_{\mu\mu}\rvert < 2.4$	89	0.465	1	1	0	0	0
$300 < m_{\mu\mu} < 500$	$0 < \lvert y_{\mu\mu} < 0.4$	1421	0.783	358	81	27	1	8
$300 < m_{\mu\mu} < 500$	$0.4 < \lvert y_{\mu\mu} < 0.8$	1198	0.782	267	66	15	1	0
$300 < m_{\mu\mu} < 500$	$0.8 < \lvert y_{\mu\mu} < 1.2$	999	0.794	144	42	4	1	2
$300 < m_{\mu\mu} < 500$	$1.2 < \lvert y_{\mu\mu} < 1.6$	735	0.807	49	19	0	0	0
$300 < m_{\mu\mu} < 500$	$1.6 < \lvert y_{\mu\mu} < 2.0$	341	0.773	6	10	0	0	0
$300 < m_{\mu\mu} < 500$	$2.0 < \lvert y_{\mu\mu} < 2.4$	83	0.629	0	0	0	0	0
$500 < m_{\mu\mu} < 1500$	$0 < \lvert y_{\mu\mu} < 0.4$	250	0.770	41	19	0	0	0
$500 < m_{\mu\mu} < 1500$	$0.4 < \lvert y_{\mu\mu} < 0.8$	208	0.779	29	14	0	0	0
$500 < m_{\mu\mu} < 1500$	$0.8 < \lvert y_{\mu\mu} < 1.2$	171	0.789	13	7	0	0	0
$500 < m_{\mu\mu} < 1500$	$1.2 < \lvert y_{\mu\mu} < 1.6$	114	0.807	1	3	0	0	0
$500 < m_{\mu\mu} < 1500$	$1.6 < \lvert y_{\mu\mu} < 2.0$	28	0.798	0	0	0	0	0
$500 < m_{\mu\mu} < 1500$	$2.0 < \lvert y_{\mu\mu} < 2.4$	5	1.023	0	0	0	0	0

Table C.3.: Table shows the number of recorded data events (N_{data}), the bin-by-bin unfolding factor (C_{DY}) and the number of background events (B) in the 2D rapidity mass binning scheme for the highest three $m_{\mu\mu}$ bins.

$m_{\mu\mu}$ bin (GeV)	$\lvert\Delta\eta_{\mu\mu}\rvert$ bin	N_{data}	C_{DY}	B_{top}	$B_{diboson}$	$B_{multi-jet}$	$B_{Z/\gamma^*\to\tau\tau}$	$B_{W\to l\nu}$
$66 < m_{\mu\mu} < 116$	$0 < \lvert\Delta\eta_{\mu\mu}\rvert < 0.25$	1340975	0.826	1465	2009	100	283	26
$66 < m_{\mu\mu} < 116$	$0.25 < \lvert\Delta\eta_{\mu\mu}\rvert < 0.5$	1249749	0.819	1458	1850	101	345	96
$66 < m_{\mu\mu} < 116$	$0.5 < \lvert\Delta\eta_{\mu\mu}\rvert < 0.75$	1135498	0.810	1335	1645	98	198	50
$66 < m_{\mu\mu} < 116$	$0.75 < \lvert\Delta\eta_{\mu\mu}\rvert < 1.0$	969942	0.789	1217	1324	91	65	42
$66 < m_{\mu\mu} < 116$	$1.0 < \lvert\Delta\eta_{\mu\mu}\rvert < 1.25$	666240	0.758	1063	987	79	51	20
$66 < m_{\mu\mu} < 116$	$1.25 < \lvert\Delta\eta_{\mu\mu}\rvert < 1.5$	285769	0.757	844	662	59	37	24
$66 < m_{\mu\mu} < 116$	$1.5 < \lvert\Delta\eta_{\mu\mu}\rvert < 1.75$	66392	0.790	547	331	37	8	15
$66 < m_{\mu\mu} < 116$	$1.75 < \lvert\Delta\eta_{\mu\mu}\rvert < 2.0$	14374	0.768	283	112	14	1	6
$66 < m_{\mu\mu} < 116$	$2.0 < \lvert\Delta\eta_{\mu\mu}\rvert < 2.25$	1721	0.762	85	20	2	0	0
$66 < m_{\mu\mu} < 116$	$2.25 < \lvert\Delta\eta_{\mu\mu}\rvert < 2.5$	48	0.776	9	2	0	0	0
$66 < m_{\mu\mu} < 116$	$2.5 < \lvert\Delta\eta_{\mu\mu}\rvert < 2.75$	0	0.000	0	0	0	0	0
$66 < m_{\mu\mu} < 116$	$2.75 < \lvert\Delta\eta_{\mu\mu}\rvert < 3.0$	0	0.000	0	0	0	0	0
$116 < m_{\mu\mu} < 150$	$0 < \lvert\Delta\eta_{\mu\mu}\rvert < 0.25$	14331	0.805	588	125	20	7	5
$116 < m_{\mu\mu} < 150$	$0.25 < \lvert\Delta\eta_{\mu\mu}\rvert < 0.5$	13475	0.798	612	123	21	15	37
$116 < m_{\mu\mu} < 150$	$0.5 < \lvert\Delta\eta_{\mu\mu}\rvert < 0.75$	12938	0.797	600	121	25	6	0
$116 < m_{\mu\mu} < 150$	$0.75 < \lvert\Delta\eta_{\mu\mu}\rvert < 1.0$	11627	0.790	593	121	30	14	3
$116 < m_{\mu\mu} < 150$	$1.0 < \lvert\Delta\eta_{\mu\mu}\rvert < 1.25$	10536	0.780	577	113	34	5	0
$116 < m_{\mu\mu} < 150$	$1.25 < \lvert\Delta\eta_{\mu\mu}\rvert < 1.5$	8955	0.774	540	109	40	4	17
$116 < m_{\mu\mu} < 150$	$1.5 < \lvert\Delta\eta_{\mu\mu}\rvert < 1.75$	7288	0.771	457	101	44	11	3
$116 < m_{\mu\mu} < 150$	$1.75 < \lvert\Delta\eta_{\mu\mu}\rvert < 2.0$	5852	0.764	383	82	48	4	14
$116 < m_{\mu\mu} < 150$	$2.0 < \lvert\Delta\eta_{\mu\mu}\rvert < 2.25$	3381	0.770	277	63	40	2	7
$116 < m_{\mu\mu} < 150$	$2.25 < \lvert\Delta\eta_{\mu\mu}\rvert < 2.5$	1218	0.780	143	31	19	0	11
$116 < m_{\mu\mu} < 150$	$2.5 < \lvert\Delta\eta_{\mu\mu}\rvert < 2.75$	232	0.842	47	11	4	0	0
$116 < m_{\mu\mu} < 150$	$2.75 < \lvert\Delta\eta_{\mu\mu}\rvert < 3.0$	7	0.835	4	0	0	0	0
$150 < m_{\mu\mu} < 200$	$0 < \lvert\Delta\eta_{\mu\mu}\rvert < 0.25$	4951	0.808	403	68	5	4	26
$150 < m_{\mu\mu} < 200$	$0.25 < \lvert\Delta\eta_{\mu\mu}\rvert < 0.5$	4626	0.801	389	67	5	4	1
$150 < m_{\mu\mu} < 200$	$0.5 < \lvert\Delta\eta_{\mu\mu}\rvert < 0.75$	4286	0.794	396	71	7	4	7
$150 < m_{\mu\mu} < 200$	$0.75 < \lvert\Delta\eta_{\mu\mu}\rvert < 1.0$	4087	0.792	414	72	9	7	0
$150 < m_{\mu\mu} < 200$	$1.0 < \lvert\Delta\eta_{\mu\mu}\rvert < 1.25$	3609	0.781	432	69	10	3	29
$150 < m_{\mu\mu} < 200$	$1.25 < \lvert\Delta\eta_{\mu\mu}\rvert < 1.5$	3229	0.778	427	79	13	3	11
$150 < m_{\mu\mu} < 200$	$1.5 < \lvert\Delta\eta_{\mu\mu}\rvert < 1.75$	2825	0.776	403	74	15	2	0
$150 < m_{\mu\mu} < 200$	$1.75 < \lvert\Delta\eta_{\mu\mu}\rvert < 2.0$	2386	0.767	377	71	19	2	8
$150 < m_{\mu\mu} < 200$	$2.0 < \lvert\Delta\eta_{\mu\mu}\rvert < 2.25$	1866	0.755	327	62	20	1	0
$150 < m_{\mu\mu} < 200$	$2.25 < \lvert\Delta\eta_{\mu\mu}\rvert < 2.5$	1476	0.764	266	66	22	1	16
$150 < m_{\mu\mu} < 200$	$2.5 < \lvert\Delta\eta_{\mu\mu}\rvert < 2.75$	1053	0.808	169	45	20	1	0
$150 < m_{\mu\mu} < 200$	$2.75 < \lvert\Delta\eta_{\mu\mu}\rvert < 3.0$	465	0.805	91	32	12	0	0

Table C.4.: Table shows the number of recorded data events (N_{data}), the bin-by-bin unfolding factor (C_{DY}) and the number of background events (B) in the 2D $\Delta\eta_{\mu\mu}$ mass binning scheme for the lowest three $m_{\mu\mu}$ bins.

$m_{\mu\mu}$ bin (GeV)	$\lvert\Delta\eta_{\mu\mu}\rvert$ bin	N_{data}	C_{DY}	B_{top}	$B_{diboson}$	$B_{multi-jet}$	$B_{Z/\gamma^*\to\tau\tau}$	$B_{W\to l\nu}$
$200 < m_{\mu\mu} < 300$	$0 < \lvert\Delta\eta_{\mu\mu}\rvert < 0.25$	2046	0.812	189	29	3	2	0
$200 < m_{\mu\mu} < 300$	$0.25 < \lvert\Delta\eta_{\mu\mu}\rvert < 0.5$	1955	0.807	201	29	3	1	0
$200 < m_{\mu\mu} < 300$	$0.5 < \lvert\Delta\eta_{\mu\mu}\rvert < 0.75$	1862	0.800	215	34	3	1	0
$200 < m_{\mu\mu} < 300$	$0.75 < \lvert\Delta\eta_{\mu\mu}\rvert < 1.0$	1802	0.790	232	40	4	1	0
$200 < m_{\mu\mu} < 300$	$1.0 < \lvert\Delta\eta_{\mu\mu}\rvert < 1.25$	1582	0.783	240	39	4	2	7
$200 < m_{\mu\mu} < 300$	$1.25 < \lvert\Delta\eta_{\mu\mu}\rvert < 1.5$	1473	0.779	266	38	6	1	0
$200 < m_{\mu\mu} < 300$	$1.5 < \lvert\Delta\eta_{\mu\mu}\rvert < 1.75$	1331	0.773	263	49	7	1	0
$200 < m_{\mu\mu} < 300$	$1.75 < \lvert\Delta\eta_{\mu\mu}\rvert < 2.0$	1170	0.768	249	52	9	0	9
$200 < m_{\mu\mu} < 300$	$2.0 < \lvert\Delta\eta_{\mu\mu}\rvert < 2.25$	979	0.759	233	45	11	0	0
$200 < m_{\mu\mu} < 300$	$2.25 < \lvert\Delta\eta_{\mu\mu}\rvert < 2.5$	787	0.779	224	42	13	1	0
$200 < m_{\mu\mu} < 300$	$2.5 < \lvert\Delta\eta_{\mu\mu}\rvert < 2.75$	676	0.793	189	54	17	0	0
$200 < m_{\mu\mu} < 300$	$2.75 < \lvert\Delta\eta_{\mu\mu}\rvert < 3.0$	506	0.779	147	41	18	0	0
$300 < m_{\mu\mu} < 500$	$0 < \lvert\Delta\eta_{\mu\mu}\rvert < 0.5$	979	0.803	76	24	1	0	0
$300 < m_{\mu\mu} < 500$	$0.5 < \lvert\Delta\eta_{\mu\mu}\rvert < 01.0$	970	0.795	92	22	0	0	0
$300 < m_{\mu\mu} < 500$	$1.0 < \lvert\Delta\eta_{\mu\mu}\rvert < 1.5$	825	0.780	108	26	1	0	0
$300 < m_{\mu\mu} < 500$	$1.5 < \lvert\Delta\eta_{\mu\mu}\rvert < 2.0$	717	0.769	134	29	3	0	0
$300 < m_{\mu\mu} < 500$	$2.0 < \lvert\Delta\eta_{\mu\mu}\rvert < 2.5$	486	0.763	152	34	5	0	0
$300 < m_{\mu\mu} < 500$	$2.5 < \lvert\Delta\eta_{\mu\mu}\rvert < 3.0$	388	0.786	127	28	8	0	0
$500 < m_{\mu\mu} < 1500$	$0 < \lvert\Delta\eta_{\mu\mu}\rvert < 0.5$	144	0.805	5	4	0	0	0
$500 < m_{\mu\mu} < 1500$	$0.5 < \lvert\Delta\eta_{\mu\mu}\rvert < 01.0$	152	0.796	4	5	0	0	0
$500 < m_{\mu\mu} < 1500$	$1.0 < \lvert\Delta\eta_{\mu\mu}\rvert < 1.5$	130	0.786	8	5	0	0	0
$500 < m_{\mu\mu} < 1500$	$1.5 < \lvert\Delta\eta_{\mu\mu}\rvert < 2.0$	128	0.775	10	5	0	0	0
$500 < m_{\mu\mu} < 1500$	$2.0 < \lvert\Delta\eta_{\mu\mu}\rvert < 2.5$	95	0.771	15	6	0	0	0
$500 < m_{\mu\mu} < 1500$	$2.5 < \lvert\Delta\eta_{\mu\mu}\rvert < 3.0$	67	0.789	16	5	0	0	0

Table C.5.: Table shows the number of recorded data events (N_{data}), the bin-by-bin unfolding factor (C_{DY}) and the number of background events (B) in the 2D $\Delta\eta_{\mu\mu}$ mass binning scheme for the highest three $m_{\mu\mu}$ bins.

$m_{\mu\mu}^{min} - m_{\mu\mu}^{max}$	$\frac{d\sigma}{dm_{\mu\mu}}$	δ^{stat}	δ^{sys}	δ^{tot}	δ_{cor}^{trig}	δ_{unc}^{trig}	δ_{cor}^{reco}	δ_{unc}^{reco}	δ_{unc}^{MSres}	δ_{unc}^{IDres}	δ_{unc}^{pT}	δ_{unc}^{Isol}	δ_{cor}^{ewk}	δ_{unc}^{ewk}	$\delta_{cor}^{mult.}$	δ_{unc}^{MC}
[GeV]	[pb/GeV]	[%]	[%]	[%]	[%]	[%]	[%]	[%]	[%]	[%]	[%]	[%]	[%]	[%]	[%]	[%]
$66 - 116$	70.23×10^{-1}	0.0	0.4	0.4	0.1	0.0	0.3	0.0	0.0	0.0	0.1	0.0	0.0	0.0	0.0	0.0
$116 - 130$	2.25×10^{-1}	0.4	0.6	0.8	0.1	0.0	0.4	0.0	0.1	0.1	0.4	0.1	0.3	0.1	0.1	0.1
$130 - 150$	1.04×10^{-1}	0.5	0.7	0.9	0.1	0.0	0.4	0.0	0.1	0.0	0.3	0.1	0.5	0.1	0.1	0.1
$150 - 175$	4.94×10^{-2}	0.7	1.0	1.2	0.1	0.0	0.4	0.0	0.0	0.0	0.2	0.1	0.8	0.2	0.2	0.1
$175 - 200$	2.50×10^{-2}	0.9	1.2	1.5	0.1	0.0	0.5	0.0	0.1	0.1	0.2	0.1	1.0	0.3	0.3	0.1
$200 - 230$	1.37×10^{-2}	1.1	1.5	1.8	0.1	0.0	0.5	0.0	0.1	0.0	0.2	0.1	1.2	0.3	0.4	0.2
$230 - 260$	7.92×10^{-3}	1.4	1.7	2.2	0.1	0.0	0.5	0.0	0.1	0.1	0.3	0.1	1.3	0.5	0.7	0.2
$260 - 300$	4.48×10^{-3}	1.6	1.7	2.4	0.1	0.0	0.6	0.0	0.1	0.1	0.2	0.2	1.4	0.5	0.6	0.2
$300 - 380$	1.91×10^{-3}	1.8	2.0	2.7	0.1	0.0	0.6	0.0	0.1	0.0	0.3	0.2	1.5	0.7	0.9	0.2
$380 - 500$	6.50×10^{-4}	2.5	1.9	3.1	0.1	0.0	0.7	0.0	0.2	0.1	0.2	0.3	1.2	0.6	1.0	0.2
$500 - 700$	1.55×10^{-4}	4.1	2.4	4.7	0.1	0.0	0.8	0.0	0.3	0.1	0.2	0.4	1.0	0.8	1.8	0.2
$700 - 1000$	2.73×10^{-5}	8.2	2.6	8.6	0.1	0.0	0.8	0.0	0.7	0.1	0.3	0.5	0.6	1.2	1.8	0.4
$1000 - 1500$	2.23×10^{-6}	21.8	3.5	22.1	0.1	0.0	1.0	0.0	0.9	0.5	0.3	0.5	0.7	2.2	2.1	0.4

Table C.6.: Muon channel Born level differential cross section $\frac{d\sigma}{dm_{\mu\mu}}$. The measurements are listed together with the statistical (δ^{stat}), systematic (δ^{sys}) and total (δ^{tot}) uncertainties. In addition the contributions from the individual correlated and uncorrelated systematic error sources are also provided consisting of the trigger efficiency (δ^{trig}), muon reconstruction efficiency (δ^{reco}), the MS resolution (δ^{MSres}), the ID resolution (δ^{IDres}), the muon transverse momentum scale (δ^{pT}), the isolation efficiency (δ^{Isol}), the electroweak background (δ^{ewk}), the multijet background (δ^{mult}) and the MC statistical uncertainty (δ^{MC}). The luminosity uncertainty of 2.8% is not included.

$m_{\mu\mu}^{min} - m_{\mu\mu}^{max}$ [GeV]	$\lvert y_{\mu\mu}^{min}\rvert - \lvert y_{\mu\mu}^{max}\rvert$	$\frac{d\sigma}{dm_{\mu\mu}d\lvert y_{\mu\mu}\rvert}$ [pb/GeV]	δ^{stat} [%]	δ^{sys} [%]	δ^{tot} [%]	δ_{cor}^{trig} [%]	δ_{unc}^{trig} [%]	δ_{cor}^{reco} [%]	δ_{unc}^{reco} [%]	δ_{unc}^{MSres} [%]	δ_{unc}^{IDres} [%]	δ_{unc}^{pT} [%]	δ_{unc}^{Isol} [%]	δ_{cor}^{ewk} [%]	δ_{unc}^{ewk} [%]	$\delta_{cor}^{mult.}$ [%]	δ_{unc}^{MC} [%]
66 – 116	0.0 – 0.2	33.93×10^{-1}	0.1	0.4	0.4	0.0	0.0	0.4	0.0	0.0	0.0	0.1	0.1	0.0	0.0	0.0	0.0
66 – 116	0.2 – 0.4	33.79×10^{-1}	0.1	0.4	0.4	0.1	0.0	0.4	0.0	0.0	0.0	0.1	0.1	0.0	0.0	0.0	0.0
66 – 116	0.4 – 0.6	33.57×10^{-1}	0.1	0.4	0.4	0.1	0.0	0.3	0.0	0.0	0.0	0.1	0.1	0.0	0.0	0.0	0.0
66 – 116	0.6 – 0.8	33.49×10^{-1}	0.1	0.3	0.4	0.1	0.0	0.3	0.0	0.0	0.0	0.1	0.0	0.0	0.0	0.0	0.0
66 – 116	0.8 – 1.0	33.18×10^{-1}	0.1	0.3	0.3	0.1	0.0	0.3	0.0	0.0	0.0	0.1	0.0	0.0	0.0	0.0	0.0
66 – 116	1.0 – 1.2	32.75×10^{-1}	0.1	0.3	0.4	0.1	0.0	0.3	0.0	0.0	0.0	0.1	0.0	0.0	0.0	0.0	0.0
66 – 116	1.2 – 1.4	32.25×10^{-1}	0.1	0.4	0.4	0.1	0.0	0.3	0.0	0.0	0.0	0.1	0.0	0.0	0.0	0.0	0.0
66 – 116	1.4 – 1.6	31.53×10^{-1}	0.1	0.4	0.4	0.1	0.0	0.3	0.0	0.0	0.0	0.2	0.0	0.0	0.0	0.0	0.0
66 – 116	1.6 – 1.8	30.42×10^{-1}	0.1	0.4	0.4	0.1	0.0	0.4	0.0	0.0	0.0	0.2	0.0	0.0	0.0	0.0	0.0
66 – 116	1.8 – 2.0	26.85×10^{-1}	0.1	0.4	0.5	0.1	0.0	0.4	0.0	0.0	0.0	0.1	0.0	0.0	0.0	0.0	0.0
66 – 116	2.0 – 2.2	18.88×10^{-1}	0.2	0.5	0.5	0.1	0.0	0.5	0.0	0.0	0.0	0.1	0.0	0.0	0.0	0.0	0.1
66 – 116	2.2 – 2.4	9.42×10^{-1}	0.3	0.6	0.7	0.1	0.0	0.6	0.0	0.0	0.0	0.1	0.0	0.0	0.0	0.0	0.1
116 – 150	0.0 – 0.2	8.05×10^{-2}	1.0	0.8	1.3	0.1	0.0	0.4	0.0	0.1	0.1	0.2	0.1	0.5	0.2	0.1	0.2
116 – 150	0.2 – 0.4	7.86×10^{-2}	1.0	0.8	1.3	0.1	0.0	0.4	0.0	0.1	0.1	0.3	0.1	0.5	0.3	0.1	0.2
116 – 150	0.4 – 0.6	7.79×10^{-2}	1.0	0.8	1.3	0.1	0.0	0.4	0.0	0.0	0.0	0.3	0.1	0.5	0.2	0.1	0.2
116 – 150	0.6 – 0.8	7.93×10^{-2}	1.0	0.7	1.3	0.1	0.0	0.4	0.0	0.2	0.1	0.2	0.1	0.5	0.1	0.1	0.2
116 – 150	0.8 – 1.0	7.87×10^{-2}	1.0	0.7	1.2	0.1	0.0	0.4	0.0	0.1	0.1	0.3	0.1	0.4	0.2	0.1	0.2
116 – 150	1.0 – 1.2	7.78×10^{-2}	1.0	0.7	1.2	0.1	0.0	0.3	0.0	0.1	0.0	0.3	0.1	0.3	0.2	0.1	0.2
116 – 150	1.2 – 1.4	7.59×10^{-2}	1.0	0.7	1.2	0.1	0.0	0.4	0.0	0.1	0.0	0.4	0.1	0.3	0.1	0.1	0.2
116 – 150	1.4 – 1.6	6.90×10^{-2}	1.1	0.7	1.3	0.1	0.0	0.4	0.0	0.1	0.1	0.4	0.1	0.2	0.2	0.1	0.3
116 – 150	1.6 – 1.8	5.87×10^{-2}	1.2	0.7	1.4	0.1	0.0	0.4	0.0	0.0	0.1	0.4	0.1	0.1	0.2	0.0	0.3
116 – 150	1.8 – 2.0	4.53×10^{-2}	1.4	0.8	1.6	0.1	0.0	0.5	0.0	0.2	0.1	0.5	0.1	0.1	0.1	0.0	0.4
116 – 150	2.0 – 2.2	3.12×10^{-2}	1.8	1.0	2.1	0.1	0.0	0.6	0.0	0.5	0.1	0.5	0.1	0.1	0.1	0.0	0.5
116 – 150	2.2 – 2.4	1.49×10^{-2}	3.3	1.7	3.7	0.1	0.0	0.7	0.0	0.7	0.2	0.9	0.1	0.1	0.2	0.0	1.0
150 – 200	0.0 – 0.2	2.03×10^{-2}	1.6	1.5	2.2	0.1	0.0	0.4	0.0	0.1	0.1	0.2	0.1	1.3	0.4	0.3	0.2
150 – 200	0.2 – 0.4	1.98×10^{-2}	1.6	1.7	2.3	0.1	0.0	0.4	0.0	0.1	0.1	0.2	0.1	1.4	0.7	0.3	0.3
150 – 200	0.4 – 0.6	1.99×10^{-2}	1.6	1.5	2.2	0.1	0.0	0.4	0.0	0.1	0.1	0.2	0.1	1.2	0.6	0.3	0.3
150 – 200	0.6 – 0.8	2.06×10^{-2}	1.6	1.3	2.0	0.1	0.0	0.4	0.0	0.1	0.1	0.2	0.1	1.1	0.5	0.2	0.3
150 – 200	0.8 – 1.0	2.01×10^{-2}	1.6	1.2	2.0	0.1	0.0	0.4	0.0	0.1	0.1	0.2	0.1	0.9	0.3	0.2	0.3
150 – 200	1.0 – 1.2	1.90×10^{-2}	1.6	1.0	2.0	0.1	0.0	0.4	0.0	0.0	0.0	0.2	0.1	0.8	0.4	0.1	0.3
150 – 200	1.2 – 1.4	1.80×10^{-2}	1.7	0.9	1.9	0.1	0.0	0.4	0.0	0.1	0.1	0.2	0.1	0.5	0.3	0.1	0.3
150 – 200	1.4 – 1.6	1.56×10^{-2}	1.9	0.9	2.1	0.1	0.0	0.5	0.0	0.0	0.1	0.3	0.1	0.4	0.5	0.1	0.3
150 – 200	1.6 – 1.8	1.31×10^{-2}	2.1	0.9	2.3	0.1	0.0	0.5	0.0	0.0	0.1	0.3	0.1	0.3	0.5	0.0	0.3
150 – 200	1.8 – 2.0	9.43×10^{-3}	2.6	0.9	2.7	0.1	0.0	0.6	0.0	0.1	0.1	0.4	0.1	0.2	0.3	0.0	0.4
150 – 200	2.0 – 2.2	6.71×10^{-3}	3.2	1.0	3.4	0.1	0.0	0.6	0.0	0.1	0.1	0.3	0.1	0.1	0.3	0.0	0.5
150 – 200	2.2 – 2.4	3.49×10^{-3}	5.5	1.5	5.7	0.1	0.0	0.7	0.0	0.2	0.3	0.6	0.1	0.1	0.3	0.0	1.1

Table C.7.: Muon channel Born level differential cross section $\frac{d\sigma}{dm_{\mu\mu}d|y_{\mu\mu}|}$ for the lowest three mass bins. The measurements are listed together with the statistical (δ^{stat}), systematic (δ^{sys}) and total (δ^{tot}) uncertainties. In addition the contributions from the individual correlated and uncorrelated systematic error sources are also provided consisting of the trigger efficiency (δ^{trig}), muon reconstruction efficiency (δ^{reco}), the MS resolution (δ^{MSres}), the ID resolution (δ^{IDres}), the muon transverse momentum scale (δ^{pT}), the isolation efficiency (δ^{Isol}), the electroweak background (δ^{ewk}), the multijet background (δ^{mult}) and the MC statistical uncertainty (δ^{MC}). The luminosity uncertainty of 2.8% is not included.

$m_{\mu\mu}^{min} - m_{\mu\mu}^{max}$ [GeV]	$\lvert y_{\mu\mu}^{min}\rvert - \lvert y_{\mu\mu}^{max}\rvert$	$\frac{d\sigma}{dm_{\mu\mu}d\lvert y_{\mu\mu}\rvert}$ [pb/GeV]	δ^{stat} [%]	δ^{sys} [%]	δ^{tot} [%]	δ_{cor}^{trig} [%]	δ_{unc}^{trig} [%]	δ_{cor}^{reco} [%]	δ_{unc}^{reco} [%]	δ_{unc}^{MSres} [%]	δ_{unc}^{IDres} [%]	δ_{unc}^{pT} [%]	δ_{unc}^{Isol} [%]	δ_{cor}^{ewk} [%]	δ_{unc}^{ewk} [%]	$\delta_{cor}^{mult.}$ [%]	δ_{unc}^{MC} [%]
200 − 300	0.0 − 0.2	4.92×10^{-3}	2.1	2.5	3.2	0.1	0.0	0.5	0.0	0.2	0.1	0.2	0.1	2.1	0.9	0.7	0.2
200 − 300	0.2 − 0.4	4.80×10^{-3}	2.1	2.3	3.2	0.1	0.0	0.5	0.0	0.2	0.0	0.2	0.1	2.0	0.7	0.6	0.2
200 − 300	0.4 − 0.6	4.65×10^{-3}	2.2	2.2	3.1	0.1	0.0	0.5	0.0	0.1	0.1	0.2	0.1	1.9	0.7	0.6	0.3
200 − 300	0.6 − 0.8	4.82×10^{-3}	2.2	1.9	2.9	0.1	0.0	0.5	0.0	0.2	0.1	0.2	0.1	1.6	0.6	0.4	0.3
200 − 300	0.8 − 1.0	4.46×10^{-3}	2.3	1.7	2.9	0.1	0.0	0.5	0.0	0.1	0.1	0.3	0.1	1.4	0.6	0.2	0.3
200 − 300	1.0 − 1.2	4.28×10^{-3}	2.4	1.4	2.8	0.1	0.0	0.5	0.0	0.1	0.1	0.2	0.1	1.0	0.6	0.2	0.3
200 − 300	1.2 − 1.4	3.81×10^{-3}	2.6	1.1	2.8	0.1	0.0	0.5	0.0	0.1	0.1	0.2	0.1	0.8	0.5	0.1	0.3
200 − 300	1.4 − 1.6	3.36×10^{-3}	2.8	1.0	3.0	0.1	0.0	0.5	0.0	0.1	0.0	0.3	0.1	0.5	0.5	0.1	0.3
200 − 300	1.6 − 1.8	2.66×10^{-3}	3.3	1.3	3.5	0.1	0.0	0.6	0.0	0.0	0.1	0.2	0.1	0.3	1.0	0.0	0.4
200 − 300	1.8 − 2.0	1.99×10^{-3}	3.9	1.0	4.1	0.1	0.0	0.7	0.0	0.1	0.2	0.3	0.1	0.2	0.4	0.0	0.5
200 − 300	2.0 − 2.2	1.17×10^{-3}	5.5	1.3	5.6	0.1	0.0	0.7	0.0	0.3	0.2	0.5	0.1	0.1	0.5	0.0	0.7
200 − 300	2.2 − 2.4	4.58×10^{-4}	10.6	2.1	10.8	0.1	0.0	0.9	0.0	0.4	0.3	0.5	0.1	0.1	0.9	0.0	1.6
300 − 500	0.0 − 0.4	7.42×10^{-4}	2.6	3.3	4.2	0.1	0.0	0.6	0.0	0.2	0.1	0.2	0.2	2.3	1.4	1.7	0.2
300 − 500	0.4 − 0.8	6.67×10^{-4}	2.9	2.5	3.8	0.1	0.0	0.6	0.0	0.1	0.0	0.2	0.2	1.9	1.0	1.1	0.2
300 − 500	0.8 − 1.2	6.24×10^{-4}	3.2	1.6	3.6	0.1	0.0	0.6	0.0	0.1	0.1	0.3	0.2	1.1	0.8	0.3	0.2
300 − 500	1.2 − 1.6	5.08×10^{-4}	3.7	1.1	3.8	0.1	0.0	0.6	0.0	0.1	0.1	0.2	0.2	0.5	0.6	0.1	0.3
300 − 500	1.6 − 2.0	2.59×10^{-4}	5.4	1.1	5.5	0.1	0.0	0.8	0.0	0.1	0.1	0.3	0.2	0.2	0.6	0.0	0.4
300 − 500	2.0 − 2.4	7.99×10^{-5}	11.0	1.9	11.1	0.1	0.0	1.0	0.0	0.3	0.1	0.5	0.2	0.1	0.7	0.0	1.3
500 − 1500	0.0 − 0.4	3.01×10^{-5}	6.3	2.6	6.8	0.1	0.0	0.7	0.0	0.3	0.3	0.2	0.4	1.4	1.6	0.9	0.3
500 − 1500	0.4 − 0.8	2.59×10^{-5}	6.9	2.2	7.3	0.1	0.0	0.7	0.0	0.2	0.3	0.2	0.4	1.1	1.5	0.6	0.3
500 − 1500	0.8 − 1.2	2.34×10^{-5}	7.7	1.6	7.8	0.1	0.0	0.8	0.0	0.1	0.2	0.3	0.4	0.6	1.1	0.2	0.3
500 − 1500	1.2 − 1.6	1.67×10^{-5}	9.4	1.3	9.5	0.1	0.0	0.8	0.0	0.1	0.1	0.3	0.4	0.2	0.7	0.0	0.5
500 − 1500	1.6 − 2.0	4.16×10^{-6}	18.9	2.3	19.0	0.1	0.0	1.1	0.0	0.8	0.5	0.2	0.4	0.2	1.0	0.0	1.3
500 − 1500	2.0 − 2.4	5.95×10^{-7}	44.7	12.0	46.3	0.1	0.0	2.0	0.0	1.9	2.8	0.5	0.4	0.1	0.5	0.0	11.3

Table C.8.: Muon channel Born level differential cross section $\frac{d\sigma}{dm_{\mu\mu}d|y_{\mu\mu}|}$ for the highest three mass bins. The measurements are listed together with the statistical (δ^{stat}), systematic (δ^{sys}) and total (δ^{tot}) uncertainties. In addition the contributions from the individual correlated and uncorrelated systematic error sources are also provided consisting of the trigger efficiency (δ^{trig}), muon reconstruction efficiency (δ^{reco}), the MS resolution (δ^{MSres}), the ID resolution (δ^{IDres}), the muon transverse momentum scale (δ^{pT}), the isolation efficiency (δ^{Isol}), the electroweak background (δ^{ewk}), the multijet background (δ^{mult}) and the MC statistical uncertainty (δ^{MC}). The luminosity uncertainty of 2.8% is not included.

$m_{\mu\mu}^{min} - m_{\mu\mu}^{max}$	$\lvert\Delta\eta_{\mu\mu}^{min}\rvert - \lvert\Delta\eta_{\mu\mu}^{max}\rvert$	$\frac{d\sigma}{dm_{\mu\mu}d\lvert\delta\eta_{\mu\mu}\rvert}$	δ^{stat}	δ^{sys}	δ^{tot}	δ_{cor}^{trig}	δ_{unc}^{trig}	δ_{cor}^{reco}	δ_{unc}^{reco}	δ_{unc}^{MSres}	δ_{unc}^{IDres}	δ_{unc}^{pT}	δ_{unc}^{Isol}	δ_{cor}^{ewk}	δ_{unc}^{ewk}	$\delta_{cor}^{multi.}$	δ_{unc}^{MC}
[GeV]		[pb/GeV]	[%]	[%]	[%]	[%]	[%]	[%]	[%]	[%]	[%]	[%]	[%]	[%]	[%]	[%]	[%]
66 – 116	0.00 – 0.25	63.87×10^{-1}	0.1	0.4	0.4	0.1	0.0	0.3	0.0	0.0	0.0	0.0	0.0	0.0	0.0	0.0	0.0
66 – 116	0.25 – 0.50	60.01×10^{-1}	0.1	0.3	0.4	0.1	0.0	0.3	0.0	0.0	0.0	0.0	0.0	0.0	0.0	0.0	0.0
66 – 116	0.50 – 0.75	55.13×10^{-1}	0.1	0.3	0.4	0.1	0.0	0.3	0.0	0.0	0.0	0.1	0.0	0.0	0.0	0.0	0.0
66 – 116	0.75 – 1.00	48.39×10^{-1}	0.1	0.4	0.4	0.1	0.0	0.3	0.0	0.0	0.0	0.1	0.0	0.0	0.0	0.0	0.0
66 – 116	1.00 – 1.25	34.55×10^{-1}	0.1	0.5	0.5	0.1	0.0	0.3	0.0	0.0	0.0	0.4	0.1	0.0	0.0	0.0	0.0
66 – 116	1.25 – 1.50	14.81×10^{-1}	0.2	0.8	0.8	0.1	0.0	0.3	0.0	0.1	0.1	0.7	0.1	0.0	0.0	0.0	0.1
66 – 116	1.50 – 1.75	3.27×10^{-1}	0.4	1.1	1.1	0.1	0.0	0.3	0.0	0.2	0.2	0.9	0.1	0.1	0.0	0.0	0.1
66 – 116	1.75 – 2.00	7.17×10^{-2}	0.8	0.8	1.1	0.1	0.0	0.3	0.0	0.1	0.1	0.6	0.1	0.1	0.1	0.0	0.3
66 – 116	2.00 – 2.25	8.34×10^{-3}	2.4	1.4	2.8	0.1	0.0	0.4	0.0	0.4	0.1	1.1	0.1	0.3	0.3	0.0	0.4
66 – 116	2.25 – 2.50	1.82×10^{-4}	14.4	5.8	15.5	0.1	0.0	0.4	0.0	1.5	1.1	2.8	0.1	1.6	4.3	0.2	0.1
66 – 116	2.50 – 2.75	0.00×10^{0}	0.0	nan	nan	0.0	0.0	0.0	0.0	0.0	0.0	0.0	0.0	0.0	nan	0.0	0.0
66 – 116	3.00 – 3.00	0.00×10^{0}	0.0	nan	nan	0.0	0.0	0.0	0.0	0.0	0.0	0.0	0.0	0.0	nan	0.0	0.0
116 – 150	0.00 – 0.25	9.79×10^{-2}	0.8	0.6	1.0	0.1	0.0	0.4	0.0	0.1	0.0	0.3	0.1	0.3	0.1	0.0	0.2
116 – 150	0.25 – 0.50	9.21×10^{-2}	0.9	0.7	1.1	0.1	0.0	0.4	0.0	0.1	0.1	0.3	0.1	0.3	0.2	0.0	0.2
116 – 150	0.50 – 0.75	8.87×10^{-2}	0.9	0.6	1.1	0.1	0.0	0.4	0.0	0.1	0.0	0.3	0.1	0.3	0.1	0.0	0.2
116 – 150	0.75 – 1.00	7.98×10^{-2}	0.9	0.7	1.2	0.1	0.0	0.4	0.0	0.1	0.1	0.4	0.1	0.3	0.1	0.1	0.2
116 – 150	1.00 – 1.25	7.29×10^{-2}	1.0	0.7	1.2	0.1	0.0	0.4	0.0	0.1	0.1	0.3	0.1	0.4	0.1	0.1	0.2
116 – 150	1.25 – 1.50	6.18×10^{-2}	1.1	0.7	1.3	0.1	0.0	0.4	0.0	0.0	0.1	0.3	0.1	0.4	0.2	0.1	0.3
116 – 150	1.50 – 1.75	5.02×10^{-2}	1.2	0.8	1.4	0.1	0.0	0.4	0.0	0.1	0.0	0.4	0.1	0.4	0.2	0.1	0.3
116 – 150	1.75 – 2.00	4.04×10^{-2}	1.3	0.9	1.6	0.1	0.0	0.4	0.0	0.2	0.1	0.4	0.1	0.4	0.3	0.2	0.3
116 – 150	2.00 – 2.25	2.25×10^{-2}	1.7	1.1	2.0	0.1	0.0	0.4	0.0	0.1	0.3	0.4	0.1	0.6	0.4	0.3	0.4
116 – 150	2.25 – 2.50	7.51×10^{-3}	2.9	1.8	3.4	0.1	0.0	0.4	0.0	0.1	0.2	0.2	0.1	0.9	1.3	0.4	0.6
116 – 150	2.50 – 2.75	1.16×10^{-3}	6.6	3.2	7.3	0.1	0.0	0.4	0.0	0.5	0.4	0.4	0.1	1.7	2.0	0.6	1.4
116 – 150	3.00 – 3.00	8.94×10^{-6}	37.8	88.4	96.2	0.4	0.1	1.6	0.1	21.5	9.7	8.6	0.3	22.7	81.6	4.2	0.7
150 – 200	0.00 – 0.25	2.17×10^{-2}	1.4	0.9	1.7	0.1	0.0	0.5	0.0	0.1	0.1	0.2	0.1	0.6	0.4	0.1	0.2
150 – 200	0.25 – 0.50	2.05×10^{-2}	1.5	0.9	1.7	0.1	0.0	0.5	0.0	0.0	0.1	0.2	0.1	0.6	0.2	0.0	0.2
150 – 200	0.50 – 0.75	1.89×10^{-2}	1.5	0.9	1.8	0.1	0.0	0.4	0.0	0.1	0.0	0.2	0.1	0.6	0.3	0.1	0.2
150 – 200	0.75 – 1.00	1.79×10^{-2}	1.6	1.0	1.8	0.1	0.0	0.4	0.0	0.1	0.0	0.2	0.1	0.7	0.3	0.1	0.3
150 – 200	1.00 – 1.25	1.55×10^{-2}	1.7	1.2	2.1	0.1	0.0	0.5	0.0	0.0	0.0	0.2	0.1	0.9	0.6	0.1	0.3
150 – 200	1.25 – 1.50	1.37×10^{-2}	1.8	1.3	2.2	0.1	0.0	0.5	0.0	0.0	0.1	0.2	0.1	1.0	0.6	0.2	0.3
150 – 200	1.50 – 1.75	1.18×10^{-2}	1.9	1.3	2.3	0.1	0.0	0.5	0.0	0.1	0.0	0.2	0.1	1.1	0.4	0.2	0.3
150 – 200	1.75 – 2.00	9.81×10^{-3}	2.0	1.5	2.6	0.1	0.0	0.5	0.0	0.0	0.0	0.2	0.1	1.2	0.7	0.3	0.4
150 – 200	2.00 – 2.25	7.60×10^{-3}	2.3	1.8	2.9	0.1	0.0	0.5	0.0	0.0	0.3	0.2	0.1	1.4	0.6	0.4	0.5
150 – 200	2.25 – 2.50	5.69×10^{-3}	2.6	2.2	3.4	0.1	0.0	0.5	0.0	0.1	0.1	0.2	0.1	1.5	1.4	0.7	0.5
150 – 200	2.50 – 2.75	3.98×10^{-3}	3.1	1.9	3.6	0.1	0.0	0.4	0.0	0.1	0.0	0.2	0.1	1.3	0.8	0.8	0.6
150 – 200	3.00 – 3.00	1.61×10^{-3}	4.6	2.9	5.4	0.1	0.0	0.4	0.0	0.3	0.1	0.4	0.1	1.7	1.5	1.1	1.0

Table C.9.: Muon channel Born level differential cross section $\frac{d\sigma}{dm_{\mu\mu}d|\delta\eta_{\mu\mu}|}$ for the lowest three mass bins. The measurements are listed together with the statistical (δ^{stat}), systematic (δ^{sys}) and total (δ^{tot}) uncertainties. In addition the contributions from the individual correlated and uncorrelated systematic error sources are also provided consisting of the trigger efficiency (δ^{trig}), muon reconstruction efficiency (δ^{reco}), the MS resolution (δ^{MSres}), the ID resolution (δ^{IDres}), the muon transverse momentum scale (δ^{pT}), the isolation efficiency (δ^{Isol}), the electroweak background (δ^{ewk}), the multijet background (δ^{mult}) and the MC statistical uncertainty (δ^{MC}). The luminosity uncertainty of 2.8% is not included.

$m_{\mu\mu}^{min} - m_{\mu\mu}^{max}$	$\lvert\Delta\eta_{\mu\mu}^{min}\rvert - \lvert\Delta\eta_{\mu\mu}^{max}\rvert$	$\frac{d\sigma}{dm_{\mu\mu}d\lvert\delta\eta_{\mu\mu}\rvert}$	δ^{stat}	δ^{sys}	δ^{tot}	$\delta_{cor}^{\text{trig}}$	$\delta_{unc}^{\text{trig}}$	$\delta_{cor}^{\text{reco}}$	$\delta_{unc}^{\text{reco}}$	$\delta_{unc}^{\text{MSres}}$	$\delta_{unc}^{\text{IDres}}$	δ_{unc}^{pT}	$\delta_{unc}^{\text{Isol}}$	$\delta_{cor}^{\text{ewk}}$	$\delta_{unc}^{\text{ewk}}$	$\delta_{cor}^{\text{multi.}}$	δ_{unc}^{MC}
[GeV]		[pb/GeV]	[%]	[%]	[%]	[%]	[%]	[%]	[%]	[%]	[%]	[%]	[%]	[%]	[%]	[%]	[%]
$200 - 300$	$0.00 - 0.25$	4.43×10^{-3}	2.2	1.0	2.4	0.1	0.0	0.5	0.0	0.1	0.1	0.3	0.1	0.6	0.4	0.1	0.2
$200 - 300$	$0.25 - 0.50$	4.20×10^{-3}	2.3	1.0	2.5	0.1	0.0	0.5	0.0	0.1	0.0	0.3	0.1	0.7	0.4	0.1	0.2
$200 - 300$	$0.50 - 0.75$	3.96×10^{-3}	2.3	1.1	2.6	0.1	0.0	0.5	0.0	0.1	0.0	0.2	0.1	0.8	0.4	0.1	0.2
$200 - 300$	$0.75 - 1.00$	3.81×10^{-3}	2.4	1.2	2.7	0.1	0.0	0.5	0.0	0.2	0.1	0.2	0.1	0.9	0.5	0.1	0.3
$200 - 300$	$1.00 - 1.25$	3.24×10^{-3}	2.5	1.6	3.0	0.1	0.0	0.5	0.0	0.1	0.0	0.2	0.1	1.1	0.8	0.1	0.3
$200 - 300$	$1.25 - 1.50$	2.94×10^{-3}	2.6	1.7	3.1	0.1	0.0	0.5	0.0	0.1	0.1	0.2	0.1	1.4	0.7	0.2	0.3
$200 - 300$	$1.50 - 1.75$	2.57×10^{-3}	2.7	1.9	3.3	0.1	0.0	0.6	0.0	0.1	0.1	0.2	0.1	1.6	0.8	0.3	0.3
$200 - 300$	$1.75 - 2.00$	2.18×10^{-3}	2.9	2.5	3.8	0.1	0.0	0.6	0.0	0.1	0.1	0.3	0.1	1.8	1.5	0.3	0.3
$200 - 300$	$2.00 - 2.25$	1.79×10^{-3}	3.2	2.5	4.1	0.1	0.0	0.6	0.0	0.1	0.2	0.2	0.1	2.1	1.1	0.5	0.4
$200 - 300$	$2.25 - 2.50$	1.28×10^{-3}	3.6	3.3	4.9	0.2	0.0	0.6	0.0	0.1	0.1	0.3	0.1	2.7	1.5	0.9	0.4
$200 - 300$	$2.50 - 2.75$	1.03×10^{-3}	3.9	3.6	5.3	0.1	0.0	0.6	0.0	0.2	0.1	0.3	0.1	2.8	1.7	1.3	0.5
$200 - 300$	$3.00 - 3.00$	7.54×10^{-4}	4.5	4.2	6.1	0.1	0.0	0.6	0.0	0.1	0.2	0.3	0.1	3.1	2.1	1.8	0.6
$300 - 500$	$0.00 - 0.50$	5.37×10^{-4}	3.2	1.1	3.4	0.1	0.0	0.6	0.0	0.1	0.1	0.2	0.2	0.6	0.5	0.2	0.2
$300 - 500$	$0.50 - 1.00$	5.30×10^{-4}	3.2	1.1	3.4	0.1	0.0	0.6	0.0	0.0	0.1	0.2	0.2	0.7	0.6	0.1	0.2
$300 - 500$	$1.00 - 1.50$	4.35×10^{-4}	3.5	1.4	3.8	0.1	0.0	0.6	0.0	0.1	0.1	0.1	0.2	1.0	0.8	0.2	0.3
$300 - 500$	$1.50 - 2.00$	3.53×10^{-4}	3.7	2.1	4.3	0.1	0.0	0.6	0.0	0.3	0.1	0.3	0.2	1.5	1.1	0.4	0.3
$300 - 500$	$2.00 - 2.50$	1.89×10^{-4}	4.5	4.1	6.1	0.2	0.0	0.7	0.0	0.1	0.2	0.4	0.2	3.2	2.1	1.2	0.4
$300 - 500$	$2.50 - 3.00$	1.40×10^{-4}	5.1	4.9	7.1	0.1	0.0	0.7	0.0	0.2	0.0	0.5	0.2	3.5	2.5	2.1	0.5
$500 - 1500$	$0.00 - 0.50$	1.63×10^{-5}	8.3	1.3	8.4	0.1	0.0	0.8	0.0	0.1	0.1	0.2	0.5	0.3	0.8	0.1	0.4
$500 - 1500$	$0.50 - 1.00$	1.76×10^{-5}	8.1	1.3	8.2	0.1	0.0	0.7	0.0	0.1	0.1	0.3	0.4	0.3	0.7	0.0	0.4
$500 - 1500$	$1.00 - 1.50$	1.45×10^{-5}	8.8	1.7	8.9	0.1	0.0	0.8	0.0	0.1	0.1	0.3	0.4	0.5	1.2	0.1	0.4
$500 - 1500$	$1.50 - 2.00$	1.42×10^{-5}	8.8	1.9	9.0	0.1	0.0	0.7	0.0	0.1	0.2	0.2	0.3	0.6	1.5	0.2	0.4
$500 - 1500$	$2.00 - 2.50$	9.39×10^{-6}	10.3	3.1	10.7	0.1	0.0	0.8	0.0	0.2	0.1	0.2	0.3	1.3	2.5	0.5	0.5
$500 - 1500$	$2.50 - 3.00$	5.61×10^{-6}	12.2	4.8	13.1	0.1	0.0	0.8	0.0	0.2	0.0	0.2	0.3	2.2	4.0	1.1	0.7

Table C.10.: Muon channel Born level differential cross section $\frac{d\sigma}{dm_{\mu\mu}d|\delta\eta_{\mu\mu}|}$ for the highest three mass bins. The measurements are listed together with the statistical (δ^{stat}), systematic (δ^{sys}) and total (δ^{tot}) uncertainties. In addition the contributions from the individual correlated and uncorrelated systematic error sources are also provided consisting of the trigger efficiency (δ^{trig}), muon reconstruction efficiency (δ^{reco}), the MS resolution (δ^{MSres}), the ID resolution (δ^{IDres}), the muon transverse momentum scale (δ^{pT}), the isolation efficiency (δ^{Isol}), the electroweak background (δ^{ewk}), the multijet background (δ^{mult}) and the MC statistical uncertainty (δ^{MC}). The luminosity uncertainty of 2.8% is not included.

Appendix D.

Theoretical Predictions Tables

Theoretical predictions of the fiducial Drell-Yan cross section have been performed to NNLO using FEWZ [35] with the CT10 PDF. Higher order electroweak corrections have been applied to NLO. The cross sections are shown in for the single differential, double differential dimuon mass and rapidity and dimuon mass and muon $\Delta\eta$ measurements in tables D.5, D.3 and D.5 respectively.

In addition to the Drell-Yan theoretical predictions, photon induced cross sections have been calculated using FEWZ with the MRST2004qed PDF. These cross sections are shown in tables D.2, D.4 and D.6 for the single differential, double differential dimuon mass and rapidity, and dimuon mass and muon $\Delta\eta$ measurements respectively.

$m_{\ell\ell}$ [GeV]	$\frac{\mathrm{d}\sigma}{\mathrm{d}m_{\ell\ell}}$ [pb/GeV]	δ^{stat} [%]	δ^{pdf} [%]	$\delta^{\alpha_{\mathrm{s}}}$ [%]
$130 - 150$	1.00×10^{-1}	0.1	$^{+1.9}_{-2.4}$	$^{+0.9}_{-0.8}$
$150 - 175$	4.72×10^{-2}	0.1	$^{+2.0}_{-2.3}$	$^{+0.8}_{-0.8}$
$175 - 200$	2.42×10^{-2}	0.1	$^{+2.0}_{-2.2}$	$^{+0.8}_{-0.7}$
$200 - 230$	1.32×10^{-2}	0.1	$^{+2.1}_{-2.2}$	$^{+0.7}_{-0.7}$
$230 - 260$	7.44×10^{-3}	0.1	$^{+2.2}_{-2.2}$	$^{+0.6}_{-0.6}$
$260 - 300$	4.18×10^{-3}	0.1	$^{+2.3}_{-2.3}$	$^{+0.5}_{-0.6}$
$300 - 380$	1.84×10^{-3}	0.0	$^{+2.5}_{-2.5}$	$^{+0.4}_{-0.5}$
$380 - 500$	5.88×10^{-4}	0.0	$^{+2.9}_{-2.8}$	$^{+0.2}_{-0.4}$
$500 - 700$	1.41×10^{-4}	0.0	$^{+3.5}_{-3.5}$	$^{+0.0}_{-0.2}$
$700 - 1000$	2.42×10^{-5}	0.0	$^{+4.4}_{-4.4}$	$^{-0.3}_{-0.1}$
$1000 - 1500$	2.83×10^{-6}	0.1	$^{+5.9}_{-5.5}$	$^{-0.5}_{+0.2}$

Table D.1.: Born level differential fiducial cross section $\frac{\mathrm{d}\sigma}{\mathrm{d}m_{\ell\ell}}$ at NNLO including NLO electroweak corrections. The calculation is performed using the CT10 NNLO PDF set and with dynamic scales $\mu_r = \mu_f = m_{\ell\ell}$. The predictions are listed together with the statistical uncertainty (δ^{stat}), the PDF eigenvector variation (δ^{pdf}) and the uncertainty from the variation of α_s ($\delta^{\alpha_{\mathrm{s}}}$).

$m_{\ell\ell}$ [GeV]	$\frac{\mathrm{d}\sigma}{\mathrm{d}m_{\ell\ell}}$ [pb/GeV]	δ^{stat} [%]	δ^{pdf} [%]	$\delta^{\alpha_{\mathrm{s}}}$ [%]
$116 - 130$	1.57×10^{-3}	0.0	$^{+36.4}_{-36.4}$	$^{+0.0}_{+0.0}$
$130 - 150$	1.15×10^{-3}	0.0	$^{+36.8}_{-36.8}$	$^{+0.0}_{+0.0}$
$150 - 175$	7.57×10^{-4}	0.0	$^{+37.2}_{-37.2}$	$^{+0.0}_{+0.0}$
$175 - 200$	4.89×10^{-4}	0.0	$^{+37.8}_{-37.8}$	$^{+0.0}_{+0.0}$
$200 - 230$	3.14×10^{-4}	0.0	$^{+38.3}_{-38.3}$	$^{+0.0}_{+0.0}$
$230 - 260$	2.00×10^{-4}	0.0	$^{+38.9}_{-38.9}$	$^{+0.0}_{+0.0}$
$260 - 300$	1.24×10^{-4}	0.0	$^{+39.5}_{-39.5}$	$^{+0.0}_{+0.0}$
$300 - 380$	6.12×10^{-5}	0.0	$^{+40.4}_{-40.4}$	$^{+0.0}_{+0.0}$
$380 - 500$	2.19×10^{-5}	0.0	$^{+41.8}_{-41.8}$	$^{+0.0}_{+0.0}$
$500 - 700$	5.83×10^{-6}	0.0	$^{+43.7}_{-43.7}$	$^{+0.0}_{+0.0}$
$700 - 1000$	1.14×10^{-6}	0.0	$^{+46.3}_{-46.3}$	$^{+0.0}_{+0.0}$
$1000 - 1500$	1.60×10^{-7}	0.1	$^{+49.5}_{-49.5}$	$^{+0.0}_{+0.0}$

Table D.2.: Photon Induced differential fiducial cross section $\frac{\mathrm{d}\sigma}{\mathrm{d}m_{\ell\ell}}$. The calculation is performed using the MRST2004QED PDF set and with dynamic scales $\mu_r = \mu_f = m_{\ell\ell}$. The predictions are listed together with the statistical uncertainty (δ^{stat}), the PDF eigenvector variation (δ^{pdf}) and the uncertainty from the variation of α_s ($\delta^{\alpha_{\mathrm{s}}}$).

$m_{\ell\ell}$ [GeV]	$\lvert y_{\ell\ell}\rvert$	$\frac{d\sigma}{dm_{\ell\ell}d\lvert y_{\ell\ell}\rvert}$ [pb/GeV]	δ^{stat} [%]	δ^{pdf} [%]	δ^{α_s} [%]
$116-150$	$0.0-0.2$	3.88×10^{-2}	0.3	$^{+2.3}_{-3.1}$	$^{+1.1}_{-0.7}$
$116-150$	$0.2-0.4$	3.88×10^{-2}	0.4	$^{+2.3}_{-3.1}$	$^{+1.0}_{-0.9}$
$116-150$	$0.4-0.6$	3.89×10^{-2}	0.4	$^{+2.2}_{-3.0}$	$^{+1.0}_{-0.8}$
$116-150$	$0.6-0.8$	3.86×10^{-2}	0.4	$^{+2.1}_{-2.8}$	$^{+1.3}_{-0.6}$
$116-150$	$0.8-1.0$	3.83×10^{-2}	0.4	$^{+2.1}_{-2.6}$	$^{+0.9}_{-0.8}$
$116-150$	$1.0-1.2$	3.78×10^{-2}	0.4	$^{+2.0}_{-2.4}$	$^{+0.9}_{-1.1}$
$116-150$	$1.2-1.4$	3.69×10^{-2}	0.4	$^{+1.9}_{-2.3}$	$^{+0.9}_{-0.7}$
$116-150$	$1.4-1.6$	3.39×10^{-2}	0.4	$^{+1.9}_{-2.2}$	$^{+0.9}_{-0.9}$
$116-150$	$1.6-1.8$	2.84×10^{-2}	0.5	$^{+1.8}_{-2.1}$	$^{+0.8}_{-0.9}$
$116-150$	$1.8-2.0$	2.20×10^{-2}	0.5	$^{+1.8}_{-2.0}$	$^{+0.8}_{-0.8}$
$116-150$	$2.0-2.2$	1.45×10^{-2}	0.6	$^{+1.8}_{-2.0}$	$^{+0.5}_{-1.0}$
$116-150$	$2.2-2.4$	7.00×10^{-3}	1.0	$^{+1.8}_{-2.0}$	$^{+0.8}_{-0.8}$
$150-200$	$0.0-0.2$	9.70×10^{-3}	0.2	$^{+2.5}_{-3.0}$	$^{+0.9}_{-0.6}$
$150-200$	$0.2-0.4$	9.69×10^{-3}	0.4	$^{+2.4}_{-2.9}$	$^{+0.9}_{-0.8}$
$150-200$	$0.4-0.6$	9.66×10^{-3}	0.4	$^{+2.3}_{-2.8}$	$^{+1.0}_{-0.6}$
$150-200$	$0.6-0.8$	9.66×10^{-3}	0.3	$^{+2.2}_{-2.6}$	$^{+0.8}_{-0.8}$
$150-200$	$0.8-1.0$	9.49×10^{-3}	0.4	$^{+2.1}_{-2.4}$	$^{+0.6}_{-0.9}$
$150-200$	$1.0-1.2$	9.28×10^{-3}	0.4	$^{+2.0}_{-2.2}$	$^{+0.9}_{-0.7}$
$150-200$	$1.2-1.4$	8.55×10^{-3}	0.4	$^{+1.9}_{-2.1}$	$^{+0.7}_{-0.8}$
$150-200$	$1.4-1.6$	7.60×10^{-3}	0.4	$^{+1.8}_{-2.0}$	$^{+0.7}_{-0.8}$
$150-200$	$1.6-1.8$	6.28×10^{-3}	0.4	$^{+1.7}_{-2.0}$	$^{+0.7}_{-0.7}$
$150-200$	$1.8-2.0$	4.68×10^{-3}	0.5	$^{+1.7}_{-1.9}$	$^{+0.7}_{-0.7}$
$150-200$	$2.0-2.2$	3.07×10^{-3}	0.6	$^{+1.7}_{-1.9}$	$^{+0.5}_{-0.8}$
$150-200$	$2.2-2.4$	1.42×10^{-3}	0.9	$^{+1.8}_{-2.0}$	$^{+0.6}_{-0.2}$
$200-300$	$0.0-0.2$	2.25×10^{-3}	0.2	$^{+2.8}_{-2.9}$	$^{+0.8}_{-0.6}$
$200-300$	$0.2-0.4$	2.24×10^{-3}	0.3	$^{+2.8}_{-2.8}$	$^{+0.7}_{-0.7}$
$200-300$	$0.4-0.6$	2.25×10^{-3}	0.3	$^{+2.6}_{-2.7}$	$^{+0.7}_{-0.6}$
$200-300$	$0.6-0.8$	2.21×10^{-3}	0.3	$^{+2.5}_{-2.5}$	$^{+0.8}_{-0.7}$
$200-300$	$0.8-1.0$	2.14×10^{-3}	0.3	$^{+2.2}_{-2.3}$	$^{+0.6}_{-0.7}$
$200-300$	$1.0-1.2$	2.03×10^{-3}	0.3	$^{+2.0}_{-2.2}$	$^{+0.6}_{-0.7}$
$200-300$	$1.2-1.4$	1.84×10^{-3}	0.3	$^{+1.9}_{-2.0}$	$^{+0.7}_{-0.7}$
$200-300$	$1.4-1.6$	1.61×10^{-3}	0.3	$^{+1.8}_{-2.0}$	$^{+0.5}_{-0.5}$
$200-300$	$1.6-1.8$	1.31×10^{-3}	0.4	$^{+1.7}_{-1.9}$	$^{+0.3}_{-0.8}$
$200-300$	$1.8-2.0$	9.46×10^{-4}	0.4	$^{+1.7}_{-1.9}$	$^{+0.6}_{-0.3}$
$200-300$	$2.0-2.2$	5.76×10^{-4}	0.5	$^{+1.7}_{-1.9}$	$^{+0.4}_{-0.4}$
$200-300$	$2.2-2.4$	2.44×10^{-4}	0.9	$^{+1.8}_{-2.0}$	$^{+0.7}_{+0.0}$
$300-500$	$0.0-0.4$	3.37×10^{-4}	0.1	$^{+3.5}_{-3.3}$	$^{+0.5}_{-0.6}$
$300-500$	$0.4-0.8$	3.27×10^{-4}	0.1	$^{+3.1}_{-3.0}$	$^{+0.4}_{-0.6}$
$300-500$	$0.8-1.2$	2.98×10^{-4}	0.1	$^{+2.5}_{-2.5}$	$^{+0.4}_{-0.5}$
$300-500$	$1.2-1.6$	2.33×10^{-4}	0.1	$^{+2.0}_{-2.2}$	$^{+0.3}_{-0.3}$
$300-500$	$1.6-2.0$	1.31×10^{-4}	0.2	$^{+1.9}_{-2.1}$	$^{+0.1}_{-0.2}$
$300-500$	$2.0-2.4$	3.57×10^{-5}	0.5	$^{+2.0}_{-2.1}$	$^{+0.1}_{+0.4}$
$500-1500$	$0.0-0.4$	1.35×10^{-5}	0.1	$^{+4.7}_{-4.7}$	$^{-0.0}_{-0.4}$
$500-1500$	$0.4-0.8$	1.28×10^{-5}	0.1	$^{+4.1}_{-4.1}$	$^{-0.0}_{-0.3}$
$500-1500$	$0.8-1.2$	1.06×10^{-5}	0.1	$^{+3.4}_{-3.4}$	$^{+0.0}_{+0.1}$
$500-1500$	$1.2-1.6$	6.60×10^{-6}	0.1	$^{+2.8}_{-2.9}$	$^{-0.3}_{+0.0}$
$500-1500$	$1.6-2.0$	2.33×10^{-6}	0.2	$^{+2.5}_{-2.6}$	$^{-0.5}_{+0.4}$
$500-1500$	$2.0-2.4$	2.57×10^{-7}	0.7	$^{+3.4}_{-3.3}$	$^{-0.4}_{+0.5}$

Table D.3.: Born level differential fiducial cross section $\frac{d\sigma}{dm_{\ell\ell}d|y_{\ell\ell}|}$ at NNLO including NLO electroweak corrections. The calculation is performed using the CT10 NNLO PDF set and with dynamic scales $\mu_r = \mu_f = m_{\ell\ell}$. The predictions are listed together with the statistical uncertainty (δ^{stat}), the PDF eigenvector variation (δ^{pdf}) and the uncertainty from the variation of α_s (δ^{α_s}).

$m_{\ell\ell}$ [GeV]	$\lvert y_{\ell\ell}\rvert$	$\frac{d\sigma}{dm_{\ell\ell}d\lvert y_{\ell\ell}\rvert}$ [pb/GeV]	$\delta^{\rm stat}$ [%]	$\delta^{\rm pdf}$ [%]	δ^{α_s} [%]
$116-150$	$0.0-0.2$	3.90×10^{-4}	0.0	$^{+35.9}_{-35.9}$	$^{+0.0}_{+0.0}$
$116-150$	$0.2-0.4$	3.87×10^{-4}	0.0	$^{+36.0}_{-36.0}$	$^{+0.0}_{+0.0}$
$116-150$	$0.4-0.6$	3.82×10^{-4}	0.0	$^{+36.0}_{-36.0}$	$^{+0.0}_{+0.0}$
$116-150$	$0.6-0.8$	3.74×10^{-4}	0.0	$^{+36.2}_{-36.2}$	$^{+0.0}_{+0.0}$
$116-150$	$0.8-1.0$	3.63×10^{-4}	0.0	$^{+36.4}_{-36.4}$	$^{+0.0}_{+0.0}$
$116-150$	$1.0-1.2$	3.49×10^{-4}	0.0	$^{+36.6}_{-36.6}$	$^{+0.0}_{+0.0}$
$116-150$	$1.2-1.4$	3.30×10^{-4}	0.0	$^{+36.9}_{-36.9}$	$^{+0.0}_{+0.0}$
$116-150$	$1.4-1.6$	2.81×10^{-4}	0.0	$^{+37.2}_{-37.2}$	$^{+0.0}_{+0.0}$
$116-150$	$1.6-1.8$	2.02×10^{-4}	0.1	$^{+37.6}_{-37.6}$	$^{+0.0}_{+0.0}$
$116-150$	$1.8-2.0$	1.31×10^{-4}	0.1	$^{+38.1}_{-38.1}$	$^{+0.0}_{+0.0}$
$116-150$	$2.0-2.2$	7.39×10^{-5}	0.1	$^{+38.7}_{-38.7}$	$^{+0.0}_{+0.0}$
$116-150$	$2.2-2.4$	3.11×10^{-5}	0.2	$^{+39.4}_{-39.4}$	$^{+0.0}_{+0.0}$
$150-200$	$0.0-0.2$	2.06×10^{-4}	0.0	$^{+36.8}_{-36.8}$	$^{+0.0}_{+0.0}$
$150-200$	$0.2-0.4$	2.04×10^{-4}	0.0	$^{+36.9}_{-36.9}$	$^{+0.0}_{+0.0}$
$150-200$	$0.4-0.6$	2.01×10^{-4}	0.0	$^{+37.0}_{-37.0}$	$^{+0.0}_{+0.0}$
$150-200$	$0.6-0.8$	1.95×10^{-4}	0.0	$^{+37.1}_{-37.1}$	$^{+0.0}_{+0.0}$
$150-200$	$0.8-1.0$	1.88×10^{-4}	0.0	$^{+37.3}_{-37.3}$	$^{+0.0}_{+0.0}$
$150-200$	$1.0-1.2$	1.73×10^{-4}	0.0	$^{+37.6}_{-37.6}$	$^{+0.0}_{+0.0}$
$150-200$	$1.2-1.4$	1.40×10^{-4}	0.0	$^{+37.9}_{-37.9}$	$^{+0.0}_{+0.0}$
$150-200$	$1.4-1.6$	1.02×10^{-4}	0.1	$^{+38.3}_{-38.3}$	$^{+0.0}_{+0.0}$
$150-200$	$1.6-1.8$	6.99×10^{-5}	0.1	$^{+38.8}_{-38.8}$	$^{+0.0}_{+0.0}$
$150-200$	$1.8-2.0$	4.39×10^{-5}	0.1	$^{+39.3}_{-39.3}$	$^{+0.0}_{+0.0}$
$150-200$	$2.0-2.2$	2.39×10^{-5}	0.1	$^{+40.0}_{-40.0}$	$^{+0.0}_{+0.0}$
$150-200$	$2.2-2.4$	9.60×10^{-6}	0.3	$^{+40.9}_{-40.9}$	$^{+0.0}_{+0.0}$
$200-300$	$0.0-0.2$	7.83×10^{-5}	0.0	$^{+38.1}_{-38.1}$	$^{+0.0}_{+0.0}$
$200-300$	$0.2-0.4$	7.74×10^{-5}	0.0	$^{+38.2}_{-38.2}$	$^{+0.0}_{+0.0}$
$200-300$	$0.4-0.6$	7.55×10^{-5}	0.0	$^{+38.3}_{-38.3}$	$^{+0.0}_{+0.0}$
$200-300$	$0.6-0.8$	7.10×10^{-5}	0.0	$^{+38.5}_{-38.5}$	$^{+0.0}_{+0.0}$
$200-300$	$0.8-1.0$	6.16×10^{-5}	0.0	$^{+38.7}_{-38.7}$	$^{+0.0}_{+0.0}$
$200-300$	$1.0-1.2$	4.86×10^{-5}	0.0	$^{+39.0}_{-39.0}$	$^{+0.0}_{+0.0}$
$200-300$	$1.2-1.4$	3.65×10^{-5}	0.1	$^{+39.4}_{-39.4}$	$^{+0.0}_{+0.0}$
$200-300$	$1.4-1.6$	2.59×10^{-5}	0.1	$^{+39.9}_{-39.9}$	$^{+0.0}_{+0.0}$
$200-300$	$1.6-1.8$	1.71×10^{-5}	0.1	$^{+40.5}_{-40.5}$	$^{+0.0}_{+0.0}$
$200-300$	$1.8-2.0$	1.01×10^{-5}	0.1	$^{+41.2}_{-41.2}$	$^{+0.0}_{+0.0}$
$200-300$	$2.0-2.2$	5.18×10^{-6}	0.2	$^{+42.2}_{-42.2}$	$^{+0.0}_{+0.0}$
$200-300$	$2.2-2.4$	1.90×10^{-6}	0.4	$^{+43.3}_{-43.3}$	$^{+0.0}_{+0.0}$
$300-500$	$0.0-0.4$	1.77×10^{-5}	0.0	$^{+40.3}_{-40.3}$	$^{+0.0}_{+0.0}$
$300-500$	$0.4-0.8$	1.40×10^{-5}	0.0	$^{+40.5}_{-40.5}$	$^{+0.0}_{+0.0}$
$300-500$	$0.8-1.2$	8.84×10^{-6}	0.0	$^{+41.1}_{-41.1}$	$^{+0.0}_{+0.0}$
$300-500$	$1.2-1.6$	4.53×10^{-6}	0.1	$^{+42.2}_{-42.2}$	$^{+0.0}_{+0.0}$
$300-500$	$1.6-2.0$	1.67×10^{-6}	0.1	$^{+43.9}_{-43.9}$	$^{+0.0}_{+0.0}$
$300-500$	$2.0-2.4$	3.23×10^{-7}	0.3	$^{+46.4}_{-46.4}$	$^{+0.0}_{+0.0}$
$500-1500$	$0.0-0.4$	8.80×10^{-7}	0.0	$^{+43.9}_{-43.9}$	$^{+0.0}_{+0.0}$
$500-1500$	$0.4-0.8$	6.07×10^{-7}	0.0	$^{+44.3}_{-44.3}$	$^{+0.0}_{+0.0}$
$500-1500$	$0.8-1.2$	3.33×10^{-7}	0.0	$^{+45.3}_{-45.3}$	$^{+0.0}_{+0.0}$
$500-1500$	$1.2-1.6$	1.32×10^{-7}	0.1	$^{+46.9}_{-46.9}$	$^{+0.0}_{+0.0}$
$500-1500$	$1.6-2.0$	3.08×10^{-8}	0.2	$^{+49.2}_{-49.2}$	$^{+0.0}_{+0.0}$
$500-1500$	$2.0-2.4$	2.58×10^{-9}	0.6	$^{+52.8}_{-52.8}$	$^{+0.0}_{+0.0}$

Table D.4.: Photon Induced differential fiducial cross section $\frac{d\sigma}{dm_{\ell\ell}d|y_{\ell\ell}|}$. The calculation is performed using the MRST2004QED PDF set and with dynamic scales $\mu_r = \mu_f = m_{\ell\ell}$. The predictions are listed together with the statistical uncertainty ($\delta^{\rm stat}$), the PDF eigenvector variation ($\delta^{\rm pdf}$) and the uncertainty from the variation of α_s (δ^{α_s}).

$m_{\ell\ell}$ [GeV]	$\lvert\delta\eta_{\ell\ell}\rvert$	$\frac{\mathrm{d}\sigma}{\mathrm{d}m_{\ell\ell}\mathrm{d}\lvert\delta\eta_{\ell\ell}\rvert}$ [pb/GeV]	δ^{stat} [%]	δ^{pdf} [%]	δ^{α_s} [%]
$116-150$	$0.0-0.2$	4.75×10^{-2}	0.3	$^{+1.8}_{-2.3}$	$^{+1.0}_{-0.8}$
$116-150$	$0.2-0.5$	4.57×10^{-2}	0.5	$^{+1.9}_{-2.3}$	$^{+0.8}_{-0.8}$
$116-150$	$0.5-0.8$	4.25×10^{-2}	0.6	$^{+1.9}_{-2.4}$	$^{+0.9}_{-0.8}$
$116-150$	$0.8-1.0$	3.89×10^{-2}	0.6	$^{+1.9}_{-2.4}$	$^{+0.9}_{-0.8}$
$116-150$	$1.0-1.2$	3.46×10^{-2}	0.7	$^{+2.0}_{-2.5}$	$^{+1.0}_{-0.8}$
$116-150$	$1.2-1.5$	3.00×10^{-2}	0.8	$^{+2.0}_{-2.6}$	$^{+1.0}_{-0.7}$
$116-150$	$1.5-1.8$	2.50×10^{-2}	0.8	$^{+2.1}_{-2.6}$	$^{+1.0}_{-0.8}$
$116-150$	$1.8-2.0$	1.94×10^{-2}	0.8	$^{+2.1}_{-2.6}$	$^{+1.1}_{-0.9}$
$116-150$	$2.0-2.2$	1.15×10^{-2}	0.8	$^{+1.9}_{-2.5}$	$^{+1.0}_{-1.2}$
$116-150$	$2.2-2.5$	4.04×10^{-3}	1.4	$^{+1.8}_{-2.4}$	$^{+1.1}_{-1.0}$
$116-150$	$2.5-2.8$	6.29×10^{-4}	1.9	$^{+1.6}_{-2.2}$	$^{+2.7}_{-0.1}$
$116-150$	$2.8-3.0$	1.05×10^{-5}	4.7	$^{+1.4}_{-2.0}$	$^{+4.2}_{+2.5}$
$150-200$	$0.0-0.2$	1.03×10^{-2}	0.3	$^{+1.8}_{-2.1}$	$^{+0.7}_{-0.8}$
$150-200$	$0.2-0.5$	9.74×10^{-3}	0.5	$^{+1.9}_{-2.1}$	$^{+0.8}_{-0.6}$
$150-200$	$0.5-0.8$	9.28×10^{-3}	0.5	$^{+1.9}_{-2.2}$	$^{+0.7}_{-0.9}$
$150-200$	$0.8-1.0$	8.48×10^{-3}	0.6	$^{+1.9}_{-2.2}$	$^{+0.8}_{-0.7}$
$150-200$	$1.0-1.2$	7.67×10^{-3}	0.6	$^{+2.0}_{-2.3}$	$^{+0.8}_{-0.6}$
$150-200$	$1.2-1.5$	6.63×10^{-3}	0.7	$^{+2.0}_{-2.3}$	$^{+0.9}_{-0.8}$
$150-200$	$1.5-1.8$	5.64×10^{-3}	0.8	$^{+2.1}_{-2.4}$	$^{+0.9}_{-0.6}$
$150-200$	$1.8-2.0$	4.52×10^{-3}	0.9	$^{+2.1}_{-2.5}$	$^{+0.9}_{-0.7}$
$150-200$	$2.0-2.2$	3.58×10^{-3}	1.1	$^{+2.2}_{-2.5}$	$^{+1.0}_{-0.6}$
$150-200$	$2.2-2.5$	2.69×10^{-3}	1.1	$^{+2.3}_{-2.6}$	$^{+0.7}_{-0.9}$
$150-200$	$2.5-2.8$	1.84×10^{-3}	1.1	$^{+2.2}_{-2.6}$	$^{+0.7}_{-0.9}$
$150-200$	$2.8-3.0$	7.94×10^{-4}	1.6	$^{+2.1}_{-2.5}$	$^{+1.5}_{-0.9}$
$200-300$	$0.0-0.2$	2.10×10^{-3}	0.3	$^{+1.9}_{-2.1}$	$^{+0.6}_{-0.6}$
$200-300$	$0.2-0.5$	2.04×10^{-3}	0.5	$^{+2.0}_{-2.1}$	$^{+0.7}_{-0.6}$
$200-300$	$0.5-0.8$	1.93×10^{-3}	0.5	$^{+2.0}_{-2.1}$	$^{+0.6}_{-0.6}$
$200-300$	$0.8-1.0$	1.79×10^{-3}	0.6	$^{+2.1}_{-2.2}$	$^{+0.6}_{-0.7}$
$200-300$	$1.0-1.2$	1.63×10^{-3}	0.6	$^{+2.1}_{-2.2}$	$^{+0.8}_{-0.6}$
$200-300$	$1.2-1.5$	1.44×10^{-3}	0.6	$^{+2.2}_{-2.3}$	$^{+0.6}_{-0.8}$
$200-300$	$1.5-1.8$	1.20×10^{-3}	0.7	$^{+2.2}_{-2.3}$	$^{+0.6}_{-0.5}$
$200-300$	$1.8-2.0$	9.99×10^{-4}	0.8	$^{+2.3}_{-2.4}$	$^{+0.9}_{-0.6}$
$200-300$	$2.0-2.2$	7.83×10^{-4}	0.9	$^{+2.4}_{-2.5}$	$^{+0.5}_{-0.8}$
$200-300$	$2.2-2.5$	6.15×10^{-4}	1.1	$^{+2.5}_{-2.5}$	$^{+1.0}_{-0.4}$
$200-300$	$2.5-2.8$	4.57×10^{-4}	1.3	$^{+2.5}_{-2.6}$	$^{+0.6}_{-0.9}$
$200-300$	$2.8-3.0$	3.34×10^{-4}	1.6	$^{+2.6}_{-2.7}$	$^{+0.5}_{-0.7}$
$300-500$	$0.0-0.5$	2.68×10^{-4}	0.2	$^{+2.4}_{-2.4}$	$^{+0.4}_{-0.3}$
$300-500$	$0.5-1.0$	2.49×10^{-4}	0.2	$^{+2.5}_{-2.4}$	$^{+0.3}_{-0.4}$
$300-500$	$1.0-1.5$	2.09×10^{-4}	0.3	$^{+2.6}_{-2.5}$	$^{+0.3}_{-0.5}$
$300-500$	$1.5-2.0$	1.56×10^{-4}	0.3	$^{+2.7}_{-2.6}$	$^{+0.5}_{-0.5}$
$300-500$	$2.0-2.5$	1.01×10^{-4}	0.4	$^{+2.9}_{-2.8}$	$^{+0.4}_{-0.6}$
$300-500$	$2.5-3.0$	5.86×10^{-5}	0.6	$^{+3.0}_{-3.0}$	$^{+0.3}_{-0.5}$
$500-1500$	$0.0-0.5$	8.26×10^{-6}	0.1	$^{+3.6}_{-3.5}$	$^{-0.1}_{-0.1}$
$500-1500$	$0.5-1.0$	8.00×10^{-6}	0.2	$^{+3.6}_{-3.5}$	$^{-0.2}_{-0.2}$
$500-1500$	$1.0-1.5$	7.07×10^{-6}	0.2	$^{+3.6}_{-3.6}$	$^{-0.0}_{-0.1}$
$500-1500$	$1.5-2.0$	5.54×10^{-6}	0.2	$^{+3.8}_{-3.7}$	$^{-0.1}_{-0.2}$
$500-1500$	$2.0-2.5$	3.76×10^{-6}	0.3	$^{+3.9}_{-3.9}$	$^{+0.1}_{-0.1}$
$500-1500$	$2.5-3.0$	2.26×10^{-6}	0.4	$^{+4.1}_{-4.1}$	$^{-0.1}_{-0.3}$

Table D.5.: Born level differential fiducial cross section $\frac{\mathrm{d}\sigma}{\mathrm{d}m_{\ell\ell}\mathrm{d}\lvert\delta\eta_{\ell\ell}\rvert}$ at NNLO including NLO electroweak corrections. The calculation is performed using the CT10 NNLO PDF set and with dynamic scales $\mu_r = \mu_f = m_{\ell\ell}$. The predictions are listed together with the statistical uncertainty (δ^{stat}), the PDF eigenvector variation (δ^{pdf}) and the uncertainty from the variation of α_s (δ^{α_s}).

$m_{\ell\ell}$ [GeV]	$\lvert\delta\eta_{\ell\ell}\rvert$	$\frac{d\sigma}{dm_{\ell\ell}d\lvert\delta\eta_{\ell\ell}\rvert}$ [pb/GeV]	$\delta^{\rm stat}$ [%]	$\delta^{\rm pdf}$ [%]	δ^{α_s} [%]
$116-150$	$0.0-0.2$	2.92×10^{-4}	0.0	$^{+36.9}_{-36.9}$	$^{+0.0}_{+0.0}$
$116-150$	$0.2-0.5$	2.92×10^{-4}	0.0	$^{+36.8}_{-36.8}$	$^{+0.0}_{+0.0}$
$116-150$	$0.5-0.8$	2.98×10^{-4}	0.0	$^{+36.7}_{-36.7}$	$^{+0.0}_{+0.0}$
$116-150$	$0.8-1.0$	3.06×10^{-4}	0.0	$^{+36.6}_{-36.6}$	$^{+0.0}_{+0.0}$
$116-150$	$1.0-1.2$	3.15×10^{-4}	0.0	$^{+36.5}_{-36.5}$	$^{+0.0}_{+0.0}$
$116-150$	$1.2-1.5$	3.22×10^{-4}	0.0	$^{+36.5}_{-36.5}$	$^{+0.0}_{+0.0}$
$116-150$	$1.5-1.8$	3.26×10^{-4}	0.0	$^{+36.4}_{-36.4}$	$^{+0.0}_{+0.0}$
$116-150$	$1.8-2.0$	2.90×10^{-4}	0.0	$^{+36.4}_{-36.4}$	$^{+0.0}_{+0.0}$
$116-150$	$2.0-2.2$	1.56×10^{-4}	0.1	$^{+36.5}_{-36.5}$	$^{+0.0}_{+0.0}$
$116-150$	$2.2-2.5$	4.15×10^{-5}	0.2	$^{+36.6}_{-36.6}$	$^{+0.0}_{+0.0}$
$116-150$	$2.5-2.8$	0.00×10^{0}	0.0	$^{+0.0}_{-0.0}$	$^{+0.0}_{+0.0}$
$116-150$	$2.8-3.0$	0.00×10^{0}	0.0	$^{+0.0}_{-0.0}$	$^{+0.0}_{+0.0}$
$150-200$	$0.0-0.2$	1.05×10^{-4}	0.0	$^{+37.9}_{-37.9}$	$^{+0.0}_{+0.0}$
$150-200$	$0.2-0.5$	1.05×10^{-4}	0.0	$^{+37.8}_{-37.8}$	$^{+0.0}_{+0.0}$
$150-200$	$0.5-0.8$	1.08×10^{-4}	0.0	$^{+37.7}_{-37.7}$	$^{+0.0}_{+0.0}$
$150-200$	$0.8-1.0$	1.11×10^{-4}	0.0	$^{+37.6}_{-37.6}$	$^{+0.0}_{+0.0}$
$150-200$	$1.0-1.2$	1.15×10^{-4}	0.0	$^{+37.5}_{-37.5}$	$^{+0.0}_{+0.0}$
$150-200$	$1.2-1.5$	1.18×10^{-4}	0.0	$^{+37.4}_{-37.4}$	$^{+0.0}_{+0.0}$
$150-200$	$1.5-1.8$	1.20×10^{-4}	0.0	$^{+37.4}_{-37.4}$	$^{+0.0}_{+0.0}$
$150-200$	$1.8-2.0$	1.20×10^{-4}	0.0	$^{+37.3}_{-37.3}$	$^{+0.0}_{+0.0}$
$150-200$	$2.0-2.2$	1.17×10^{-4}	0.0	$^{+37.2}_{-37.2}$	$^{+0.0}_{+0.0}$
$150-200$	$2.2-2.5$	1.13×10^{-4}	0.0	$^{+37.1}_{-37.1}$	$^{+0.0}_{+0.0}$
$150-200$	$2.5-2.8$	7.82×10^{-5}	0.1	$^{+37.2}_{-37.2}$	$^{+0.0}_{+0.0}$
$150-200$	$2.8-3.0$	3.23×10^{-5}	0.1	$^{+37.4}_{-37.4}$	$^{+0.0}_{+0.0}$
$200-300$	$0.0-0.2$	2.73×10^{-5}	0.1	$^{+39.3}_{-39.3}$	$^{+0.0}_{+0.0}$
$200-300$	$0.2-0.5$	2.76×10^{-5}	0.1	$^{+39.2}_{-39.2}$	$^{+0.0}_{+0.0}$
$200-300$	$0.5-0.8$	2.85×10^{-5}	0.1	$^{+39.1}_{-39.1}$	$^{+0.0}_{+0.0}$
$200-300$	$0.8-1.0$	2.96×10^{-5}	0.1	$^{+39.0}_{-39.0}$	$^{+0.0}_{+0.0}$
$200-300$	$1.0-1.2$	3.09×10^{-5}	0.1	$^{+38.9}_{-38.9}$	$^{+0.0}_{+0.0}$
$200-300$	$1.2-1.5$	3.19×10^{-5}	0.1	$^{+38.8}_{-38.8}$	$^{+0.0}_{+0.0}$
$200-300$	$1.5-1.8$	3.25×10^{-5}	0.1	$^{+38.7}_{-38.7}$	$^{+0.0}_{+0.0}$
$200-300$	$1.8-2.0$	3.26×10^{-5}	0.1	$^{+38.6}_{-38.6}$	$^{+0.0}_{+0.0}$
$200-300$	$2.0-2.2$	3.22×10^{-5}	0.1	$^{+38.5}_{-38.5}$	$^{+0.0}_{+0.0}$
$200-300$	$2.2-2.5$	3.13×10^{-5}	0.1	$^{+38.5}_{-38.5}$	$^{+0.0}_{+0.0}$
$200-300$	$2.5-2.8$	2.98×10^{-5}	0.1	$^{+38.4}_{-38.4}$	$^{+0.0}_{+0.0}$
$200-300$	$2.8-3.0$	2.78×10^{-5}	0.1	$^{+38.4}_{-38.4}$	$^{+0.0}_{+0.0}$
$300-500$	$0.0-0.5$	4.17×10^{-6}	0.0	$^{+41.5}_{-41.5}$	$^{+0.0}_{+0.0}$
$300-500$	$0.5-1.0$	4.51×10^{-6}	0.0	$^{+41.3}_{-41.3}$	$^{+0.0}_{+0.0}$
$300-500$	$1.0-1.5$	4.98×10^{-6}	0.0	$^{+41.1}_{-41.1}$	$^{+0.0}_{+0.0}$
$300-500$	$1.5-2.0$	5.28×10^{-6}	0.0	$^{+40.9}_{-40.9}$	$^{+0.0}_{+0.0}$
$300-500$	$2.0-2.5$	5.25×10^{-6}	0.0	$^{+40.7}_{-40.7}$	$^{+0.0}_{+0.0}$
$300-500$	$2.5-3.0$	4.84×10^{-6}	0.0	$^{+40.6}_{-40.6}$	$^{+0.0}_{+0.0}$
$500-1500$	$0.0-0.5$	1.52×10^{-7}	0.0	$^{+45.0}_{-45.0}$	$^{+0.0}_{+0.0}$
$500-1500$	$0.5-1.0$	1.68×10^{-7}	0.0	$^{+45.0}_{-45.0}$	$^{+0.0}_{+0.0}$
$500-1500$	$1.0-1.5$	1.92×10^{-7}	0.0	$^{+44.9}_{-44.9}$	$^{+0.0}_{+0.0}$
$500-1500$	$1.5-2.0$	2.11×10^{-7}	0.0	$^{+44.8}_{-44.8}$	$^{+0.0}_{+0.0}$
$500-1500$	$2.0-2.5$	2.18×10^{-7}	0.0	$^{+44.6}_{-44.6}$	$^{+0.0}_{+0.0}$
$500-1500$	$2.5-3.0$	2.08×10^{-7}	0.0	$^{+44.4}_{-44.4}$	$^{+0.0}_{+0.0}$

Table D.6.: Photon Induced differential fiducial cross section $\frac{d\sigma}{dm_{\ell\ell}d|\delta\eta_{\ell\ell}|}$. The calculation is performed using the MRST2004QED PDF set and with dynamic scales $\mu_r = \mu_f = m_{\ell\ell}$. The predictions are listed together with the statistical uncertainty ($\delta^{\rm stat}$), the PDF eigenvector variation ($\delta^{\rm pdf}$) and the uncertainty from the variation of α_s (δ^{α_s}).

Appendix E.

Electron Channel Comparison

In parallel to the dimuon Drell-Yan measurement described in this analysis a preliminary dielectron measurement has also been carried out. The fiducial volume described in section 6.1 has been constructed to allow comparisons between the two channels. Initial work into combining the two channels into a single measurement has begun but is beyond the scope of this thesis. Figures E.1, E.2 and E.3 show the fiducial cross sections for both the dimuon and dielectron channels for the single differential, double differential mass and rapidity and double differential mass and $\Delta\eta$ measurements respectively. The electron channel analysis has not made a 2D measurement in the $66 < m_{ll} < 116$GeV bin so this comparison has had to be omitted.

The dimuon and dielectron channel single differential measurements show agreement to within 6% for all but the highest $1000 < m_{ll} < 1500$ GeV mass bin where statistics are limited. Within the dielectron channel a similar discrepancy is seen between the data and the theory, which is mirrored in the relevant dielectron control plots. For the $m_{ll} < 300$ GeV region the dimuon channel cross sections are slightly larger than the dielectron channel and for the $m_{ll} < 300$ GeV region this trend is reversed albeit with large uncertainties.

For the double differential mass and rapidity measurement there is a broad level of agreement between the two channels to 10% for $116 < m_{ll} < 500$ GeV. The $500 < m_{ll} < 1500$ GeV mass bin shows agreement to within expected statistical fluctuations. There is a slight deviation between the channels for the central rapidity region $0 < |y_{ll}| < 0.8$ in the mass region $116 < m_{ll} < 300$ GeV. The dielectron channel is still investigating this discrepancy as the fiducial cross sections are not finalised.

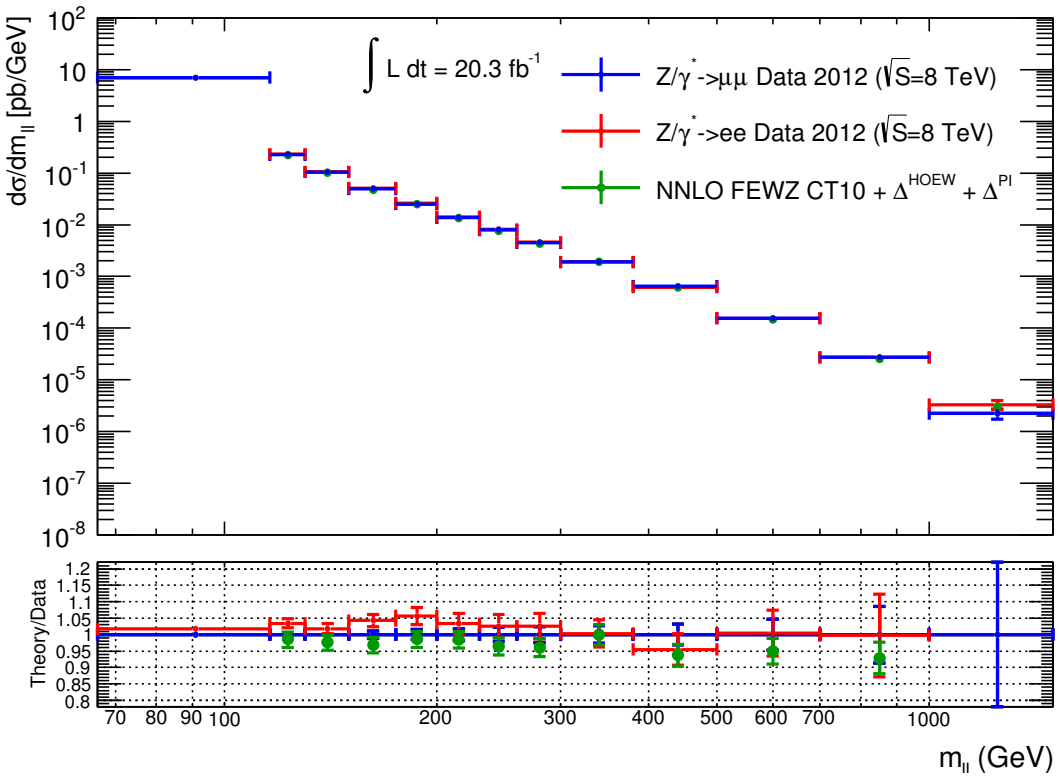

Figure E.1.: The single differential Drell-Yan dimuon and dielectron channel fiducial cross section compared to NNLO theory, which includes NLO higher order electroweak corrections (Δ^{HOEW}) and the photon induced contribution (Δ^{PI}). The error bars show the total uncertainty. The lower plot shows the ratio of theory to muon data as well as showing the ratio of electron data to muon data.

The double differential mass and $\Delta\eta$ measurement again shows a broad level of agreement between the two channels to 10% for the $116 < m_{ll} < 300$ GeV region. There is a slight deviation between these channels in this mass region at higher $\Delta\eta$ but this is likely be due to the falling cross section and different handling of the multi-jet background which dominates this region. In the two highest mass bins there are some large $\geq 20\%$ deviations but these can be explained by statistical fluctuations.

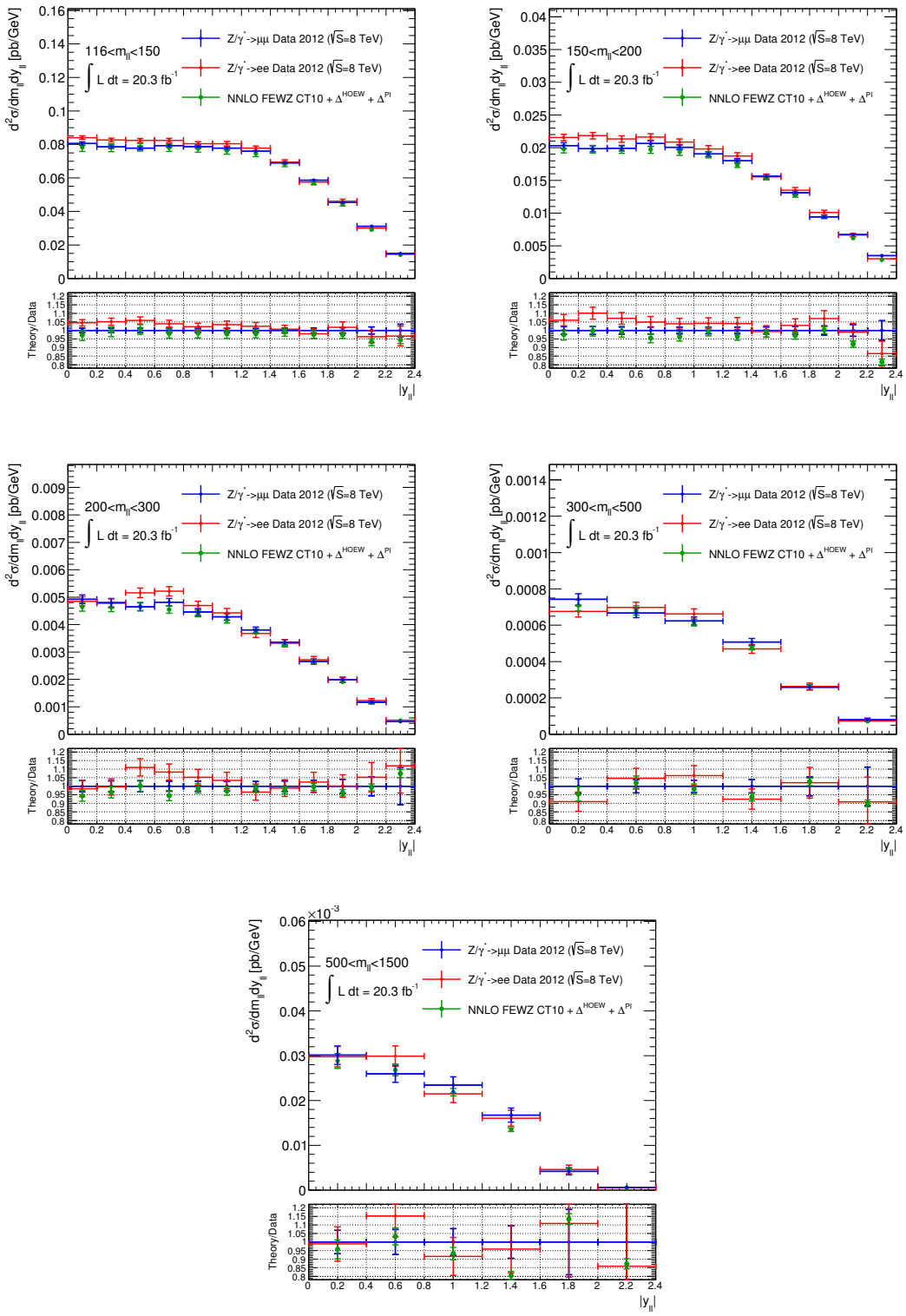

Figure E.2.: The double differential mass and rapidity Drell-Yan dimuon and dielectron channel fiducial cross section compared to NNLO theory, which includes NLO higher order electroweak corrections (Δ^{HOEW}) and the photon induced contribution (Δ^{PI}). The error bars show the total uncertainty. The lower plot shows the ratio of theory to muon data as well as showing the ratio of electron data to muon data.

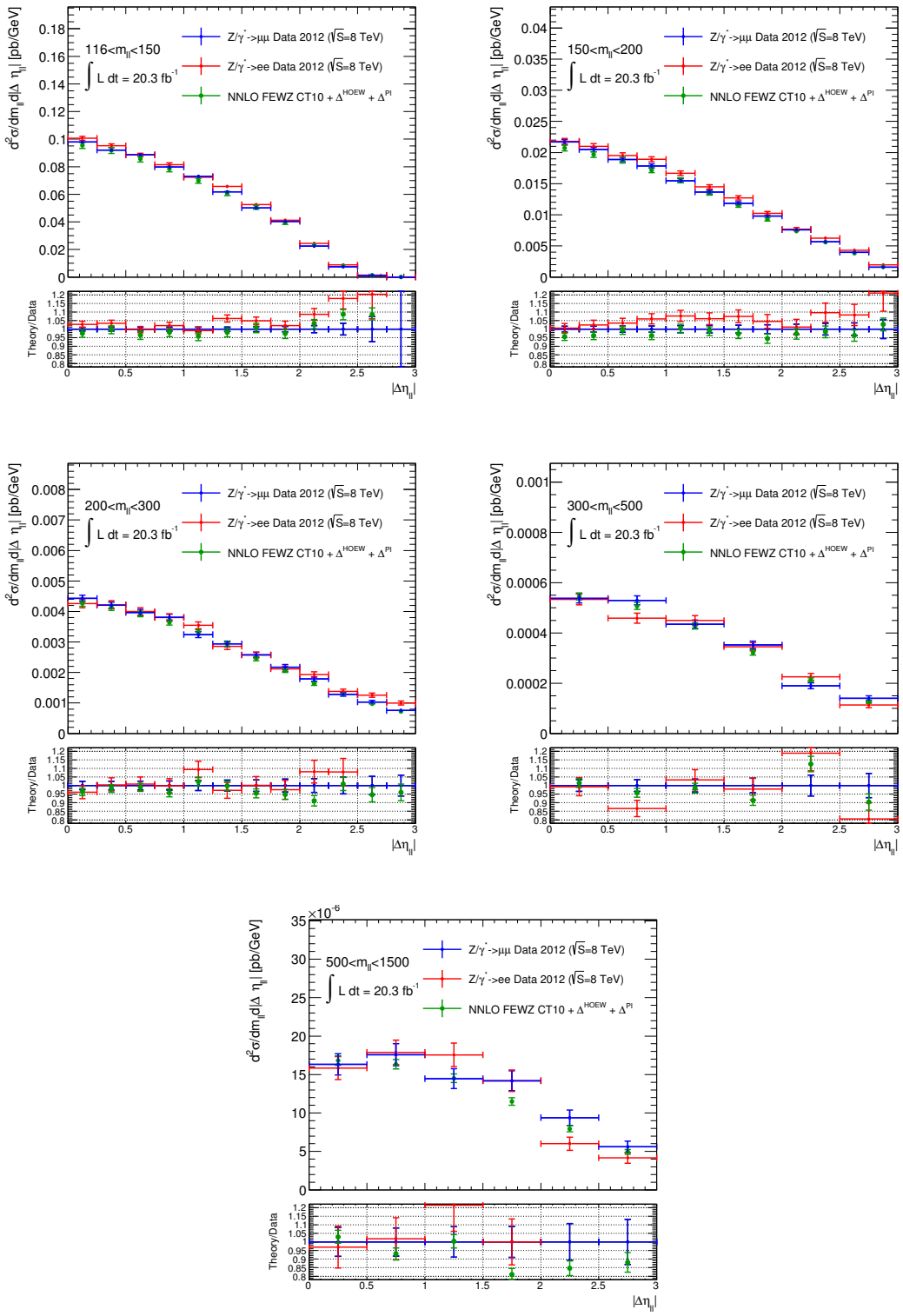

Figure E.3.: The double differential mass and $\Delta\eta$ Drell-Yan dimuon and dielectron channel fiducial cross section compared to NNLO theory, which includes NLO higher order electroweak corrections (Δ^{HOEW}) and the photon induced contribution (Δ^{PI}). The error bars show the total uncertainty. The lower plot shows the ratio of theory to muon data as well as showing the ratio of electron data to muon data.

Appendix F.

Alternative Fiducial Volume Analysis ($p_T < 25$ GeV)

Gaining access to the photon PDFs can be achieved using a Drell-Yan analysis to great effect. The most sensitive kinematic region for the photon induced processes is low muon pT and high dimuon mass. In order to analyse this region the muon pT fiducial selection is reduced to pT>25 GeV for both muons. The selection cannot be lowered below 25 GeV as the lowest pT single muon trigger has a pT threshold of 24 GeV. The reconstruction level selection is identical to the nominal analysis with the exception of lowering the muon pT cuts to pT<25 Gev and only requiring the EF_mu24i_tight trigger. The following sections show distributions for alternative analysis multi-jet background estimation, the kinematics and the cross section and its systematic uncertainties.

F.1. Backgrounds

As with the nominal analysis the backgrounds are all estimated using MC apart form the multi-jet which is estimated using the data driven method described in section 7.1.2. Figures F.1, F.2 and show the fractional background contribution for the single differential, double differential dimuon mass and rapidity and double differential dimuon mass and $\Delta\eta$ measurements respectively. The background composition in the alternative analysis is largely the same as the nominal analysis apart from the increased photon induced contribution at higher $\Delta\eta$.

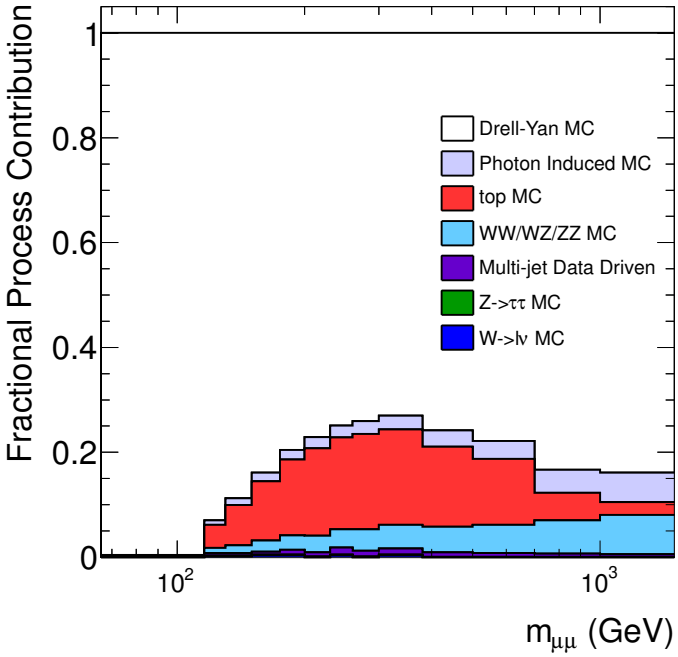

Figure F.1.: The fractional contribution each backgrounds has to the total background and signal prediction displayed in a stack histogram.

The multi-jet estimation in the 1D and 2D dimuon mass bins are given in tables F.1 and F.2. The estimated mulit-jet rapidity and delta eta spectra are given in figures F.4 and F.5. As expected the multi-jet estimation is larger with the reduced p_T cuts. The maximum fraction of multi-jet to data is 0.5% in the $116 < m_{\mu\mu} < 200$ GeV region.

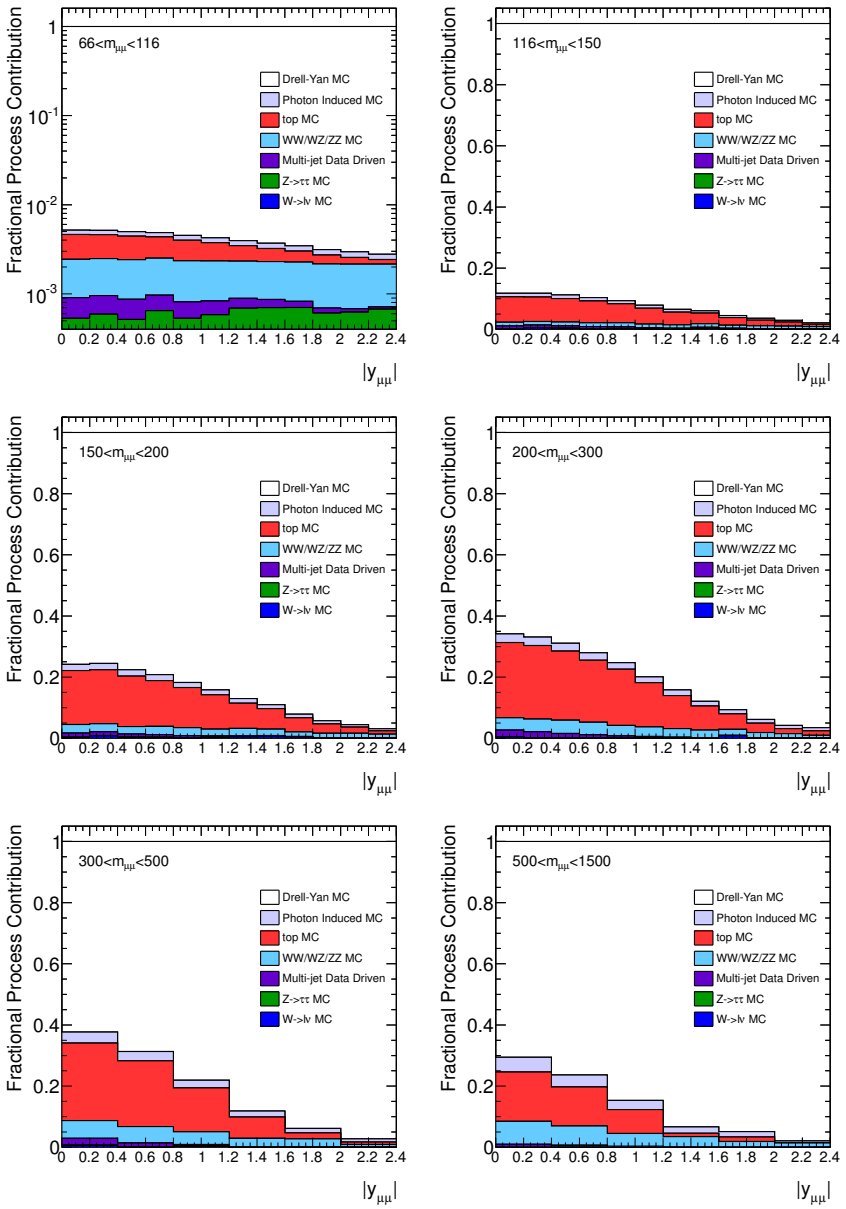

Figure F.2.: The fractional contribution each backgrounds has to the total background and signal prediction displayed in a stack histogram.

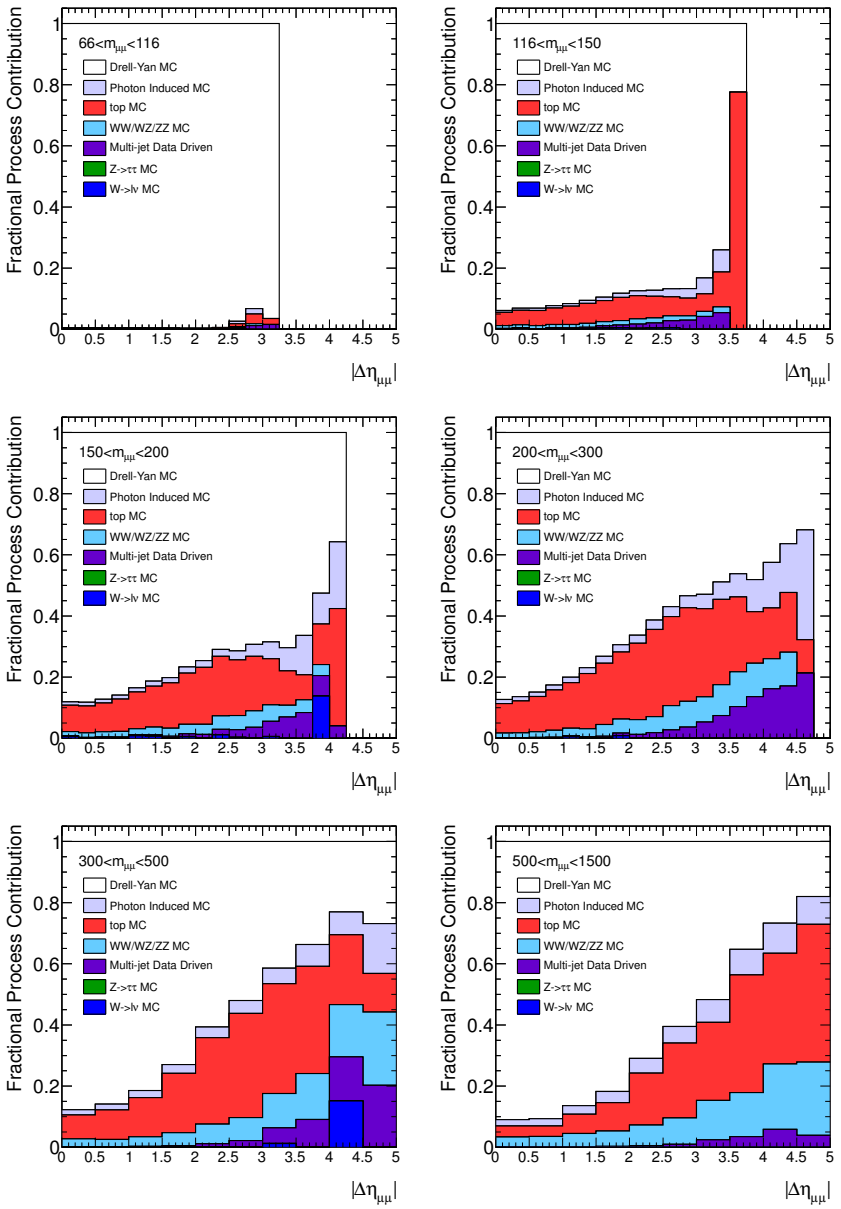

Figure F.3.: The fractional contribution each backgrounds has to the total background and signal prediction displayed in a stack histogram.

	Data and Electroweak (EW) Events in Region							Predicted
$m_{\mu\mu}$ Bin (GeV)	Data B	EW B	Data C	EW C	Data D	EW D	F_{ABCD}	Multi-jet
$66 < m_{\mu\mu} < 116$	1405.00	546.91	193134.00	1555.95	95852.00	602.52	1.185	2036.62
$116 < m_{\mu\mu} < 130$	225.00	93.07	18324.00	68.88	9683.00	67.83	1.189	295.56
$130 < m_{\mu\mu} < 150$	204.00	111.95	15396.00	61.62	8318.00	57.33	1.141	201.64
$150 < m_{\mu\mu} < 175$	164.00	102.89	9935.00	55.96	5409.00	37.15	1.167	132.61
$175 < m_{\mu\mu} < 200$	124.00	66.86	4780.00	21.15	2841.00	18.06	1.165	113.66
$200 < m_{\mu\mu} < 230$	84.00	51.72	2965.00	13.86	1654.00	9.15	1.093	68.34
$230 < m_{\mu\mu} < 260$	62.00	29.48	1370.00	6.97	803.00	7.66	1.116	65.77
$260 < m_{\mu\mu} < 300$	45.00	24.61	845.00	5.57	500.00	5.51	1.212	40.84
$300 < m_{\mu\mu} < 380$	44.00	27.02	529.00	1.17	270.00	3.44	1.189	39.67
$380 < m_{\mu\mu} < 500$	20.00	13.77	114.00	-0.07	66.00	0.26	1.189	12.76
$500 < m_{\mu\mu} < 700$	5.00	5.12	27.00	0.02	12.00	0.00	1.189	4.20
$700 < m_{\mu\mu} < 1000$	3.00	2.06	2.00	0.00	0.00	0.00	1.189	0.90
$1000 < m_{\mu\mu} < 1500$	0.00	0.49	0.00	0.00	0.00	0.00	1.189	0.15

Table F.1.: The table lists the number of data or MC predicted electroweak (EW) background events in each region defined by the modified ABCD method for the 1D binning scheme. The F_{ABCD} factor calculated in each mass bin is given apart from the highest five $m_{\mu\mu}$ bins where the data has been merged to improve statistics. The final column shows the estimated number of multi-jet events calculated using the weighted average F_{ABCD} factor. For the highest three $m_{\mu\mu}$bins the extrapolation of the multi-jet prediction is given in the final column. A negative value is shown for a bin in the electroweak region C column due to the $t\bar{t}$ background having some events with negative MC generator weights.

	Data and Electroweak (EW) Events in Region							Predicted
$m_{\mu\mu}$ Bin (GeV)	Data B	EW B	Data C	EW C	Data D	EW D	F_{ABCD}	Multi-jet
$66 < m_{\mu\mu} < 116$	1405.00	546.91	193134.00	1555.95	95852.00	602.52	1.185	2036.63
$116 < m_{\mu\mu} < 150$	429.00	205.02	33720.00	130.51	18001.00	125.16	1.166	496.63
$150 < m_{\mu\mu} < 200$	288.00	169.76	14715.00	77.11	8250.00	55.21	1.164	249.23
$200 < m_{\mu\mu} < 300$	191.00	105.81	5180.00	26.41	2957.00	22.32	1.126	176.54
$300 < m_{\mu\mu} < 500$	64.00	40.79	643.00	1.10	336.00	3.71	1.186	52.90
$500 < m_{\mu\mu} < 1500$	8.00	7.67	29.00	0.02	12.00	0.00	0.810	4.04

Table F.2.: The table lists the number of data or MC predicted electroweak (EW) background events in each region defined by the modified ABCD method for the 2D binning scheme. The final column shows the estimated number of multi-jet events calculated using the weighted average F_{ABCD} factor. For the highest $m_{\mu\mu}$bin the extrapolation of the multi-jet prediction is given in the final column.

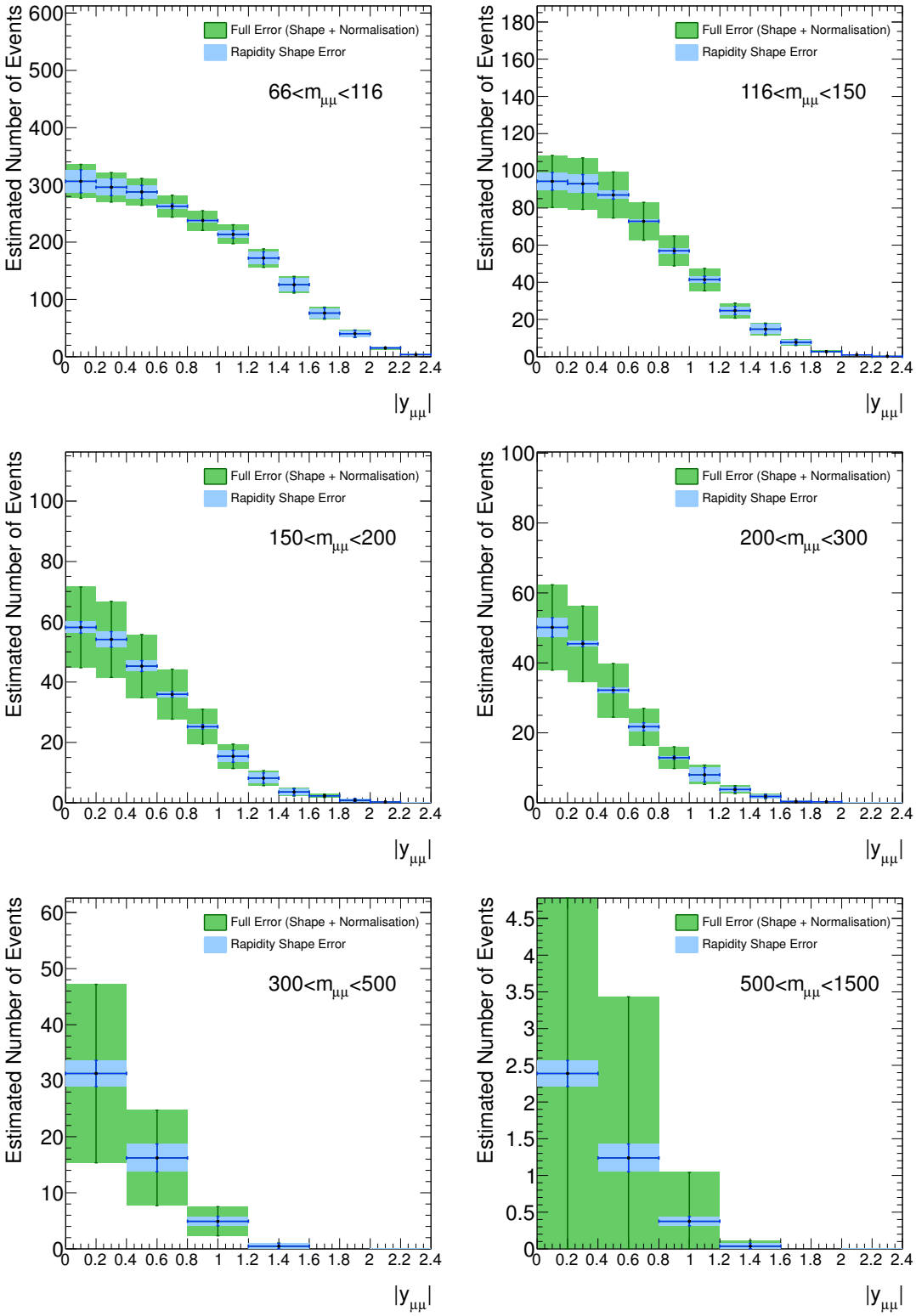

Figure F.4.: Estimated number of multi-jet events. Blue error bars show the error derived from the estimated multi-jet rapidity shape and the green error bars include the error from the modified ABCD method in each mass bin. For the $500 < m_{\mu\mu} < 1500$ GeV bin the shape is taken from the $300 < m_{\mu\mu} < 500$ GeV region.

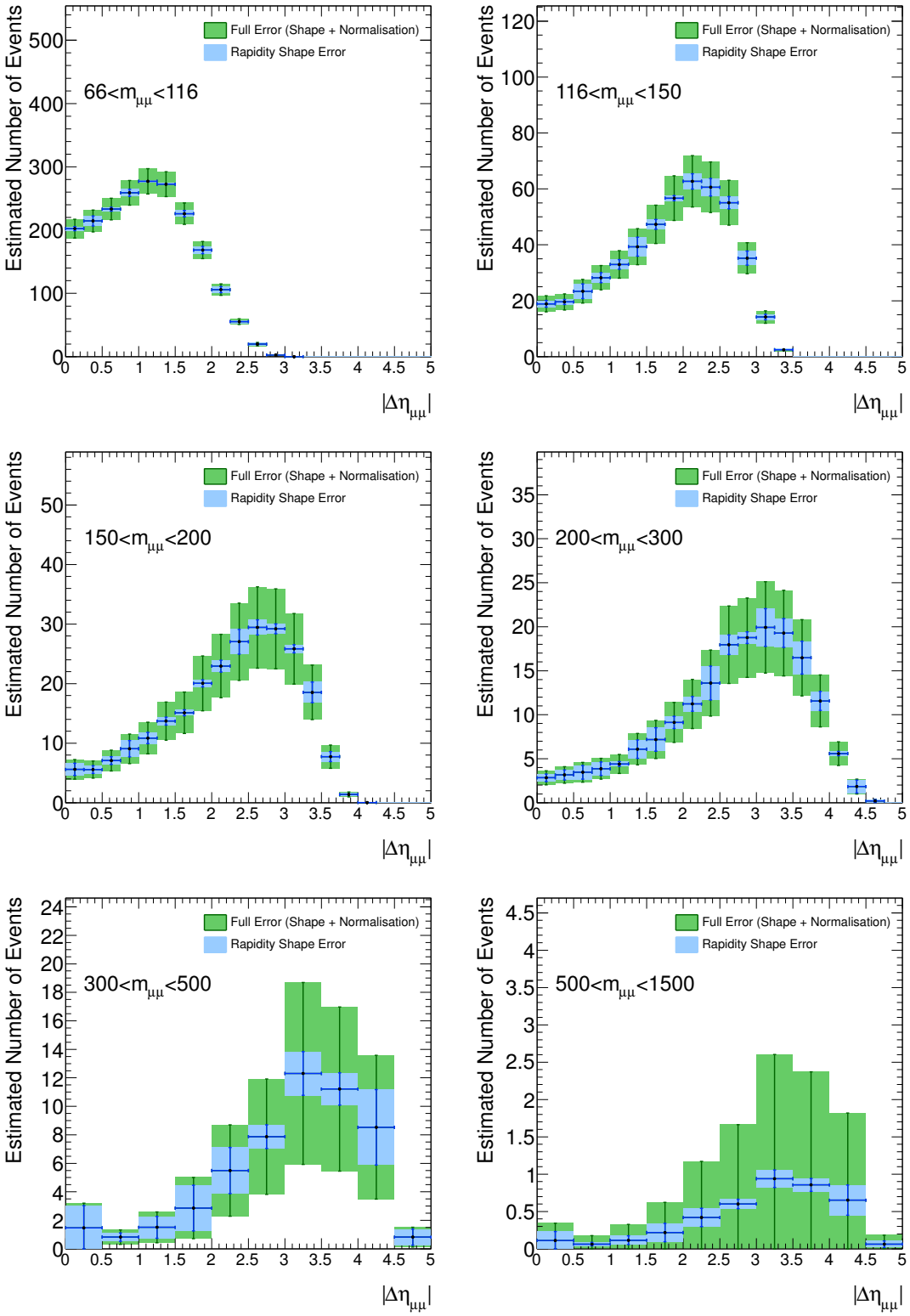

Figure F.5.: Estimated number of multi-jet events. Blue error bars show the error derived from the estimated multi-jet rapidity shape and the green error bars include the error from the modified ABCD method in each mass bin. For the $500 < m_{\mu\mu} < 1500$ GeV bin the shape is taken from the $300 < m_{\mu\mu} < 500$ GeV region.

F.2. Control Distributions

As with the nominal analysis a normalisation difference is observed between data and MC. In the nominal analysis this disagreement is at the 4.0% level for $m_{\mu\mu} > 66$ GeV, for the alternative analysis this figure drops to 3.3%. The muon control distributions are shown for the $m_{\mu\mu} > 116$ GeV region in figure F.8 Good agreement is observed in the shapes of the muon η and ϕ spectra. The muon p_T spectra shown in figure F.7 also show good agreement in the statistic rich low p_T region. The dimuon plots showing the mass, rapidity and p_T spectra are shown in figures F.6 and F.9.

The 2D cross section variables are shown in figure F.10 and F.11. The agreement seen here is good, as the nominal analysis. Figures F.12, F.13, F.14 and F.15 show the muon and dimuon control distributions for the $66 < m_{\mu\mu} < 116$ GeV region.

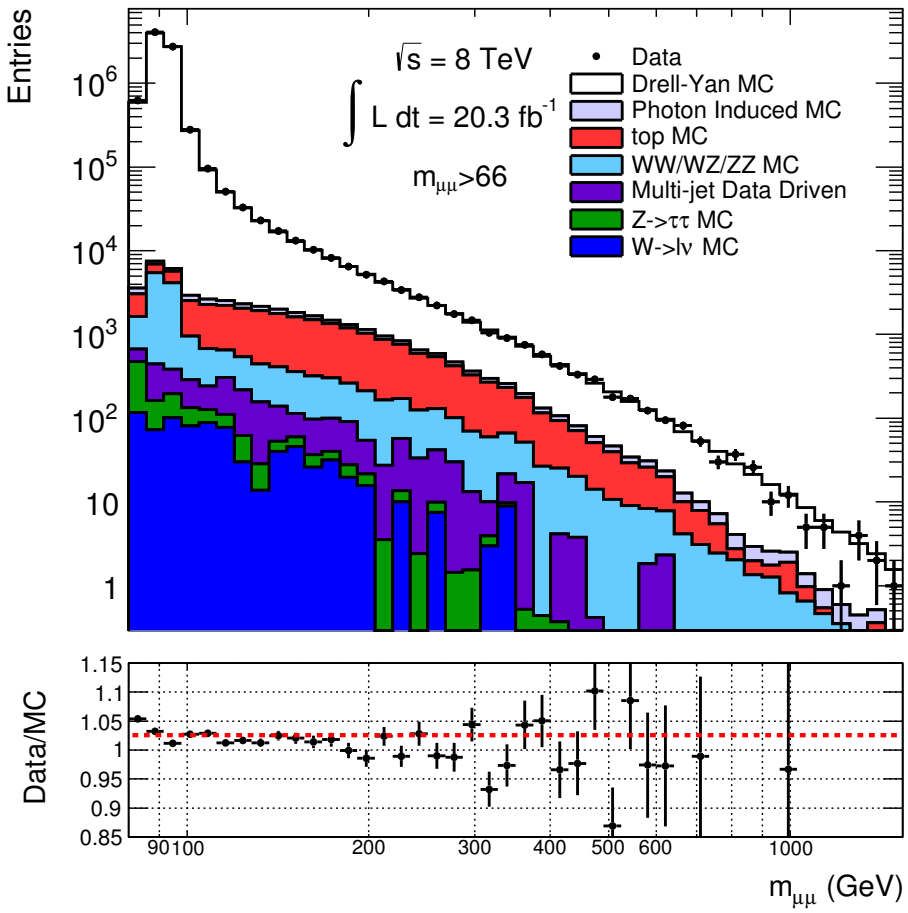

Figure F.6.: Dimuon invariant mass ($m_{\mu\mu}$) distribution after full event selection and detector response corrections applied.

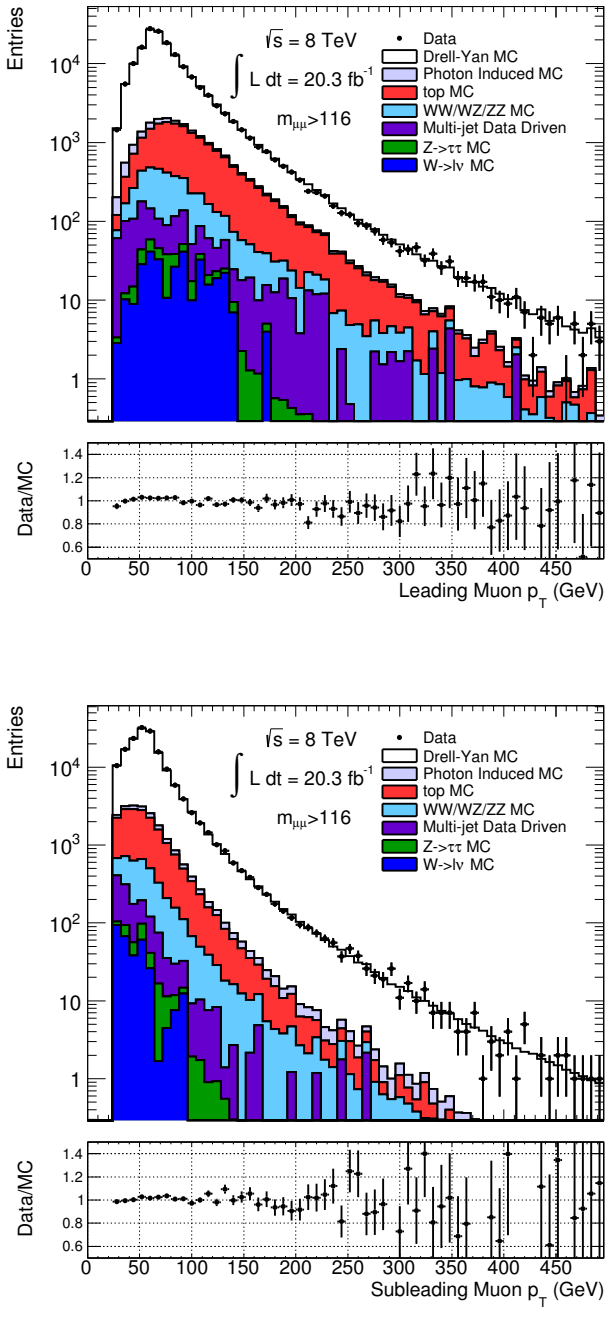

Figure F.7.: Leading (top) and subleading (bottom) muon p_T distributions for $m_{\mu\mu} > 116$ GeV after full event selection and detector response corrections applied.

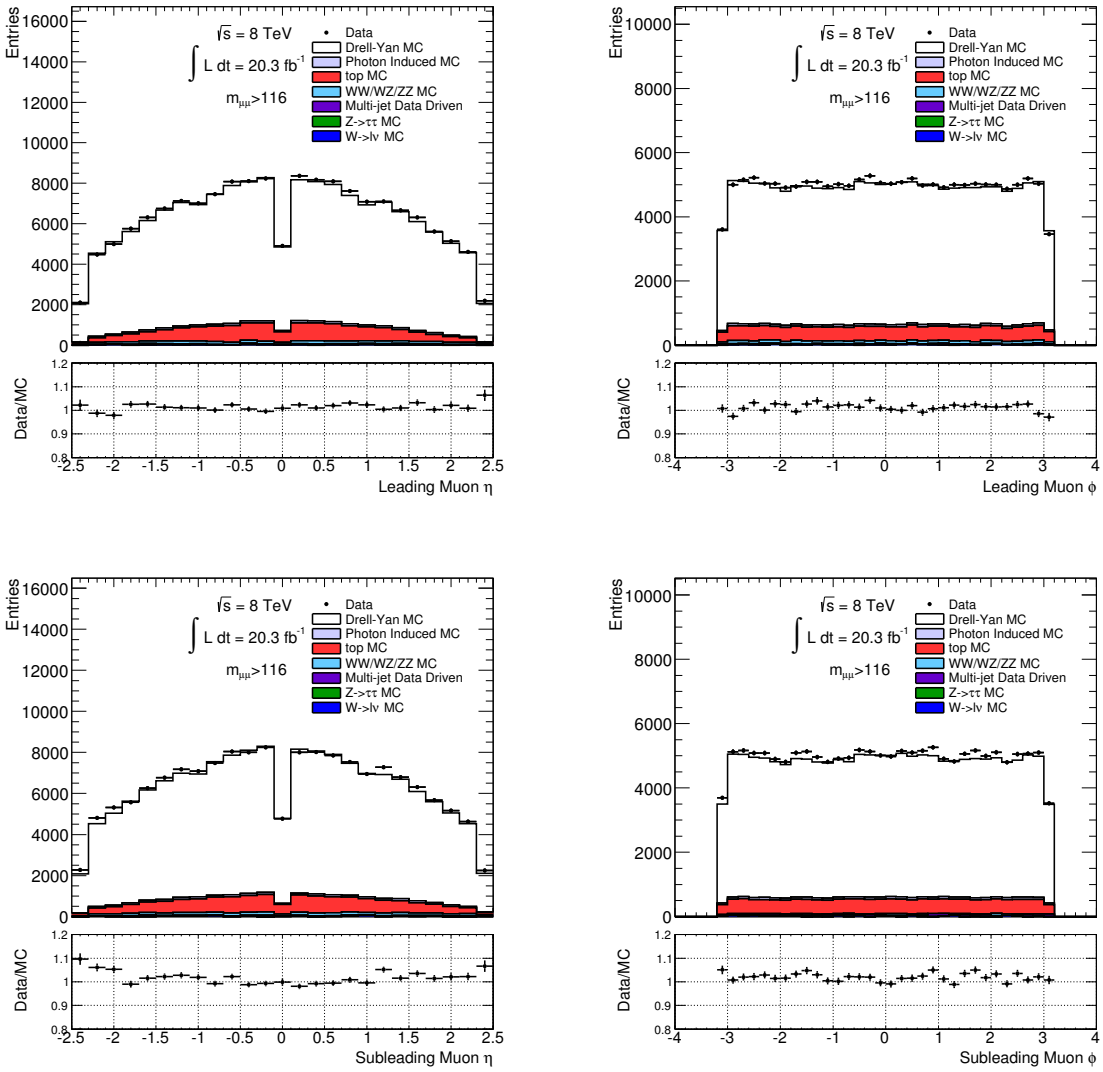

Figure F.8.: Leading (upper row) and subleading (lower row) muon η (left) and ϕ (right) distributions for $m_{\mu\mu} > 116$ GeV after full event selection and detector response corrections applied.

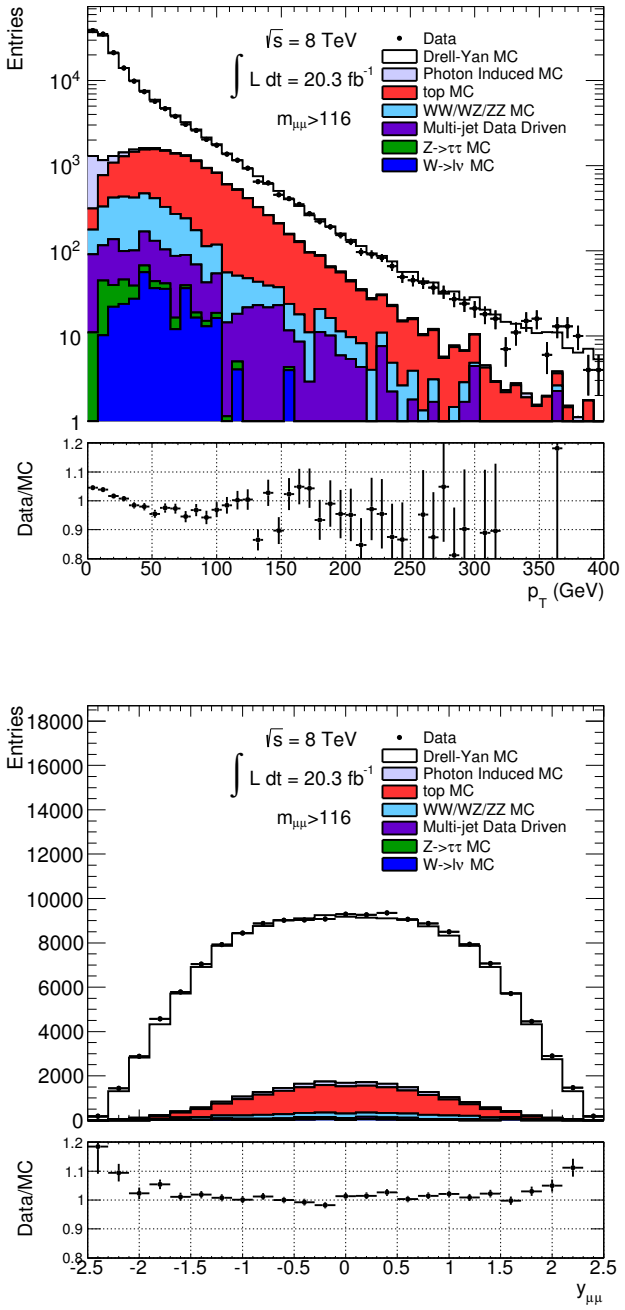

Figure F.9.: Dimuon p_T (top) and $y_{\mu\mu}$ (bottom) distributions for $m_{\mu\mu} > 116$ GeV after full event selection and detector response corrections applied.

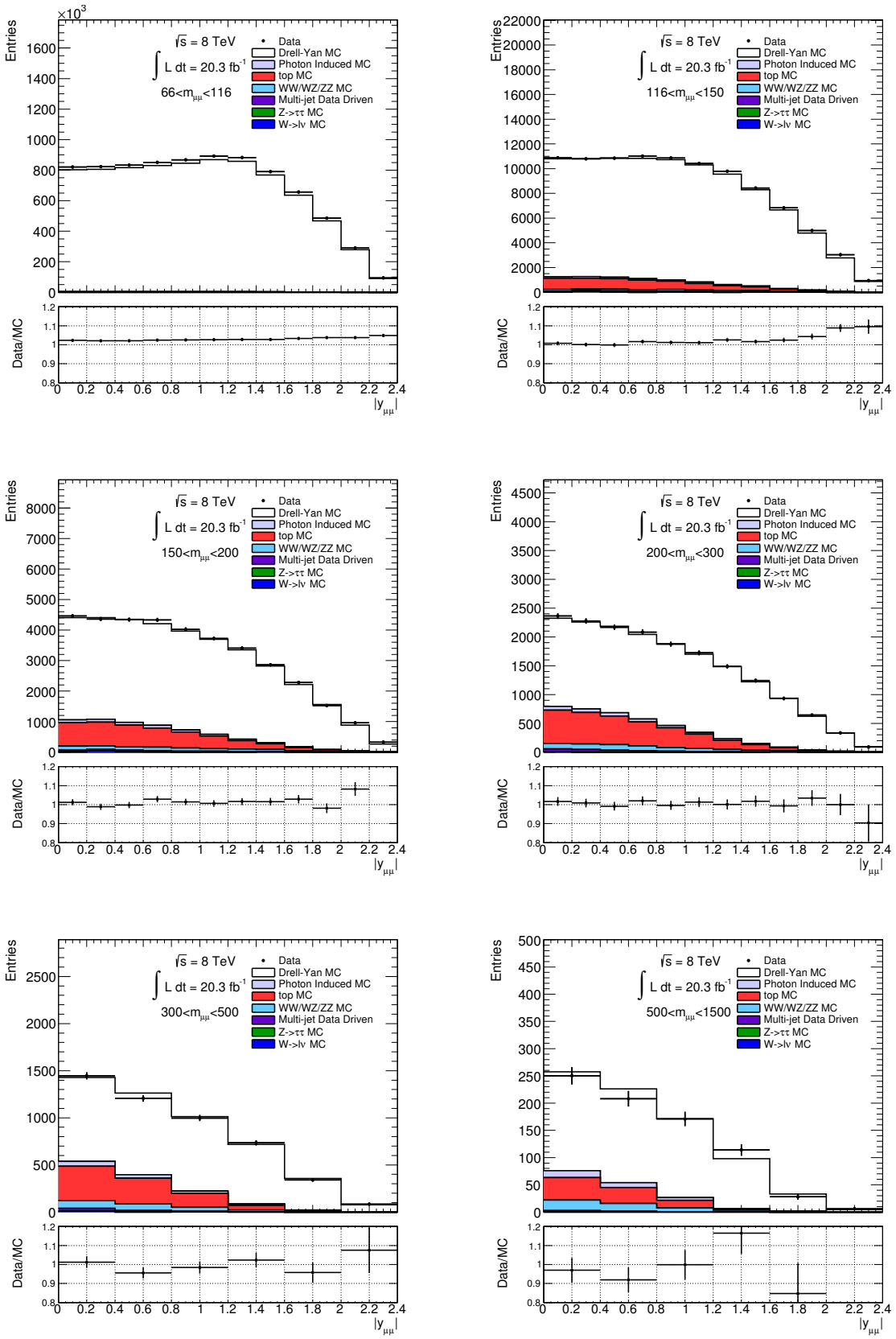

Figure F.10.: Dimuon $y_{\mu\mu}$ distributions for the 2D $m_{\mu\mu}$ binning scheme after full event selection and detector response corrections applied.

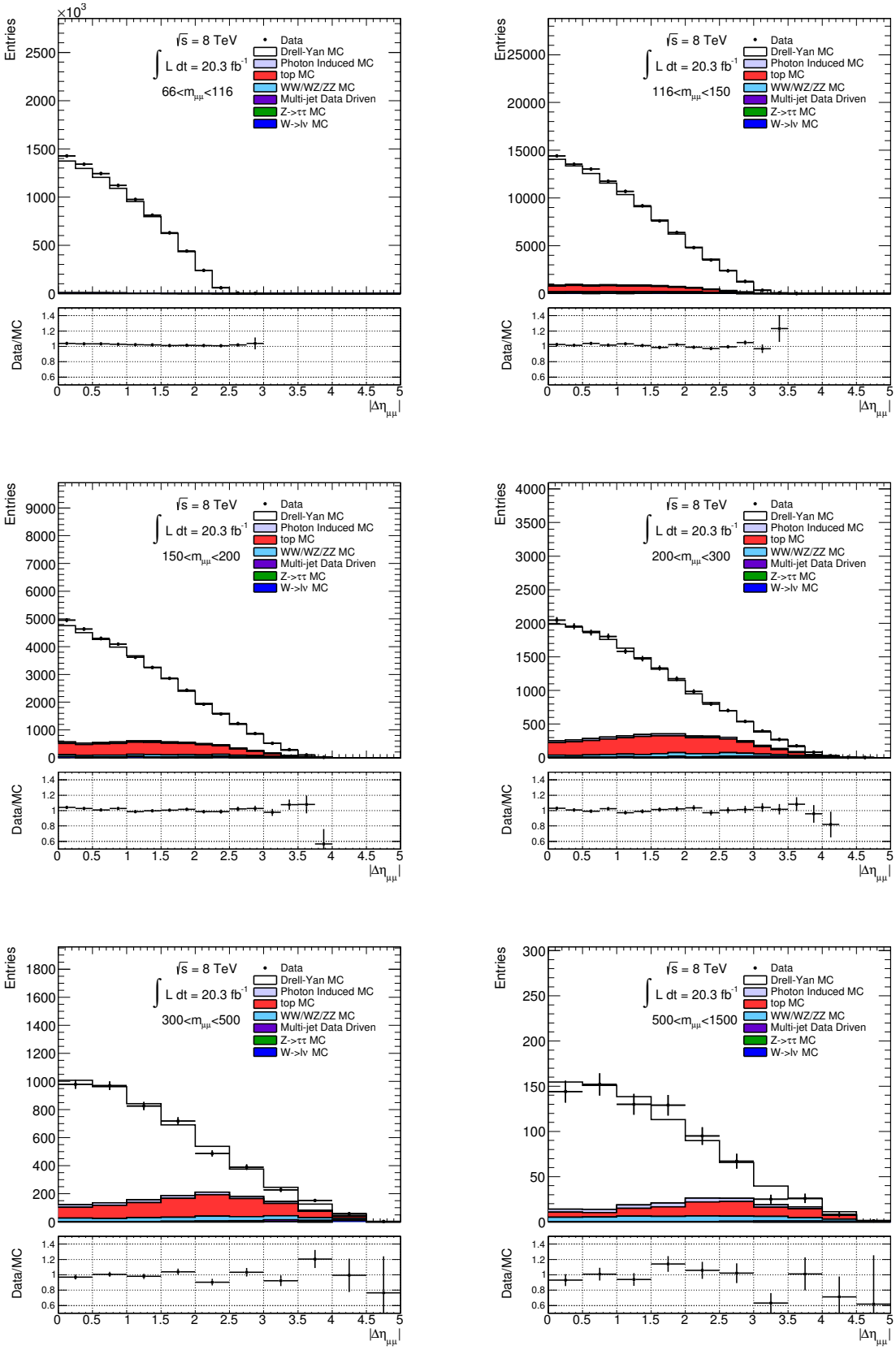

Figure F.11.: Muon $\Delta\eta$ distributions for the 2D $m_{\mu\mu}$ binning scheme after full event selection and detector response corrections applied.

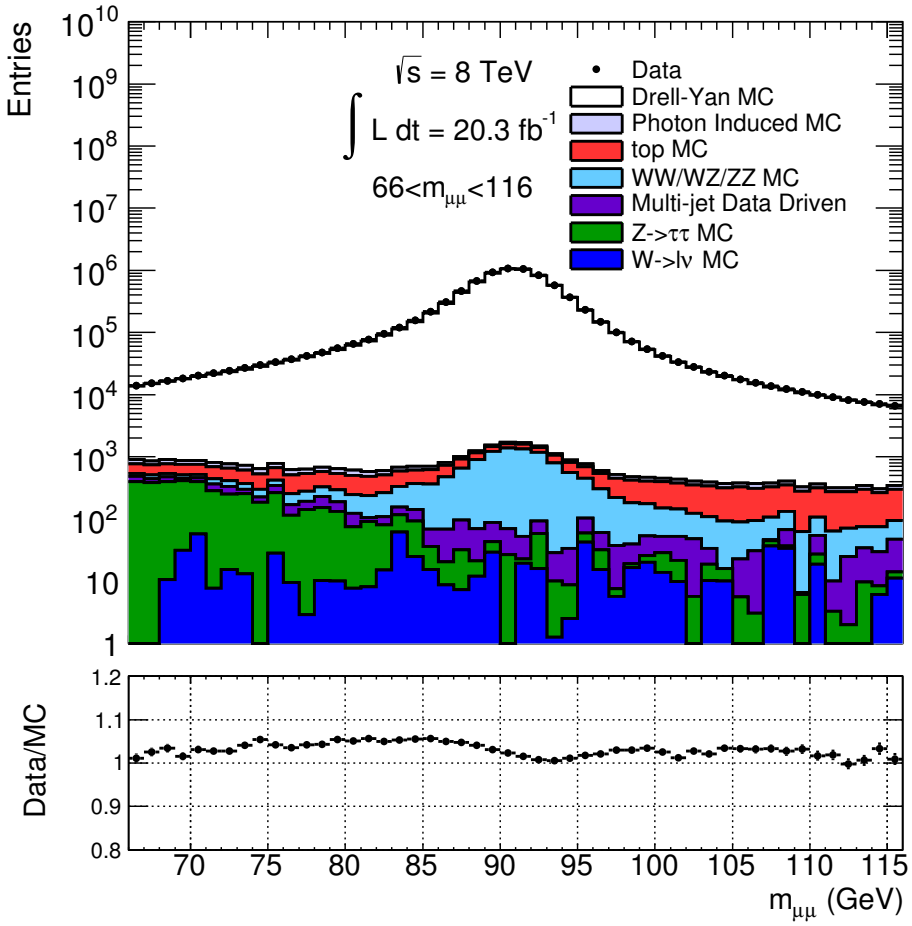

Figure F.12.: Dimuon invariant mass ($m_{\mu\mu}$) distribution after full event selection and detector response corrections applied ($66 < m_{\mu\mu} < 116$ GeV).

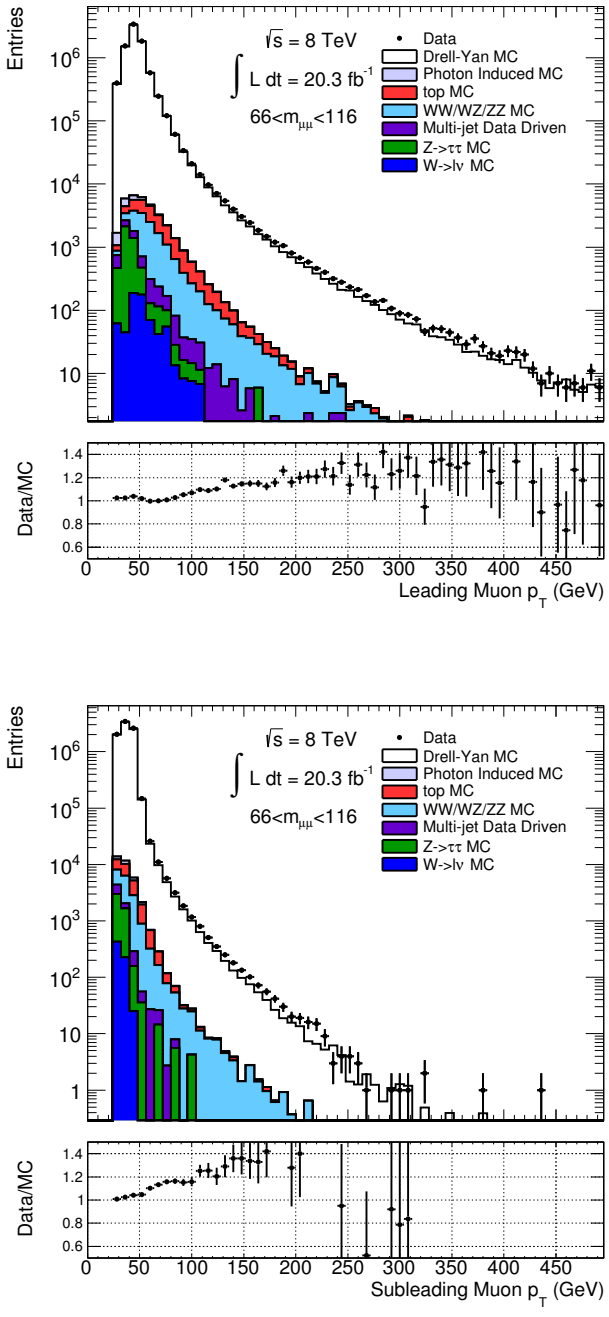

Figure F.13.: Leading (top) and subleading (bottom) muon p_T distributions for $66 < m_{\mu\mu} < 116$ GeV after full event selection and detector response corrections applied.

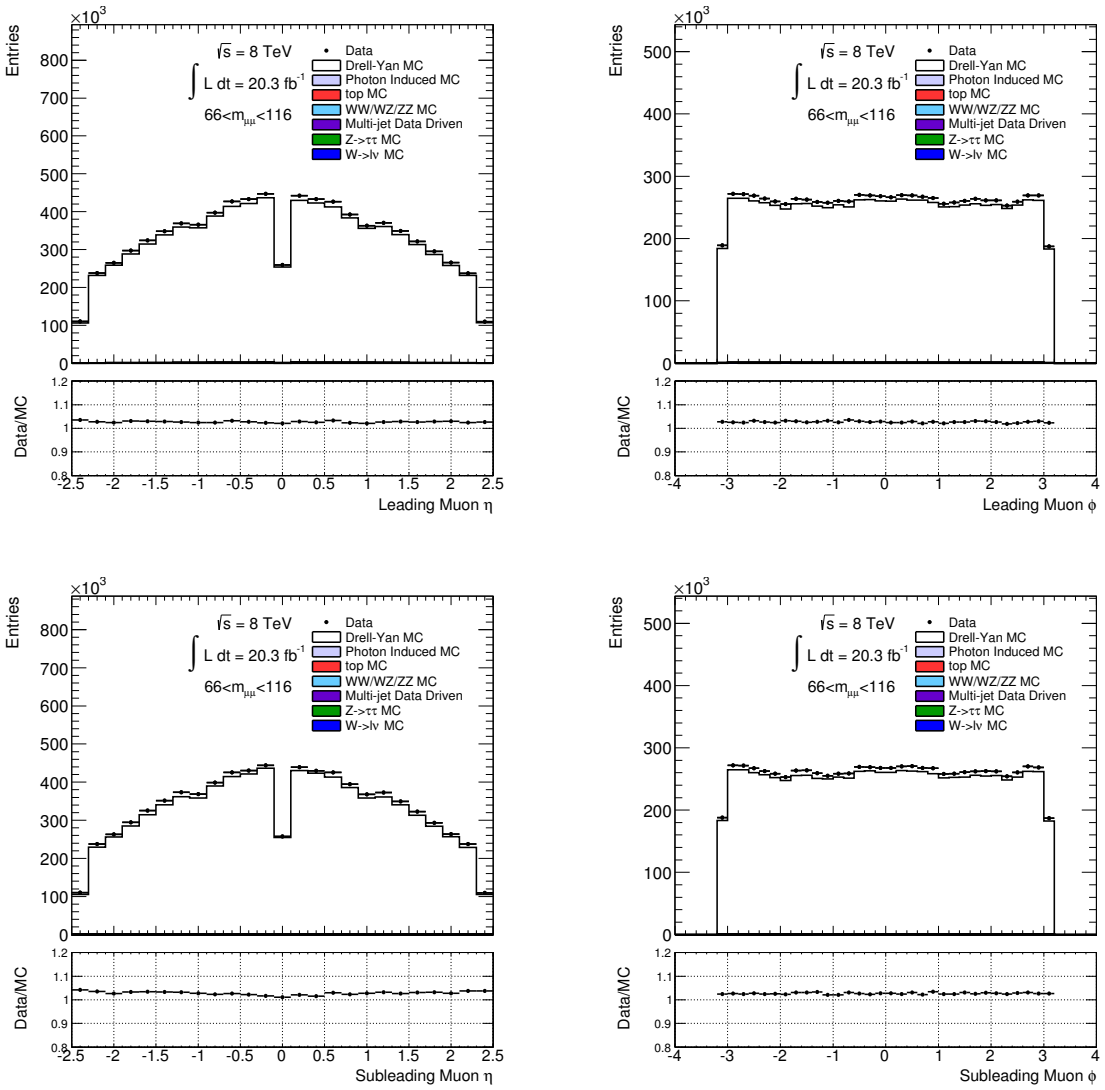

Figure F.14.: Leading (upper row) and subleading (lower row) muon η (left) and ϕ (right) distributions for $66 < m_{\mu\mu} < 116$ GeV after full event selection and detector response corrections applied.

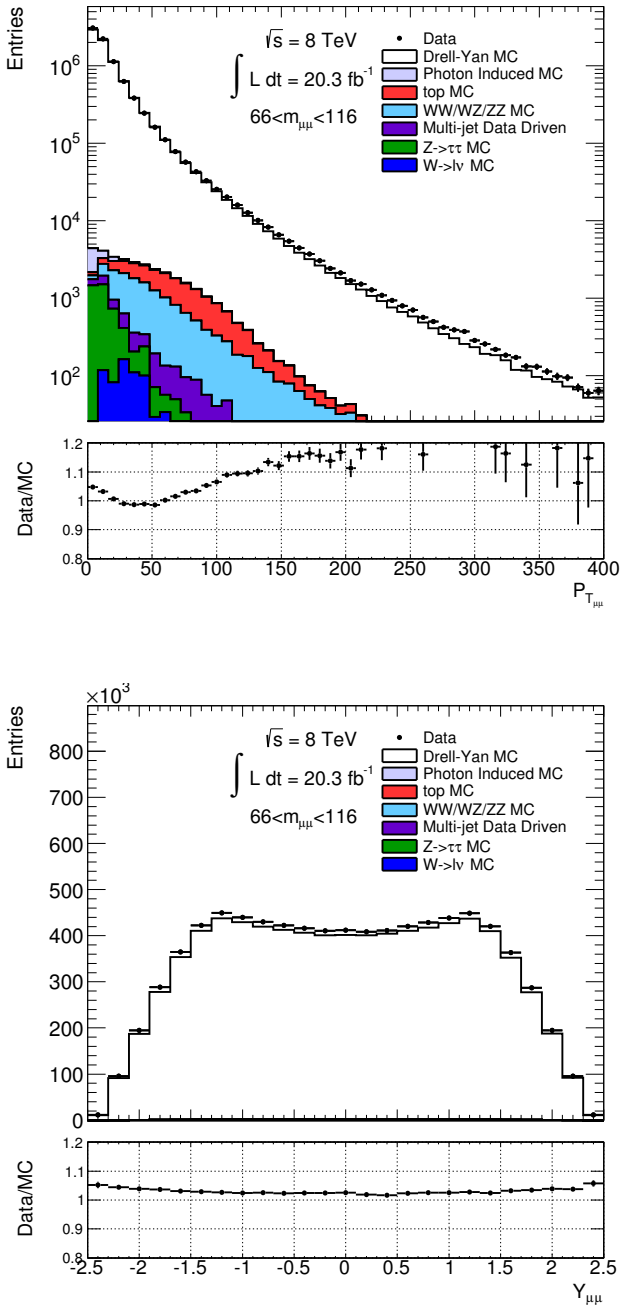

Figure F.15.: Dimuon p_T (top) and $y_{\mu\mu}$ (bottom) distributions for $66 < m_{\mu\mu} < 116$ GeV after full event selection and detector response corrections applied.

F.3. Cross Sections and Systematic Uncertainties

The Drell-Yan and photon induced fiducial cross sections are shown for the single differential, double differential dimuon mass and rapidity and double differential dimuon mass and muon $\Delta\eta$ measurements in figures F.16, F.17 and F.18 respectively. The cross section values are shown numerically in tables F.3, F.4, F.5, F.6 and F.7

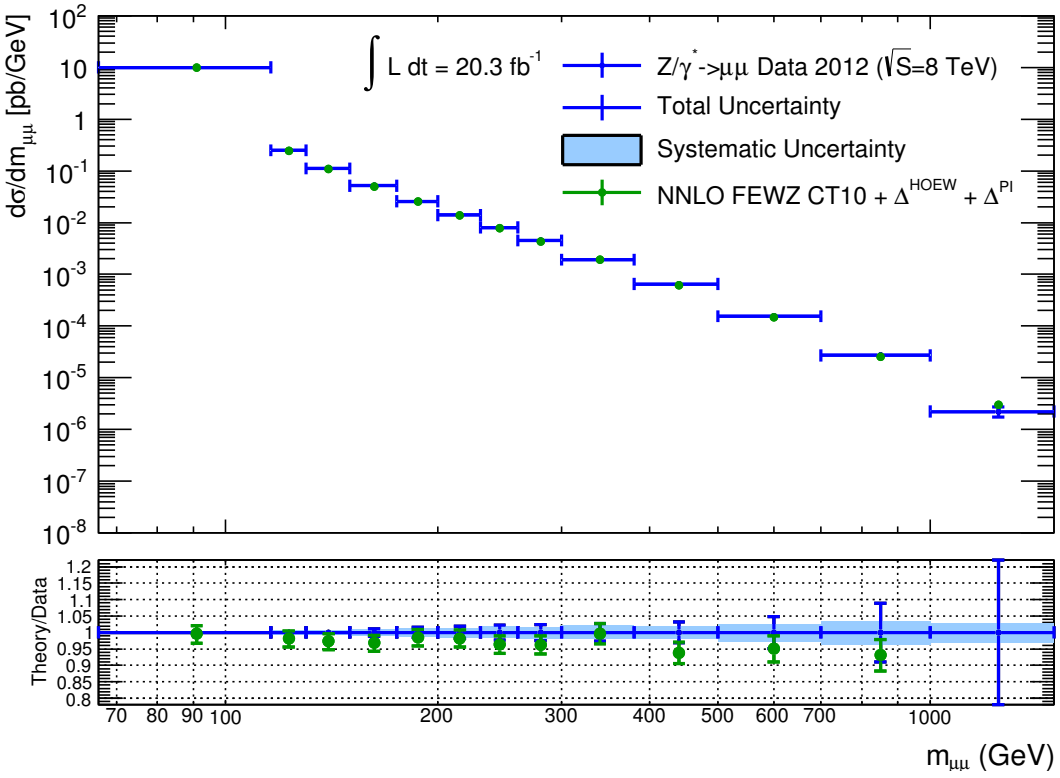

Figure F.16.: The single differential Drell-Yan dimuon channel fiducial cross section (muon $p_T < 25$ GeV) compared to NNLO theory, which includes NLO higher order electroweak corrections (Δ^{HOEW}) and the photon induced contribution (Δ^{PI}). The shaded errors on the data show the systematic uncertainty and the error bars show the total uncertainty. The lower plot shows the ratio of theory to data.

$m_{\mu\mu}^{min} - m_{\mu\mu}^{max}$	$\frac{d\sigma}{dm_{\mu\mu}}$	δ^{stat}	δ^{sys}	δ^{tot}	δ_{cor}^{trig}	δ_{unc}^{trig}	δ_{cor}^{reco}	δ_{unc}^{reco}	δ_{unc}^{MSres}	δ_{unc}^{IDres}	δ_{unc}^{pT}	δ_{unc}^{Isol}	δ_{cor}^{ewk}	δ_{unc}^{ewk}	$\delta_{cor}^{mult.}$	δ_{unc}^{MC}
[GeV]	[pb/GeV]	[%]	[%]	[%]	[%]	[%]	[%]	[%]	[%]	[%]	[%]	[%]	[%]	[%]	[%]	[%]
$66 - 116$	10.01×10^{0}	0.0	0.4	0.4	0.1	0.0	0.3	0.0	0.0	0.0	0.1	0.1	0.0	0.0	0.0	0.0
$116 - 130$	2.51×10^{-1}	0.4	0.6	0.8	0.1	0.0	0.4	0.0	0.1	0.1	0.4	0.1	0.3	0.1	0.1	0.1
$130 - 150$	1.12×10^{-1}	0.5	0.7	0.9	0.1	0.0	0.4	0.0	0.1	0.0	0.3	0.1	0.5	0.1	0.1	0.1
$150 - 175$	5.17×10^{-2}	0.7	1.0	1.2	0.1	0.0	0.4	0.0	0.0	0.0	0.2	0.1	0.8	0.2	0.2	0.1
$175 - 200$	2.58×10^{-2}	0.9	1.3	1.6	0.1	0.0	0.5	0.0	0.1	0.1	0.2	0.1	1.1	0.3	0.3	0.1
$200 - 230$	1.40×10^{-2}	1.1	1.5	1.9	0.1	0.0	0.5	0.0	0.1	0.0	0.2	0.1	1.3	0.3	0.4	0.2
$230 - 260$	8.04×10^{-3}	1.4	1.7	2.2	0.1	0.0	0.5	0.0	0.1	0.1	0.3	0.1	1.4	0.5	0.6	0.2
$260 - 300$	4.52×10^{-3}	1.6	1.8	2.4	0.1	0.0	0.6	0.0	0.1	0.1	0.2	0.2	1.4	0.5	0.7	0.2
$300 - 380$	1.92×10^{-3}	1.8	2.0	2.7	0.1	0.0	0.6	0.0	0.1	0.0	0.3	0.2	1.5	0.7	0.9	0.2
$380 - 500$	6.50×10^{-4}	2.5	1.9	3.2	0.1	0.0	0.7	0.0	0.2	0.1	0.2	0.3	1.2	0.6	1.1	0.2
$500 - 700$	1.55×10^{-4}	4.1	2.6	4.8	0.1	0.0	0.8	0.0	0.3	0.1	0.2	0.4	1.0	0.8	2.0	0.2
$700 - 1000$	2.72×10^{-5}	8.2	3.6	8.9	0.1	0.0	0.8	0.0	0.7	0.1	0.3	0.5	0.6	1.2	3.1	0.4
$1000 - 1500$	2.22×10^{-6}	21.8	3.0	22.0	0.1	0.0	1.0	0.0	0.9	0.5	0.3	0.5	0.7	2.2	0.8	0.4

Table F.3.: Muon channel Born level differential cross section $\frac{d\sigma}{dm_{\mu\mu}}$. The measurements are listed together with the statistical (δ^{stat}), systematic (δ^{sys}) and total (δ^{tot}) uncertainties. In addition the contributions from the individual correlated and uncorrelated systematic error sources are also provided consisting of the trigger efficiency (δ^{trig}), muon reconstruction efficiency (δ^{reco}), the MS resolution (δ^{MSres}), the ID resolution (δ^{IDres}), the muon transverse momentum scale (δ^{pT}), the isolation efficiency (δ^{Isol}), the electroweak background (δ^{ewk}), the multijet background (δ^{mult}) and the MC statistical uncertainty (δ^{MC}). Note that the $m_{\mu\mu} = 91$ GeV bin is shown here for completeness but is not intended for publication. The luminosity uncertainty of 2.8% is not included.

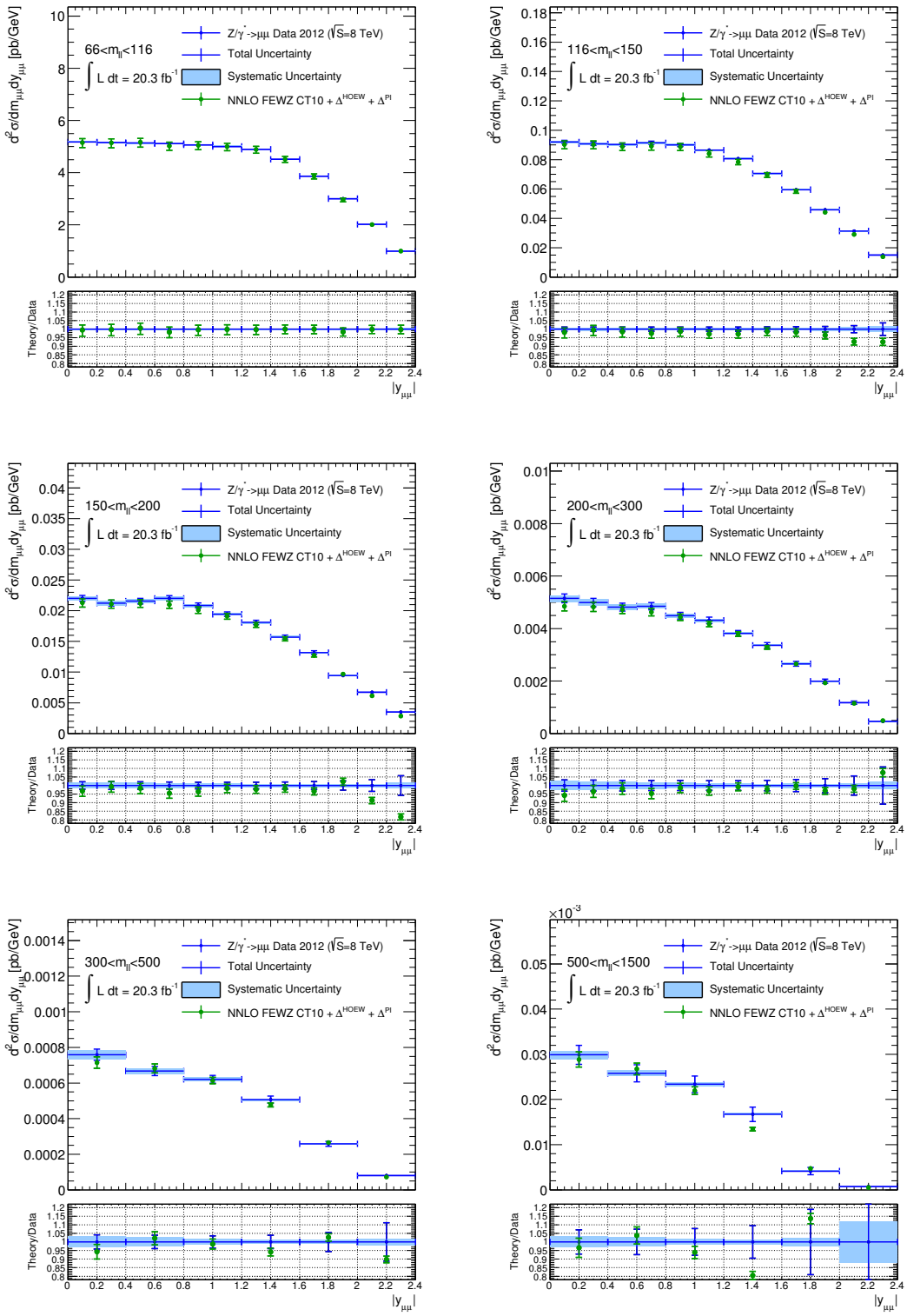

Figure F.17.: The double differential mass and rapidity Drell-Yan dimuon channel fiducial cross section (muon $p_T < 25$ GeV) compared to NNLO theory, which includes NLO higher order electroweak corrections (Δ^{HOEW}) and the photon induced contribution (Δ^{PI}). The shaded errors on the data show the systematic uncertainty and the error bars show the total uncertainty. The lower plot shows the ratio of theory to data.

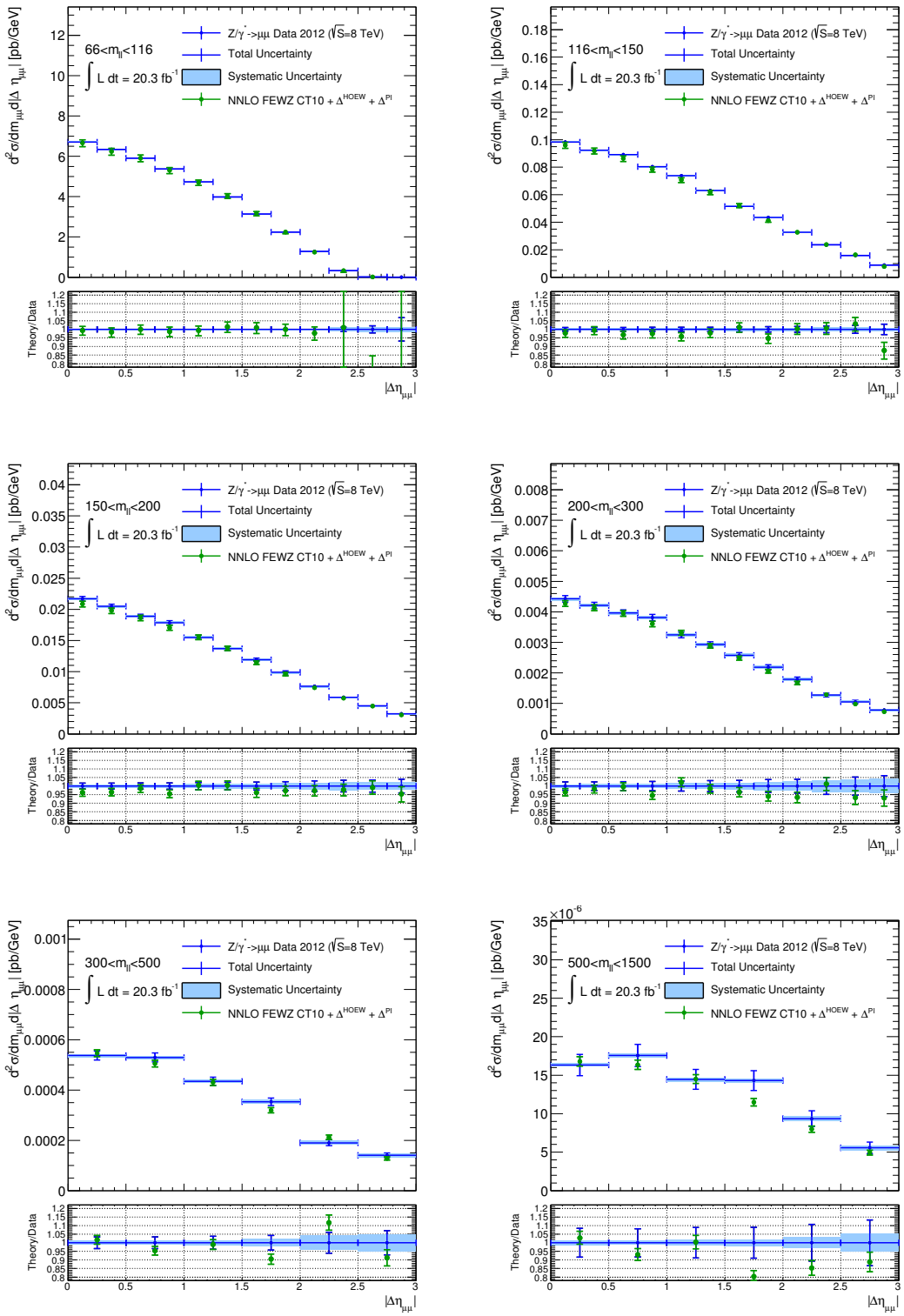

Figure F.18.: The double differential mass and $\Delta\eta$ Drell-Yan dimuon channel fiducial cross section (muon $p_T < 25$ GeV) compared to NNLO theory, which includes NLO higher order electroweak corrections (Δ^{HOEW}) and the photon induced contribution (Δ^{PI}). The shaded errors on the data show the systematic uncertainty and the error bars show the total uncertainty. The lower plot shows the ratio of theory to data.

$m_{\mu\mu}^{min} - m_{\mu\mu}^{max}$	$\lvert y_{\mu\mu}^{min}\rvert - \lvert y_{\mu\mu}^{max}\rvert$	$\frac{d\sigma}{dm_{\mu\mu}d\lvert y_{\mu\mu}\rvert}$	δ^{stat}	δ^{sys}	δ^{tot}	$\delta_{cor}^{\text{trig}}$	$\delta_{unc}^{\text{trig}}$	$\delta_{cor}^{\text{reco}}$	$\delta_{unc}^{\text{reco}}$	$\delta_{unc}^{\text{MSres}}$	$\delta_{unc}^{\text{IDres}}$	δ_{unc}^{pT}	$\delta_{unc}^{\text{Isol}}$	$\delta_{cor}^{\text{ewk}}$	$\delta_{unc}^{\text{ewk}}$	$\delta_{cor}^{\text{mult.}}$	δ_{unc}^{MC}
[GeV]		[pb/GeV]	[%]	[%]	[%]	[%]	[%]	[%]	[%]	[%]	[%]	[%]	[%]	[%]	[%]	[%]	[%]
$66 - 116$	$0.0 - 0.2$	51.74×10^{-1}	0.1	0.3	0.4	0.0	0.0	0.3	0.0	0.0	0.0	0.1	0.1	0.0	0.0	0.0	0.0
$66 - 116$	$0.2 - 0.4$	51.55×10^{-1}	0.1	0.3	0.4	0.1	0.0	0.3	0.0	0.0	0.0	0.1	0.1	0.0	0.0	0.0	0.0
$66 - 116$	$0.4 - 0.6$	51.34×10^{-1}	0.1	0.3	0.4	0.1	0.0	0.3	0.0	0.0	0.0	0.1	0.1	0.0	0.0	0.0	0.0
$66 - 116$	$0.6 - 0.8$	51.11×10^{-1}	0.1	0.3	0.3	0.1	0.0	0.3	0.0	0.0	0.0	0.1	0.1	0.0	0.0	0.0	0.0
$66 - 116$	$0.8 - 1.0$	50.68×10^{-1}	0.1	0.3	0.3	0.1	0.0	0.3	0.0	0.0	0.0	0.1	0.1	0.0	0.0	0.0	0.0
$66 - 116$	$1.0 - 1.2$	50.05×10^{-1}	0.1	0.3	0.3	0.1	0.0	0.3	0.0	0.0	0.0	0.1	0.1	0.0	0.0	0.0	0.0
$66 - 116$	$1.2 - 1.4$	48.98×10^{-1}	0.1	0.3	0.3	0.1	0.0	0.3	0.0	0.0	0.0	0.0	0.1	0.0	0.0	0.0	0.0
$66 - 116$	$1.4 - 1.6$	45.14×10^{-1}	0.1	0.4	0.4	0.1	0.0	0.3	0.0	0.0	0.0	0.0	0.1	0.0	0.0	0.0	0.0
$66 - 116$	$1.6 - 1.8$	38.65×10^{-1}	0.1	0.4	0.4	0.1	0.0	0.4	0.0	0.0	0.0	0.0	0.1	0.0	0.0	0.0	0.0
$66 - 116$	$1.8 - 2.0$	30.06×10^{-1}	0.1	0.4	0.5	0.1	0.0	0.4	0.0	0.0	0.0	0.0	0.1	0.0	0.0	0.0	0.0
$66 - 116$	$2.0 - 2.2$	20.18×10^{-1}	0.2	0.5	0.5	0.1	0.0	0.5	0.0	0.0	0.0	0.1	0.1	0.0	0.0	0.0	0.1
$66 - 116$	$2.2 - 2.4$	9.95×10^{-1}	0.3	0.6	0.7	0.1	0.0	0.6	0.0	0.0	0.0	0.1	0.1	0.0	0.0	0.0	0.1
$116 - 150$	$0.0 - 0.2$	9.20×10^{-2}	1.0	0.8	1.2	0.1	0.0	0.3	0.0	0.1	0.1	0.2	0.1	0.6	0.2	0.1	0.2
$116 - 150$	$0.2 - 0.4$	9.08×10^{-2}	1.0	0.8	1.3	0.1	0.0	0.4	0.0	0.1	0.1	0.3	0.1	0.5	0.3	0.1	0.2
$116 - 150$	$0.4 - 0.6$	9.02×10^{-2}	1.0	0.8	1.2	0.1	0.0	0.4	0.0	0.1	0.0	0.3	0.1	0.5	0.2	0.1	0.2
$116 - 150$	$0.6 - 0.8$	9.14×10^{-2}	0.9	0.7	1.2	0.1	0.0	0.4	0.0	0.2	0.0	0.2	0.1	0.5	0.1	0.1	0.2
$116 - 150$	$0.8 - 1.0$	9.00×10^{-2}	1.0	0.7	1.2	0.1	0.0	0.4	0.0	0.1	0.1	0.3	0.1	0.4	0.2	0.1	0.2
$116 - 150$	$1.0 - 1.2$	8.65×10^{-2}	1.0	0.7	1.2	0.1	0.0	0.4	0.0	0.1	0.1	0.4	0.1	0.3	0.2	0.1	0.2
$116 - 150$	$1.2 - 1.4$	8.07×10^{-2}	1.0	0.7	1.2	0.1	0.0	0.4	0.0	0.1	0.0	0.4	0.1	0.3	0.1	0.1	0.2
$116 - 150$	$1.4 - 1.6$	7.05×10^{-2}	1.1	0.7	1.3	0.1	0.0	0.4	0.0	0.1	0.1	0.4	0.1	0.2	0.2	0.1	0.3
$116 - 150$	$1.6 - 1.8$	5.95×10^{-2}	1.2	0.7	1.4	0.1	0.0	0.4	0.0	0.0	0.1	0.4	0.1	0.2	0.2	0.0	0.3
$116 - 150$	$1.8 - 2.0$	4.58×10^{-2}	1.4	0.8	1.6	0.1	0.0	0.5	0.0	0.1	0.1	0.5	0.1	0.1	0.1	0.0	0.4
$116 - 150$	$2.0 - 2.2$	3.14×10^{-2}	1.8	1.0	2.1	0.1	0.0	0.6	0.0	0.5	0.1	0.5	0.1	0.1	0.1	0.0	0.5
$116 - 150$	$2.2 - 2.4$	1.50×10^{-2}	3.2	1.7	3.6	0.1	0.0	0.7	0.0	0.7	0.2	0.9	0.1	0.1	0.2	0.0	1.0
$150 - 200$	$0.0 - 0.2$	2.20×10^{-2}	1.5	1.6	2.2	0.1	0.0	0.4	0.0	0.0	0.1	0.2	0.1	1.4	0.4	0.4	0.2
$150 - 200$	$0.2 - 0.4$	2.12×10^{-2}	1.5	1.7	2.3	0.1	0.0	0.4	0.0	0.0	0.0	0.2	0.1	1.4	0.7	0.3	0.3
$150 - 200$	$0.4 - 0.6$	2.16×10^{-2}	1.5	1.5	2.2	0.1	0.0	0.4	0.0	0.1	0.1	0.2	0.1	1.3	0.6	0.3	0.2
$150 - 200$	$0.6 - 0.8$	2.20×10^{-2}	1.5	1.3	2.0	0.1	0.0	0.4	0.0	0.1	0.1	0.2	0.1	1.1	0.5	0.2	0.3
$150 - 200$	$0.8 - 1.0$	2.09×10^{-2}	1.6	1.2	2.0	0.1	0.0	0.4	0.0	0.1	0.1	0.2	0.1	0.9	0.3	0.2	0.3
$150 - 200$	$1.0 - 1.2$	1.94×10^{-2}	1.6	1.1	2.0	0.1	0.0	0.4	0.0	0.0	0.0	0.2	0.1	0.8	0.4	0.1	0.3
$150 - 200$	$1.2 - 1.4$	1.81×10^{-2}	1.7	0.9	1.9	0.1	0.0	0.4	0.0	0.1	0.1	0.2	0.1	0.6	0.4	0.1	0.3
$150 - 200$	$1.4 - 1.6$	1.57×10^{-2}	1.9	0.9	2.1	0.1	0.0	0.5	0.0	0.0	0.1	0.3	0.1	0.5	0.5	0.1	0.3
$150 - 200$	$1.6 - 1.8$	1.32×10^{-2}	2.1	0.9	2.3	0.1	0.0	0.5	0.0	0.0	0.1	0.3	0.1	0.3	0.5	0.0	0.3
$150 - 200$	$1.8 - 2.0$	9.44×10^{-3}	2.6	0.9	2.7	0.1	0.0	0.6	0.0	0.1	0.1	0.4	0.1	0.2	0.3	0.0	0.4
$150 - 200$	$2.0 - 2.2$	6.71×10^{-3}	3.2	1.0	3.4	0.1	0.0	0.6	0.0	0.1	0.1	0.3	0.1	0.1	0.3	0.0	0.5
$150 - 200$	$2.2 - 2.4$	3.49×10^{-3}	5.5	1.5	5.7	0.1	0.0	0.7	0.0	0.1	0.3	0.6	0.1	0.1	0.4	0.0	1.1

Table F.4.: Muon channel Born level differential cross section $\frac{d\sigma}{dm_{\mu\mu}d|y_{\mu\mu}|}$. Note that the $m_{\mu\mu} = 91$ GeV bin is shown here for completeness but is not intended for publication. The measurements are listed together with the statistical (δ^{stat}), systematic (δ^{sys}) and total (δ^{tot}) uncertainties. In addition the contributions from the individual correlated and uncorrelated systematic error sources are also provided consisting of the trigger efficiency (δ^{trig}), muon reconstruction efficiency (δ^{reco}), the MS resolution (δ^{MSres}), the ID resolution (δ^{IDres}), the muon transverse momentum scale (δ^{pT}), the isolation efficiency (δ^{Isol}), the electroweak background (δ^{ewk}), the multijet background (δ^{mult}) and the MC statistical uncertainty (δ^{MC}). The luminosity uncertainty of 2.8% is not included.

$m_{\mu\mu}^{min} - m_{\mu\mu}^{max}$	$\lvert y_{\mu\mu}^{min}\rvert - \lvert y_{\mu\mu}^{max}\rvert$	$\frac{d\sigma}{dm_{\mu\mu}d\lvert y_{\mu\mu}\rvert}$	δ^{stat}	δ^{sys}	δ^{tot}	δ_{cor}^{trig}	δ_{unc}^{trig}	δ_{cor}^{reco}	δ_{unc}^{reco}	δ_{unc}^{MSres}	δ_{unc}^{IDres}	δ_{unc}^{pT}	δ_{unc}^{Isol}	δ_{cor}^{ewk}	δ_{unc}^{ewk}	$\delta_{cor}^{mult.}$	δ_{unc}^{MC}
[GeV]		[pb/GeV]	[%]	[%]	[%]	[%]	[%]	[%]	[%]	[%]	[%]	[%]	[%]	[%]	[%]	[%]	[%]	[%]
200 − 300	0.0 − 0.2	5.15×10^{-3}	2.1	2.5	3.3	0.1	0.0	0.5	0.0	0.2	0.1	0.2	0.1	2.1	0.9	0.7	0.2
200 − 300	0.2 − 0.4	5.00×10^{-3}	2.1	2.4	3.2	0.1	0.0	0.5	0.0	0.2	0.0	0.2	0.1	2.1	0.7	0.7	0.2
200 − 300	0.4 − 0.6	4.82×10^{-3}	2.1	2.2	3.1	0.1	0.0	0.5	0.0	0.1	0.0	0.2	0.1	1.9	0.7	0.5	0.2
200 − 300	0.6 − 0.8	4.85×10^{-3}	2.2	1.9	2.9	0.1	0.0	0.5	0.0	0.2	0.1	0.2	0.1	1.6	0.7	0.4	0.3
200 − 300	0.8 − 1.0	4.49×10^{-3}	2.3	1.7	2.9	0.1	0.0	0.5	0.0	0.1	0.1	0.3	0.1	1.4	0.6	0.2	0.3
200 − 300	1.0 − 1.2	4.31×10^{-3}	2.4	1.4	2.8	0.1	0.0	0.5	0.0	0.1	0.0	0.2	0.1	1.1	0.6	0.2	0.3
200 − 300	1.2 − 1.4	3.82×10^{-3}	2.6	1.1	2.8	0.1	0.0	0.5	0.0	0.1	0.1	0.2	0.1	0.8	0.5	0.1	0.3
200 − 300	1.4 − 1.6	3.36×10^{-3}	2.8	1.0	3.0	0.1	0.0	0.5	0.0	0.1	0.0	0.3	0.1	0.5	0.5	0.1	0.3
200 − 300	1.6 − 1.8	2.66×10^{-3}	3.3	1.3	3.5	0.1	0.0	0.6	0.0	0.1	0.1	0.2	0.1	0.3	1.0	0.0	0.4
200 − 300	1.8 − 2.0	1.99×10^{-3}	3.9	1.0	4.1	0.1	0.0	0.7	0.0	0.1	0.2	0.3	0.1	0.2	0.4	0.0	0.5
200 − 300	2.0 − 2.2	1.17×10^{-3}	5.5	1.3	5.6	0.1	0.0	0.7	0.0	0.3	0.2	0.5	0.1	0.1	0.5	0.0	0.7
200 − 300	2.2 − 2.4	4.58×10^{-4}	10.6	2.1	10.8	0.1	0.0	0.9	0.0	0.4	0.3	0.5	0.1	0.1	0.9	0.0	1.6
300 − 500	0.0 − 0.4	7.58×10^{-4}	2.6	3.2	4.2	0.1	0.0	0.6	0.0	0.1	0.0	0.2	0.2	2.3	1.4	1.6	0.2
300 − 500	0.4 − 0.8	6.68×10^{-4}	2.9	2.5	3.8	0.1	0.0	0.6	0.0	0.1	0.0	0.2	0.2	2.0	1.0	1.0	0.2
300 − 500	0.8 − 1.2	6.21×10^{-4}	3.2	1.6	3.6	0.1	0.0	0.6	0.0	0.1	0.1	0.3	0.2	1.1	0.8	0.3	0.2
300 − 500	1.2 − 1.6	5.07×10^{-4}	3.7	1.1	3.8	0.1	0.0	0.6	0.0	0.1	0.1	0.2	0.2	0.5	0.6	0.1	0.3
300 − 500	1.6 − 2.0	2.59×10^{-4}	5.4	1.2	5.5	0.1	0.0	0.8	0.0	0.2	0.1	0.3	0.2	0.2	0.6	0.0	0.4
300 − 500	2.0 − 2.4	7.99×10^{-5}	11.0	1.9	11.1	0.1	0.0	1.0	0.0	0.3	0.1	0.5	0.2	0.1	0.7	0.0	1.3
500 − 1500	0.0 − 0.4	2.99×10^{-5}	6.3	3.2	7.1	0.1	0.0	0.7	0.0	0.3	0.3	0.2	0.4	1.4	1.6	2.1	0.3
500 − 1500	0.4 − 0.8	2.58×10^{-5}	6.9	2.5	7.4	0.1	0.0	0.7	0.0	0.2	0.3	0.3	0.4	1.2	1.5	1.3	0.3
500 − 1500	0.8 − 1.2	2.34×10^{-5}	7.7	1.7	7.8	0.1	0.0	0.8	0.0	0.1	0.2	0.3	0.4	0.6	1.1	0.4	0.3
500 − 1500	1.2 − 1.6	1.67×10^{-5}	9.4	1.3	9.5	0.1	0.0	0.8	0.0	0.1	0.0	0.3	0.4	0.2	0.7	0.1	0.5
500 − 1500	1.6 − 2.0	4.16×10^{-6}	18.9	2.3	19.0	0.1	0.0	1.1	0.0	0.8	0.5	0.2	0.4	0.2	1.0	0.0	1.3
500 − 1500	2.0 − 2.4	7.15×10^{-7}	40.8	12.0	42.5	0.1	0.0	2.0	0.0	1.9	2.8	0.5	0.4	0.1	0.4	0.0	11.3

Table F.5.: Muon channel Born level differential cross section $\frac{d\sigma}{dm_{\mu\mu}d|y_{\mu\mu}|}$. Note that the $m_{\mu\mu} = 91$ GeV bin is shown here for completeness but is not intended for publication. The measurements are listed together with the statistical (δ^{stat}), systematic (δ^{sys}) and total (δ^{tot}) uncertainties. In addition the contributions from the individual correlated and uncorrelated systematic error sources are also provided consisting of the trigger efficiency (δ^{trig}), muon reconstruction efficiency (δ^{reco}), the MS resolution (δ^{MSres}), the ID resolution (δ^{IDres}), the muon transverse momentum scale (δ^{pT}), the isolation efficiency (δ^{Isol}), the electroweak background (δ^{ewk}), the multijet background (δ^{mult}) and the MC statistical uncertainty (δ^{MC}). The luminosity uncertainty of 2.8% is not included.

$m_{\mu\mu}^{min} - m_{\mu\mu}^{max}$ [GeV]	$\lvert\Delta\eta_{\mu\mu}^{min}\rvert - \lvert\Delta\eta_{\mu\mu}^{max}\rvert$	$\frac{d\sigma}{dm_{\mu\mu}d\lvert\delta\eta_{\mu\mu}\rvert}$ [pb/GeV]	δ^{stat} [%]	δ^{sys} [%]	δ^{tot} [%]	δ_{cor}^{trig} [%]	δ_{unc}^{trig} [%]	δ_{cor}^{reco} [%]	δ_{unc}^{reco} [%]	δ_{unc}^{MSres} [%]	δ_{unc}^{IDres} [%]	δ_{unc}^{pT} [%]	δ_{unc}^{Isol} [%]	δ_{cor}^{ewk} [%]	δ_{unc}^{ewk} [%]	$\delta_{cor}^{multi.}$ [%]	δ_{unc}^{MC} [%]
66 – 116	0.00 – 0.25	67.03×10^{-1}	0.1	0.4	0.4	0.1	0.0	0.3	0.0	0.0	0.0	0.0	0.1	0.0	0.0	0.0	0.0
66 – 116	0.25 – 0.50	63.41×10^{-1}	0.1	0.3	0.4	0.1	0.0	0.3	0.0	0.0	0.0	0.0	0.1	0.0	0.0	0.0	0.0
66 – 116	0.50 – 0.75	59.12×10^{-1}	0.1	0.3	0.4	0.1	0.0	0.3	0.0	0.0	0.0	0.0	0.1	0.0	0.0	0.0	0.0
66 – 116	0.75 – 1.00	53.72×10^{-1}	0.1	0.3	0.4	0.1	0.0	0.3	0.0	0.0	0.0	0.0	0.1	0.0	0.0	0.0	0.0
66 – 116	1.00 – 1.25	47.27×10^{-1}	0.1	0.3	0.4	0.1	0.0	0.3	0.0	0.0	0.0	0.0	0.1	0.0	0.0	0.0	0.0
66 – 116	1.25 – 1.50	39.78×10^{-1}	0.1	0.4	0.4	0.1	0.0	0.3	0.0	0.0	0.0	0.0	0.1	0.0	0.0	0.0	0.0
66 – 116	1.50 – 1.75	31.31×10^{-1}	0.1	0.4	0.4	0.1	0.0	0.3	0.0	0.0	0.0	0.1	0.1	0.0	0.0	0.0	0.0
66 – 116	1.75 – 2.00	22.43×10^{-1}	0.1	0.4	0.4	0.1	0.0	0.3	0.0	0.0	0.0	0.1	0.1	0.0	0.0	0.0	0.0
66 – 116	2.00 – 2.25	12.76×10^{-1}	0.2	0.5	0.6	0.1	0.0	0.3	0.0	0.0	0.0	0.4	0.1	0.0	0.0	0.0	0.1
66 – 116	2.25 – 2.50	3.26×10^{-1}	0.4	1.2	1.3	0.1	0.0	0.3	0.0	0.1	0.1	1.1	0.1	0.0	0.0	0.0	0.1
66 – 116	2.50 – 2.75	2.11×10^{-2}	1.5	1.3	2.0	0.1	0.0	0.3	0.0	0.4	0.1	1.2	0.1	0.1	0.1	0.0	0.3
66 – 116	3.00 – 3.00	1.12×10^{-3}	6.6	1.5	6.8	0.1	0.0	0.3	0.0	1.1	0.3	0.5	0.1	0.2	0.6	0.1	0.2
116 – 150	0.00 – 0.25	9.82×10^{-2}	0.8	0.6	1.0	0.1	0.0	0.4	0.0	0.1	0.0	0.3	0.1	0.3	0.1	0.0	0.2
116 – 150	0.25 – 0.50	9.24×10^{-2}	0.9	0.7	1.1	0.1	0.0	0.4	0.0	0.1	0.1	0.3	0.1	0.3	0.2	0.0	0.2
116 – 150	0.50 – 0.75	8.92×10^{-2}	0.9	0.7	1.1	0.1	0.0	0.4	0.0	0.1	0.0	0.3	0.1	0.3	0.1	0.0	0.2
116 – 150	0.75 – 1.00	8.04×10^{-2}	0.9	0.7	1.2	0.1	0.0	0.4	0.0	0.1	0.1	0.4	0.1	0.3	0.2	0.1	0.2
116 – 150	1.00 – 1.25	7.38×10^{-2}	1.0	0.7	1.2	0.1	0.0	0.4	0.0	0.1	0.1	0.3	0.1	0.4	0.1	0.1	0.2
116 – 150	1.25 – 1.50	6.30×10^{-2}	1.0	0.7	1.3	0.1	0.0	0.4	0.0	0.0	0.1	0.3	0.1	0.4	0.2	0.1	0.3
116 – 150	1.50 – 1.75	5.16×10^{-2}	1.1	0.8	1.4	0.1	0.0	0.4	0.0	0.0	0.0	0.4	0.1	0.5	0.3	0.1	0.3
116 – 150	1.75 – 2.00	4.35×10^{-2}	1.2	0.9	1.5	0.1	0.0	0.4	0.0	0.1	0.1	0.4	0.1	0.5	0.3	0.2	0.3
116 – 150	2.00 – 2.25	3.27×10^{-2}	1.4	1.0	1.7	0.1	0.0	0.4	0.0	0.1	0.1	0.4	0.1	0.5	0.3	0.2	0.4
116 – 150	2.25 – 2.50	2.36×10^{-2}	1.7	1.0	2.0	0.1	0.0	0.4	0.0	0.2	0.1	0.4	0.1	0.5	0.5	0.3	0.4
116 – 150	2.50 – 2.75	1.58×10^{-2}	2.0	1.1	2.3	0.1	0.0	0.3	0.0	0.1	0.1	0.5	0.1	0.4	0.6	0.3	0.5
116 – 150	3.00 – 3.00	8.85×10^{-3}	2.8	1.0	3.0	0.1	0.0	0.3	0.0	0.2	0.1	0.4	0.1	0.4	0.4	0.2	0.6
150 – 200	0.00 – 0.25	2.17×10^{-2}	1.4	0.9	1.7	0.1	0.0	0.5	0.0	0.1	0.1	0.2	0.1	0.6	0.4	0.0	0.2
150 – 200	0.25 – 0.50	2.05×10^{-2}	1.5	0.9	1.7	0.1	0.0	0.5	0.0	0.0	0.1	0.2	0.1	0.6	0.2	0.0	0.2
150 – 200	0.50 – 0.75	1.89×10^{-2}	1.5	0.9	1.8	0.1	0.0	0.4	0.0	0.1	0.0	0.2	0.1	0.6	0.3	0.1	0.2
150 – 200	0.75 – 1.00	1.78×10^{-2}	1.6	1.0	1.8	0.1	0.0	0.4	0.0	0.1	0.0	0.2	0.1	0.7	0.3	0.1	0.3
150 – 200	1.00 – 1.25	1.55×10^{-2}	1.7	1.2	2.1	0.1	0.0	0.5	0.0	0.0	0.0	0.2	0.1	0.9	0.6	0.1	0.3
150 – 200	1.25 – 1.50	1.37×10^{-2}	1.8	1.3	2.2	0.1	0.0	0.5	0.0	0.0	0.1	0.2	0.1	1.0	0.6	0.1	0.3
150 – 200	1.50 – 1.75	1.19×10^{-2}	1.9	1.3	2.3	0.1	0.0	0.5	0.0	0.1	0.0	0.2	0.1	1.1	0.4	0.2	0.3
150 – 200	1.75 – 2.00	9.89×10^{-3}	2.0	1.6	2.6	0.1	0.0	0.5	0.0	0.0	0.1	0.2	0.1	1.3	0.7	0.3	0.4
150 – 200	2.00 – 2.25	7.65×10^{-3}	2.3	1.9	3.0	0.1	0.0	0.5	0.0	0.1	0.3	0.2	0.1	1.5	0.8	0.4	0.5
150 – 200	2.25 – 2.50	5.89×10^{-3}	2.5	2.3	3.4	0.1	0.0	0.5	0.0	0.1	0.0	0.2	0.1	1.7	1.3	0.6	0.5
150 – 200	2.50 – 2.75	4.51×10^{-3}	2.9	2.0	3.5	0.1	0.0	0.4	0.0	0.1	0.1	0.3	0.1	1.5	0.9	0.8	0.6
150 – 200	3.00 – 3.00	3.22×10^{-3}	3.4	2.2	4.1	0.1	0.0	0.4	0.0	0.0	0.1	0.3	0.1	1.5	1.0	1.0	0.7

Table F.6.: Muon channel Born level differential cross section $\frac{d\sigma}{dm_{\mu\mu}d|\delta\eta_{\mu\mu}|}$. Note that the $m_{\mu\mu} = 91$ GeV bin is shown here for completeness but is not intended for publication. The measurements are listed together with the statistical (δ^{stat}), systematic (δ^{sys}) and total (δ^{tot}) uncertainties. In addition the contributions from the individual correlated and uncorrelated systematic error sources are also provided consisting of the trigger efficiency (δ^{trig}), muon reconstruction efficiency (δ^{reco}), the MS resolution (δ^{MSres}), the ID resolution (δ^{IDres}), the muon transverse momentum scale (δ^{pT}), the isolation efficiency (δ^{Isol}), the electroweak background (δ^{ewk}), the multijet background (δ^{mult}) and the MC statistical uncertainty (δ^{MC}). The luminosity uncertainty of 2.8% is not included.

$m_{\mu\mu}^{min} - m_{\mu\mu}^{max}$	$\lvert\Delta\eta_{\mu\mu}^{min}\rvert - \lvert\Delta\eta_{\mu\mu}^{max}\rvert$	$\frac{d\sigma}{dm_{\mu\mu}d\lvert\delta\eta_{\mu\mu}\rvert}$	δ^{stat}	δ^{sys}	δ^{tot}	$\delta_{cor}^{\text{trig}}$	$\delta_{unc}^{\text{trig}}$	$\delta_{cor}^{\text{reco}}$	$\delta_{unc}^{\text{reco}}$	$\delta_{unc}^{\text{MSres}}$	$\delta_{unc}^{\text{IDres}}$	δ_{unc}^{pT}	$\delta_{unc}^{\text{Isol}}$	$\delta_{cor}^{\text{ewk}}$	$\delta_{unc}^{\text{ewk}}$	$\delta_{cor}^{\text{multi.}}$	δ_{unc}^{MC}
[GeV]		[pb/GeV]	[%]	[%]	[%]	[%]	[%]	[%]	[%]	[%]	[%]	[%]	[%]	[%]	[%]	[%]	[%]
$200 - 300$	$0.00 - 0.25$	4.43×10^{-3}	2.2	1.0	2.4	0.1	0.0	0.5	0.0	0.1	0.1	0.3	0.1	0.6	0.4	0.1	0.2
$200 - 300$	$0.25 - 0.50$	4.21×10^{-3}	2.3	1.0	2.5	0.1	0.0	0.5	0.0	0.1	0.0	0.3	0.1	0.7	0.4	0.1	0.2
$200 - 300$	$0.50 - 0.75$	3.97×10^{-3}	2.3	1.1	2.6	0.1	0.0	0.5	0.0	0.1	0.0	0.2	0.1	0.8	0.4	0.1	0.2
$200 - 300$	$0.75 - 1.00$	3.81×10^{-3}	2.4	1.2	2.7	0.1	0.0	0.5	0.0	0.2	0.1	0.2	0.1	0.9	0.5	0.1	0.3
$200 - 300$	$1.00 - 1.25$	3.24×10^{-3}	2.5	1.6	3.0	0.1	0.0	0.5	0.0	0.1	0.0	0.2	0.1	1.1	0.8	0.1	0.3
$200 - 300$	$1.25 - 1.50$	2.93×10^{-3}	2.6	1.7	3.1	0.1	0.0	0.5	0.0	0.1	0.1	0.2	0.1	1.4	0.7	0.2	0.3
$200 - 300$	$1.50 - 1.75$	2.58×10^{-3}	2.7	1.9	3.3	0.1	0.0	0.6	0.0	0.1	0.1	0.2	0.1	1.6	0.8	0.2	0.3
$200 - 300$	$1.75 - 2.00$	2.18×10^{-3}	2.9	2.5	3.8	0.1	0.0	0.6	0.0	0.1	0.1	0.3	0.1	1.8	1.5	0.3	0.3
$200 - 300$	$2.00 - 2.25$	1.79×10^{-3}	3.2	2.5	4.1	0.1	0.0	0.6	0.0	0.1	0.2	0.2	0.1	2.1	1.1	0.4	0.4
$200 - 300$	$2.25 - 2.50$	1.28×10^{-3}	3.5	3.4	4.9	0.2	0.0	0.6	0.0	0.1	0.1	0.3	0.1	2.8	1.5	0.8	0.4
$200 - 300$	$2.50 - 2.75$	1.05×10^{-3}	3.8	3.7	5.3	0.1	0.0	0.6	0.0	0.1	0.1	0.2	0.1	3.0	1.7	1.1	0.5
$200 - 300$	$3.00 - 3.00$	7.87×10^{-4}	4.3	4.3	6.1	0.1	0.0	0.6	0.0	0.1	0.2	0.3	0.1	3.2	2.1	1.6	0.6
$300 - 500$	$0.00 - 0.50$	5.37×10^{-4}	3.2	1.1	3.4	0.1	0.0	0.6	0.0	0.1	0.1	0.2	0.2	0.6	0.5	0.2	0.2
$300 - 500$	$0.50 - 1.00$	5.30×10^{-4}	3.2	1.1	3.4	0.1	0.0	0.6	0.0	0.0	0.1	0.2	0.2	0.7	0.6	0.1	0.2
$300 - 500$	$1.00 - 1.50$	4.35×10^{-4}	3.5	1.4	3.8	0.1	0.0	0.6	0.0	0.0	0.1	0.2	0.2	1.0	0.8	0.2	0.3
$300 - 500$	$1.50 - 2.00$	3.53×10^{-4}	3.7	2.1	4.3	0.1	0.0	0.6	0.0	0.3	0.1	0.3	0.2	1.5	1.1	0.4	0.3
$300 - 500$	$2.00 - 2.50$	1.90×10^{-4}	4.5	4.1	6.1	0.2	0.0	0.7	0.0	0.1	0.2	0.3	0.2	3.2	2.1	1.1	0.4
$300 - 500$	$2.50 - 3.00$	1.40×10^{-4}	5.1	4.8	7.0	0.1	0.0	0.7	0.0	0.1	0.1	0.6	0.2	3.5	2.5	1.9	0.5
$500 - 1500$	$0.00 - 0.50$	1.63×10^{-5}	8.3	1.3	8.4	0.1	0.0	0.8	0.0	0.1	0.1	0.2	0.5	0.3	0.8	0.2	0.4
$500 - 1500$	$0.50 - 1.00$	1.76×10^{-5}	8.1	1.3	8.2	0.1	0.0	0.7	0.0	0.1	0.1	0.3	0.4	0.3	0.7	0.1	0.4
$500 - 1500$	$1.00 - 1.50$	1.45×10^{-5}	8.8	1.7	8.9	0.1	0.0	0.8	0.0	0.1	0.1	0.3	0.4	0.5	1.2	0.2	0.4
$500 - 1500$	$1.50 - 2.00$	1.43×10^{-5}	8.8	1.9	9.0	0.1	0.0	0.7	0.0	0.1	0.2	0.2	0.3	0.6	1.4	0.3	0.4
$500 - 1500$	$2.00 - 2.50$	9.36×10^{-6}	10.3	3.2	10.7	0.1	0.0	0.8	0.0	0.2	0.1	0.2	0.3	1.3	2.5	1.0	0.5
$500 - 1500$	$2.50 - 3.00$	5.56×10^{-6}	12.2	5.3	13.3	0.1	0.0	0.8	0.0	0.2	0.0	0.2	0.3	2.3	4.0	2.3	0.7

Table F.7.: Muon channel Born level differential cross section $\frac{d\sigma}{dm_{\mu\mu}d|\delta\eta_{\mu\mu}|}$. Note that the $m_{\mu\mu} = 91$ GeV bin is shown here for completeness but is not intended for publication. The measurements are listed together with the statistical (δ^{stat}), systematic (δ^{sys}) and total (δ^{tot}) uncertainties. In addition the contributions from the individual correlated and uncorrelated systematic error sources are also provided consisting of the trigger efficiency (δ^{trig}), muon reconstruction efficiency (δ^{reco}), the MS resolution (δ^{MSres}), the ID resolution (δ^{IDres}), the muon transverse momentum scale (δ^{pT}), the isolation efficiency (δ^{Isol}), the electroweak background (δ^{ewk}), the multijet background (δ^{mult}) and the MC statistical uncertainty (δ^{MC}). The luminosity uncertainty of 2.8% is not included.

Bibliography

[1] *Review of Particle Physics*, vol. 86. American Physical Society, Jul, 2012. http://link.aps.org/doi/10.1103/PhysRevD.86.010001.

[2] P. W. Higgs, *Broken Symmetries and the Masses of Gauge Bosons*, Phys. Rev. Lett. **13** (Oct, 1964) 508–509. http://link.aps.org/doi/10.1103/PhysRevLett.13.508.

[3] F. Englert and R. Brout, *Broken Symmetry and the Mass of Gauge Vector Mesons*, Phys. Rev. Lett. **13** (Aug, 1964) 321–323. http://link.aps.org/doi/10.1103/PhysRevLett.13.321.

[4] ATLAS Collaboration Collaboration, G. Aad et al., *Observation of a new particle in the search for the Standard Model Higgs boson with the ATLAS detector at the LHC*, Phys.Lett. **B716** (2012) 1–29, arXiv:1207.7214 [hep-ex].

[5] CMS Collaboration Collaboration, S. Chatrchyan et al., *Observation of a new boson at a mass of 125 GeV with the CMS experiment at the LHC*, Phys.Lett. **B716** (2012) 30–61, arXiv:1207.7235 [hep-ex].

[6] G. Altarelli and G. Parisi, *Asymptotic freedom in parton language*, Nuclear Physics B **126** (1977) no. 2, 298 – 318. http://www.sciencedirect.com/science/article/pii/0550321377903844.

[7] A. Martin, W. Stirling, R. Thorne, and G. Watt, *Parton distributions for the LHC*, Eur.Phys.J. **C63** (2009) 189–285, arXiv:0901.0002 [hep-ph].

[8] H.-L. Lai, M. Guzzi, J. Huston, Z. Li, P. M. Nadolsky, et al., *New parton distributions for collider physics*, Phys.Rev. **D82** (2010) 074024, arXiv:1007.2241 [hep-ph].

[9] R. D. Ball, V. Bertone, S. Carrazza, C. S. Deans, L. Del Debbio, et al., *Parton distributions with LHC data*, Nucl.Phys. **B867** (2013) 244–289, arXiv:1207.1303

[hep-ph].

[10] S. Forte and G. Watt, *Progress in the Determination of the Partonic Structure of the Proton*, Ann.Rev.Nucl.Part.Sci. **63** (2013) 291–328, arXiv:1301.6754 [hep-ph].

[11] S. D. Drell and T.-M. Yan, *Massive Lepton-Pair Production in Hadron-Hadron Collisions at High Energies*, Phys. Rev. Lett. **25** (Aug, 1970) 316–320. http://link.aps.org/doi/10.1103/PhysRevLett.25.316.

[12] ATLAS Collaboration Collaboration, G. Aad et al., *Measurement of the high-mass Drell–Yan differential cross-section in pp collisions at sqrt(s)=7 TeV with the ATLAS detector*, Phys.Lett. **B725** (2013) 223–242, arXiv:1305.4192 [hep-ex].

[13] R. Boughezal, Y. Li, and F. Petriello, *Disentangling radiative corrections using high-mass Drell-Yan at the LHC*, Phys.Rev. **D89** (2014) 034030, arXiv:1312.3972 [hep-ph].

[14] L. Evans and P. Bryant, *LHC Machine*, JINST **3** (2008) .

[15] CMS Collaboration, *The CMS experiment at the CERN LHC*, JINST **3** (2008) .

[16] ATLAS Collaboration, G. Aad et al., *The ATLAS Experiment at the CERN Large Hadron Collider*, J. Instrum. **3** (2008) S08003.

[17] LHCb Collaboration, *The LHCb Detector at the LHC*, JINST **3** (2008) .

[18] ALICE Collaboration, *The ALICE experiment at the CERN LHC*, JINST **3** (2008) .

[19] ATLAS Collaboration, G. Aad et al., September, 2013. https://twiki.cern.ch/twiki/bin/view/AtlasPublic/LuminosityPublicResults.

[20] E. Moyse, A. Nisati, A. Oh, and D. Quarrie, *REPORT OF THE MUON RECONSTRUCTION SELECTION PANEL*, Tech. Rep. ATL-COM-MUON-2011-040, CERN, Geneva, Dec, 2011.

[21] ATLAS Collaboration Collaboration, G. Aad et al., *Measurement of the muon reconstruction performance of the ATLAS detector using 2011 and 2012 LHC proton-proton collision data*, arXiv:1407.3935 [hep-ex].

[22] ATLAS Collaboration Collaboration, G. Aad et al., *Electron reconstruction and identification efficiency measurements with the ATLAS detector using the 2011 LHC proton-proton collision data*, Eur.Phys.J. **C74** (2014) 2941, arXiv:1404.2240

[hep-ex].

[23] W. Buttinger, A. Daniells, R. Hickling, and G. Anders, *Performance of the ATLAS Level-1 Trigger System in 2011/12*, tech. rep. https://cds.cern.ch/record/1445272?

[24] GEANT4 Collaboration, S. Agostinelli et al., *GEANT4: A Simulation toolkit*, Nucl.Instrum.Meth. **A506** (2003) 250–303.

[25] T. Sjostrand, S. Mrenna, and P. Z. Skands, *A Brief Introduction to PYTHIA 8.1*, Comput.Phys.Commun. **178** (2008) 852–867, arXiv:0710.3820 [hep-ph].

[26] P. Nason, *A New method for combining NLO QCD with shower Monte Carlo algorithms*, JHEP **0411** (2004) 040, arXiv:hep-ph/0409146 [hep-ph].

[27] S. Frixione, P. Nason, and C. Oleari, *Matching NLO QCD computations with Parton Shower simulations: the POWHEG method*, JHEP **0711** (2007) 070, arXiv:0709.2092 [hep-ph].

[28] S. Alioli, P. Nason, C. Oleari, and E. Re, *A general framework for implementing NLO calculations in shower Monte Carlo programs: the POWHEG BOX*, JHEP **1006** (2010) 043, arXiv:1002.2581 [hep-ph].

[29] S. Frixione and B. R. Webber, *Matching NLO QCD computations and parton shower simulations*, JHEP **0206** (2002) 029, arXiv:hep-ph/0204244 [hep-ph].

[30] S. Frixione, F. Stoeckli, P. Torrielli, and B. R. Webber, *NLO QCD corrections in Herwig++ with MC@NLO*, JHEP **1101** (2011) 053, arXiv:1010.0568 [hep-ph].

[31] G. Corcella, I. Knowles, G. Marchesini, S. Moretti, K. Odagiri, et al., *HERWIG 6: An Event generator for hadron emission reactions with interfering gluons (including supersymmetric processes)*, JHEP **0101** (2001) 010, arXiv:hep-ph/0011363 [hep-ph].

[32] B. Andersson, G. Gustafson, G. Ingelman, and T. Sjostrand, *Parton fragmentation and string dynamics*, Physics Reports **97** (1983) no. 2–3, 31 – 145. http://www.sciencedirect.com/science/article/pii/0370157383900807.

[33] B. Webber, *A {QCD} model for jet fragmentation including soft gluon interference*, Nuclear Physics B **238** (1984) no. 3, 492 – 528. http://www.sciencedirect.com/science/article/pii/055032138490333X.

[34] P. Golonka and Z. Was, *PHOTOS Monte Carlo: A Precision tool for QED corrections in Z and W decays*, Eur.Phys.J. **C45** (2006) 97–107, arXiv:hep-ph/0506026 [hep-ph].

[35] R. Gavin, Y. Li, F. Petriello, and S. Quackenbush, *FEWZ 2.0: A code for hadronic Z production at next-to-next-to-leading order*, Comput.Phys.Commun. **182** (2011) 2388–2403, arXiv:1011.3540 [hep-ph].

[36] ATLAS Collaboration Collaboration, G. Aad et al., *Measurement of the low-mass Drell-Yan differential cross section at $\sqrt{s}$ = 7 TeV using the ATLAS detector*, JHEP **1406** (2014) 112, arXiv:1404.1212 [hep-ex].

[37] K. Bachas et al., *Measurement and QCD Analysis of Differential Inclusive $W^{+/-} \to l\nu$ and $Z/\gamma^* \to ll$ Production and Leptonic Decay Cross Sections with ATLAS: Analysis STDM-2012-20: W and Z inclusive cross section with 2011 data*, Tech. Rep. ATL-COM-PHYS-2013-217, CERN, Geneva, Feb, 2012.

[38] *Preliminary results on the muon reconstruction efficiency, momentum resolution, and momentum scale in ATLAS 2012 pp collision data*, Tech. Rep. ATLAS-CONF-2013-088, CERN, Geneva, Aug, 2013.

[39] ATLAS Collaboration Collaboration, G. Aad et al., *Performance of the ATLAS muon trigger in pp collisions at $\sqrt{s} = 8$ TeV*, arXiv:1408.3179 [hep-ex].

[40] R. Barlow and C. Beeston, *Fitting using finite Monte Carlo samples*, Computer Physics Communications **77** (1993) no. 2, 219 – 228. http://www.sciencedirect.com/science/article/pii/001046559390005W.

[41] g. Z', *Search for high-mass dilepton resonances in 21 fb-1 of pp collisions at sqrt(s) = 8 TeV*, Tech. Rep. ATL-COM-PHYS-2013-1033, CERN, Geneva, Jul, 2013. Supporting documentation for the paper on the full 2012 data set at 8 TeV.

[42] M. Cacciari, M. Czakon, M. Mangano, A. Mitov, and P. Nason, *Top-pair production at hadron colliders with next-to-next-to-leading logarithmic soft-gluon resummation*, Phys.Lett. **B710** (2012) 612–622, arXiv:1111.5869 [hep-ph].

[43] M. Beneke, P. Falgari, S. Klein, and C. Schwinn, *Hadronic top-quark pair production with NNLL threshold resummation*, Nucl.Phys. **B855** (2012) 695–741, arXiv:1109.1536 [hep-ph].

[44] *Percent Level Precision Physics at the Tevatron: First Genuine NNLO QCD Corrections to $q\bar{q} \to t\bar{t} + X$*, Phys.Rev.Lett. **109** (2012) 132001, arXiv:1204.5201 [hep-ph].

[45] M. Czakon and A. Mitov, *NNLO corrections to top-pair production at hadron colliders: the all-fermionic scattering channels*, JHEP **1212** (2012) 054, arXiv:1207.0236 [hep-ph].

[46] M. Czakon and A. Mitov, *NNLO corrections to top pair production at hadron colliders: the quark-gluon reaction*, JHEP **1301** (2013) 080, arXiv:1210.6832 [hep-ph].

[47] M. Czakon, P. Fiedler, and A. Mitov, *The total top quark pair production cross-section at hadron colliders through $\mathcal{O}(\alpha_S^4)$*, Phys. Rev. Lett **110** (2013) .

[48] M. Czakon and A. Mitov, *Top++: A Program for the Calculation of the Top-Pair Cross-Section at Hadron Colliders*, Comput.Phys.Commun. **185** (2014) 2930, arXiv:1112.5675 [hep-ph].

[49] M. Botje, J. Butterworth, A. Cooper-Sarkar, A. de Roeck, J. Feltesse, et al., *The PDF4LHC Working Group Interim Recommendations*, arXiv:1101.0538 [hep-ph].

[50] A. Martin, W. Stirling, R. Thorne, and G. Watt, *Uncertainties on alpha(S) in global PDF analyses and implications for predicted hadronic cross sections*, Eur.Phys.J. **C64** (2009) 653–680, arXiv:0905.3531 [hep-ph].

[51] J. Gao, M. Guzzi, J. Huston, H.-L. Lai, Z. Li, et al., *The CT10 NNLO Global Analysis of QCD*, Phys.Rev. **D89** (2014) 033009, arXiv:1302.6246 [hep-ph].

[52] B. Laforge and L. Schoeffel, *Elements of statistical methods in high-energy physics analyses*, Nuclear Instruments and Methods in Physics Research Section A: Accelerators, Spectrometers, Detectors and Associated Equipment **394** (1997) no. 1–2, 115 – 120. http://www.sciencedirect.com/science/article/pii/S0168900297006499.

[53] G. D'Agostini, *A multidimensional unfolding method based on Bayes' theorem*, Nuclear Instruments and Methods in Physics Research Section A: Accelerators, Spectrometers, Detectors and Associated Equipment **362** (1995) no. 2–3, 487 – 498. http://www.sciencedirect.com/science/article/pii/016890029500274X.

[54] *Proceedings of the PHYSTAT 2011 Workshop on Statistical Issues Related to Discovery Claims in Search Experiments and Unfolding*. 2011. https://cdsweb.cern.ch/record/1306523.

[55] L. Armitage, F. Ellinghaus, R. Hickling, U. Klein, M. Lisovyi, E. Rizvi, and M. Zinser, *Measurement of the high-mass Drell-Yan double-differential cross-section in pp collisions at sqrt(s) = 8 TeV*, Tech. Rep. ATL-COM-PHYS-2014-376, CERN, Geneva, Apr, 2014.

[56] A. Andonov, A. Arbuzov, D. Bardin, S. Bondarenko, P. Christova, et al., *SANCscope - v.1.00*, Comput.Phys.Commun. **174** (2006) 481–517, arXiv:hep-ph/0411186 [hep-ph].

[57] A. Arbuzov, R. Sadykov, and Z. Was, *QED Bremsstrahlung in decays of electroweak bosons*, Eur.Phys.J. **C73** (2013) 2625, arXiv:1212.6783 [hep-ph].

[58] ATLAS Collaboration, G. Aad et al., *Improved luminosity determination in pp collisions at $\sqrt{s}$ = 7 TeV using the ATLAS detector at the LHC*, Eur.Phys.J. **C73** (2013) 2518, arXiv:1302.4393 [hep-ex].

[59] M. Lisovyi, *Private Communication*. DESY.

[60] ATLAS Collaboration Collaboration, G. Aad et al., *Measurement of the inclusive $W^{\pm}$ and Z/gamma cross sections in the electron and muon decay channels in pp collisions at $\sqrt{s} = 7$ TeV with the ATLAS detector*, Phys.Rev. **D85** (2012) 072004, arXiv:1109.5141 [hep-ex].

List of Figures

List of Tables